

Investigation on the Electrical and Cold Emission Properties of Wide Band Gap Perovskite Oxide BaSnO_3

THESIS SUBMITTED FOR THE DEGREE OF
DOCTOR OF PHILOSOPHY (SCIENCE)
OF
JADAVPUR UNIVERSITY



By

Suvra Pal

Thin Film & Nanoscience Laboratory,
Department of Physics,
Jadavpur University, Kolkata-700032, India
May 2023



JADAVPUR UNIVERSITY
KOLKATA – 700 032, INDIA
Telephone – 9133-24138917

FACULTY OF SCIENCE
DEPARTMENT OF PHYSICS

Ref. No. _____

Dated 22.05.2023

CERTIFICATE FROM THE SUPERVISORS

This is to certify that the thesis entitled “Investigation on the Electrical and Cold Emission Properties of Wide Band Gap Perovskite Oxide BaSnO_3 ” submitted by Suvra Pal, who got her name registered on 20/09/2018 for the award of Ph.D. (Science) degree of Jadavpur University, is absolutely based upon her own work under the supervision of Prof. K. K. Chattopadhyay and Prof. S. Mukhopadhyay and that neither this thesis nor any part of it has been submitted for either any degree/diploma or any other academic award anywhere before.


22.5.23


Prof. (Dr.) Kalyan Kumar Chattopadhyay

Signature of the supervisor

Date with official seal



Professor
Department of Physics
Jadavpur University
Kolkata – 700 032


22.05.23

Prof. (Dr.) Subhadipta Mukhopadhyay

Signature of the supervisor

Date with official seal

Dr. Subhadipta Mukhopadhyay
Professor Dept. of Physics
Jadavpur University, Kolkata-700 032

To my beloved parents

for standing always by my side

&

To my husband

for believing in me

Acknowledgement

The PhD thesis entitled “**Investigation on the Electrical and Cold Emission Properties of Wide Band Gap Perovskite Oxide BaSnO₃**” is the ultimate outcome of my five years long journey of struggle and patience. In addition to science and academics, I have had the incredible good fortune to gain valuable lessons regarding life at Jadavpur University over the years. It’s true that the journey wasn’t always easy, but as the time went on everything seems to be more and more interesting and discovering new things became joyful. My PhD thesis submission marks the culmination of this fantastic journey. I believe that I could not be able to succeed this roller-coaster period without the advice, motivation, support and help of some wonderful people. I feel incredibly fortunate to be able to express to them my appreciation and acknowledgement.

First and foremost, I would like to thank God for giving me the strength to complete the dissertation.

I would like to express my deepest gratitude to my proficient guide Prof. (Dr.) Kalyan Kumar Chattopadhyay, HOD, Department of Physics, Jadavpur University for providing me the opportunity to carry out my research work in his group. His guidance, constant support and motivation have made me confident and motivated during my hard times. His insight in the field of materials physics and nanotechnology has inspired me to undertake my own journey in this fascinating branch of science. I feel contented to have him for his constructive and precious suggestions, active teamwork and constant back-up.

I gratefully acknowledge my other supervisor Prof. (Dr.) Subhadipta Mukhopadhyay, faculty member, Department of Physics, Jadavpur University for his valuable suggestions, constant motivation and friendly behavior. It would have been impossible to get so far without his continuous support and understanding.

I am indebted to Prof. (Dr.) Sukhen Das, Ex-HOD of the Department of Physics, Jadavpur University and all other authorities for their support and providing necessary instrumental and laboratory facilities during my research work. I am also thankful to all the faculty members and non-teaching staffs of Department of Physics and the School of Materials Science and Technology, Jadavpur University for their support.

My sincere gratitude goes out to Dr. Chandan Kumar Ghosh, faculty member of School of Materials Science and Technology, Jadavpur University for being my RAC member and also for his valuable suggestions during the assessment periods. I convey my heartiest greetings to Dr. Sourav Sarkar, Director of School of Materials Science and Technology, Jadavpur University for his wholehearted support and encouragements.

I shall always be grateful to my senior Dr. Nirmalya Sankar Das (Nirmalya Da) for his cordial demeanor and brotherly attitude. His enthusiasm for research and commitment to it have inspired me to become a more driven researcher overall. His vast knowledge, talent at composing manuscripts, thoughts, and suggestions really helped me along the way.

In this connection, I should mention with a great pleasure the names of all my former and present senior lab mates; Bikram da, Biswajit da, Karamjyoti da, Kausik da (Chanda), Madhupriya di, Missisipi di, Nripen da, Pramita di, Rimpa di, Rituparna Di, Saikat da, Shrabani di, Subhasis da, Tufan da for their help throughout my journey. I would like to specially mention Dimitra di for her elder sister like nature and commitment towards work.

I would like to thank all my junior lab colloques; Anibrata, Ankita, Arnab, Nabanita, Pulok, Souvik, Suvankar (Poddar). I am also thankful to my colleagues; Dipanwita, Kausik (Sardar), Ratna, Suvankar (Mondal). Their presence made me stronger and motivated into my work.

Special thanks goes to Brahami for being there always for me and for helping me a lot during my research work. I must thank her for always listening to me and helping me to find a solution, whatever it be my personal problems or related to my research.

I would like to thank all the graduate (M.Sc and M.Tech) students in Prof. Chattopadhyay's Lab who helped me during this period.

I am grateful to Council of Scientific & Industrial Research (CSIR), Government of India, for rewarding me CSIR-SRF [File no. 09/096(0911)/2017-EMR-I] during the execution of my PhD research work. Furthermore, I would also like to thank University with Potential for Excellence scheme (UPE-II), Department of Science and Technology (DST) and TEQIP programme for funding various projects during my PhD days to our Lab.

Acknowledgement

The endeavor would not have been successful without my parents' unwavering support and motivation, who made a lot of sacrifices to keep me committed to my goal. They have quietly contributed to all of my life's achievements, which is priceless. Last but not least, I would like to thank my spouse from the bottom of my heart. Truly, I have no words to express my gratitude to him, because I believe that our association is beyond to this sort of writing. Finally, I would like to dedicate this thesis in honor of my 'Baba', 'Ma' and my husband 'Krishnendu'.

22nd May 2023 (22/05/2023)

Department of Physics, Jadavpur University
Kolkata-700032, India

Suvra Pal
(Suvra Pal)

Table of Contents

Acknowledgement	vii
Table of Contents	xi
Abstract	xix
List of publications	xxi
1. Introduction	1
1.1. Perovskite oxides	3
1.2. Barium Stannate (BaSnO_3)	4
1.2.1. Crystal structure	5
1.2.2. Electronic structure	6
1.2.3. Electrical properties	6
1.2.4. Optical properties	7
1.2.5. Thermal properties	9
1.3. Basic theory of Complex Impedance Spectroscopy (CIS) analysis to study the electrical properties	10
1.3.1. Dielectric property	13
1.3.2. Dielectric relaxation analysis	15
1.3.3. Complex impedance analysis	17
1.3.4. AC conductivity analysis	19
1.3.5. Modulus spectroscopy analysis	20
1.3.5.1. Scaling of modulus spectra	22
1.4. Basic theory of Cold-Cathode Emission	22
1.5. Basic theory on the improvement of electrical properties of perovskite ceramic/polymer composite	28

1.5.1. Why to form?	28
1.5.2. Relation between dielectric permittivity and the piezoelectric coefficients	29
1.6. Aims and objectives	31
1.7. Outlines of the thesis	32
1.8. References	33
2. Literature Survey	41
2.1. Previous reports on synthesis of BaSnO_3	43
2.1.1. Solid-State Reaction (SSR) method	43
2.1.2. Sol-Gel method	46
2.1.3. Solution Combustion Synthesis (SCS)	48
2.1.4. Hydro/Solvothermal method	48
2.1.5. Co-precipitation method	50
2.1.6. Film deposition	52
2.2. Stability issues	53
2.3. BaSnO_3 : previous reports on applications	54
2.3.1. Ceramic Capacitors	54
2.3.2. Gas Sensors	58
2.4. Electron field-emission as a non-trivial application	60
2.5. Improvement of the electrical properties of perovskite/polymer composite	62
2.6. References	63
3. Instruments and apparatus	71
3.1. Major synthesis apparatus	73
3.1.1. Furnace	73
3.1.2. Oven	73

3.1.3. Autoclave	73
3.2. Characterization techniques	74
3.2.1. Crystallographic study: X-ray diffraction (XRD)	74
3.2.2 Microscopic techniques	75
3.2.2.1 Field emission scanning electron microscopy (FESEM)	75
3.2.2.2. Transmission electron microscopy (TEM)	76
3.2.3 Spectroscopic techniques	78
3.2.3.1 Energy Dispersive X-ray Spectroscopy (EDX)	78
3.2.3.2 X-ray Photoelectron Spectroscopy (XPS)	78
3.2.3.3. UV-Vis-NIR Spectroscopy	79
3.2.3.4. Fourier Transform Infra-red (FTIR) Spectroscopy	80
3.3. Impedance analyzer	81
3.4. Field emission measurement apparatus	82
3.4.1. High voltage D. C. power supply	83
3.5. Oscilloscope	83
3.6. References	84
4. Effect of calcination temperature on structural and electrical properties of nanocrystalline BaSnO₃	85
Abstract	87
4.1. Introduction	87
4.2. Experimental	89
4.2.1. Synthesis of BaSnO ₃ powders	89
4.2.2. Characterizations	89
4.3. Results and discussion	89
4.3.1. Structural studies	89
4.3.2. Morphological studies	93

4.3.3. Compositional and Optical studies	94
4.3.4. Electrical properties studies	95
4.3.4.1. Dielectric permittivity analysis and relaxation formalism	95
4.3.4.2. Tangent loss and Electrical conductivity studies	97
4.3.4.3 Complex Impedance Spectra (CIS) analysis	98
4.4. Conclusion	101
4.5. References	102
5. Exploring DC bias tuned electrical properties and non-Debye relaxation of vanadium doped BaSnO₃ nanocubes	105
Abstract	107
5.1. Introduction	107
5.2. Experimental	109
5.2.1. Synthesis of vanadium doped BaSnO ₃ nanocubes	109
5.2.2. Characterizations	109
5.3. Results and discussion	110
5.3.1. Crystallographic studies	110
5.3.2. Morphological studies	111
5.3.3. Compositional studies	112
5.3.4. Electrical properties studies	115
5.3.4.1. Dielectric permittivity, loss and electrical conductivity studies	115
5.3.4.2. Complex Impedance Spectra (CIS) analysis and DC bias	116

5.3.4.3. Effect of DC bias on dielectric permittivity	118
5.3.4.4. Modulus spectroscopy studies	119
5.3.4.5. Dielectric relaxation formalism analysis	121
5.4. Conclusion	122
5.5. References	122
6. V doped BaSnO₃ nanocubes as a potential cold cathode: Theoretical and experimental investigation	127
Abstract	129
6.1. Introduction	129
6.2. Experimental	131
6.2.1. Synthesis of BaSn _{1-x} V _x O ₃ nanocubes	131
6.2.2. Characterizations	131
6.3. Results and discussion	132
6.3.1. Structural studies	132
6.3.2. Morphological studies	133
6.3.3. Compositional studies	133
6.3.4. Dielectric constant and resistivity analysis	135
6.3.5. ANSYS simulation studies	136

6.3.6. Density Functional Theory (DFT) studies for work function	138
6.3.7. Cold Cathode emission studies	139
6.3.7.1. Field emission behaviour analysis and Fowler-Nordheim (FN) plot	139
6.3.7.2. Effect of inter-electrode separation for optimum device configuration	142
6.7. Conclusion	144
6.8. References	145
7. Enhanced electrical properties of BaSnO₃/PVDF nanocomposite: Mechanical energy harvesting	149
Abstract	151
7.1. Introduction	151
7.2. Methods & enumeration	153
7.2.1. Materials	153
7.2.2. BaSnO ₃ nanorod synthesis	153
7.2.3. PVDF film fabrication	153
7.2.4. BSO/PVDF composite film fabrication	154
7.2.5. Experimental techniques	154
7.3. Results and discussion	154
7.3.1. Structural analysis	154
7.3.2. Optical property studies	155
7.3.3. Morphological studies	155
7.3.4. Compositional analysis	156
7.3.5. FTIR analysis	157

7.3.6. Electrical properties studies	160
7.3.7. The output performance of BSO/PVDF nanocomposite films	162
7.4. Conclusion	165
7.5. References	165
8. Conclusion and Future outlook	169
8.1. Conclusion	171
8.2. Future outlook	172

Thesis title:

Investigation on the Electrical and Cold Emission Properties of Wide Band Gap Perovskite Oxide BaSnO₃

Abstract

Ternary metal oxides with the chemical formula ABO₃ and crystal structure resembling CaTiO₃ are typically referred as perovskite oxide in the honor of Russian scientist L. A. Perovski. Perovskite oxides have received tremendous attention in recent years from both theoretical and practical perspectives due to their fascinating characteristics, such as their high energy storage capacity, visible light transparency, ferroelectricity etc. In this family, the interplay among structural, optical and transport properties are noted frequently which helps to integrate a number of intriguing features. Recently a lot of interest on wide band gap perovskite oxides especially on barium stannate (BaSnO₃) has grown due to its exciting optical, thermal and electrical properties. BaSnO₃ is visibly transparent having a wide band gap of ~3.1 eV and high thermal stability (>1000 °C). By simply changing the processing temperature and doping with right cation, it is possible to readily modify the electrical properties of BaSnO₃, as example dielectric permittivity, electrical conductivity etc. Additionally, in the display sectors, BaSnO₃ in nano/micro form can be used to design numerous electronic devices, including flexible screens and other forms of field emission display units due to its desirable work function, electron affinity and tunable electrical property.

Even though there have been numerous studies on barium stannate and its properties published in the literature, there are still certain issues remain unresolved. The aim of this doctoral thesis, "**Investigation on the Electrical and Cold Emission Properties of Wide Band Gap Perovskite Oxide BaSnO₃**," is to investigate the synthesis methods, various properties, and different uses of both pure and doped barium stannate. Another important objective is to fabricate BaSnO₃/polymer nanocomposite and exploring their structural and electrical characteristics to improve their multipurpose performances. This dissertation firstly describes the synthesis process to prepare barium stannate and then modify the pure system to study different properties of the altered system.

Aiming to this, the nanocrystalline barium stannate powder was synthesized following traditional solid-state reaction route. The grain size as well as the density (or in other word, porosity) of the samples were varied by varying synthesis temperature. With routine structural, morphological, compositional and optical characterizations, the effects of grain size and density alteration on the electrical properties of the system were analyzed. It was found that the overall polarization *i.e.* the dielectric permittivity was increased with the grain size and the density of the sample. Also, the conductivity was enhanced due to the grain size increment which provides better ordered path in order to transport the charge carriers. Hence, the nanocrystalline BaSnO₃ is inferred as potential candidate for thermally stable ceramic capacitor.

Encouraged by the results, investigations were done to study the changes in the electrical properties of transition metal ion doped BaSnO₃, due to an alteration in external DC bias. Although, due to the smaller grain size and higher porosity, the room temperature permittivity and the conductivity were decreased for

the doped sample, but the application of DC bias was more prominent for the doped samples. Being smaller in size, vanadium plays important role in formation of lighter dipoles which helps in dipolar polarization in presence of external DC bias. The dielectric permittivity was increased with DC bias, whereas the grain and grain boundary resistances were reduced resulting an indirect enhancement in conductivity. Thus, the vanadium doped BaSnO_3 can serve as a tuning capacitive material at room temperature.

The suitable work function (3.04 eV), tunable electrical property, visible light transparency motivated us to find out whether the material can be used in a true multipurpose way. Aiming to this, simulation-based field electron emission was carried out using ANSYS-MAXWELL software. Encouraged by the positive results, the actual field emission experiment was investigated for pure and vanadium doped barium stannate nanocubes. The particle size variation has a significant impact on improving the emission efficiency of the doped samples. The turn on field was reduced and the enhancement factor was elevated for the vanadium doped BaSnO_3 . For practical use in microelectronics, the optimum device condition was achieved by analyzing the effect of inter-electrode separation on the emission properties. Also, the doped sample showed a high temporal stability which is another important factor to consider.

The easily tunable electrical properties, as observed from the above studies, can further be extended in fulfilling the need for lead free perovskite/polymer nanocomposite with high dielectric permittivity, superior flexibility, large breakdown strength and low loss, $\text{BaSnO}_3/\text{PVDF}$ nanocomposite films were prepared. Targeting this, BaSnO_3 nanorods were purposely synthesized for less agglomeration and easy achievement to the percolation threshold. The electrical properties were enhanced for the hybrid films along with an enhancement in electroactive phase of the polymer. Additionally, the composite films exhibited high transparency in visible region. These highly flexible, transparent hybrid films with high permittivity, better conductivity and low loss showed an enhanced open circuit voltage and short circuit current under free hand hammering. This work opens up newer possible applications for BaSnO_3 based composites beyond the traditional applications like sensors, ceramic capacitors etc.

Signature of the candidate: *Suvra Pal*

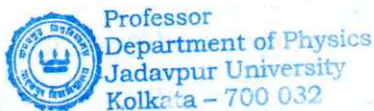
Date: 22.05.2023

[Signature] 22.5.23

Prof. (Dr.) Kalyan Kumar Chattopadhyay

Signature of the supervisor

and Date with Office seal



Subhadipta Mukhopadhyay
22/5/23

Prof. (Dr.) Subhadipta Mukhopadhyay

Signature of the supervisor

and Date with Office seal

Dr. Subhadipta Mukhopadhyay
Professor Dept. of Physics
Jadavpur University, Kolkata-700 032

List of publications

List of publications (presented in this thesis)

1. Bias-tuned dielectric properties and Non-Debye relaxation in vanadium doped BaSnO₃ nanocubes
Suvra Pal, Nirmalya Sankar Das, Souvik Bhattacharjee, Subhadipta Mukhopadhyay and Kalyan Kumar Chattopadhyay
Materials Research Express 6 (10) (2019)105029
2. V doped BaSnO₃ nanocubes as a Field emitting material: Experimental and theoretical investigation
Suvra Pal, Nirmalya Sankar Das, Brahami Das, Bikram Kumar Das, Subhadipta Mukhopadhyay and Kalyan Kumar Chattopadhyay
Applied Surface Science 530 (2020) 147102
3. Calcination Temperature Dependent Dielectric Properties of Nanocrystalline BaSnO₃
Suvra Pal, Nirmalya S. Das, Brahami Das, Subhadipta Mukhopadhyay and Kalyan K. Chattopadhyay
ECS Journal of Solid State Science and Technology 10 (2021) 071018
4. Enhanced electrical properties of BaSnO₃/PVDF nanocomposite for mechanical energy harvesting
Suvra Pal, Nirmalya Sankar Das, Suvankar Mondal, Suvankar Poddar, Subhadipta Mukhopadhyay and Kalyan Kumar Chattopadhyay
Ready for Communication

List of other publications (not included in this thesis)

5. Novel Ag₂O-Ga₂O₃ type II p-n heterojunction as efficient water cleanser for green cleaning technology
Brahami Das, Biswajit Das, Nirmalya Sankar Das, **Suvra Pal**, Bikram Kumar Das, Subrata Sarkar, and Kalyan K. Chattopadhyay

Applied Surface Science 515 (2020) 145958

6. Enhanced field emission properties of rGO wrapped Ga₂O₃ micro/nanobricks: Experimental investigation with theoretical validation
Brahami Das, Biswajit Das, Nirmalya Sankar Das, **Suvra Pal**, Bikram Kumar Das, Ratna Sarkar, Rimpa Khan, Subrata Sarkar, and Kalyan K. Chattopadhyay
Journal of Alloys and Compounds 902 (2022) 163726
7. Experimental and theoretical approaches of electron emission from hydrophobic rGO modified silicon nanowires
Ankita Chandra, Shrabani Ghosh, Bikram Kumar Das, **Suvra Pal**, Supratim Maity, Biswajit Das, Sourav Sarkar, KK Chattopadhyay
Applied Surface Science 608 (2023) 155174

Publications in conference proceedings and book chapter

8. BaSnO₃ nanoparticles as blue emitting phosphor and efficient photocatalyst
Suvra Pal, Nirmalya Sankar Das, Brahami Das, Biswajit Das, Subhadipta Mukhopadhyay and Kalyan Kumar Chattopadhyay
AIP Conference Proceedings 2220 (2020) 020014
9. Facile Preparation of Porous Ga₂O₃ Nano/microbars for Highly Efficient Photocatalytic Degradation
Brahami Das, Biswajit Das, Nirmalya Sankar Das, **Suvra Pal**, Ratna Sarkar, Subrata Sarkar and Kalyan K. Chattopadhyay
AIP Conference Proceedings 2220 (2020) 020013
10. Morphological tuning of low dimensional β -Ga₂O₃ for enhanced photocatalytic performance
Brahami Das, Nirmalya Sankar Das, Biswajit Das, Ratna Sarkar, **Suvra Pal**, Subrata Sarkar, and Kalyan K. Chattopadhyay
Basic and Applied Sciences into next frontiers, 2021, New Delhi Publishers, ISBN No: 978-81-948993-0-3

Papers presented in national and international level conferences

1. National Seminar on ‘Recent Trend in Frontier Research in Physics’ (**RTFRP-2018**).
Venue: Organized by Department of Physics, Jadavpur University, Kolkata, West Bengal (March 6, 2018)
Presentation Mode- **Poster** (*Morphology tuned BaSnO₃ for photocatalysis in UV region*)
2. National Seminar on ‘Physics at Surfaces and Interfaces of Soft Materials’ (**PSISM-2019**). Venue: Organized by Department of Physics, Jadavpur University, Kolkata, West Bengal. (September 26-27, 2019)
Presentation Mode- **Poster** (*Tuning of electrical properties of BaSnO₃ via vanadium doping*)
3. International Conference on Condensed Matter & Applied Physics (**ICC-2019**).
Venue: Govt. Engineering College, Bikaner, Rajasthan. (October 14-15, 2019)
Presentation Mode- **Poster** (*BaSnO₃ nanoparticles as blue emitting phosphor and efficient photocatalyst*)
4. National Conference on ‘Frontiers of Material Science and Photonics: Issues and Developments’ (**NCFMSP-2020**). Venue: Organized by Department of Physics, Sidhu-Kanhu-Birsha University, Purulia, West Bengal (March 5-6, 2020)
Presentation Mode- **Oral** (*Particle size dependent electrical properties of BaSnO₃ nanocrystals*)
5. International Conference on Recent Trends in Basic and Applied Sciences (**VirtCon2020**). Venue: Organized by Department of Physics, Bhairab Ganguly College and Dam Dam Motijheel College (6th -7th July, 2020)
Presentation Mode- **Oral** (*Colloidally prepared BaSnO₃ nanoparticles for photocatalytic degradation of organic pollutant eosin B*)
6. International Web Conference on Recent Advances in Nanoscience & Nanotechnology for High-end Applications (**IWCRAHA-2020**). Organized by Department of Applied Science and Humanities, Assam University Silchar (25th - 26th July, 2020)
Presentation Mode- **Oral** (*V doped low dimensional BaSnO₃ cold cathodes: Experimental verification of simulation based prediction*)

7. National Conference on Materials and Devices (**NCMD-2020**). Organized by Department of Physics, Faculty of Engineering and Computing Sciences, Teerthanker Mahaveer University, Moradabad (18th -19th December, 2020)

Presentation Mode- ***Oral*** (*Realization of theretically predicted cold electron emission from oxide perovskite: vanadium doped BaSnO₃ nanocubes*)

8. 6th International Conference on Nanoscience and Nanotechnology (Virtual Conference) (**ICONN 2021**). Organized by SRM Institute of Science and Technology, India, (1st – 3rd February, 2021)

Presentation Mode- ***Oral*** (*Calcination temperature dependent dielectric propreties of nanocrystalline BaSnO₃*)

Introduction

Over the course of human history, materials science has left a remarkable footprint on the development of civilizations. Better materials have ever enriched the mankind by providing tools to spread and conquer.

In the recent, the emerging thrust of lead free perovskites has pushed the researchers to search for alternative perovskite materials to use in the fast changing world of modern inexpensive electronic devices, such as multilayered energy storing capacitors, superior ultrasonic transducers, efficient field emission display units, gas sensing devices etc. The growth of microelectronics demands designing smaller and faster devices. Thus, the highly dense ultrafine particles of perovskite oxides not only increase the surface area, energy density and breakdown strength of the materials but also help in miniaturization of the devices. In addition, the wide band gap (> 3.1 eV) with significant visible light transparency ($> 85-90\%$) and large surface area makes them compatible for transparent electronic devices.

1.1. Perovskite Oxides

Perovskites have emerged as one of the auspicious and efficient cost-effective energy materials having large-scale technological applications in optoelectronic and photonic devices. In the year of 1839, a German scientist discovered calcium titanate type materials.¹ His name was Gustav Rose. He found the materials in Ural Mountains of Russia. This newly discovered material was referred to as ‘Perovskite’ to respect the Russian mineralogist Lev Von Perovski, who did pioneering work in this field after G. Rose.² Over the years, with the discovery of newer materials having similar crystalline structure of ABO_3 (*i.e.* $CaTiO_3$) are now generally recognized as Perovskites. The ideal cubic perovskite is composed of very simple arrangements of cation and anion elements. The typical crystal structure of any cubic perovskite is shown in **Figure 1.1**. For cubic one, the lattice parameters are $a = b = c$ and $\alpha = \beta = \gamma = 90^\circ$.³ However, Goldschmidt introduced ‘tolerance factor’ (t) to check the stability of perovskite structure for a given set of positive and negative ions. A, B are the cations and O is the anion. Commonly, the ionic radius of A is greater than that of B. For the ideal cubic perovskite, the B cation has 6-fold

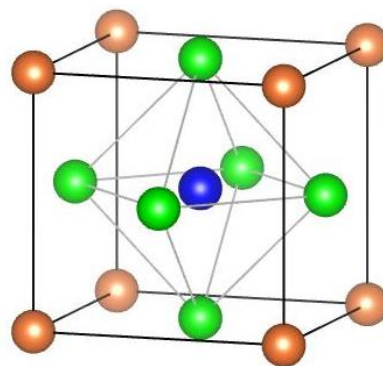


Fig. 1.1. General crystal structure of a cubic perovskite

coordination encircled with anionic octahedron and the A cation has 12-fold cuboctahedral coordination. The oxygen anions are surrounded by a pair of B cations and two pairs of A cations. From **Figure 1.1** it can be seen that for the stability of cubic perovskite structure (R_A+R_O) must be equal to $\sqrt{2}(R_B+R_O)$. R_A , R_B and R_O are radii of corresponding ions. The tolerance factor 't' is written as

$$t = \frac{(R_A+R_O)}{\sqrt{2}(R_B+R_O)} \quad (1.1)$$

called, Goldschmidt's tolerance factor. Distortions from the value of $t = 1$ can arise due to the radii mismatch of the two types of ions, resulting in non-ideal perovskite and also other nonperovskite structures.⁴ the value of 't' should be in between 0.825 and 1.059 for perovskite structure.⁵ If B cation is smaller in size than A cation then 't' is greater than 1 and in opposite case 't' is less than 1. Actually, the tolerance factor denotes the level of packing of ions in the unit cell of perovskites. A deviation of 't' from 1 designates deformation in perovskite structure with lower symmetry.⁶ There are mainly two types of perovskites: oxides (ABO_3) and halides (ABX_3 , $X = Cl, Br, I$). Three more categories are used to further categorize the halide type perovskites: inorganic, organic and hybrid type. The oxide family has a huge branch of different anion-cation combination. Apart from the original ABO_3 structure, various types of other perovskite oxides can be found, such as double perovskite, triple perovskite, layered perovskite etc. The chemical formulae of these perovskites are A_2BO_4 (eg. Sr_2RuO_4), $A_2B'B''O_6$ (eg. Ba_2FeReO_6), $A_2A'B_2B'O_9$ (eg. $La_2SrCo_2FeO_9$).⁷⁻⁹ From time to time many researchers also reported about other perovskite oxides having different structural formulae and are called homologous series of perovskite oxides. For example, $A_{n+1}B_nO_{3n+1}$, $A_nB_nO_{3n+1}$, $Bi_2A_{n-1}B_nO_{3n+1}$ etc.¹⁰⁻¹² The names of corresponding structures are Ruddlesden-Popper, Dion-Jacobson and Aurivillius respectively. The development of Chalcogenide based perovskites is also under research.¹³

1.2. Barium Stannate ($BaSnO_3$)

In BaO-SnO₂ binary system, three oxostannates (IV) are there: $BaSnO_3$, Ba_2SnO_4 and $Ba_3Sn_2O_7$. Among them $BaSnO_3$ (BSO) becomes popular among researchers in the past few decades due to its intriguing properties and its plausible application in diverse fields. It works well in the fields

of sensing devices, ceramic capacitors, memory devices, etc. because of its elevated thermal stability and large dielectric permittivity. ¹⁴ **Table 1.1** provides a summary of the reported values of the prime physical parameters of BaSnO₃.

Table 1.1. Physical properties of BaSnO₃

Property	Value	Reference
Crystal system	Cubic	[15]
Space group	Pm $\bar{3}$ m	[15]
Lattice parameters		[16]
a = b = c	4.115 Å	
$\alpha = \beta = \gamma$	90°	
Molar mass	278.08 gm	[16]
Density	7.24 g/cm ³	[17]
Melting point	2333 K	[18]
Band gap	3.1 eV	[19]
Thermal conductivity	9.68 Wm ⁻¹ K ⁻¹	[20]
Electronic effective mass	0.4 m ₀	[21]
Dielectric constant	20	[22]

1.2.1. Crystal structure

The cubic BaSnO₃ belonging from pm $\bar{3}$ m space group have four atoms present per unit crystallographic cell. The unit cell of cubic BaSnO₃ is exhibited in **Figure 1.2**. In the cubic structure, the eight corners are hold by Ba²⁺ ions, whereas the Sn⁴⁺ ion occupies the volume center and the six O²⁻ ions occupy the surface centers. The Ba²⁺ and O²⁻ ions combinedly form a compact cubic ball packing structure and the remaining octahedral hole is filled with smaller cation; Sn⁴⁺. Each Ba²⁺ ion is bonded with twelve O²⁻ ions resulting in formation of BaO₁₂ cuboctahedra. This cuboctahedra shares its twelve corners to twelve more identical BaO₁₂ cuboctahedra. It also shares faces with eight similar SnO₆ octahedra. Each

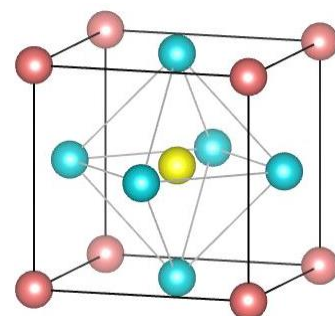


Fig. 1.2. Crystal structure of BaSnO₃

Sn^{4+} ion is connected to six equivalent O^{2-} ions to make SnO_6 octahedra. The octahedra shares its six corners with six identical SnO_6 octahedra and faces with eight alike BaO_{12} cuboctahedra. The SnO_6 octahedra are highly symmetric and non-tiled which is the base of the ideal cubic perovskite formation. The lattice parameters of BaSnO_3 are $a = b = c = 4.115 \text{ \AA}$ and $\alpha = \beta = \gamma = 90^\circ$.¹⁶ The Ba–O bond length is 2.96 \AA and the bond length of Sn–O is 2.09 \AA .²³ The X-ray density measured at room temperature by Swanson *et al.* is 7.238 g/cm^3 .¹⁷

1.2.2. Electronic structure

Since last few decades, numerous theoretical simulations have been performed to identify the electronic structure of BaSnO_3 . In most cases, Density Functional Theory (DFT) with Local Density Approximation (LDA) or Generalized Gradient Approximation (GGA) is employed for theoretical simulations.²⁴⁻²⁹ This LDA and GGA approximations are not so successful in the calculation of band gap. The hybrid functional approach proposed by Heyd, Scuzeria, and Ernzerhof (HSE06) provides better structural representation and an improved band gap value.³⁰⁻³⁴ The lattice constants of BSO was evaluated using PBEsol functional with an outcome value of 4.127 \AA , very close to experimental value (4.116 \AA).³⁵ The electronic structure of any material is based on the valance band (VB) and conduction band (CB). The VB is predominated by $O-p$ states and the CB shows $\text{Sn}-s$ character having minor involvement from $O-s$ orbitals. $\text{Ba}-d$ states in the conduction band is dominated in the range from 5 to 9 eV and the $\text{Ba}-f$ band arise for greater than 9 eV. The indirect band gap (IBG) having value 0.9 eV was found using PBEsol approach. For this the valance-band maximum (VBM) was at Γ point and the conduction-band minimum (CBm) was resided at R point of Brillouin zone. The VBM at Γ point has three fold degeneracy, exhibiting $O-p$ character. Kim *et. al* reported that BSO has an IBG of 2.48 eV using hybrid model of DFT which is near to the value of experimental band gap than what comes from LDA and GGA approach.³⁶ Also, the effective mass of electron may be computed using this approach. The value of the effective mass of electron was found at R- Γ combination is $1.463m_0$. This small value of electron effective mass suggests a good mobility of electrons in BSO.³⁶

1.2.3. Electrical properties

Fundamentally, polycrystalline BSO is a wide band gap semiconducting material having an indirect band gap of $\sim 3.1 \text{ eV}$ shows n-type behavior below 900°C .²² The pure material shows

conductivity within $10^{-2} \Omega/\text{cm}$. Thus the pure BSO can be used as transparent semiconducting oxide (TSO) in transparent optoelectronics. High dielectric constant along with high temperature stability (upto 1000°C) makes the material a potential candidate as thermally stable ceramic capacitor, gas sensor, memory device etc. As the inherent material is n-type, electrons are the primary charge carriers in this oxide. The oxygen vacancy generated due to high temperature preparation of the material is the main cause for being n-type. The frequency dependent conductivity of BSO was measured by Upadhyay and coworkers.³⁷ They reported that correlated barrier hopping of bipolarons is responsible for the conduction mechanism in the ceramic below 420 K, however above 420 K the conduction is due to the excitation of electrons to the conduction band from the localized state. The electrical transport parameters of pristine BSO can easily be tuned via suitable cation doping and creating oxygen vacancy.³⁸⁻⁴⁰ as the perovskite structure has a tendency to form solid solutions easily.

1.2.4. Optical properties

Pure BSO powder is white in color having a wide band gap of 3.1 eV. It shows a huge transparency in the visible regime of electromagnetic spectrum.⁴¹⁻⁴³ BSO exhibits a very strong and intense absorption band near 360 nm which becomes weaker with increasing wavelength *i.e.* in visible region. The band to band

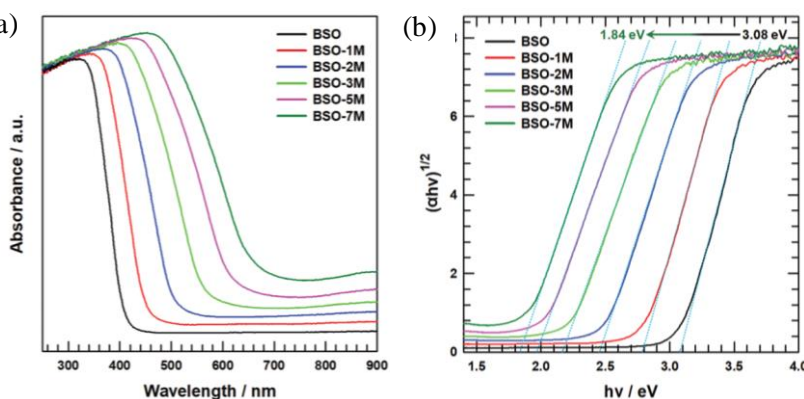


Fig. 1.3. (a) UV-Vis DRS spectra, (b) Plots of the transformed Kubelka-Munk function for different amount of oxygen vacancy

transition between 2p (O) and 5s (Sn) states is responsible for this intense and broad absorption.⁴⁴ It was proven by various groups of researchers that BSO possesses indirect type of optical band gap.⁴⁵ However, there are several methods to tune the band gap of BSO like oxygen pressure, oxygen vacancy incorporation, doping etc.⁴⁶⁻⁴⁷ According to Kim *et al.* the band gap of BSO can be decreased from 3.08 eV to 1.84 eV by systematic incorporation of oxygen vacancies.⁴⁷ The UV-Vis DRS spectra of the samples and the band gap variation are shown in **Figure 1.3**. Also, the sample color turns from white to dark

red with a decrement of the band gap. Due to the narrow band gap the photocurrent density or the conductivity was also found to increase. The doping of appropriate cation can lead a change in the optical band gap of BSO which was reported from many research groups.⁴⁸⁻⁵⁰ It was also found that a broad absorption band appeared around 1200-1300 nm causing a appreciable drop in Vis-NIR transparency for heavy Sb doped BSO and the color of white BSO gradually turns to blue and then finally black.¹⁹ The strong UV absorption makes the material a good UV detector, filter and sensor in for UV light.⁵¹ The very high value of the excitation binding energy for BSO at room temperature compared to the thermal energy (26 meV) makes it potential candidate for photoluminescence (PL) application.²⁴ As the absorbance spectra shows highest absorption at about 400 nm thus the excitation wavelength is chosen in UV region. At ambient condition, the strong emission in visible spectrum corresponds to the energy levels of barium and tin, whereas, the weaker emissions corresponds to the defects associated with impurity, oxygen vacancy etc.⁵¹⁻⁵² In some reports NIR PL spectra was identified for high temperature annealed BSO due to Sn^{4+} -O covalency and linear geometry of O-Sn-O.⁴¹ Broad green emission can be found for iron doped BSO caused by surface related defects associated with oxygen vacancies.⁵³ Appreciable percentage of Eu and La doping gives rise to multicolor emission also.⁵⁴ Pure BaSnO_3 belongs to the space group $\text{pm}\bar{3}\text{m}$ with cubic symmetry.¹⁵ Group theoretical analysis at $k = 0$, permits BSO to have 12 Raman forbidden modes and 9 infrared active modes.⁵⁵

$$T = 3 F_{1u} + F_{2u} \quad (1.2)$$

The above irreducible relation suggests that cubic BSO has no Raman active modes due to centrosymmetric crystal structure and cannot be able to give a first-order Raman scattering.⁵⁶ Although, the theoretical study tells that there are no permitted phonons in the pure BSO perovskite, some peaks can be detected in experimental Raman spectra arising from the first order Raman activity. The introduction of defects, (such as oxygen vacancy, presence of BaCO_3 due to moisture absorption) can lead to hamper the translational lattice symmetry and giving rise to a distorted perovskite structure.⁵⁷⁻⁵⁹ The SnO_6 octahedra have six vibrational modes: symmetric stretching mode ($\nu_1\text{A}_{1g}$), asymmetric stretching mode ($\nu_2\text{E}_g$ and $\nu_3\text{F}_{1u}$), symmetric bending mode ($\nu_3\text{F}_{2g}$), asymmetric bending mode ($\nu_4\text{F}_{1u}$) and inactive mode ($\nu_6\text{F}_{2u}$). The Raman active mode $\nu_2\text{E}_g$ is also active in IR spectrum. This mode appears as doublet. The intense peak at

629 cm^{-1} corresponds to the Sn-O bonds ($\nu_6\text{F}_{1u}$ mode). The Raman and IR modes of BSO are written in **Table 1.2**.

Table 1.2. Optical vibrational modes of BaSnO_3 (Deepa *et al.*⁵¹)

Raman		IR	
Wavenumber (cm^{-1})	Mode	Wavenumber (cm^{-1})	Mode
690	$\nu_1\text{A}_{1g}$	629	$\nu_3\text{F}_{1u}$
570, 549	$\nu_2\text{E}_g$	568, 579	$\nu_2\text{E}_g$
225	$\nu_4\text{F}_{1u}$		
182	$\nu_6\text{F}_{1u}$		
154, 137	$\nu_5\text{F}_{2g}$		

1.2.5. Thermal properties

The total thermal conductivity is a sum of two contributions, one from lattice and another from electronic thermal conductivity.

$$k_{total} = k_{lat} + k_{elec} \quad (1.3)$$

and k_{elec} can be evaluated from Widemann-Franz law. At room temperature, the thermal conductivity of polycrystalline BSO is $9.7 \text{ Wm}^{-1}\text{K}^{-1}$ which reduces with the rise in temperature and reaches to $3.2 \text{ Wm}^{-1}\text{K}^{-1}$ at 1262 K. The lowering tendency of thermal conductivity with temperature suggests that the phonon conduction is predominant over the electrical part.⁶⁰ Also, the thermal conductivity of BSO single crystal, measured employing 3ω method shows a dependency on T^{-1} in between 20 K and 300 K. The heat transfer mechanism in non-magnetic BSO is dominated by phonons, which are scattered by other phonons with increasing temperature, resulting in a lowering of k_{total} .⁶¹ The Debye temperature and linear expansion coefficient in the temperature range between 300 K and 1773 K of polycrystalline BSO were investigated by Maekawa *et al.* and the values are 522 K and $9.3 \times 10^{-6} \text{ K}^{-1}$ respectively.⁶² From computational method it was found that the Debye temperature is 496 K and thermal expansion coefficient is $5.518 \times 10^{-5} \text{ K}^{-1}$ at 300 K and zero pressure.⁶³

1.3. Basic theory of Complex Impedance Spectroscopy (CIS) analysis to study the electrical properties

Complex impedance spectroscopy (CIS) is a non-invasive technique to study and analyze the electrical properties of solids. This AC method is advantageous than the traditional DC method as it distinguishes the real and imaginary parts separately and help to analyze the electrical properties in a clean and unambiguous way. Also, this method is free from geometrical properties of sample and thus more reliable. In this method, a small amplitude AC signal is applied onto electro-ceramic compounds to study the electrical behavior of the material. The non-linear current (I)-voltage (V) graph for a theoretical electro-chemical arrangement is depicted in **Figure 1.4**. In general, a sinusoidal signal ($\Delta E \sin \omega t$) with a small amplitude ΔE and

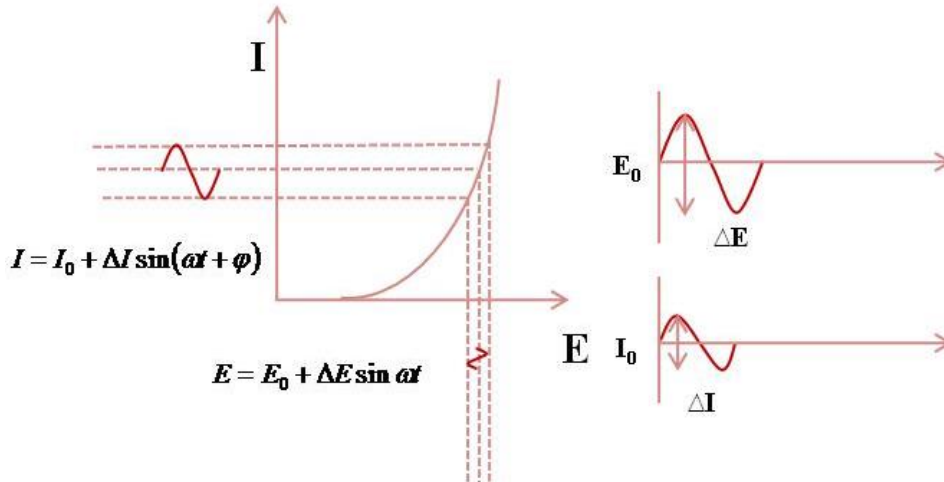


Fig. 1.4. A non-linear I-V curve for a theoretical electrochemical system

frequency ω is employed along with the DC voltage E_0 . As a result, the current is shifted by some phase ϕ with respect to the applied voltage. Hence, the current can be expressed as a sum of a sinusoidal signal $\Delta I \sin(\omega t + \phi)$ and a DC part I_0 . According to the Taylor series one can expand the expression of current as,

$$\Delta I = \left(\frac{dI}{dE} \right)_{I_0, E_0} \Delta E + \frac{1}{2} \left(\frac{d^2 I}{dE^2} \right)_{I_0, E_0} \Delta E^2 + \dots \quad (1.4)$$

If the amplitude of the applied AC signal *i.e.* ΔE is very small then the higher order terms can be neglected in Equation 1.4 So, we can write the equation 1.4 by considering the above fact as,

$$\Delta I = \left(\frac{dI}{dE} \right)_{I_0, E_0} \Delta E \quad (1.5)$$

Thus, the impedance of the electro-chemical material is evaluated using Ohm's law as

$$Z(\omega) = \frac{\Delta E(\omega)}{\Delta I(\omega)} \quad (1.6)$$

The impedance $Z(\omega)$ is a complex parameter which consists of a magnitude $|Z(\omega)|$ and a phase $\theta(\omega)$ determined by the frequency of the signal. Therefore, the impedance of a system can be easily be evaluated as a function of frequency. In polar coordinate, the complex impedance can be written as

$$Z^*(\omega) = |Z(\omega)|e^{j\theta(\omega)} \quad (1.7)$$

In case of Cartesian system the complex impedance $Z(\omega)$ can be written like

$$Z^*(\omega) = Z'(\omega) - jZ''(\omega) \quad (1.8)$$

Here, $Z'(\omega)$ and $Z''(\omega)$ are the real (resistance) and imaginary (reactant) components of the complex impedance $Z^*(\omega)$ of the system and $j = \sqrt{-1}$.

$$Z^*(\omega) = Z'(\omega) - jZ''(\omega) = \frac{1}{j\omega C_0 \varepsilon^*(\omega)} \quad (1.9)$$

$$\varepsilon^*(\omega) = \varepsilon'(\omega) - j\varepsilon''(\omega) \quad (1.10)$$

$\varepsilon^*(\omega)$ is the complex permittivity associated to the ceramic material under concerned. The real component of $\varepsilon^*(\omega)$ i.e. $\varepsilon'(\omega)$ stands for the energy storage per cycle of the dielectric material. In contrast, the imaginary part ($\varepsilon''(\omega)$) depicts the energy loss per cycle of it. The value of $\varepsilon'(\omega)$ can be calculated considering the parallel plate capacitor model as

$$\varepsilon'(\omega) = \frac{Cd}{\varepsilon_0 A} \quad (1.11)$$

where, C , d , A and are the capacitance, thickness, area of the MIM pellet respectively. $\varepsilon_0 (= 8.854 \times 10^{-14} \text{ F/cm})$ is the permittivity of vacuum.

According to Maxwell, if a dielectric medium is put in an alternating electromagnetic field $\vec{E}(\omega) = \vec{E}_0 e^{j\omega t}$, the resultant current becomes sum of conduction current (1st term) and displacement current (2nd term). The associated current density can be written as

$$\vec{J} = \sigma + \varepsilon \frac{\delta \vec{E}}{\delta t} \quad (1.12)$$

$$\vec{J} = (\sigma + j\omega\varepsilon)\vec{E}_0 e^{j\omega t} \quad (1.13)$$

The effective current density leads the applied field by an angle θ (as said earlier) where $\cos\theta$ denotes the power of the dielectric medium sandwiched between two conductors. Conventionally, the phase angle θ is denoted by δ and referred to as the loss angle. $\tan\delta = \sigma/\omega\varepsilon$ is called ‘tangent loss’ which is the dissipation factor of the dielectric material arises from the relaxation mechanism because of the phase difference between the dipoles and the applied field, electrical conduction and many other non-linear phenomena.⁶⁴ The current density can also be expressed in an alternative way as

$$\begin{aligned} \vec{J} &= j\omega \left(\varepsilon + \frac{\sigma}{j\omega} \right) \vec{E}_0 e^{j\omega t} \\ &= j\omega \left(\varepsilon - j \frac{\sigma}{\omega} \right) \vec{E}_0 e^{j\omega t} \\ &= j\omega (\varepsilon'(\omega) - j\varepsilon''(\omega)) \vec{E}_0 e^{j\omega t} \\ &= j\omega \varepsilon^*(\omega) \vec{E}_0 e^{j\omega t} \end{aligned} \quad (1.14)$$

Hence, the tangent loss can be written as

$$\tan\delta = \frac{\varepsilon''(\omega)}{\varepsilon'(\omega)} \quad (1.15)$$

The complex admittance ($Y^*(\omega)$) and modulus ($M^*(\omega)$) are related with complex impedance and permittivity by following relations

$$\begin{aligned} Y^*(\omega) &= Y'(\omega) + jY''(\omega) \\ &= \frac{1}{Z^*(\omega)} = j\omega C_0 \varepsilon^*(\omega) \end{aligned} \quad (1.16)$$

$$M^*(\omega) = M'(\omega) + jM''(\omega) = \frac{1}{\varepsilon^*(\omega)} = j\omega C_0 Z^*(\omega) \quad (1.17)$$

Thus,

$$\tan\delta = \frac{\varepsilon''}{\varepsilon'} = \frac{Z'}{Z''} = \frac{Y'}{Y''} = \frac{M''}{M'} \quad (1.18)$$

The imaginary component of complex permittivity is

$$\varepsilon''(\omega) = \varepsilon'(\omega)\tan\delta \quad (1.19)$$

1.3.1. Dielectric property

The dielectric dispersion is an electrical property of material which is able to be polarized in presence of external electric field. This intriguing property of matter can be interpreted with the help of molecular theory in which a link between the macroscopic result and the microscopic cause (like molecular/atomic dipole moment) can be obtained.⁶⁵ In wide band gap semiconductors the electrons are more tightly bound to positive core of the atoms than conductors and thus are not able to move in absence of any sufficient external force. In this situation, the positive and negative charge centers coincide with each other. But as the electric field is applied externally, a slight displacement between the centers of opposite charges gives rise to atomic dipoles and polarization happens. The ‘induce dipole moment per unit electric field’ is called the ‘polarizability’ of the dielectric material. The total polarization in a material is the contributions from the following four types of polarizations.

(i) Electronic Polarization:

Due to external electric field an electric strain is created within an atom. Hence, positive nucleus and negative electron cloud gets attracted in opposite direction. As a result, the difference in two opposite charge centers within an atom form a tiny dipole. The net dipole moment due to all atoms contributes as electronic polarization.

(ii) Ionic Polarization:

The ionic polarization typically can be seen in ionic molecules only where positive and negative ions form ionic bonds. When the electric field is employed from outside, the separation between

cation and anion increases, resulting in an increment in the total dipole moment. This increment in dipole moment ultimately contributes in polarization.

(iii) Orientational Polarization:

When an external electric field is employed on a sample then the charge distribution of the molecules gets affected and tiny dipoles are formed, called induced dipole moment. This dipole moment effectively causes polarization. In polar molecules, the opposite charge centers do not coincide with each other and thus form a permanent dipole moment. Due to thermal agitation net dipole moment of these materials is zero but they get aligned as soon as an external electric field is applied.

(iv) Space-charge or interfacial Polarization:

The space charge polarization is also alternatively known as interfacial polarization. In case of heterogeneous material the free charge carriers move in accordance with the externally used electric field and for this they accumulate in the interfacial region of two differently conducting material. This accumulation of space charges gives rise to polarization effect. For the polycrystalline substances, at the grain-grain boundary interfaces the charges can be accumulated due to the presence of external electric field. Also, interfacial polarization could be noticed at the electrode-dielectric interface.

At frequencies below ~ kHz, all the four polarizations are in phase with the applied AC field. Thus the resultant dielectric constant in this region is high and no such losses are found. But, as the frequency rises, more and more difficulties will be there to synchronize (especially the interfacial and orientational polarizations) with the applied field *i.e.* the input AC field changes its direction prior to the completion of the polarization. According to Koop's phenomenological theory, this momentary delay results a monotonic decay in the value of total polarization (or indirectly dielectric constant) in the low frequency regime which ultimately at high frequency zone settles down to a nearly constant value. Atomic and electronic polarizations are accountable for the polarization mechanism in high frequency regime. This resultant out of phase component of the polarization eventually manifested as thermal dissipation of energy or the 'dielectric loss'.⁶⁵

The charge aggregation at the grain-grain boundary interfaces along with internal barrier layer capacitance (IBLC) model promotes the validation of Maxwell-Wagner interfacial polarization (MWIP).⁶⁶⁻⁶⁹ According to Raevski the effective dielectric constant of a core (grain)-shell (grain-zone is boundary) structure in low frequency

$$\varepsilon' = \varepsilon'_{gb} \left(1 + \frac{t_g}{t_{gb}} \right) \quad (1.20)$$

here, ε'_{gb} , t_g and t_{gb} denote the dielectric permittivity of grain boundaries, thickness of grains and thickness of grain boundaries respectively.⁷⁰

1.3.2. Dielectric relaxation analysis

Dielectric spectroscopy is a twin representation of complex impedance spectroscopy and these two representations together recognize the complete characteristics as well as reason of polarization; like dielectric relaxation (*e.g.* dipolar/orientational, space charge) or other deformational parts of ionic or electronic polarizability for better understanding of electrical properties of a non-homogeneous material in microscopic level. As previously discussed in

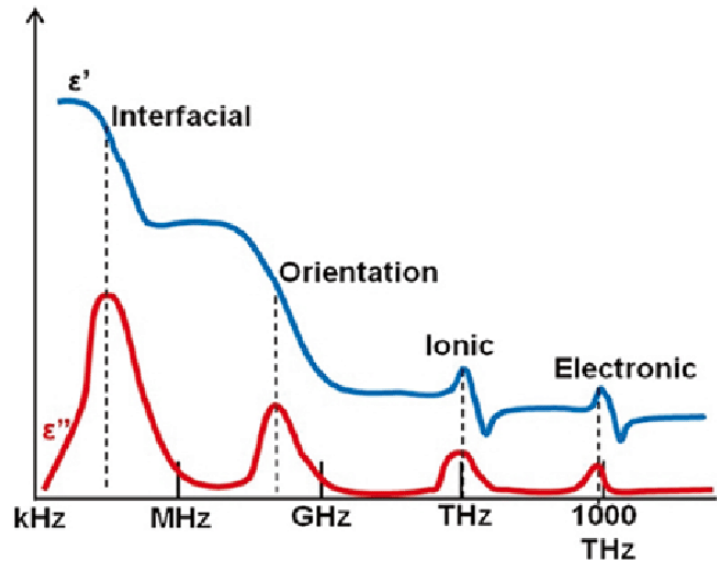


Fig. 1.5. Dependence of real and imaginary part of the relative dielectric permittivity on frequency due to application of an alternating electric Field; Contributions of different polarization in the total polarization are shown

section 1.3.1, with the increment in frequency, the polarizations cannot be able to follow the instantaneous polarity variation of the input field due to the inertia. Thus a phase lag creates between the input field and the polarization. The resulting time lag is known as relaxation time, and the phenomenon is known as dielectric relaxation. Different polarization mechanism has different range of frequency upto which the polarization can act in phase with the externally applied electric field, is shown in **Figure 1.5**. There are different theoretical models used to interpret the relaxation mechanism of molecular dipoles. Among those models, the Debye theory of dipolar

relaxation is the oldest one and is applicable for an ideal system where all the dipoles are non-interacting and have a single relaxation frequency. According to Debye equation, the dielectric permittivity can be written as

$$\varepsilon^*(\omega) = \varepsilon_\infty + \frac{\Delta\varepsilon}{1+j\omega\tau} = \left(\varepsilon_\infty + \frac{\Delta\varepsilon}{1+\omega^2\tau^2} \right) - j \left(\frac{\omega\tau\Delta\varepsilon}{1+\omega^2\tau^2} \right) = \varepsilon' - j\varepsilon'' \quad (1.21)$$

where, ω is the angular frequency, $\Delta\varepsilon (= \varepsilon_s - \varepsilon_\infty)$ is the dielectric strength (the difference between relaxed and unrelaxed permittivity) and τ is the relaxation time. The relaxation time (τ) is defined as the time required by the oscillating dipoles to rearrange themselves in accordance to the applied electric field. It can alternatively be stated as the restoration time to regain an equilibrium condition following the removal of the external field. In real situation, dispersion in relaxation times occurs due to the inter-dipole interactions or the interactions between dipoles and their surroundings leads to an asymmetric broadening of the dielectric loss ($\tan\delta$ vs f) peaks.⁷¹ To account the difference in relaxation times shape-parameter β is added into the dielectric relaxation equation. In our work, the frequency dependent dielectric spectra were analyzed using Cole-Davidson theory. The modified equation can be written as

$$\varepsilon^*(\omega) = \varepsilon_\infty + \frac{\Delta\varepsilon}{(1+j\omega\tau)^\beta} \quad (1.22)$$

Where, β satisfies the condition $0 \leq \beta \leq 1$. For $\beta = 1$, Debye equation is obtained. The Cole-Davidson equation can be rewritten in the following form after substituting $\omega\tau = \tan\phi$ and $(1 + j\omega\tau) = \sqrt{(1 + \omega^2\tau^2)}e^{j\phi}$.

$$\begin{aligned} \varepsilon^*(\omega) &= \varepsilon_\infty + \frac{\Delta\varepsilon}{(e^{j\phi})^\beta (\sqrt{1+\omega^2\tau^2})^\beta} \\ &= \varepsilon_\infty + \Delta\varepsilon(\cos\phi)^\beta e^{-j\beta\phi} \\ &= \varepsilon_\infty + \Delta\varepsilon(\cos\phi)^\beta (\cos\beta\phi - j\sin\beta\phi) \\ &= [\varepsilon_\infty + \Delta\varepsilon(\cos\phi)^\beta \cos\beta\phi] - j[\Delta\varepsilon(\cos\phi)^\beta \sin\beta\phi] \end{aligned} \quad (1.23)$$

$$= \varepsilon' - j\varepsilon'' \quad (1.24)$$

Comparing equation 1.23 and 1.24 we can write the simplified forms of real and imaginary components of dielectric permittivity as

$$\varepsilon' = [\varepsilon_{\infty} + \Delta\varepsilon(\cos\phi)^{\beta}\cos\beta\phi] \quad (1.25)$$

$$\varepsilon'' = \Delta\varepsilon(\cos\phi)^{\beta}\sin\beta\phi \quad (1.26)$$

The frequency dependent dielectric permittivity curves were fitted using equations 1.25 and 1.26 and the fitting parameters were found. In our work, the shape parameter β lies below 1, which is an indication of non-Debye type relaxation followed by BSO.

1.3.3. Complex impedance analysis

Generally, insulating grain boundaries separate semiconducting/conducting grains in polycrystalline materials. According to IBLC model along with Maxwell-Wagner effect and Koop's theory the polycrystalline materials are equivalent to the heterogeneous system having different relaxation times and conductivities. Thus the core-shell structure of grain-grain boundary can be represented by double layer dielectrics. Also, the electrode-ceramic interface can be considered as similar inhomogeneous system and this interface has a significant contribution in total polarization. So, there are three parts in any MIM (Metal-Insulator-Metal) capacitor model which contribute in polarization; electrodes, grains and grain boundaries. To understand the contributions of each part distinctly, Cole-Cole plot is used.

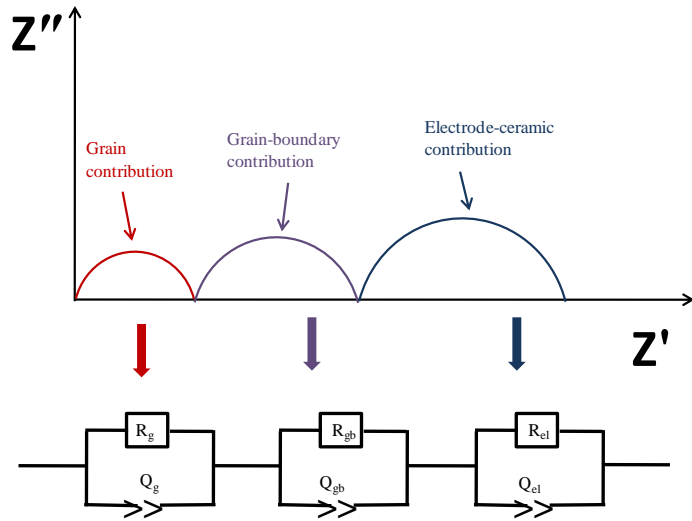


Fig. 1.6. Cole-Cole Plot and possible equivalent circuit for a heterogeneous solid with multiple polarization mechanisms

The real part of the complex impedance is represented in the X-axis and the imaginary component is plotted on the Y-axis in this graph. The scale of real and imaginary axis of the plot should be same so that the actual shape of the curve is not disturbed because the shape of the curve is very important to interpret the data qualitatively. Generally, three overlapping

semicircular arcs can be found in Cole-Cole plot for polycrystalline material as shown in **Figure 1.6**. The low frequency, mid-frequency and high frequency arcs are correlated with electrode-ceramic polarization, grain-boundary polarization and grain/ bulk polarization. In our study, one single semicircular arc can be found as a joint effect of grain and grain-boundary. The contribution of electrode polarization is negligible here. An equivalent circuit made up of a series combination of two pairs of parallel R-Q (resistance, constant phase element) is used to model this core-boundary system. These combinations generate a depressed semicircle in the complex plane of Z'' vs. Z' . The true capacitance (C) can be evaluated using the relation

$$C = R^{\frac{1-\alpha}{\alpha}} Q^{\frac{1}{\alpha}} \quad (1.27)$$

where, α is the distributing factor which interprets the deviation from the value of ideal capacitor arising from non-Debye type relaxation and asymmetric broadening in $\tan\delta$ vs. f graph. Basically, as the movement of free charge carriers gets restricted by a structural difference in the grain core-grain boundary (GC-GB) interface regions, space charges begin to build up in accordance with MWIP theory. The complex impedance can be written as

$$Z^*(\omega) = \frac{R_{gb} + R_g \{1 + (j\omega)^{\alpha_{gb}} Q_{gb} R_{gb}\}}{1 + (j\omega)^{\alpha_{gb}} Q_{gb} R_{gb} + (j\omega)^{\alpha_g} Q_g [R_{gb} + R_g \{1 + (j\omega)^{\alpha_{gb}} Q_{gb} R_{gb}\}]} \quad (1.28)$$

here, the subscripts 'g' denotes grain and 'gb' means grain-boundary. This circuit gives rise to a Nyquist (or Cole-Cole) plot consist of two semicircular arcs. In our work one depressed semicircle consists of two overlapped semicircular arcs is obtained assenting the Cole-Davidson model of dipolar relaxation.⁷²⁻⁷³

The Cole-Cole plots can be fitted to the equivalent circuit using EC lab software to determine the values of resistances and capacitances correspond to the grain and grain-boundary. The corresponding relaxation times (τ) can be calculated from the following relations

$$\tau_g = R_g C_g \quad (1.29)$$

$$\tau_{gb} = R_{gb} C_{gb} \quad (1.30)$$

The grain and grain boundary conductivities can be evaluated using the equations written below.

$$\sigma_i = \frac{t}{R_i A} \quad (1.31)$$

here, A and t are the area and thickness of the pellet respectively, R_i ($= R_g$ or R_{gb}).

1.3.4. AC conductivity analysis

In general, the frequency dispersion of conductivity of solids is composed of a frequency independent and strongly frequency dependent part. The complex conductivity with respect to frequency is interrelated with complex dielectric permittivity as

$$\sigma^*(\omega) = j\omega\epsilon_0\epsilon^*(\omega) = \sigma'(\omega) + j\sigma''(\omega) \quad (1.32)$$

The real part of the conductivity is

$$\sigma'(\omega) = \omega\epsilon_0\epsilon'' = \omega\epsilon_0\epsilon'\tan\delta \quad (1.33)$$

The archetypal σ_{ac} vs. f plot is shown in **Figure 1.7** having three distinct regions. The low frequency dispersion is created due to the electrode-ceramic interfacial polarization. At mid-frequency range as the charges accumulate at the GC-GB interface region thus the conduction of mobile charges decreases and a nearly independent value of conductivity is obtained. After a certain frequency, if frequency is increased again then a significant enhancement in conductivity can be noticed. The frequency dependent conductivity can be fitted using Jonscher's power law (JPL);

$$\sigma_{ac} = \sigma_{dc} + A\omega^n \quad (1.34)$$

where, σ_{dc} , A and n are the dc conductivity (frequency independent part), the pre-exponential factor (related with polarizability strength) and frequency exponent ($0 < n < 1$) respectively. The dc conductivity arises due to the drift velocity of mobile charge carriers and the high frequency dispersion in conductivity arises due to relaxation of bound charges. The value of all the parameters does not only depend on the

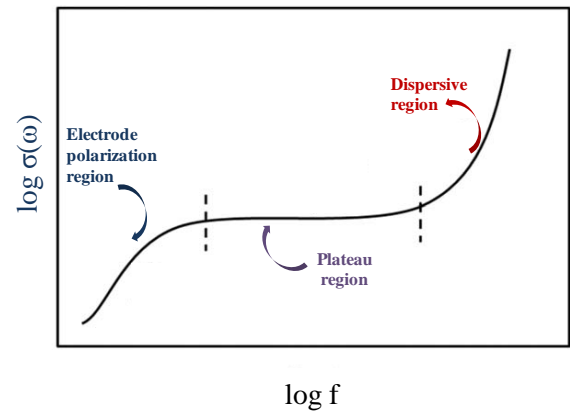


Fig. 1.7. Typical frequency dependence of real part of complex conductivity

type of material but also on the applied field and temperature.⁷⁴⁻⁷⁵ The exponent ‘n’ represents the interaction of the charge carriers with their neighboring environment. According to Jonscher, the frequency dependent conductivity arises from the relaxation phenomena due to the hopping mechanism of the mobile charge carriers. The value of ‘n’ decides the type of hopping mechanism is responsible for the electrical transport within a particular material, such as correlated barrier hopping, variable range hopping, quantum tunneling etc. In σ_{ac} vs. f plot, the frequency in high frequency regime where the slope of the curve changes is known as hopping or the crossover frequency ω_H . According to Almond-West relation⁷⁶

$$\sigma_{ac} = \sigma_{dc} \left[1 + \left(\frac{\omega}{\omega_H} \right)^n \right] \quad (1.35)$$

1.3.5. Modulus spectroscopy analysis

Modulus spectroscopy is very useful and important way to analyze the electrical transport phenomenon and the relaxation formalism of charge carriers. Macedo proposed that the modulus formalism is almost free from the low frequency electrode-ceramic polarization and thus the polarization mechanism of ceramic can be well understood from this.^{74,77} Analogous to the mechanical modulus of any mechanical system, electric modulus in an electro-ceramic system is defined as the measure of the relaxation of the charge carriers or the tendency to come back to the original state after removing the external electric field. Complex modulus can be written as the reciprocal of the permittivity.

$$\begin{aligned} M^*(\omega) &= \frac{1}{\varepsilon^*(\omega)} = M_\infty \left[1 - \int_0^\infty e^{-j\omega t} \left\{ \frac{d\phi(t)}{dt} \right\} dt \right] \\ &= \left(\frac{\varepsilon'}{\varepsilon'^2 + \varepsilon''^2} \right) + j \left(\frac{\varepsilon''}{\varepsilon'^2 + \varepsilon''^2} \right) \\ &= M' + jM'' \end{aligned} \quad (1.36)$$

The function $\phi(t) = \phi(0) \exp(-t/\tau_0)^\eta$ denotes the change of electric field inside the dielectrics with time and is called relaxation function. τ_0 and η are relaxation time (the time at which $\phi(t)$ decays to $1/e$) and stretched exponent respectively. For a typical polycrystalline material, frequency dispersion of real and imaginary parts of complex modulus is exhibited in **Figure 1.8**. The variation of electrical stiffness is associated with the real component of the complex modulus

(M') in lower frequency regime. M' shows minimum value which increases monotonically with frequency and reaches to an asymptotic maximum $M_\infty (= 1/\epsilon_\infty)$ at high frequency zone.⁷⁸⁻⁸⁰ The low frequency small value of M' arises due to the long range hopping of charge carriers as a result of electrode polarization for the external electric field. The distance travelled by charge carriers become shorter as frequency increases and ultimately they

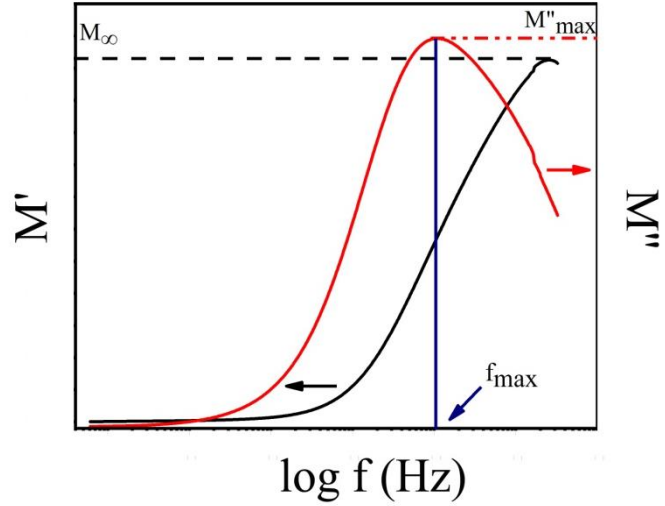


Fig.1.8. Frequency dispersion of real and imaginary components of complex modulus

confined into the potential wells.⁸¹ The imaginary section of complex modulus indicates the energy dissipated within the substance as an effect of applied electric field. A broad peak with asymmetric nature can be noted in M'' vs. f graph where the transition between large ranges to short range carrier hopping takes place. The asymmetric non-Debye type broadening is represented using Kohlrausch-William-Watts (KWW) function as,

$$M''(f) = \frac{M''_{max}}{(1-\beta) + \left(\frac{\beta}{1+\beta}\right) \left[\beta \left(\frac{f_{max}}{f}\right) + \left(\frac{f}{f_{max}}\right)^\beta \right]} \quad (1.37)$$

The value of the stretched exponent β indicates the type of relaxation taking place within the solid electrolyte. Typically, in case of insignificant dipole-dipole interaction the value of β is taken as unity but in real case, where the inter-dipole interaction is significant enough the value of β usually lies within $0 \leq \beta \leq 1$. The value of β is evaluated using the relation mentioned below.

$$(1 - \beta) = 1.047[1 - (W_n)^{-1}] \quad (1.38)$$

here, W_n is the normalized width which can be derived from ratio of the FWHM of M'' vs. f graph and the Debye width ($= 1.142$ decade). The characteristic relaxation time is usually estimated from the corresponding frequency of imaginary part of $M^*(\omega)$ as,

$$\tau_0 = \frac{1}{f_{max}} \quad (1.39)$$

For universal Debye response (UDR) the equation 1.37 reduced to the following form taking $\beta = 1$,

$$M''(f) = \frac{M''_{max}}{\left(\frac{1}{2}\right)\left[\left(\frac{f_{max}}{f}\right) + \left(\frac{f}{f_{max}}\right)\right]} \quad (1.40)$$

1.3.5.1. Scaling of modulus spectra

The scaling of modulus spectra is necessary to understand the relaxation mechanism within the material under any external parameter like dc bias, temperature etc. The X-axis is scaled by (f/f_{max}) and the Y-axis scaled by (M''/M''_{max}) . A master curve was created in our work when all the curves for various dc biases approximately overlap. This indicates the independence of the relaxation mechanism from DC bias. The modulus master curve for different dc bias voltage is shown in **Figure 1.9**.⁸²

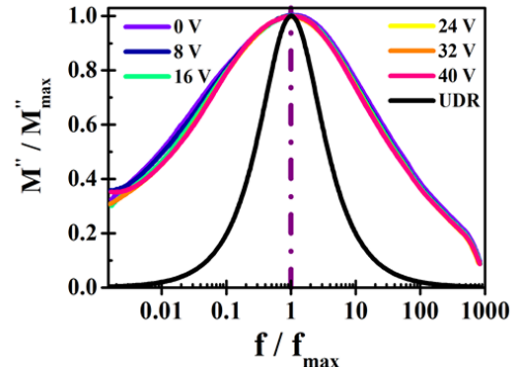


Fig. 1.9. Modulus master curve for different dc bias voltages and the Debye curve for comparison⁸²

1.4. Basic theory of Cold-Cathode Emission

Low dimensional electron emission cathodes are very much useful in flat panel displays, electron guns, vacuum microelectronic amplifiers, dynamic computerized topography (CT) scanners etc. There are several methods to eject the electrons from the surface of a matter. For understanding the basic mechanism of electron emission from metal surface, the fundamental concept of work function and surface potential barrier must be known properly. The surface potential barrier is created by a non-zero force worked on the charges residing at the surface of the materials due to ion cores within it. The electrons of a material can be able to eject from the surface only if they can occupy sufficient kinetic energy to defeat the barrier. The work function (ϕ) is the minimum energy required by the electrons of a material to eject from the solid surface to a point in vacuum just outside it. For semiconductor specially, the energy requires emitting the electrons into vacuum from the Fermi level is generally termed as ϕ . The work function ϕ is

measured in eV. External energy has to be employed to release electrons from a material's surface. As the electron emission takes place from the surface of the material, this is a surface property of a solid. There are different energy sources which can be employed externally to overcome the potential barrier. Depending on the kind of the external energy, electron emission can be mainly classified into four categories: (a) thermionic emission, (b) photo emission, (c) secondary electron emission and (d) field emission.

(i) Thermionic emission:

The primary driving energy source to provide the necessary kinetic energy to cross the potential barrier is 'Therm' means heat. The electrons emitted following this phenomenon are called thermal electrons or thermions. Although the thermionic emission is used widely but there are various disadvantages of the heating elements which encourage other emission mechanisms. Some disadvantages are

The heating filament gets damaged after certain use,

High heat generated source is required

It takes warm up time

(ii) Photo emission:

When photon i.e. a beam of light having frequency equal or more than the threshold frequency is incident upon the metal surface, the electrons gain sufficient kinetic energy to emit from the solid. This phenomenon is called The Photo emission or Photoelectron emission and the emitted electrons are called photoelectrons. Also this emission is highly dependent on the intensity and the frequency of light source.

(iii) Secondary electron emission:

In secondary electron emission process, the fast-moving highly energetic primary electrons bombard onto a metal surface and transfer their energies to the free electrons of the metal so that the secondary electrons can gain kinetic energy more than the work function resulting in the emission of secondary electrons.

(iv) Field emission:

Field emission is an electrical property of a material that can be demonstrated as electric field induced electron emission on which our study is focused. Thus the phenomena of field emission must be understood properly.

Field emission (FE) is the electron extraction phenomenon from a metal or semiconductor by applying a strong external electric field to vacuum. Usually, high positive voltage supply is connected to a metal plate (anode) and the negative end of it is connected to the metal or semiconductor under concerned (cathode). When the two electrodes are placed close to each other the positive charges of anode attract the electrons of the cathode material whereas the negative voltage supply of cathode repels them. Due to the combined effect if the electrons accumulate adequate kinetic energy to beat the restrictive forces, electron emission happens.⁸³ The schematic of field electron emission process is shown

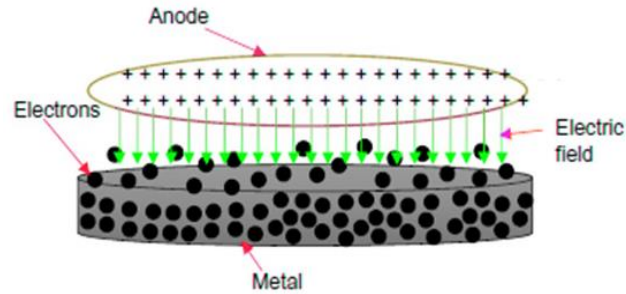


Fig. 1.10. Schematic diagram of field emission process from an emitter surface

in **Figure 1.10**. This particular emission process has various advantages over others, such as taking lesser input energy, no warm up time, lesser sensitive to temperature variations etc. Moreover, very high electron emission efficiency due to quantum tunneling compared to other emission mechanisms has made this emission phenomenon very significant for device applications. Because the emission happens at room temperature, the emission procedure may also called as ‘cold field electron emission’ (CFE) and the emitted electrons are known as ‘cold’ electrons. Prior to talk over the working principle of field emission, to understand the fundamental theory of Schottky effect/ emission is essential, because of its notable in the field emission mechanism. In case of thermionic emission the electrons get emitted from the solid leaving a positive hole into it. This arouses a self limiting condition because after certain time, no more electrons can come out from the solid. Thus for practical application, an electric field is applied along with the heat for continuous emission. The electric field not only helps to neutralize the cathode but also it helps to collect the electrons by attractive force or in other words, by reducing the barrier height. Hence, this emission process is also called field assisted thermionic emission. At a distance ‘ x ’ outside the conducting surface the electrons experience an electrostatic force by considering that the conductor surface is uniform. The image force can be expressed as⁸⁴:

$$F_{image} = -\frac{e^2}{16\pi\epsilon_0 x^2} \quad (1.41)$$

And the potential energy associate with the force can be written as:

$$V_{image}(x) = -\frac{e^2}{16\pi\epsilon_0 x} \quad (1.42)$$

The potential energy will diminish for large x and within the conductor. In Schottky emission, a constant potential is present which actually spreads over a very small distance of few angstroms.

So the potential energy of the electron is expressed as

$$V_{total} = (E_F + \phi) - \frac{e^2}{16\pi\epsilon_0 x} \quad (1.43)$$

Where, E_F is the Fermi level energy of the conductor/ semiconductor.

Now, the electrons escaped from the conducting surface experiences another force due to the externally applied field of strength E . Thus the total potential acting on the electron is⁸⁴:

$$V_{total} = (E_F + \phi) - \frac{e^2}{16\pi\epsilon_0 x} - eEx \quad (1.44)$$

The distance (x_{max}) at which the potential energy becomes maximum is derived by differentiating the equation 1.44 and set it equal to zero.

$$x_{max} = \left(\frac{e}{16\pi\epsilon_0 E}\right)^{1/2} \quad (1.45)$$

And the effective work function is

$$\phi_{eff} = \phi - e\left(\frac{eE}{4\pi\epsilon_0}\right)^{1/2} \quad (1.46)$$

Thus, the barrier height is reduced by a factor dependent of the strength of applied electric field.

The modified emission current density can be written as:

$$J_{modified} = BT^2 \exp\left[-\frac{\phi - e\left(\frac{eE}{4\pi\epsilon_0}\right)^{1/2}}{kT}\right] \quad (1.47)$$

Equation (1.47) is called Schottky equation⁸⁵.

The barrier height reduction is depicted in **Figure 1.11(a)**. Thus, in Schottky emission, electrons gain enough energy to jump over the barrier height and reach to the anode with the help of thermal energy along with an external electric field. In case of high field application ($E > 10^7$ V/cm) the electric field can sucks out the electrons from the cathode material. Due to high field strength, the potential energy $V_{total}(x)$ outside cathode bend steeply and a narrow barrier is formed. As a result, there is a finite probability for the electrons lie at Fermi level for tunnelling through the barrier into vacuum despite crossing it. As tunneling phenomenon does not require

heating the cathode, the field electron emission is often called as ‘cold cathode emission’. The reduction of barrier height as a result of the application of electric field further promotes the tunneling process. In the year of 1897, an American physicist R. W. Wood first reported this barrier deformation phenomenon.⁸⁶

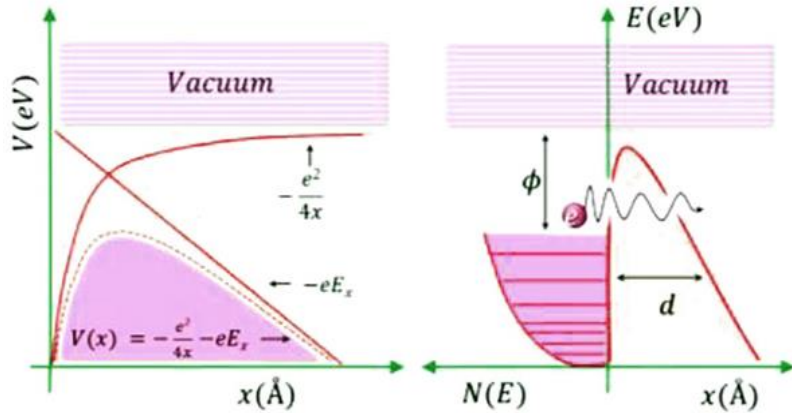


Fig. 1.11. Potential bending because of the application of external electric field, (b) Schematic of field electron emission

For better understanding, a schematic diagram of cold electron emission is presented in **Figure 1.11(b)**. If barrier width d is less than 10 \AA then only the electrons close to Fermi level can be able to tunnel through the barrier. However, many researchers proposed various theories towards the development of a formula considering the tunneling of electrons lie below Fermi level along with those lie at Fermi level. Among all the existing formulae, the most recognized one is which proposed by Fowler and Nordheim.⁸⁷⁻⁹⁰ According to them, the emission current or the anode current (I_A) can be written as

$$I_A = CV^k \exp\left(-\frac{B}{V}\right) \quad (1.48)$$

where, B and C are the structure of field emitter dependent constants. Different groups of scientists take different values of constant K . Millikan and Lauritsen set $K = 0$ and the plot $\ln I$ vs I/V becomes a straight line.⁸⁷ Abbott and Hendersen had taken $K=4$ and it gave rise to the most desirable straight-line form of the plot.⁸⁹ However, the most accepted value of K is 2 as suggested by Fowler and Nordheim. Fowler and Nordheim first proposed the quantum mechanical tunnelling model for field electron emission from a metal surface in 1928. The Fowler- Nordheim theory is based on the following assumptions:

- (i) Metal has a free electron band structure
- (ii) The emission takes place at absolute zero temperature
- (iii) Electrons obey the Fermi-Dirac statistics
- (iv) The emitter surface is assumed to be plane and uniform; irregularities of atomic dimensions are neglected

(v) Classical image potential is taken into consideration

(vi) The value of work-function is constant for the sample

Under this consideration the emission current density can be expressed as:

$$J_A = e \int_0^\infty n E_x D(E_x, F) dE_x \quad (1.49)$$

where, e is the electronic charge, n is the electrons emitted per second with energy range in between E_x and $(E_x + dE_x)$ incident on unit area of the barrier from inside. D is the tunneling probability of electrons or barrier transparency and can be written as:

$$D(E_x, F) = \exp \left[-\frac{8\pi(2m)^{1/2}}{3eh} \frac{E_x^{3/2}}{F} V(y) \right] \quad (1.50)$$

The term $V(y)$ is known as Nordheim function. After applying proper approximation the final expression of Fowler-Nordheim (F-N) equation becomes

$$I_A = \frac{AaF^2}{\phi} \exp \left(-\frac{b\phi^{3/2}}{f} \right) \quad (1.51)$$

where, A is the area of emission. The values of Fowler-Nordheim constants are $a = 1.54 \times 10^{-6}$ A eV² and $b = 6.83 \times 10^7$ eV^{-3/2}Vcm⁻¹. Sommerfield and Bethe further worked to develop the F-N equation including the effect of local electric field.⁹¹ The field enhancement factor (β), which they introduced, denotes the augmentation of the local field relative to the macroscopic field applied. Thus the emission current density J_A can be as

$$J_A = \frac{a\beta^2 E^2}{\phi} \exp \left(-\frac{b\phi^{3/2}}{\beta E} \right) \quad (1.52)$$

In equation 1.52, E is the external electric field and ϕ is the work function of the material. For BaSnO₃, $\phi = 3.04$ eV. The value of field enhancement factor (β) can be calculated from the slope of $\ln(J/E^2)$ vs. $1/E$ plot. Various parameters such as morphology of emitter sample, conductivity, work function etc. have a great role on the value of β .

The increasing demand of field emission driven electron generators become high in recent days for their applications in field emission displays (FEDs), X-ray tubes, electron guns, vacuum micro and nanoelectronic devices, infrared imaging devices, microwave amplifiers etc.⁹²⁻⁹⁷ Carbon derivatives (like CNTs) are already very famous for their excellent field emission behavior at low operating field for their low tip radius curvature but they have own limitations forbidding them to be used in practical field. For example, under high field CNTs often suffer from morphological changes and also they become oxidized easily in presence of residue

oxygen/ air in the vacuum chamber. Additionally, low electron affinity, good stability both thermally and chemically along with visible light transparency are challenging to obtain in one material to use it as highly efficient cold cathode in transparent electronics. The emission current density and the field enhancement factor highly dependent on several parameters like the aspect ratio of the nano emitters, inter-electrode distance, density of the sample, geometry of the nanostructure etc.⁹⁸⁻⁹⁹ The cold emission application is one of the unexplored applications for BSO so far.

1.5. Basic theory on the improvement of electrical properties of perovskite ceramic/polymer composite

1.5.1. Why to form?

Materials possessing superior dielectric permittivity with low loss are extensively studied because of their huge utilization in the field of sensor, energy storage devices, gate dielectrics etc.¹⁰⁰⁻¹⁰⁴ In general, perovskite ceramic materials show good dielectric permittivity along with low loss but they are fragile and also have lower breakdown strength. In contrast, polymers are flexible, durable, having simple preparation techniques and have higher breakdown voltage. But maximum polymer shows small value of dielectric permittivity. Hence effort should be made to prepare such perovskite ceramic/polymer composite with best properties of the components. So, the perovskite ceramic/polymer composite having high valued dielectric permittivity, minimum dissipation factor, superior flexibility, better durability and large breakdown strength are main requirements for the miniaturization of electronic devices. Polyvinylidene fluoride (PVDF) is popular for such composite formation as it has higher dielectric permittivity than other polymers and the optical transparency of PVDF film is relevant for transparent electronics. Among the five phases of PVDF the most electroactive crystalline phase is the β phase. Another aim to prepare the perovskite ceramic/PVDF composite is to convert the non-polar α phase of PVDF into electroactive β phase which is polar in nature. The surface charges of perovskite helps in self-poling process of PVDF and to orient the dipoles into ordered direction (TTTT configuration). This ordered form of PVDF phase is called the electroactive phase of PVDF and exhibits piezoelectric properties. Thus, the quantity of β phase (or in another term the piezoelectric performance) of PVDF into the composite system depends on the content of

perovskite into it. Although the surface charges play the key role for this behavior but the individual dielectric permittivity of the perovskite is also a prime matter for consideration. The dielectric permittivity of the perovskite should be higher than that of bare PVDF but not so high that the dielectric properties become incompatible between the two components of the hybrid system.¹⁰⁵ To understand the output results of the hybrid system under mechanical stress, the relation between the dielectric permittivity of the nano-composite system and the piezoelectric behavior of it also should be studied.

1.5.2. Relation between dielectric permittivity and the piezoelectric coefficients

The term ‘piezoelectricity’ roughly indicates to ‘pressure electricity’ which means the generation of electricity due to mechanical stress or pressure. In the piezoelectric materials, the positive and negative charge centers get separated maintaining their original crystal structure under the external mechanical stress/strain and get polarized. The reversibility of the effect is what makes piezoelectricity so beautiful. In this effect, the amount of mechanical strain exerted determines how much electric polarisation is produced. Thus for the piezoelectric materials the dielectric permittivity is an crucial parameter.

To explain the fundamental theory of piezoelectricity, most of the materials are assumed to show linear relations among different parameters. The Maxwell’s 4th equation in electromagnetism is used to understand the connection between polarization and mechanical stress. The equation is actually Ampere’s circuital law with Maxwell’s correction¹⁰⁶

$$\vec{\nabla} \times \vec{B} = \mu_0 \left(\vec{J}_f + \epsilon_0 \frac{\partial \vec{E}}{\partial t} \right) \quad (1.53)$$

Where, \vec{E} and \vec{B} are the electric and magnetic field respectively, ρ_f and \vec{J}_f denote the free electrical charge and current density respectively.

The second term in RHS of the equation 1.53 is called the displacement current which arises for time varying electric field.

The displacement vector (\vec{D}) is connected to the polarization vector (\vec{P}) by the relation written below.

$$\vec{D} = \epsilon_0 \vec{E} + \vec{P} \quad (1.54)$$

In the year of 2006, professor Z. L. Wang introduced another extra term \vec{P}_s into the equation 1.54. \vec{P}_s is the polarization arises because of the ‘+’ve and ‘-’ve charge center separation into the unit cells due to mechanical stress. As a result, the material experiences polarization due to the electric field development. Thus, the equation 1.54 for piezoelectric material becomes,

$$\vec{D} = \epsilon_0 \vec{E} + \vec{P} + \vec{P}_s \quad (1.55)$$

If a mechanical stress $\Delta\sigma$ is applied on the film having surface area A, the total surface charge (Q) generated in the film is

$$Q = d_{33} A \Delta\sigma \quad (1.56)$$

here, d_{33} is the piezoelectric charge coefficient in 33 mode and it is related to the dielectric permittivity of the film as¹⁰⁷

$$d_{33} = k_{33} \sqrt{(S_{33} \epsilon_{33})} \quad (1.57)$$

Where, k_{33} is the electromechanical coupling factor, S_{33} is the mechanical strain and ϵ_{33} is the dielectric permittivity at constant stress.

In open circuit condition, we can write

$$Q = CV \quad (1.58)$$

here, C is the capacitance of the MIM capacitor film and V is the voltage. Now combining equation 1.56 and 1.58 it can be written that,

$$V = \frac{d_{33} A \Delta\sigma}{C} = \frac{d_{33} A \Delta\sigma}{\frac{\epsilon A}{t}} = \frac{d_{33} \Delta\sigma t}{\epsilon} = g_{33} A \Delta\sigma \quad (1.59)$$

Here, t is the thickness of the film and g_{33} is the piezoelectric voltage coefficient. Thus the piezoelectric coefficients have a major dependency on the dielectric permittivity of the film.

Encouraged by the impressive electrical polarization properties of BSO we thought to extend our research to enhance the structural as well as the electrical properties of BSO/PVDF nanocomposite films.

1.6. Aims and Objectives

Barium Stannate (BaSnO_3) is very useful and important perovskite oxide under alkaline earth stannate group having intriguing electrical, optical, physical and chemical properties. Although there are several fields like capacitor, gas sensor, dye-sensitized solar cells etc. in which the material has already showed impressive performance, many more are there to improve and also to explore.

After a through literature survey, the aim and objective of this thesis was decided and listed below.

- BaSnO_3 is typically investigated for its tunable electrical properties for ceramic capacitor application. However, the porous nature of the ceramic material is the main blockage for good capacitive application. Also, the generation of larger grain and smaller grain boundary boosts the polarization phenomenon of the ceramic material. Hence, the aim is to develop highly dense BaSnO_3 ceramics with comparatively larger grain and smaller grain boundaries, study the transport properties (like conductivity, permittivity, loss etc.) and to understand the underlying mechanism of controlling different electrical parameters by varying the grain size and density of the ceramic for energy storage purpose.
- To enhance the tunability of electrical properties of BaSnO_3 at room temperature with suitable cation doping, like transition metal ions. The generation of ordered path due to application of external DC bias enhances the permittivity as well as the conductivity of the perovskite. The motive is to explain the formation of double Schottky barrier at the grain-grain boundary interface due to DC bias application and its effect on the overall polarization. Another aim is to understand the relaxation formalism obeyed by the pure and doped system from the frequency dispersion dielectric permittivity and complex modulus spectra.
- High cost of lanthanum in lanthanum based perovskite oxides and toxicity of lead in lead based perovskite halides generate a thrust to explore some other perovskite material as field electron emitter. Also, the miniaturization of electronic devices urges nano/micro emitter with significant performance. Hence, the aim is to prepare a nano- BaSnO_3 based electron

emitter system with lower work function and better stability, and to explain the role of grain size behind the enhanced electron tunneling from the modified system.

- Purpose-built synthesis of BaSnO_3 nanorods to enhance the electroactive phase of perovskite/polymer. The easy achievement of percolation threshold by high aspect ratio nanorods improves the electrical conductivity of the composite. The high permittivity BaSnO_3 nanorods increase the interfacial polarization between the polymer and perovskite which in turn enhances the piezoelectric coefficient of the composite system. Also, the surface energy gets reduced due to high aspect ratio of BaSnO_3 which prevents agglomeration in hybrid films and boosts overall performance of the composite devices.

1.7. Outline of the thesis

Chapter 1 : Introduction

The thesis contains overall eight chapters. The first chapter named as chapter 1 bears brief the introduction to perovskite structure, its discovery and classification. Some basic ideas on the crystal structure, electronic structure and various intriguing properties of BaSnO_3 are mentioned. The fundamental theory on measurements of electrical properties via Complex Impedance Spectroscopy (CIS) using AC technique and the analysis method for different parameters are elaborately discussed. The basic theory of electron emission along with a thorough discussion on cold cathode emission or field electron emission is also delivered. Furthermore, the aim and objectives of the thesis are sum up and each chapter is briefly stated in an outline.

Chapter 2: Literature survey

With a literature survey of past work on various synthesis protocols and some traditional application aspects, a review on some of the areas to be explored areas for BaSnO_3 is also addressed in chapter 2.

Chapter 3: Instruments and apparatus

Chapter 3 contains general description of the major synthesis apparatus, characterization tools and working principle of the instruments used for application.

Chapter 4: work 1

Chapter 4 illustrates the effect of calcination temperature on the structural properties of BaSnO_3 which further alter the electrical properties of the same. This chapter is based on the publication of the *ECS Journal of solid state Science and Technology* **10** (2021) 071018.

Chapter 5: Work 2

Chapter 5 targets to prepare vanadium doped BaSnO_3 nanocubes that can show better tuning in electrical properties under external DC voltage at room temperature. This work is based on the publication of the *Materials Research Express* **6** (10) (2019) 105029.

Chapter 6: Work 3

Chapter 6 explores simulation based study of the field electron emission (cold cathode) properties of vanadium doped BaSnO_3 nanocubes and validates the result experimentally also. This chapter is based on the publication of the *Applied Surface Science* **530**, 2020, 147102.

Chapter 7: Work 4

Chapter 7 focuses on the fabrication of $\text{BaSnO}_3/\text{PVDF}$ nanocomposite films to enhance the electrical properties of the hybrid films. With increasing perovskite content in the hybrid films, the electroactive phase of the nanocomposite films increases. High aspect ratio of the nanorod BaSnO_3 is responsible for the enhancement in polarization, less agglomeration and overall performance of the hybrid films. This work is *ready for communication*.

Chapter 8: Conclusion and future outlook

Ultimately, this chapter narrates the grand conclusions of this thesis containing the sum up of the main achievements and also discusses some plausible future aspects.

1.8. References

1. S. K. Sahoo, B. Manoharan and N. Sivakuma, Chapter 1 - Introduction: Why Perovskite and Perovskite Solar Cells?, Perovskite Photovoltaics, Academic Press, ISBN 9780128129159 (2018) 1-24

2. E. A. Katz, Perovskite: name puzzle and German-Russian odyssey of discovery, *Helvetica Chimica Acta*, 103(6) (2020) e2000061
3. Johnsson M, Lemmens P. Crystallography and chemistry of perovskites. arXiv preprint cond-mat/0506606. (2005)
4. J. Bartel, C. Sutton, B. R. Goldsmith, R. Ouyang, C. B. Musgrave, L. M. Ghiringhelli, M. Scheffler, *Science Advances*, 5 (2019) eaav0693
5. V. M. Goldschmidt, "Die Gesetze der Krystallochemie". *Die Naturwissenschaften.*, 14 (21) (1926) 477–485
6. X. C. Liu, R. Hong and C. Tian, *Journal of Materials Science: Materials in Electronics*, 20 (4) (2008) 323–327
7. W. J. Merz, Switching time in ferroelectric BaTiO₃ and its dependence on crystal thickness, *Journal of Applied Physics*, 27 (1956) 938-943
8. K. Leng, Q. Tang, Y. Wei, L. Yang, Y. Xie, Z. Wu, and X. Zhu, *AIP Advances*, 10 (2020) 120701
9. H. Asano, J. Hayakawa and M. Matsui, *Applied physics letters*, 71 (1997) 844-846
10. R. E. Schaak and T. E. Mallouk, *Chem. Materials*, 12 (2000) 3427-3434
11. S. Uma, A. R. Raju and J. Gopalakrishnan, *Journal of Materials Chemistry*, 3 (1993) 709-713
12. Y. Tsunoda, W. Sugimoto and Y. Sugahara, *Chemistry of materials*, 15 (2003) 632-635
13. W. Meng, B. Saparov, F. Hong, J. Wang, D. B. Mitzi and Y. Yan, *Chem. Mater.* 28 (3) (2016) 821-829
14. C. Huang, X. Wang, X. Liu, M. Tian and T. Zhang, *Journal of the European Ceramic Society* 36 (2016) 583–592
15. N. Purushothamreddy, M. Kovendhan, R. K. Dileep, G. Veerappan, K. Saravana Kumar and D. P. Joseph, *Materials Chemistry and Physics* 250 (2020) 123137
16. P. V. Wadekar, J. Alaria and M. O'Sullivan, *Applied Physics Letters*, 105 (2014) 052104.
17. H. E. Swanson, M.C. Morris, E. H. Evans, and L. Ulmer, 3 (1864) 1 – 64
18. G. Wagner, H. Binder, *Z. Anorg. U. Allgem. Chem.* 297 (1958) 334
19. H. Mizoguchi, P. Chen, P. Boolchand, V. Ksenofontov, C. Felser, P. W. Barnes and P. M. Woodward, *Chemical Materials*, 25 (2013) 3858–3866

20. T. Maekawa, K. Kurosaki and S. Yamanaka, *Journal of Alloys and Compounds* 416 (2006) 214–217
21. H. J. Kim, U. Kim, T. H. Kim, J. Kim, H. M. Kim, B. G. Jeon, W. J. Lee, H. S. Mun, K. Taek Hong, J. Yu, K. Char and K. H. Kim, *Physical Review B*, 86 (2012) 165205
22. P. Singh, Benjamin J. Brandenburg, C. P. Sebastian, P. Singh, S. Singh, D. Kumar, and Om Parkash, *Japanese Journal of Applied Physics*, 47(5) (2008) 3540–3545
23. The Materials Project. Materials Data on BaSnO_3 by Materials Project. United States: N. p., 2017
24. W. Aggoune, A. Eljarrat, D. Nabok, K. Irmscher, M. Zupancic, Z. Galazka, M. Albrecht, C. Koch and C. Draxl, *Communications Materials*, 3 (12) (2022)
25. D.J. Singh, D.A. Papaconstantopoulos, J.P. Julien and F. Cyrot-Lackmann, *Physical Reviews B*, 44 (1991) 9519
26. H. Mizoguchi, H.W. Eng and P.M. Woodward, *Inorganic Chemistry*, 43 (2004) 1667
27. P.D. Seson, *Journal of Physics: Condensed Matter* 22 (2010) 435801
28. D. Yamashita, S. Takefuji, M. Tsubomoto and T. Yamamoto, *Materials Science and Engineering: B* 173 (2010) 33
29. E. Moreira, J.M. Henriques, D.L. Azevedo, E.W.S. Caetano, V.N. Freire and E.L. Albuquerque, *Journal of Solid State Chemistry* 184 (2011) 921
30. J. Heyd, G.E. Scuseria and M. Ernzerhof, *Journal of Chemical Physics*, 118 (2003) 8207
31. B.G. Kim, *Physical Review Letters*, 108 (2012) 259601
32. M. V. Ganduglia-Pirovano, J. L.F. DaSilva and J. Sauer, *Physical Review Letters*, 102 (2009) 026101
33. Y. Kim, K. Hummer and G. Kresse, *Physical Review B*, 80 (2009) 035203
34. P. Deak, B. Aradi, T. Frauenheim, E. Janzen and A. Gali, *Physical Review B* 81 (2010) 153203
35. H. J. Kim, *Applied Physics Express*, 5 (2012) 061102
36. B. G. Kim, J. Y. Jo and S. W. Cheong, *Journal of Solid State Chemistry* 197 (2013) 134–138
37. S. Upadhyay, A. K. Sahu, D. Kumar and O. Parkash, *Journal of Applied Physics* 84 (1998) 828
38. A. Kumar, B.P. Singh, R. N. P. Choudhary and A. K. Thakur, *Journal of Alloys and Compounds* 394 (2005) 292–302

39. A. Adak (Maity), S. Mukherjee, M. Ghosh Chaudhuri and S. Mukherjee, *AIMS Materials Science*, 3(3) (2016) 1281-1293
40. Q. Liu, J. Dai, Y. Zhang, H. Li, B. Li, Z. Liu and W. Wang, *Journal of Alloys and Compounds*, 655 (2016) 389-394
41. H. Mizoguchi, P. M. Woodward, C.H. Park and D. A. Keszler, *Journal of the American Chemical Society*, 126 (31) (2004) 9796-9800
42. G. Larramona, C. Gutierrez, I. Pereira, M. R. Nunes, F. M. da Costa, *Journal of Chemical Society, Faraday Trans. 1: Physical Chemistry in Condensed Phases*, 85 (1989) 907–916
43. R. J. Cava, P. Gammel, B. Batlogg, J.J. Krajewski, W.F. Peck, Jr., L.W. Rupp, Jr., R. Felder, R. B. van Dover, *Physical Reviews B* 42 (1990) 4815–4818
44. D. T. Anh and N. T. Thanh, *Universal Journal of Physics and Application*, 11(6) (2017) 235-238
45. B. S. Joo, Y. J. Chang, L. Moreschini, A. Bostwick, E. Rotenberg and M. Han, *Current Applied Physics* 17 (5) (2017) 595-599
46. J. John, S. R. Chalana, R. Prabhu and V. P. M. Pillai, *Applied Physics A*, 125 (2019) 155
47. M. Kim, B. Lee, H. Ju, J. Y. Kim, J. Kim and S. W. Lee, *Advance Materials*, 31 (2019) 1903316
48. J. John, S. Suresh, S. S. Pillai, R. Philip and V. P. M. Pillai, *Journal of Electronic Materials*, 50 (2021) 5868–5880
49. Q. Liu, J. Dai, Z. Liu, X. Zhang, G. Zhu and G. Ding, *Journal of Physics D: Applied Physics*, 43 (2010) 455401
50. S. Lee, H. Wang, P. Gopal, J. Shin, H. I. Jaim, X. Zhang, S. Y. Jeong, D. Usanmaz, S. Curtarolo, M. Fornari and M. Buongiorno Nardelli, *Chemistry of Materials*. 29 (21) (2017) 9378-85
51. A. S. Deepa, S. Vidya, P. C. Manua, S. Solomon, A. John and J. K. Thomas, *Journal of Alloys and Compounds* 509 (2011) 1830–1835
52. U. Kumar, Md. J. Ansaree and Shail Upadhyay, *Processing and Application of Ceramics* 11 (3) (2017) 177–184
53. N. Rajamanickam, K. Jayakumar and K. Ramachandran, *Journal of Materials Science: Materials in Electronics* 29 (2018) 19880–19888

-
54. S. K. Gupta, B. Modak, D. Das, P. Modak, A. K. Yadav and K. Sudarshan, *Physical Chemistry Chemical Physics*, 23 (2021) 17479
55. E. Moreira, J. M. Henriques and D. L. Azevedo, *Journal of Applied Physics*, 112 (2012) 043703
56. J. John, S. Suresh, S. Pillai S, R. Philip and V. P. Mahadevan Pillai, 2021, Preprint (Version 1) available at Research Square [<https://doi.org/10.21203/rs.3.rs-193316/v1>]
57. S. Bajpai, and P. K. Bajpai, (2017) Defect Structure in Charge Compensated Lanthanu Doped BaSnO₃ as Probed by Raman Spectroscopy
58. R. Kurre, S. Bajpai and P. K. Bajpai, *Materials Sciences and Applications*, 9 (2018) 92-110
59. K. Balamurugan, N. HarishKumar, J. A. Chelvane and P.N.Santhosh, *Physica B*, 407 (2012) 2519–2523
60. P. Rajasekaran, M. Arivanandhan, N. Sato, Y. Kumaki, T. Mori, Y. Hayakawa, K. Hayakawa, Y. Kubota, R. Jayavel and M. Shimomura, *Journal of Alloys and Compounds*, 894 (2022) 162335
61. H. J. Kim, T. H. Kima, W. J. Leea, Y. Chai, J. W. Kima, Y. J. Jwaa, S. Chunga, S. J. Kima, E. Sohna, S. M. Leec, K.Y. Choi and K. H. Kim, *Thermochimica Acta*, 585 (2014) 16–20
62. T. Maekawa, K. Kurosaki and S.Yamanaka, *Journal of Alloys and Compounds*, 416 (2006) 214–217
63. A. Bouhemadou and K. Haddadi, *Solid State Sciences*, 12 (2010) 630–636
64. M. T. Sebastian, *Dielectric Materials for Wireless Communication*, (2008) 11–47
65. T. P. Iglesias, G. Vilao, ~ 1,2 and J. C. R. Reis, *Journal of Applied Physics*, 122 ((2017)) 074102.
66. T. Mitsui and W.B. Westphal, *Physical Review*, 124(5) (1961) 1354.
67. L. Zhang, X. Wang, W. Yang, H. Liu and X. Yao, *Journal of Applied Physics*, 104(1) (2008) 014104
68. B. Jiang, J. Iocozzia and L. Zhao, *Chemical Society Reviews*, 48(4) (2019) 1194-1228
69. M. Liu, J. Liu and C. Ma, *Crystal Engineering Communications*, 15(34) (2013) 6641-6644
70. I. Raevski, S. Prosandeev, A. Bogatin, M. Malitskaya and L. Jastrabik, *Journal of Applied Physics*, 93 (7) (2003) 4130-4136
71. S. Bhattacharjee, A. Banerjee, N. Mazumder, K. Chanda, S. Sarkar and K.K. Chattopadhyay, *Nanoscale*, 12(3) (2020) 1528-1540

72. S. Bhattacharjee, S. Mondal, A. Banerjee and K.K. Chattopadhyay, *Materials Research Express*, 7(4) (2020) 044001
73. D. C. Sinclair and A. R. West, *Journal of Applied Physics*, 66 (1989) 3850
74. P. Sengupta, P. Sadhukhan, A. Ray, R. Ray, S. Bhattacharyya and S. Das, *Journal of Applied Physics*, 127(20) (2020) 204103
75. S. Bhattacharjee, A. Banerjee and K.K. Chattopadhyay, *Journal of Physics D: Applied Physics* 54(29) (2021) 295301
76. D.P. Almond, G.K. Duncan and A. R. West, *Solid State Ionics* 8 (1983) 159
77. T. Ghosh, A. Bhunia, S. Pradhan and S. Sarkar, *Journal of Material Science: Material in Electronics*, 31(18) (2020) 15919-15930
78. P. Macedo, C. Moynihan and R. Bose, *Phys. Chem Glasses* 13 (1972) 171
79. C. Moynihan, L. Boesch and N. Laberge, *Phys. Chem. Glasses* 14(6) (1973) 122
80. A. Molak, M. Paluch, S. Pawlus, J. Klimontko, Z. Ujma and I. Gruszka, *Journal of Physics D: Applied Physics*, 38 (2005) 1450–1460
81. B. Deb, S. Bhattacharya and A. Ghosh, *Europhysics Letters*, 96 (2011) 37005
82. S. Bhattacharjee, R. Sarkar, P. Chattopadhyay, A. Banerjee, N. S. Das, D. Das, and K. K. Chattopadhyay, *Applied Physics A*, 128 (2022) 501
83. T. I. Awan, A. Bashir and A. Tehseen and S. Bibi, *Chemistry of Nanomaterials*, (2020) 179-206
84. Carbon Based Nanostructures for Field Emission Applications by D. Banerjee
85. W. Schottky, *Z. Phys.*, 14 (1923) 63
86. R. H. Good and E.W. Müller, Field emission. In *Electron-Emission Gas Discharges /Elektronen-Emission GasentladungenI* (1956) 176-231, Springer, Berlin, Heidelberg
87. R.A. Millikan and C.C. Lauritsen, *Proceedings of the National Academy of Sciences of the United States of America (U.S.A.)*, 14 (1928) 45
88. T.E. Stern, B.S. Gossling and R.H. Fowler, *Proceedings of the Royal Society of London, Ser. A*, 124(1929) 699
89. F.R. Abbott and J.E. Henderson, *Physical Review*, 56 (1939) 113
90. R. H. Fowler and L. Nordheim, *Proceedings of the Royal Society of London, Ser. A* , 119 (1928) 173

-
91. Sommerfeld and H. Bethe, *Handbuch der Physik*, 24 (1933) 441
 92. S. Babel and T. A. Kurniawan, *Journal of Hazardous Materials*, 97 (2003) 219-243
 93. Q. H. Wang, M. Yan and R. P. H. Chang, *Applied Physics Letters*, 78 (2001) 1294-1296
 94. H. Sugie, M. Tanemura, V. Filip, K. Iwata, K. Takahashi and F. Okuyama, *Applied Physics Letters*, 78 (2001) 2578-2580
 95. G. Cao, Y. Z. Lee, R. Peng, Z. Liu, R. Rajaram, X. Calderon-Colon, L. An, P. Wang, T. Phan, S. Sultana, D. S. Lalush, J. P. Lu and O. Zhou, *Physics in Medicine and Biology*, 54 (2009) 2323-2340
 96. X. M. H. Huang, C. A. Zorman, M. Mehregany and M. L. Roukes, *Nature*, 421 (2003) 496
 97. K. Korsah, L. R. Baylor, J. B. Caughman, R. A. Kisner, P. D. Rack and I. N. Ivanov, *US Patent Specification*, (2009) 7608824 B2
 98. T. Serin, A. Yildiz, S. H. Sahin and N. Serin, *Physica B: Condensed Matter*, 406 (2011) 575-578
 99. T. Serin, A. Yildiz, S. H. Sahin and N. Serin, *Physica B*, 406 (2011) 3551-3555
 100. M. Arbatti, X. Shan and Z.Y. Cheng, *Advanced Materials*, 19 (2007) 1369-1372
 101. L. Shaohui, Z. Jiwei, W. Jinwen, X. Shuangxi and Z. Wenqin, *ACS Applied Materials & Interfaces*, 6 (2014) 1533-1540
 102. S. Liu, S. Xue, B. Shen and J. Zhai, *Applied Physics Letters*, 107 (2015) 032907
 103. L. Su, Y. Wang, Y. Sha and M. Hao, *Journal of Alloys and Compounds*, 656 (2016) 585-589
 104. S. Liu, B. Shen, H. Hao and J. Zhai, *Journal of Materials Chemistry C*, 7 (2019) 15118-15135
 105. A. Sasmal, A. Patra, P. S. Devi and S. Sen, *Composites Science and Technology*, 213 (2021) 108916
 106. J. C. J. T. L. Maxwell, *Edinburgh, D.P. Magazine, J.o. Science*, 21 (1861) 161-175
 107. J. F. Li, *Lead-Free Piezoelectric Materials*, First Edition, (2021)

Literature Survey

The hazardous properties of lead (Pb) has attracted considerable attention towards the development of tin (Sn) based perovskites. Due to this, the alkaline-earth stannates gain more importance in the research area of Perovskites. Being an emerging semiconductor, barium stannate (BSO) has grabbed a great interest among the scientists and researchers for the unique combination of electrical, optical and thermal properties. BSO is a wide band gap semiconductor having an indirect band gap of ~ 3.1 eV shows efficient luminescence properties.¹ Whereas, the incorporation of sufficient oxygen vacancy in the interstitial sites promotes BSO to become an promising gas sensor material.² Moreover, the high dielectric constant along with good thermal stability makes the perovskite a potential candidate as ceramic capacitor in transparent electronics.³⁻⁴ The intriguing properties of BSO highly depends on the particle size and synthesis strategies followed. In this review chapter, detail discussion will be summarized on the popular synthesis methods along with current and plausible applications of barium stannate.

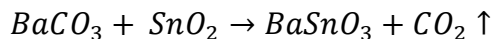
2.1. Previous reports on synthesis of BaSnO_3

2.1.1. Solid-State reaction (SSR) method

SSR or ceramic route is very popular to prepare ceramic materials with high thermodynamic stability. Two or more solids were mixed together via ball milling or agate mortar followed by heating at high temperature (generally, > 1000 °C) to produce a new solid material. This synthesis procedure solely depends upon the diffusion rates of the cations of reactants. To initiate the reaction, atleast one precursor material has to be diffused into another. There are generally a number of annealing steps followed by grinding of the intermediate products were carried out to complete the reaction. The multiple grinding processes help to expose the non-active surface of the reagents to one another and thereby increasing the reaction rate. Extra grinding makes the solid mixture more active in heating treatment.⁵⁻⁷

For the preparation of fine barium stannate powder the most popular and widely used route is the SSR method. In general, high purity barium carbonate (BaCO_3) and stannic oxide (SnO_2) are used as starting materials to prevent any presence of impurity phases. In a typical synthesis process, the precursor materials are mixed together with the help of a mortar pestle by keeping the stoichiometric ratio of the compositional elements. Some volatile liquids like ethanol, acetone, methanol etc. are used to mix the solid materials well.⁸⁻¹⁰ These liquids ease homogenization process to the mixture. After grinding, the volatile liquid is allowed to

evaporate completely from the solid mixture before heating. Although the principle of this synthesis method is to anneal the precursor materials, researchers followed different steps of annealing for different spans of time. The equation followed in this process is



Upadhyay and co-workers used ball mill in acetone media for better grinding followed by calcination at 1200 °C for 6 h.¹¹ To get maximum density the pellets prepared from the synthesized powder sample was pressed with a load of 50 kN. Then the prepared pellets were grind and pelletized again to increase homogeneity of the sample. Ultimately the pellets were employed to 1250 °C for 6 h for sintering. The reported values of the porosity and dimension of the cubic grains were 20% and 2-4 µm respectively. The same group reported that the sintering process has a signature effect on density and homogeneity of the prepared sample.¹² They sintered the pellets at 1250 °C and 1377 °C for 12 h. The cooling rate was maintained at 5 °C/ min using a programmable temperature controller. The values of porosity of the samples were 23% and 21% respectively, which indicates that high sintering temperature results high density or low porosity. The grain size lied in between 2-4 µm. The FESEM image of the samples prepared by the group is shown in **Figure 2.1(a, b)**..¹¹⁻¹² Singh *et al.* followed the same solid state reaction method in which they obtained pure barium stannate after calcining the powder mix of the reagents at 1250 °C for a span of 12 h followed by a sintering 1350 °C for same time.¹³ The sizes of the agglomerated microstructures were in between 1 and 3 µm. The FESEM image of the microcuboids is presented in **Figure 2.1(c)**.¹³ In 2013, Upadhyay followed two steps of sintering to increase homogeneity of the sample.¹⁴ He annealed the powder precursor mixture at 1000 °C for 8 h followed by pelletization under a pressure of 5 ton. Two stage sintering process was done for the pellets; firstly at 1250 °C for 12 h and then re-sintered at 1300 °C for 12h. The average crystallizes size and the density of the sample was 80 nm and 5.97 g/cm³ respectively. Homogeneous distribution of pores was observed from the SEM images. In 2016, Huang and team thoroughly analyzed the effect of calcination temperature on the phase formation of BaSnO₃.¹⁵ The temperature was varied from 600 °C to 1200 °C for 4 h. Although the formation of barium stannate was started at 700 °C, to get phase pure sample the sintering temperature raised to 1200 °C. The SEM image and EDX mapping are shown in **Figure 2.1(e-h)**. The formation of pure barium stannate from the powder mixture of BaCO₃ and SnO₂ is presented in **Figure 2.2**.¹⁵

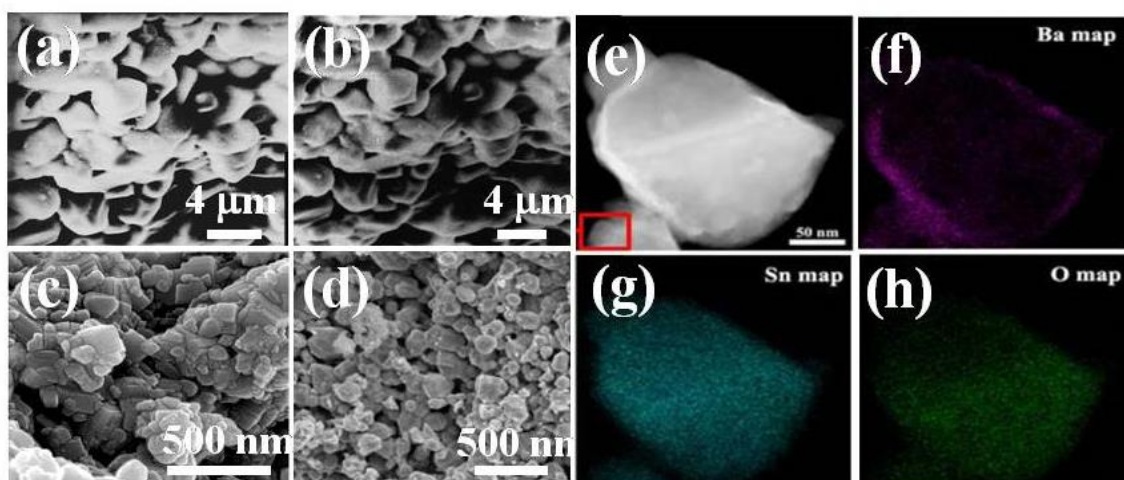


Fig. 2.1. FESEM images of barium stannate prepared using solid state ceramic route by (a) Upadhyay et al.¹¹, (b) Upadhyay et al.¹², (c) Singh et al.¹³, (d) John et al.¹⁷, (e-h) SEM micrograph and EDX mapping reported by Huang et al.¹⁵

Islam and his group reported the formation of polygonal structure containing rectangular sheets (width ~ 170 nm) along with nanodiscs (50-100 nm).¹⁶ The effect of multiple grinding followed by annealing was the key to obtain this kind of morphology for the stannate. The average crystallite size of pure BaSnO_3 was 66 nm. John and co-workers studied the optical and magnetic behaviour of nickel doped barium stannate in which they annealed the precursor materials at a temperature of 1250 °C for a span of 12 hrs following the process of several intermediate grinding to get single phase barium stannate powder.¹⁷ The mean value of crystallite size and the density of pure barium stannate were 49 nm and 7.237 g/cm³ respectively. The morphology of the sample changes from nanocuboids to nanorod after doping. The FESEM images of pristine and doped sample were shown in **Figure 2.1(d)**.

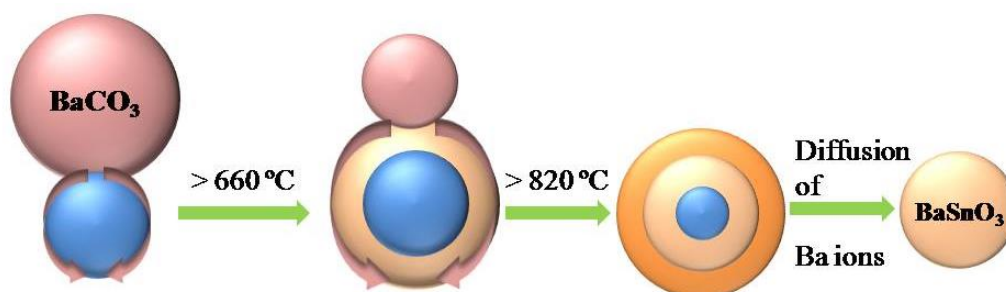
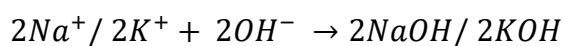
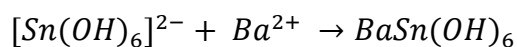
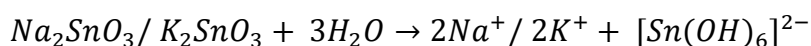
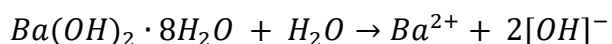


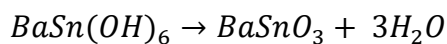
Fig. 2.2. Formation mechanism of BaSnO_3 from powder mixture of BaCO_3 and SnO_2 using solid-state reaction method¹⁵

2.1.2. Sol-Gel method

The sol-gel process is a enormously followed chemical synthesis procedure to prepare multicomponent oxide materials in which molecular precursors are allowed to dissolve into water or alcohol to make a sol and stirred constantly to form an amorphous gel under heating. The gel is then dried to form powder followed by calcination to get the desired product. The best features of this method are high purity and outstanding control over stoichiometry of the sample.¹⁸⁻¹⁹

Azad *et al.* employed sol-gel method for the synthesis of barium stannate using barium ethoxide and tin ethoxide as the precursor materials.²⁰ Appropriate amounts of metal ethoxides were dissolved into absolute ethanol and the solution was subjected to a magnetic stirrer at 70 °C until it turned into a transparent gel. The gel was then dried at 110 °C overnight. The gel powder formed from the mixture solution of the metal ethoxides was converted into pellets which were sintered at different temperature for different time. The microstructure variation is shown in **Figure 2.3(a-f)**. The pellets sintered at 1500 °C for a time of 2 h exhibited high density compared to the stannate synthesized via solid state or self sustain route. Cerda reported a low temperature aqueous sol-gel synthesis route in which aqueous solution of Ba(OH)₂ and K₂SnO₃·3H₂O was magnetically stirred with high speed at 80°C keeping the pH of the mixed solution strictly at 11 until a white coloured xerogel was formed.²¹ The xerogel was then fired separately at 1000 °C and 1400 °C for a period of 8 h. It was found from Raman spectra that there was trace of BaCO₃ present in the sample heated at 1000 °C but the peak was disappeared for the same sample heated at 1400 °C. The mean size of the quasispherical nanoparticles prepared using this method was 200 nm.²¹ Later on, Kumar used Na₂SnO₃·3H₂O instead of K₂SnO₃·3H₂O as sodium reacts faster with water than potassium and hence the formation of NaOH fastens the reaction rate.²² After annealing at 1400 °C for 4 h pure barium stannate powder was formed. The possible reaction steps for the above two synthesis processes can be written as follows





Cube like morphology was obtained with a size variation in the range between 10-40 nm. In 2020, following sol gel Pechini mechanism with some modification Yakout *et al.* prepared polyhedron particle with an average dimension of 1.98 μm .²³ Before stating the actual synthesis, ethylene glycol and and citric acid (1 M) were mixed together maintaining the volumetric ratio at 4:1. Then stoichiometric amount of tin (II) chloride and barium nitrate were dissolved separately into ethanol which were poured into the mixed solution of $\text{C}_2\text{H}_6\text{O}_2$ and $\text{C}_6\text{H}_8\text{O}_7$ under rigorous stirring. The temperature was kept at 80 °C to form a homogeneous sol which was further stirred at continuously at 135 °C until converts to a brown resin. The resin was autocombusted at 350 °C and grey coloured powder was obtained which was then calcined at 1150 °C for a span of 5 h to get phase pure BaSnO_3 . The FESEM image and EDX spectrum of the sample is shown in **Figure 2.3(g, h)**. In 2021, phase pure BaSnO_3 with a very high density by employing comparatively low temperature was achieved by Wang *et al.*²⁴ They have prepared two different solutions. At first, SnC_2O_4 was dissolved in aqueous solution of H_2O_2 under constant stirring. The temperature of the solution was mentioned at 80 °C for half an hour. The solution was then vigorously stirred while being added a stoichiometric amount of citric acid. Also, the pH was mentioned at 7 by adding the proper amount of ammonium hydroxide into it. The citric acid solution containing barium acetate was then poured slowly to the SnC_2O_4 final solution at 80 °C to form the required gel which was heated at 120 °C to form the precursor powder. Finally, the desired stannate in powder form was obtained after calcination at 900 °C for 3 h.

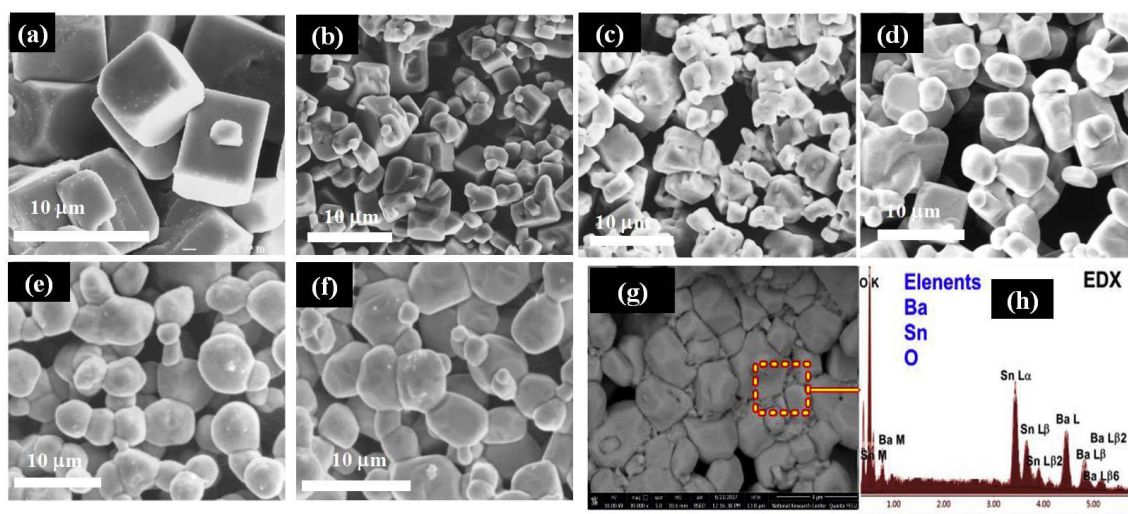


Fig. 2.3. (a-f) the microstructure variation of the ethoxide gel soaked at different temperature for different time by Azad *et al.*²⁰, (g) FESEM image and (h) EDX spectrum for barium stannate prepared via sol-gel Pechini mechanism by Yakout *et al.*²³

2.1.3. Solution Combustion Synthesis (SCS)

Solution combustion synthesis (SCS) is generally adopted to prepare the metal oxide nanomaterials with desired morphology.²⁵ The method is energy efficient, versatile, simple and fast, in which self sustained exothermic reactions occur either in homogeneous aqueous or sol-gel medium containing different oxidants and fuels. This self sustained thermal process produces a huge amount of gaseous products which in turn helps to prepare porous and finely dispersed product. The steps of SCS methods are almost same as sol-gel method but in general, auto combustion happens in the time of gel formation for SCS which produces ash like products. Finally, the ash is calcined to get the desired final product.²⁶⁻²⁷

In 2007, Wang and team reported a combustion method to prepare the stannate nanocrystals.²⁸ In 2011, a modified combustion method was addressed to prepare BaSnO₃ nanoparticles.²⁹ Aqueous solution of Ba(NO₃)₂ and SnCl₄·5H₂O was prepared using double distilled water. Citric acid was introduced to the solution maintaining cation to citric acid ratio 1:1. HNO₃ was added to the precursor solution under a good stirring to form a transparent solution without any precipitation or sedimentation. The pH was neutralised using liquor ammonia solution and heated at 250 °C until pale yellow powder was formed because of self propagating combustion process. The as prepared sample contained trace of BaCO₃ which was eliminated by heating the sample at 1200 °C. Cuboidal shaped agglomerated nanoparticles with a size variation from 20-30 nm were found from TEM images. In 2018, Kumar and co-workers followed another citrate-nitrate route for combustion method.³⁰ Appropriate amount of SnO₂ was dissolved into dilute nitric acid at a temperature of 100°C to form of tin (II) nitrate. An aqueous solution of C₆H₈O₇ was poured into the mixture of aqueous solution of two metal nitrates. For controlled combustion the ratio of C/N was kept at ~0.3. The precursor solution was heated at 200 °C under rigorous stirring to form a gel which was foamed and finally burnt on its own and turned into ash. The ash was finally heated at 1000 °C for 8 h. Nearly round shaped features were found from the FESEM images with an average size of 4.9 µm.³⁰

2.1.4. Hydro/ Solvothermal method

Hydrothermal/solvothermal method is a well-established method for the preparation of BaSnO₃. The aqueous or organic solvent solution of starting material is generally poured into one teflon lined autoclave in which the solution is heated above the boiling point under a

higher pressure than the ambient pressure. Various types of morphology can be obtained depending upon the synthesis parameters.³¹⁻³²

Although Kutty and co-workers synthesized fine barium stannate powder at comparatively low temperature (260 °C) but the micrometer sized particles were not suitable for sensing devices.³³ Later, Lu and Schmidt modified the hydrothermal process followed earlier by Kutty and his team.³⁴ $\text{SnO}_2 \cdot x\text{H}_2\text{O}$ gel was suspended in barium hydroxide solution with the help of argon gas. The suspension then was poured in a teflon-lined autoclave for heating treatment with temperature varied from 130 °C to 350 °C. The as prepared powder contained traces of barium hydroxide within it. To obtain pure phase the as prepared powder was calcined at 260°C.³⁴ Despite the fact that the agglomeration was found to be decreased but the particle size was still in the micrometer range. To eliminate the presence of hydroxide phase a new surfactant dependent hydrothermal method was introduced by Habeeba and co-workers in 2019.³⁵ Aqueous solution of Na_2SnO_3 was transferred into the aqueous solution of $((\text{CH}_3\text{COO})_2\text{Ba})$ drop by drop until the pH of the mixed solution reaches 12. The final solution was then shifted into a teflon coated autoclave and heated at 180°C for 6h followed by calcination at 1000°C for 2h. The involvement of high temperature and the presence of alkaline medium reduced the chance of impurity to be present in the final product. Broken nanosticks with smooth surfaces were formed. The size of the elongated cubes lied within 1-2.5 μm .³⁵ The FESEM, TEM images and EDX spectrum of the sample is presented in **Figure 2.4(a-c)**.

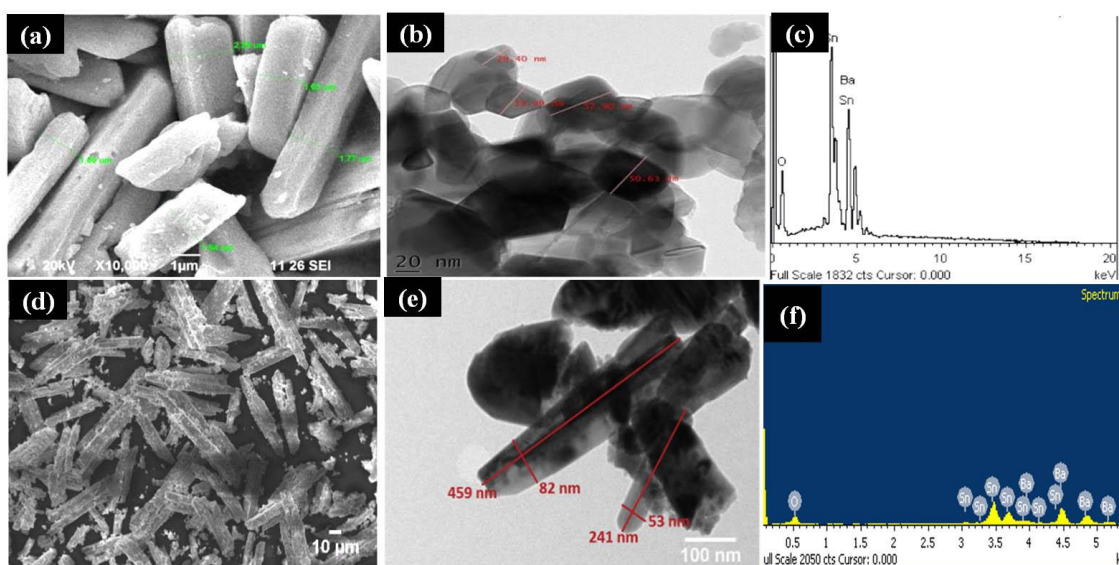


Fig. 2.4. (a-c) FESEM, TEM images and EDX spectrum of BaSnO_3 elongated cubes prepared by Habeeba et al.³⁵, (d-f) FESEM, TEM images and EDX spectrum of BaSnO_3 nano-micro rods prepared by Purushothamreddy et al.³⁶

In next year, another group took the similar hydrothermal synthesis method in which they used chlorides of metals ($\text{BaCl}_2 \cdot 2\text{H}_2\text{O}$ and $\text{SnCl}_4 \cdot 5\text{H}_2\text{O}$) and aqueous solution of sodium hydroxide (NaOH) to make the precursor solution alkaline.³⁶ Rod like morphology was found from TEM images with diameter between 50-90 nm and length between 200-460 nm. The FESEM and TEM images with EDX spectra of the sample are presented in **Figure 2.4d-f**.

2.1.5. Co-precipitation method

For controlling physical and chemical properties of the solid samples researchers often prefer wet chemical synthesis path.³⁷ The presence of base into the solution helps to precipitate the metals in the form of metal hydroxide from the salt reagents. Well dispersed products are prepared due to the controlled release of both types of ions which helps for the nucleation and growth of the product.³⁸ The precipitate is washed, collected and sometimes heated to get the desired phase pure powder sample.

In 2015, liquid phase synthesis method was reported.³⁹ In controlled precipitation method, tin (II) chloride and barium acetate were dissolved in HNO_3 separately and stirred constantly at 50 °C. After cooling down at room temperature, ammonium hydroxide was added to both the precursor solutions and aged for 24 h before mixing. By vacuum filtration the precipitate was collected and dried at 80°C. The dried powder was further washed with hydrochloric acid to wash out remaining barium carbonate. Heat treatment at different temperature showed that at 500 °C SnO was transformed to SnO_2 . At 800 °C the presence of single peak of BaSnO_3 denotes the product formation was started at that temperature. The peak at 1422 cm^{-1} in FTIR spectra present for the samples heated below 1250 °C indicates the existence of BaCO_3 as an impurity. After a heat treatment at 1250°C for 2h finally pure BaSnO_3 powder was obtained. The XRD and FTIR spectra of the products calcined at different temperature along with the SEM images for the final pure product calcined at 1250 °C are presented in **Figure 2.5(a-c)**. Rajamanickam and co-workers proposed a new modified oxalate co-precipitation method to synthesize barium stannate nanostructure.⁴⁰ Under stirring, appropriate amount of BaCl_2 and SnCl_4 were allowed to dissolve in distilled water separately and mixed together to form stock solution. Aqueous solution of oxalic acid was shifted to the stock solution under continual stirring for 3h to get precipitation. The precipitate was collected and washed with deionized water followed by calcination (900°C for 3h). Agglomerated cuboids like structure with a dimension of 139-458 nm was found from FESEM study. Using chloride salts of barium and tin, Kurre and his team tried to synthesize the desired stannate material.⁴¹ The starting

materials were taken in similar proportion and mixed into distilled water under vigorous stirring. Certain amount of sodium hydroxide was added to the mixture suspension to make the medium basic. The precipitate was collected, washed and dried. Finally to get crystalline barium stannate powder the prepared powder was heated at 800 °C. Agglomerated particles with size $\sim 2 \mu\text{m}$ were found in FESEM image.⁴¹

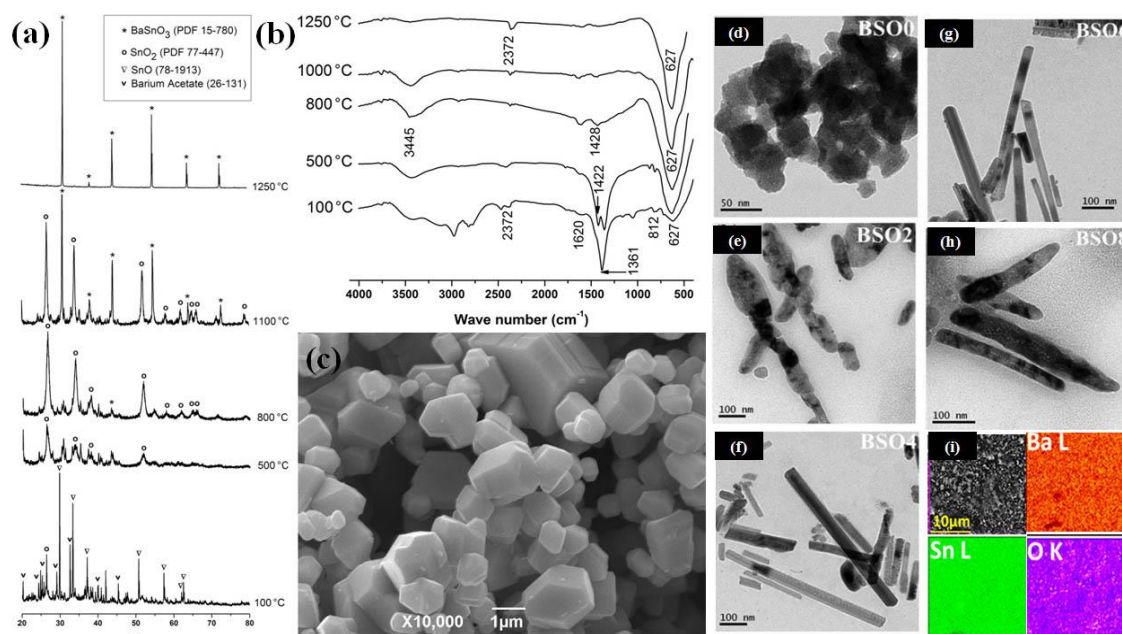
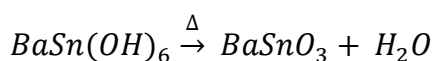
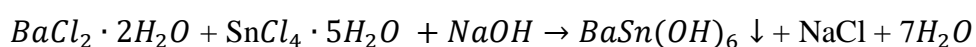


Fig. 2.5. (a) XRD, (b) FTIR spectra of different temperature calcined and (c) FESEM image of the final product reported by Muñoz *et al.*³⁹, (d-h) TEM images of BaSnO₃ with prepared with different dextron concentration and (i) elemental mapping of 6% dextron used BaSnO₃ sample reported by Roy *et al.*⁴³

In 2018, a new colloidal method was introduced by Shin and associated researchers in which 10 mmol BaCl₂·2H₂O, 10 mmol SnCl₄·5H₂O and 5 mmol citric acid (C₆H₈O₇) were dissolved in H₂O₂ while stirring.⁴² The aging temperature and time was varied from room temperature to 90 °C and from 0 min to 60 min. The concentration of H₂O₂ was also varied from 0-30%. The precipitate was cleaned with D.I. and ethanol to eliminate any impurity and then dried. The resultant powder was calcined at various temperatures. It was found that the powder sample prepared at room temperature was amorphous whether the other samples (prepared in higher temperature) shows major XRD peak of crystalline BaSnO₃. The optimum synthesis temperature, concentration of H₂O₂, stirring time and calcination temperature to get pure crystalline stannate were 50 °C, 30%, 1h and 200 °C respectively. The average size of the nanoparticles was 18.6 (± 1.36) nm which was found to be righteous for film deposition. The incorporation of dextron enabled the morphology of the prepared sample to change from nanoparticle to micro-nanorod having a diameter and length of 30-70 nm and $>1 \mu\text{m}$

respectively.⁴³ The TEM images of the synthesized materials with various concentration of dextran are shown in **Figure 2.5 (d-h)** and the EDX mapping for 6% dextran is shown in **Figure 2.5 (i)**. In 2020, Sharma and Chhoker reported a low temperature method to synthesize barium stannate microrods. Under constant stirring, NaOH was added to aqueous solution of $\text{BaCl}_2 \cdot 2\text{H}_2\text{O}$ at 75 °C to make the pH of the mixture above 9.⁴⁴ Aqueous solution of $\text{SnCl}_4 \cdot 5\text{H}_2\text{O}$ was poured to the mixture solution and precipitates formed. Then the solution was heated at 95 °C for a period of 1 h and then allowed to dry at 400 °C in an oven. The as-synthesized powder was then calcined at 1100 °C for 4 h in furnace to form crystalline BaSnO_3 . Plausible reactions can be written as



2.1.6. Film deposition

The impact of lattice-strain on the physical characteristics of thin films as a result of the differences in the lattice parameters of the base material and the coated samples has always been a fascinating area of research. Several techniques were adopted by researchers to deposit films of BaSnO_3 , such as pulse laser deposition (PLD), molecular beam epitaxy (MBE), radio frequency (RF) sputtering etc. In 2012, Balamurugan *et al.* reported growth of BSO thin films on Silicon substrate (exhibiting n-character) using PLD method.⁴⁵ To achieve high quality films, substrate temperature and pressure were optimized. They found that the films were either polycrystalline or preferred to grow in (2 0 0) direction. Wang reported that the La and Sb doped BSO films fabricated on SrTiO_3 substrate using laser ablation technique exhibits a carrier concentration $2 \times 10^{21} \text{ cm}^{-3}$ and a mobility of $0.69 \text{ cm}^2/\text{Vs}$.⁴⁶ For the improvement in the conductivity and the electronic structure of the films James and his team prepared BSO films with lanthanum doping deposited on inexpensive substrate fused silica using laser ablation. They reported a conductivity ($\sim 9 \text{ Scm}^{-1}$) for 7% doping.⁴⁶ There are many reports in literature to improve the structural properties and electrical conductivity of pure and modified BSO thin films prepared following PLD method.⁴⁷⁻⁵⁰ Although, La doped BSO in form of single crystals showed a mobility $\sim 300 \text{ cm}^2 \text{ V}^{-1} \text{ s}^{-1}$ at 27 °C reported by Luo and co-researchers, high quality films with low defects were still to be investigated.⁵¹ In 2015, Raghavan *et al.* reported high mobility films of BSO using MBE method.⁵² They found a room temperature mobility of $150 \text{ cm}^2 \text{ V}^{-1} \text{ s}^{-1}$ for the films prepared on PrScO_3 substrate.

Another improvement in the mobility was reported by Paik and team in 2018.⁵³ Films of La doped BSO was grown on (0 0 1) DyScO₃ substrate showed a room temperature mobility of 183 cm²V⁻¹s⁻¹ at and as the temperature went down the mobility acquired a value of 400 cm²V⁻¹s⁻¹ at 10 K. A RF sputtered La doped BSO thin film grown on (LaAlO₃)_{0.3}(SrAl_{0.5}Ta_{0.5}O₃)_{0.7} (001) substrates exhibited an effective mass 0.39m₀ for electrons.⁵⁴ They also reported that Fowler-Nordheim tunneling was prime reason for the conduction. In 2020, Wang and Luo empirically showed that substitution of nitrogen in the anionic site could lead to the *p*-type conductivity of radio-frequency sputtered BSO thin films.⁵⁵ The room temperature mobility was 0.86 cm² V⁻¹ s⁻¹ and the carrier concentration was 4.15 × 10¹⁶ cm⁻³, which were significantly higher than other previous results for *p*-type BSO. In recent years, a few inexpensive and simple techniques for film deposition were reported but the quality of the films utilizing these simpler techniques is not up to the mark as the complicated techniques mentioned above. In 2019, Zhang and team took the idea of colloidal synthesis of BSO nanoparticles from Shin and using spin coating fabricated films on FTO substrates.^{42,56} The presence of nanopores in the films helps to enhance the surface area which is very important for any absorbance related phenomenon. In 2022, thin films of BSO were grown on glass substrate via simple hydrothermal route by Muraleedharan and Ashok.⁵⁷ High conductivity (carrier concentration: 9.83 × 10¹⁸ cm⁻³) along with >82% visible light transparency was reported.

2.2. Stability issues

Although there are different synthesis procedures for the preparation of barium stannate powder sample but many of them have drawback of impurity related issues especially those with a low synthesis temperature. Barium reacts easily with moisture to form Ba(OH)₂ which being a corrosive material further interacts with the CO₂ in air to be sedimented as BaCO₃. This impurity in the form of BaCO₃ is very difficult to get rid of.⁵⁸⁻⁵⁹ There are ways to remove BaCO₃ as to anneal the sample at a high temperature and to wash off the sample with acetic acid in which BaCO₃ got dissolved easily but not BaSnO₃.^{21,60} Both the ways have their own limitations. Using high temperature to remove impurities after the full synthesis procedure done at low temperature can hamper the particle size achieved at low temperature. Acid wash can also affect the quality of the sample like the particle size, shape and structure.

2.3. BaSnO₃: previous reports on applications

2.3.1. Ceramic Capacitors

Barium Stannate has been utilized as a promising thermally stable ceramic capacitor for decades due to its high dielectric constant and thermal stability ($> 1000\text{ }^{\circ}\text{C}$).⁴ As the capacitance is proportionally related to the dielectric permittivity, thus the material with large dielectric permittivity proves to be a good candidate for capacitive application in microelectronics. Another important factor for being an effective capacitor material is ‘low dielectric loss’.⁶¹ Dielectric properties of a material like dielectric permittivity, tangent loss, ac conductivity generally depends on various parameters like frequency, temperature, DC bias, particle size, degree of porosity etc.⁶²⁻⁶⁴ Thus for capacitor material, study of dielectric properties is utmost important. AC Impedance spectroscopy analysis is the well known technique to understand the changes in dielectric properties with various parameters.

It is well established fact that the compactness of the ceramic body has a great impact on the dielectric constant. The porosity or alternatively the relative density of a material solely depends on the synthesis method and temperature. Azad *et al.* reported that the porosity level can easily alter the dielectric constant of porous barium stannate.⁶⁵ The denser ceramic exhibits high dielectric constant compared to a porous one. Also they showed that fully dense BaSnO₃ ceramic could not be obtained even after sintering at very high temperature ($1650\text{ }^{\circ}\text{C}$). In 1997, Upadhyay and Prakash synthesized agglomerated microcubes following standard solid-state reaction path held at $1200\text{ }^{\circ}\text{C}$ for 6 h in air atmosphere.¹¹ It was found that the size of the microcubes varies from 2 to $4\text{ }\mu\text{m}$ with 20% porosity. Pronounced frequency dispersion in dielectric constant with temperature was explained with interfacial polarization resulting from high temperature ($1250\text{ }^{\circ}\text{C}$) sintering of the pellets. The dielectric loss was found to be associated with the oxygen deficiency generated from high temperature firing. Singh and co-workers followed a similar synthesis route with a calcination temperature of $1250\text{ }^{\circ}\text{C}$ for 12 h to observe the changes in dielectric constant and the loss below room temperature (300 K).¹³ Agglomerated microcubes were observed with a dimension of $1\text{--}3\text{ }\mu\text{m}$ and high level porosity was confirmed from the FESEM images. When the temperature lowers down to 178 K from the room temperature, the dielectric constant and the dissipation factor both have shown a decreasing tendency. As the capacitance of the capacitor containing a dielectric is proportional to its dielectric constant, so it showed the

same trend with the variation of temperature. They proposed that interfacial polarization along with orientational polarization were responsible for that behavior. The high temperature sintering boosts the oxygen vacancy generation which further captured by Sn^{4+} to form Sn^{2+} . The effective negative charge $(\text{Sn}_{\text{Sn}^{2+}}^{4+})^-$ forms a dipole with oxygen vacant site which contributes in dipolar polarization. At higher temperature the dissociation of defect pairs causes charge transportation through the bulk. At grain boundaries these charges face high resistance and space charge polarization occurs. The activation energy was evaluated using Arrhenius relation and the reported values were 0.25 eV for AC and 0.52 eV for DC conduction.¹³ In 2013, nanograined barium stannate powder was synthesized by Katiliute and colleagues following sol-gel synthesis method in which the annealing temperature was set at 800 °C.⁶⁶ They found that the dielectric spectra were suppressed by the humidity induced conductivity within the temperature between 300 K to 1000 K. Due to low temperature annealing the sample formed with high porosity helps to absorb moisture from the atmosphere. In 2018, for the first time, Nunn and his team reported the role of frequency and temperature on the electrical properties of BaSnO_3 films.⁶⁷ Thin films of barium stannate were grown on a conducting substrate following MBE method. The substrate used was Nb doped (0.5 wt%) SrTiO_3 oriented in (001) direction. By controlling the ratio of beam equivalent pressure for Sn:Ba stoichiometric and non-stoichiometric films were fabricated. The thickness of the films was kept in between 40 to 49 nm. Ba and Sn deficient films were grown to study the influence of cation stoichiometry upon the electrical properties within a temperature range between 77 K and 300 K. The dielectric constant was unchanged for all the films which indicate that the dielectric constant independent on the cationic stoichiometry of the films, whereas the tangent loss showed a higher value for non-stoichiometric films. The authors suggested that the defects generated because of the cation vacancy might be the cause for the enhancement in $\tan\delta$. The dielectric constant was also found to be nearly independent of thickness of the films, whereas the loss factor dropped hyperbolically with the increase in film thickness to $\sim 1 \times 10^{-3}$. They proposed that interfacial ‘dead layer’ effect might be responsible for this behaviour.⁶⁷ In the next year, Mushen and co-researchers observed giant dielectric constant of BaSnO_3 with 30% porosity at high temperature aroused from space charge polarization at grain boundaries.⁴ Also they proposed the generation of oxygen vacancy due to high temperature sintering (1400 °C) is another source of high polarization. The reported values of the capacitances at 1 kHz were 27.47 pF cm^{-1} (at room temperature) and 6.01 nF cm^{-1} (at 220°C).

Doping is a widely used way to alter the electrical properties of materials.⁶⁸ Doping in cation sites is one of the best methods to tailor the dielectric properties of BaSnO₃ as it was observed that the partial substitution of barium or tin by other isovalent or aliovalent cations cause a significant change in its microstructure which further can affect the electrical characteristics as well.⁶⁹⁻⁷⁰ In 2005, Kumar *et al.* reported the effect of calcium doping (at Ba site) on the electrical properties of BaSnO₃ in which they have followed traditional solid state reaction path to anneal the precursor mixture at 1000 °C for 12 h.⁷¹ The temperature dependent complex impedance spectroscopy analysis confirmed the NTCR behaviour of the doped samples. They observed that there was a reduction in the magnitude of the modulus spectra suggesting an enhancement of capacitance after doping. Also, the partial substitution of Ca in BaSnO₃ led to enhance the bulk resistance resulting in a significant reduction in electrical conductivity. They correlated the behaviour with the lattice distortion as an after effect of doping. The mismatch between the radius of Ca²⁺ and Ba²⁺ ions results a suppression in the conduction path through the lattice which further promotes the barrier property of the doped stannate.⁷¹ In the same year, the same group of researchers reported the effect of Te modification (at Sn site) on the electrical properties of micrograined barium stannate.⁷² The enhancement of dielectric constant (38 times at 1 kHz) due to Te⁴⁺ doping was correlated with the spontaneous polarization created by highly polarized Te⁴⁺ ion. The electrical conductivity was found to be increased for the doped systems at high temperature due to the hopping conduction mechanism.⁷² In 2018, Rajamanickam and co-workers synthesized Fe doped BaSnO₃ via modified oxalate route where the calcination temperature was fixed at 900 °C for 3 h.⁴⁰ Giant dielectric constant was observed for every sample. The rise in dielectric constant after doping with non-isovalent Fe²⁺ ion at Sn⁴⁺ site was correlated with particle size enhancement after doping. The reported value of the average crystallite size for undoped sample was 22 nm, which increased to 26 nm after 5% Fe doping. Similarly, the group observed that the morphology was changed from cuboids (138-458 nm) to nanomicrorod (diameter of 51-210 nm and length 0.253-1.57 µm). In the year of 2021, John and team also studied the dielectric properties of Fe doped BaSnO₃ system following standard solid state synthesis method.¹⁷ Although the similar type of morphology was found in undoped and doped samples as reported by Rajamanickam *et al.* but the density and the mean value of the crystallite size of the sample were decreased with doping percentage resulting a decreasing tendency of the dielectric constant for doped samples. Another factor suggested by the authors was the suppression of the polarizability because of the charge neutralization

of Fe^{3+} ions with O^{2-} ions. It was reported that the electrical conductivity showed an appreciable reduction after doping due to defect formation in host BaSnO_3 which leads to create blockage to the carriers near grain boundaries. In the same year, Islam and colleagues reported the temperature dependent study for the dielectric constant and tangent loss of heavily Mn doped (30%) barium stannate synthesized by solid state reaction path.¹⁶ The linear angulated growth of dielectric constant with temperature was described with the internal barrier layer capacitor (IBLC) model of grain and grain-boundary. The presence of maxima in $\tan\delta$ vs temperature graph entitled to the themally activated orientational polarization. Also the effect of doping via Ni, Pb, Ce, Co etc. on the dielectric constant or alternatively capacitance was reported.^{17,72-74} The dielectric constant and tangent loss for BaSnO_3 based systems reported earlier are enlisted in **Table 2.1**.

Fig. 2.1. Table for different values of dielectric constant reported previously

Synthesis method	Precursors used	Calcination temperature (°C)	Pellet sintering temperature (°C)	Room temperature Dielectric constant	Reference
Solid-state	BaCO_3 , SnO_2	1200 °C for 6 h	1252 °C for 6 h	~60 at 1KHz	[11]
Solid-state	BaCO_3 , SnO_2	1250 °C for 12 h	1350 °C for 12 h	~25 at 1 kHz	[13]
Solid-state	BaCO_3 , SnO_2	1350 °C for 6 h	1400 °C for 8 h	~27 at 1 kHz	[4]
Sol-gel	SnC_2O_4 , $\text{Ba}(\text{OH})_2$, H_2O_2 , $\text{C}_6\text{H}_8\text{O}_7$, liquor NH_3	800 °C for 5 h	800 °C for 5 h	~100 at 396 Hz	[66]
Solid-state	BaCO_3 , SnO_2 , PbO	1000 °C for 24 h	1200 °C for 12 h	~50 at 100 Hz (pristine) ~140 at 100 Hz (Pb doped)	[72]
Solid-state	BaCO_3 , SnO_2 , Fe_2O_3	1250 °C for 12 h	—	~82 at 1 KHz (pristine) ~20 at 1 kHz (Fe doped)	[17]
Solid-state	BaCO_3 , SnO_2 , MnCO_3	1000 -1100 °C for 24 h	1200 °C for 24 h	Between 15-18 at 500 Hz for all	[16]

2.3.2. Gas Sensors

In polycrystalline materials, the barrier potential and the donor concentration level can be altered by the adsorption process of gaseous molecules by the grain boundaries of the solids. The barrier potential increases due to the chemisorption of oxygen by the grains of the semiconductors. In some metal oxide semiconductors, the diffusion of oxygen into the grains at high temperature to annihilate the vacancies and thus donor concentration is reduced. Oxide semiconductors with large oxygen vacancy are popular in this field showing their *n*-character. BSO is one of them.⁷⁵ The exquisite property of BSO having a band gap of 3.4 eV is compatible with the gas sensor materials.⁷⁶⁻⁷⁷ It was experimentally proved that the oxygen adsorbed by the surface of the material is the prime reason for the electron diffusion from the semiconductor grains to the chemisorbed oxygen.⁷⁸⁻⁸⁰ The working principle of the sensor devices is subjected to the changes in the electrical resistance of the sensor material with respect to that in air/vacuum when the gaseous species are present. Hence, the change in electrical conductivity or resistance in presence of gas can be said as the measure of the ability of the sensor, called sensitivity. Mathematically, the sensitivity of a gas sensor is expressed as,

$$S = \frac{R_g}{R_a} \quad (2.1)$$

Where, R_g and R_a are the resistances measured in presence of gas and that in presence of air respectively.⁸¹⁻⁸² The resistances depend on the operating temperature and the volumetric fraction of gas present in the chamber. The electrical properties of BSOs are highly sensitive to the atmospheric parameters like humidity, presence of gas etc. This intriguing property of the sample makes it appropriate for gas sensing purpose. There are a number of research works reported in literature based on the gas sensing property of BaSnO_3 . Shimizu *et al.* reported the changes in the electrical properties of barium stannate in presence of the exhaust gas of $\text{C}_3\text{H}_8\text{-O}_2$ combustion and he for the first time reported that this perovskite oxide can be used as a promising gas sensor.⁸³ At early stage of research in this field, various reports were documented regarding different gas (like NO , CH_4 , CO , ammonia etc.) sensing property of barium stannate either in ceramic or in thick film form.⁸⁴⁻⁸⁵ In all cases the highest sensitivity was obtained at elevated temperature. In 2000, Lu *et al.* studied the oxygen partial pressure dependent electrical conductivity at high temperature ($843^\circ\text{C} - 1000^\circ\text{C}$) and found that the main reason for gas sensing is presence of oxygen vacancy.⁸⁶ Cerda *et al.* reported the high

sensitivity for CO gas between 400 °C and 600 °C as within this temperature range, the decrement in Schottky barrier height promotes the kinetic reaction rate.⁸⁷ Cavanagh *et al.* reported that the thick films of BaSnO₃ could be a promising CO₂ sensor in the range between 0 to 2500 ppm.⁸⁸ They have also found that the enhancement in reversible carbonate formation in humid atmosphere is the reason for better CO₂ sensitivity in presence of humidity than in dry air condition. In the year of 2015, Ochoa and co-workers fabricated BSO thick films using screen printing methods in which they used two types of BSO powder, one prepared via controlled precipitation (CP) method and another using Pechini method.⁸⁹ They found that although both the films exhibited good response as sensor in presence of oxygen at 300 °C but the film prepared by Pechini method is better than the other one. They also found that the films of Pechini method showed significant sensitivity towards CO at 450 °C. They explained the lack of sensitivity of the CP films by accounting the fact of higher grain size. Even at higher temperature, the equilibrium condition between the grain boundaries and the atmosphere was not become possible by the CP films having average grain size of 3.5 µm. Hence, oxygen could not be able to diffuse into the grain boundaries completely and the inner part of the sample would not be affected by the changing atmosphere resulting a low conductivity.⁸⁹ Wang *et al.* synthesized mesoporous BSO using mannitol assisted hydrothermal-annealing process for ethanol sensing.⁹⁰ They reported that the sensor device was able to detect lowest concentration of ethanol (50 ppm) at 350 °C due to the mesoporus nature which enhances the surface area of the sample. The BET surface area of the BSO powder was 121.9 m²/g, with a pore size of 8 nm. They also claimed that the device functioning was rapid and the response time was only 10 s. Chu and team in 2020, reported BSO microtubes by electrospinning method for the first time.⁹¹ The length and the outer diameter of the microtubes were 10 mm and 700 nm -2 µm respectively. The tube wall was made up with nanoparticles of size 40 nm. They demonstrated that the microtubes' acetic acid detection limit was 0.3 ppm at 254 °C, making it a superior sensor than many other oxide sensors. The electrons from CH₃COOH captured by the adsorbed oxygen species and then returned to the conduction band of BSO resulting an enhancement in conductivity. They also reported the response time of the sensor film for 0.3 ppm acetic acid was only 3 s. Ongun *et al.* proposed optical gas sensing can be performed by the BSO films prepared following one flame spray pyrolysis method.⁹² The emission and excitation spectra of BSO showed sudden fall in presence of ethanol, acetone and ammonia. They claimed that the surface related defects created by the polyhedral semimicron particle (70-980 nm) were the main

reason for the sensitivity of the sensor. The highest selectivity toward ammonia compared to ethanol and acetone was attributed either due to the unshared electrons in NH_3 structure or the easy diffusion of ammonia molecule having smaller radius (0.18 nm) into polymeric membrane. In 2022, Verma and co-workers reported a one step hydrothermal-annealing process to synthesize BSO nanorods which showed good selectivity towards acetone among many volatile organic compounds exhaled by human breath.⁹³ The sensor device was able to detect low concentration (1 ppm) of acetone at 80 °C with response time 3.325 s. They recommended that diabetes individuals can utilise the device as a non-invasive monitoring tool. There were many more articles regarding the gas sensing capability of BSO in literature.⁹⁴⁻⁹⁷

2.4. Electron field emission as a non-trivial application

Leveraging its excellent dielectric properties, ceramic capacitor applications have always been in lime light for alkaline earth stannate perovskites. Cold electron emission or field emission is one of the uncharted possible applications, which shows huge contribution in display system due to low power consumption, high image quality and no warm up time.⁹⁵ Although a large number of reports are there on traditional binary oxides (ZnO, MnO_2 etc.), inorganic semiconductors (Si, SiC etc.) and carbon (carbon nanotubes) based cold cathode emission, very few studies can however be reported for wide band gap perovskite oxides.

In 2012, Yang *et al.* showed that the field emission behavior of ZnO can be improved by preparing heterostructure of ZnO- LaNiO_3 on seeding layer of GZO (Ga doped ZnO).⁹⁸ They have prepared GZO seed layer on Si/glass substrate using radio frequency sputtering method on which ZnO layer was fabricated following hydrothermal method. The thin film layer of LNO (LaNiO_3) was deposited by radio frequency sputtering method. The vertical alignment of nanorods was presented in FESEM images and the core-shell heterostructure of ZnO-LNO was confirmed from HRTEM images. The thickness of the LNO layer was 10-20 nm and the diameter of the nanorods was in between 50-100 nm. The turn on were 29.2, 22.9 and 8.6 V/ μm for LNO film, ZnO film and ZnO-LNA film respectively. Also the threshold field showed the similar lowering pattern for the films. The highest emission current density was reported for the ZnO-LNA film for which the enhancement factor was 673. The authors explained the high emission properties of the heterostructure film by addressing different factors. The low work function of LNO (4.5 eV) promotes the electron emission capability compared to that for ZnO film having higher work function (5.3 eV). Additionally, the

electron transport from ZnO to LNO layer is facilitated by the absence of a Schottky barrier at the junction between the two layers. As the interfacial defect density is comparatively small for nano-heterostructure, a large number of electrons can be transferred from n type GZO layer to LNO layer by passing through ZnO layer easily which improves the electron emission of the core-shell. The FESEM, HRTEM images and the field emission characteristics graphs are presented in **Figure 2.6(A)**.⁹⁸ Kamble and co-workers found strong localization effect on field electron emission of LaNiO_3 nanoparticles.⁹⁹ The sol-gel processed sample showed pyramidal shape in FESEM and HRTEM images **Figure 2.6(B)**. Several pyramidal and whisker type growth of average size 300 nm was confirmed from AFM image **Figure 2.6(B)**. The reported values of emission current density and threshold field were 3.37 mA/cm^2 and $19.23 \text{ V}/\mu\text{m}$ respectively. The turn on field to achieve a current density of 0.1 mA/cm^2 was $16.91 \text{ V}/\mu\text{m}$. The high aspect ratio of pyramidal and whisker shape is accountable for better electron emission and a large value of field enhancement factor $\beta = 249.37$. The emission current density vs. applied electric field graph is presented in **Figure 2.6(B)**.⁹⁹ In the year of 2020, Yang *et al.* observed thickness dependency of the field electron emission of SrTiO_3 films deposited on ITO substrate using electron vapor deposition method.¹⁰⁰ The highest emission current density ($88.96 \mu\text{A}/\text{cm}^2$ at $10.45 \text{ V}/\mu\text{m}$) was reported for the film with thickness of 45 nm. Also, the impact of hydrogen plasma treatment on the cold emission properties of SrTiO_3 films were thoroughly investigated and published by Wang *et al.*¹⁰¹

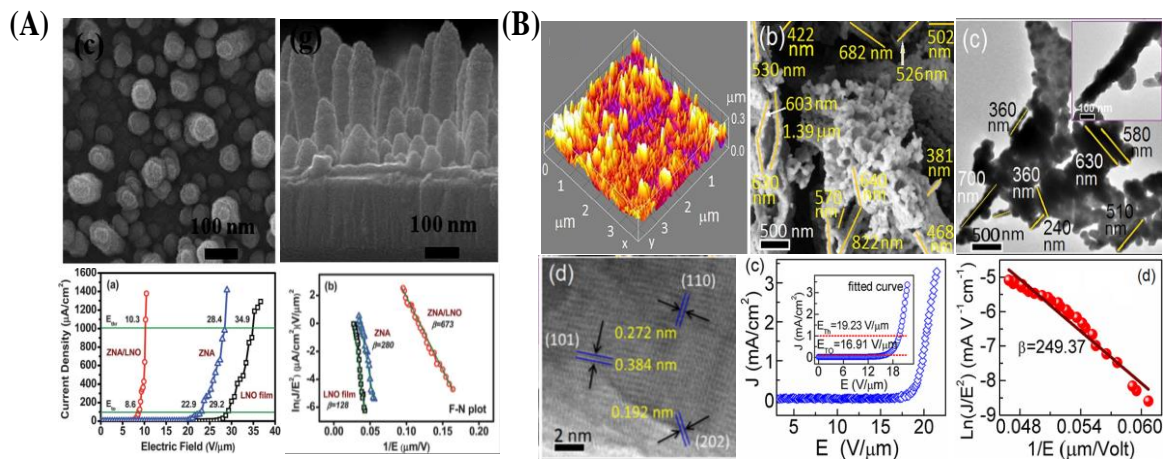


Fig. 2.6. (A) FESEM, HRTEM images and the field emission characteristics for LaNiO_3 reported by Yang *et al.*⁹⁸; (B) AFM, FESEM, HRTEM images, lattice image and FE characteristics graphs for LaNiO_3 by Kamble *et al.*⁹⁹.

2.5. Improvement of the electrical properties of perovskite/polymer composite

The ceramics like BSO generally show high dielectric constant but also they are fragile as well as having low dielectric strength. In contrast, polymers are flexible, simply processed and exhibits high dielectric breakdown voltage but possess low permittivity. Thus to get better properties of both, composites are prepared with comparatively high dielectric permittivity and a large breakdown strength.

Impressed by the electrical properties of BSO, we further studied the previous works on the improvement in the electrical properties of perovskite/polymer composites. The high dielectric permittivity and thermal stability of BSO motivates to expand our work into composite system with polymer. In general, the electroactive phase of polymer polyvinylidene fluoride (PVDF) is very much popular for its piezoelectric behavior.¹⁰² The polymer film is a potential candidate in the field of high energy densities electronic applications like capacitors, mechanical energy harvester etc.¹⁰³⁻¹⁰⁵ But the dielectric permittivity of the polymer is quite small for real life application. Sasmal *et al.* reported that the dielectric constant of the additive material should be greater than that of PVDF but not so high that the dielectric compatibility between the two parts of the composite becomes impaired.¹⁰⁶

In 2021, Mondal *et al.* reported that the low temperature oil bath processed halide perovskite CsPbCl_3 (with cubelike morphology) with PVDF matrix served as a good mechanical energy harvesting device.¹⁰⁷ The electroactive phase of the polymer was enhanced >86% for 3 wt% perovskite involvement. Also, the dielectric permittivity and the conductivity were increased with perovskite content within composite system. The dielectric permittivity directly enhanced the piezoelectric coefficient of the system too, as the two parameters bear a linear relation. Upon freehand hammering with a pressure ~ 100 MPa, the best hybrid film showed an open circuit voltage of ~ 168 V and a short circuit current of ~ 2 μA . The interfacial interplay of the surface charge of perovskite nanocubes with the polymer chain was responsible for conversion to all-trans configuration of the polymer which promotes the output performance of the hybrid devices. Xue *et al.* studied self polarization of $\text{CsPbBr}_3/\text{PVDF}$ composite using electrospinning technique.¹⁰⁸ For 4% perovskite present into the composite film, the electroactive β phase was increased to 94.6%. The uniform

distribution of the perovskite into the composite system at the time of electrospinning was the key factor for self-poling effect. Kum-onsa and team observed that the composite system of perovskite oxide LaFeO_3 (5 vol%) and PVDF exhibits a high dielectric permittivity (~ 54.6) and low dissipation (~ 0.059) at a frequency of 1 kHz.¹⁰⁹ The charge carriers were trapped at the interfacial areas between the semiconducting perovskite and the insulating polymer because of the intense interfacial polarization at those sites. This in turn enhanced the dielectric permittivity of the system. Also, the electroactive β phase of PVDF was found to increase for the hybrid films, which is another factor for the better electrical properties. The same group in 2022, synthesized nAu decorated LaFeO_3 nanoparticles to combine with PVDF for a better result.¹¹⁰ For a volume fraction of 0.491, the electroactive β phase was increased upto 64% from 43%. The dielectric permittivity was doubled of its original value due to Au particle attachment with LaFeO_3 . The three-phase nano-composite showed 11 times higher value of dielectric constant with respect to the bare PVDF also. There are several reports regarding the enhancement of electrical properties of perovskite/PVDF composites.¹¹¹⁻¹¹⁴

2.6. References

1. H Takashima and Y Inaguma, *Applied Physics Letters*, 111(9) (2017) 091903
2. M. Souri and H. S. Amoli, *Materials Science in Semiconductor Processing*, 156 (2023) 107271
3. A. Marikutsa, M. Rumyantseva, A. Baranchikov and A. Gaskov, *Materials*, 8 (2015) 6437-6454
4. K. N. D. K. Muhsen, R. A. M. Osman and M. S. Idris, *Journal of Materials Science: Materials in Electronics*, 30 (2019) 7514–7523
5. A. Buekenhoudt, A. Kovalevsky, Ir. J. Luyten and F. Snijkers, 1.11 - Basic Aspects in Inorganic Membrane Preparation, *Comprehensive Membrane Science and Engineering*, (2010) 217–252
6. S. Ivanov, Chapter 7 - Multiferroic complex metal oxides: Main features of preparation, structure, and properties, *Science and Technology of Atomic, Molecular, Condensed Matter & Biological Systems*, 2 (2012) 163–238
7. M. Aykol, J. H. Montoya, and J. Hummelshøj, *Journal of the American Chemical Society*, 143 (24) (2021) 9244-9259

8. M. A. Janifer, S. Anand, C. J. Prabagar and S. Pauline, *Materials Today: Proceedings*, 47 (2021) 2067–2070
9. A. Kumar, B. P. Singh, R. N. P. Choudhary and A. K. Thakur, *Journal of Alloys and Compounds*, 394 (1–2) (2005) 292–302
10. H. Mizoguchi, P. Chen, P. Boolchand, V. Ksenofontov, C. Felser, P. W. Barnes and P. M. Woodward, *Chemical Materials*, 25 (2013) 3858–3866
11. Shail Upadhyay, Om Parkash and Devendra Kumar, *Journal of Materials Science Letters*, 16 (1997) 1330–1332
12. S. Upadhyay, O. Parkash and D. Kumar, *Materials Letters*, 49 (2001) 251–255
13. P. Singh, B. J. Brandenburg, C. P. Sebastian, P. Singh, S. Singh, D. Kumar and O. Parkash, *Japanese Journal of Applied Physics*, 47 (5) (2008) 3540–3545
14. S. Upadhyay, *Bulletin of Materials Science*, 36 (6) (2013) 1019–1036
15. C. Huang, X. Wang, X. Liu, M. Tian and T. Zhang, *Journal of the European Ceramic Society* 36 (2016) 583–592
16. I. Islam, S. A. Khandy, M. B. Zaman, A. K. Hafiz, A. M. Siddiqui and Jeng-Da Chai, *Journal of Alloys and Compounds* 867 (2021) 158900
17. J. John, S. Suresh, S. S. Pillai, R. Philip and V. P. M. Pillai, *Journal of Electronic Materials*, 50 (2021) 5868–5880
18. H. Dislich, *Journal of Non-Crystalline Solids*, 80 (1986) 115–121
19. N. Ugemuge, Y. R. Parauha, S. J. Dhoble, Chapter 15 - Synthesis and luminescence study of silicate-based phosphors for energy-saving light-emitting diodes, *Energy Materials Fundamentals to Applications*, (2021) 445–480
20. A. M. Azad, M. Hashim, S. Baptist, A. Badri and A. Ul. Haq, *Journal of Materials Science*, 35 (2000) 5475 – 5483
21. J. Cerda, J. Arbiol, R. Diaz, G. Dezanneau, J. R. Morante, *Materials Letters* 56 (2002) 131–136
22. U. Kumar, J. Ansaree and S. Upadhyay, *Processing and Application of Ceramics* 11 (3) (2017) 177–184
23. S. M. Yakout, H. A. Mousa, H. T. Handal and W. Sharmoukh, *Journal of Solid State Chemistry* 281 (2020) 121028
24. J. Wang, A. Han, M. Ye, C. Chen, X. Chen, and X. Zhu, *ACS Sustainable Chemistry and Engineering*, 9 (2021) 16328–16337

25. A. Varma, A. S. Mukasyan, A. S. Rogachev and K. V. Manukyan, *Chemical Reviews*, 116 (2016) 14493–14586
26. S. T. Aruna and A. S. Mukasyan, *Current Opinion in Solid State and Materials Science* 12 (2008) 44–50
27. E. Carlos, R. Martins, E. Fortunato and R. Branquinho, *Solution Combustion Synthesis: Towards a Sustainable Approach for Metal Oxides*, *Chemistry–A European Journal*, 26 (42) (2020) 9099–125
28. S. Wang, Z. Yang, G. Zhou, M. Lu, Y. Zhou and H. Zhang, *Journal of Material Science*, 42 (2007) 6819–6823
29. A. S. Deepa, S. Vidya, P. C. Manu, S. Solomon, A. John and J. K. Thomas, *Journal of Alloys and Compounds* 509 (2011) 1830–1835
30. U. Kumar, D. Yadav, S. Upadhyay and A. K. Thakur, *AIP Conference Proceedings*, 1942 (1) (2018) 140031)
31. E. Suvaci, E. Özel, *Hydrothermal Synthesis*, *Encyclopedia of Materials Technical Ceramics and Glasses*, 1 (2021), 59–68
32. Y. X. Gan, A. H. Jayatissa, Z. Yu, X. Chen and M. Li, *Journal of Nanomaterials*, 2020 (2020) 1–3
33. T. R. N. Kutty and R. Vivekanadan, *Materials Research Bulletin*, 22, (1987) 1457–1465
34. W. Lu and H. Schmidt, *Journal of Material Science*, 42 (2007) 10007–10013
35. K. Habeeba, T. E. Manjulavalli, D. V. E. G. Kumari and V. Karthikadevi, *Materials Research Express* 6 (2019) 094004
36. N. Purushothamreddy, M. Kovendhan, R. K. Dileep, G. Veerappan, K. S. Kumar and D. P. Joseph, *Materials Chemistry and Physics*, 250 (2020) 123137
37. N. S. Bajaj and R. A. Joshi, *Energy Materials Fundamentals to Applications*, (2021) 61–82
38. U. P. Ashik, S. Kudo and J. I. Hayashi, *Synthesis of inorganic nanomaterials*, (2018) 19–57
39. Y. H. O. Muñoz, M. Ponce and J. E. R. Páez, *Powder Technology* 279 (2015) 86–95
40. N. Rajamanickam, K. Jayakumar and K. Ramachandran, *Journal of Materials Science: Materials in Electronics*, 29 (2018) 19880–19888
41. R. Kurre, S. Bajpai and P. K. Bajpai, *Materials Sciences and Applications*, 9, (2018) 92–110
42. S. S. Shin, E. J. Yeom, W. S. Yang, S. Hur, M. G. Kim, J. Im, J. Seo, J. H. Noh and S. I. Seok, *Science*, 356 (2017) 167–71

43. A. Roy, P. P. Das, P. S. S. Sundaram and P. S. Devi, *ACS Sustainable Chemistry and Engineering*, 6 (2018) 3299–3310
44. S. Sharma and S. Chhoker, *Scientific Reports*, 10(1) (2020) 1-11
45. K. Balamurugan, E. Senthil Kumar and B. Ramachandran, *Journal of Applied Physics*, 111 (2012) 074107
46. H. F. Wang, Q.Z. Liu, F. Chen, G.Y. Gao and W. Wu, *Journal of Applied Physics*, 101 (2007) 106105
47. K. K. James, P. S. Krishnaprasad, K. Hasna and M. K. Jayaraj, *Journal of Physics and Chemistry of Solids*, 76 (2015) 64–69
48. U. S. Alaan, P. Shafer, A. T. N'Diaye, E. Arenholz and Y. Suzuki, *Applied Physics Letters*, 108 (2016) 042106
49. J. John, S. R. Chalana, R. Prabhu and V. P. M. Pillai, *Applied Physics A*, 125 (2019) 155
50. Y. Matsubayashi, J. Nomoto, I. Yamaguchi, D. Nishio-Hamane and T. Tsuchiya, *Applied Surface Science* 506 (2020) 144915
51. X. Luo, Y. S. Oh, A. Sirenko, P. Gao, T. A. Tyson, K. Char and S. W. Cheong, *Applied Physics Letters*, 100 (2012) 172112
52. S. Raghavan, T. Schumann, H. Kim, J. Y. Zhang, T. A. Cain and S. Stemmer, *APL Materials*, 4 (2016) 016106
53. H. Paik, Z. Chen, E. Lochocki, H. A. Seidner, A. Verma, N. Tanen, J. Park, M. Uchida, S. Shang, B. C. Zhou and M. Brützm, *Apl Materials*, 5(11) (2017) 116107
54. B. C. Luo, X. S. Cao, K. X. Jin and C. L. Chen, *Current Applied Physics*, 16 (2016) 20-23
55. J. Wang and B. Luo, *Ceramics International*, 46 (2020) 25678–25682
56. T. T. Zhang, X. D. Gao, Y. Q. Wu, J. N. Yang and X. M. Li, *Chemical Physics*, 522 (2019) 91–98
57. S. Muraleedharan and A. M. Ashok, *Physica B: Physics of Condensed Matter*, 625 (2022) 413463
58. R. C. Ropp, Chapter 1 - The Alkaline Earths as Metals, Editor(s): R.C. Ropp, *Encyclopedia of the Alkaline Earth Compounds*, Elsevier, (2013) 1-23
59. T. W. Clarkson, Chapter 61 - Inorganic and Organometal Pesticides, Editor(s): Robert I. Krieger, William C. Krieger, *Handbook of Pesticide Toxicology (Second Edition)*, Academic Press, 2 (2001) 1357-1428

-
60. Q. Liu, J. Liu, L. Bing, L. Hong, G. Zhu, D. Kai, Z. Liu, Z. Peng and J. Dai, *Applied Physics Letters*, 101 (2012) 241901
61. L. Dong, C. Xiong, H. Quan and G. Zhao, *Scripta Materialia*, 55 (2006) 835–837
62. N. Kumar, E. A. Patterson, T. Frohling and D. P. Canna, *Journal of Materials Chemistry C*, 4 (2016) 1782—1786
63. B. Mandal and P. Mitra, *Materials Chemistry and Physics*, 251 (2020) 123095
64. Q. Wang, K. Xue, P. Fu, F. Du, Z. Lin, Z. Chen, S. Wang and G. Wang, *Journal of Materials Science: Materials in Electronics*, 30 (2019) 6475-81
65. A. M. Azad, L. L. W. Shyan, T. Y. Pang and C. H. Nee, *Ceramics International*, 26 (2000) 685-692
66. R. M. Katiliute, P. Seibutas, M. Ivanov, R. Grigalaitis, A. Stanulis, J. Banys and A. Kareiva, *Ferroelectrics*, 464 (2014) 49-58
67. W. Nunn, A. Prakash, A. Bhowmik, R. Haislmaier, J. Yue, J. M. G. Lastra, and B. Jalan, *APL Materials*, 6 (2018) 066107
68. S. Rhouma, S. Saïd, C. Autret, S. De Almeida-Didry, M. El Amrani and A. Megriche, *Journal of Alloys and Compounds*, 717 (2017) 121-6
69. P. Rajasekaran, M. Arivanandhan, N. Sato, Y. Kumaki, T. Mori, Y. Hayakawa, K. Hayakawa, Y. Kubota, R. Jayavel and M. Shimomura, *Journal of Alloys and Compounds*, 894 (2022) 1623352
70. K. Balamurugan, N. H. Kumar, J. A. Chelvane and P. N. Santhosh, *Physica B: Condensed Matter*, 407(13) (2012) 2519-23
71. A. Kumar, B. P. Singh, R. N. P. Choudhary and A. K. Thakur, *Materials Letters* 59 (2005) 1880–1888
72. A. Kumar, B. P. Singh, R. N. P. Choudhary and A. K. Thakur, *Materials Chemistry and Physics*, 99 (2006) 150–159
73. S. Lilly Angel, K. Deepa, N. Rajamanickam, K. Jayakumar, and K. Ramachandran, *AIP Conference Proceedings*, 1942 (2018) 050004
74. A. Adak (Maity), S. Mukherjee, M. Ghosh Chaudhuri and S. Mukherjee, *AIMS Materials Science*, 3(3) (2016) 1281-1293
75. G. Larramona, C. Gutierrez, I. Pereira, M. R. Nunes and F.M.A. Da Costa, *Journal of Chemical Society, Faraday Transactions 1*, 85 (1989) 907
76. M. J. Madou and S. R. Morrison, Chapter 3. In *Chemical Sensing with Solid State Devices*, Academic Press: New York, (1989)

77. B. Ostrick, M. Fleischer and H. Meixner, *Journal of American Ceramic Society*, 80 (8) (1997) 2153–2156
78. N. Yamazoe, J. Fuchigami, M. Kishikawa, and T. Seiyama, *Surface Science*, 86 (1979) 335
79. S. C. Chang, *Journal of Vacuum Science and Technology*, 17 (1980) 366
80. M. A. Ponce, C. Malagu, M. C. Carotta, G. Martinelli and C.M. Aldao, *Journal of Applied Physics*, 104 (2008) 054907
81. C. V. G. Reddy , S. V. Manorama, V. J. Rao , A. Lobo and S. K. Kulkarni, *Thin Solid Films*, 348 (1999) 261-265
82. S. V. Manorama , C. V. G. Reddy, V. J. Rao, *Applied Surface Science*, 174 (2001) 93-105
83. Y. Shimizu, Y. Fukuyama, T. Narikiyo, H. Arai and T. Seiyama, *Chemistry Letters*, 14 (1985) 377
84. B. Ostrick, M. Fleischer, U. Lampe and H. Meixner, *Sensor and Actuators B*, 44 (1997) 601–606
85. U. Lampe, J. Gerblinger and H. Meixner, *Sensor and Actuators B*, 26 (1-3) (1995) 97–98
86. W. Lu, S. Jiang, D. Zhou and S. Gong, *Sensor and Actuators B*, 80 (2000) 35–37
87. J. Cerda`, J. Arbiol, G. Dezanneau, R. Di´az and J. R. Morante, *Sensors and Actuators B*, 84 (2002) 21–25
88. L. M. Cavanagh, P. Smith and R. Binions, *Journal of the Electrochemical Society*, 159 (3) (2012) J67-J71
89. Y. H. Ochoa, F. Schipani, C. M. Aldao, J. E. Rodríguez-Páez and M. A. Ponce, *Journal of Materials Research*, 30 (22) (2015) 3423-30
90. G. Wang, J. Bai, C. Shan, D. Zhang, N. Lu, Q. Liu, Z. Zhou, S. Wang and C. Liu, *Materials Letters* 205 (2017) 169–172
91. X. Chu, Z. Gan, L. Bai, Y. Dong and M. N. Rumyantseva, *Materials Science & Engineering B*, 259 (2020) 114606
92. M. Z. Ongun, S. Oguzlar, S. A. Akalin, and S. Yildirim, *Journal of Materials Science: Materials in Electronics*, (2021) 32:15160–15170
93. A. Verma, D. Yadav, A. Singh, M. Gupta, K. B. Thapa and B. C. Yadav, *Sensors and Actuators: B. Chemical*, 361 (2022) 131708
94. X. Chu, *Materials Science and Engineering, B* 106 (2004) 305–307

-
95. A. Marikutsa, M. Rumyantseva, A. Baranchikov and Alexander Gaskov, *Materials*, 8 (2015) 6437-6454
96. Y. H. Ochoa-Muñoz, R. Mejía de Gutiérrez, J. E. Rodríguez-Páez, I. Gràcia and S. Vallejos, *Molecules*, 27(2022) 2889
97. F. Giubileo, A. Di Bartolomeo, L. Iemmo, G. Luongo and F. Urban, *Applied Science*, 8 (2018) 526
98. T. H. Yang, Y. W. Harn, K. C. Chiu, C. L. Fan and J. M. Wu, *Journal of Materials Chemistry*, 22 (2012) 17071–17078
99. R. B. Kamble, N. Tanty, A. Patra and V. Prasad, *Applied Physics Letters*, 109 (2016) 083102
100. Y. Yang, L. J. Wang, X. P. Wang, J. X. Chen, X. W. Yang, M. H. Li and M. J. Deng, *Vacuum*, 178 (2020) 109466
101. J. Z. Wang, X. P. Wang, L. J. Wang, J. Bao, M. Y. Zhao and P. Y. Xie, *Physica status solidi (a)*, 219(21) (2022) 2200257
102. Y. Zhao, W. Yang, Y. Zhou, Y. Chen, X. Cao, Y. Yang, J. Xu and Y. Jiang, *Journal of Materials Science: Materials in Electronics*, 27 (2016) 7280–72
103. T. Hu, J. Juuti, H. Jantunen and T. Vilkman, *Journal of European Ceramic Society*, 27 (2007) 3997–4001
104. Z. M. Dang, H. Y. Wang and H. P. Xu, *Applied Physics Letters*, 89 (2006)
105. Y. Rao, S. Ogitali, P. Kohl and C. P. Wong, *Journal of Applied Polymer Science*, 83 (2002) 1084–1090
106. A. Sasmal, A. Patra, P. S. Devi and S. Sen, *Composites Science and Technology*, 213 (2021) 108916
107. S. Mondal, S. Maiti, T. Paul, A. Sahoo, S. Bhattacharjee, N. S. Das and K. K. Chattopadhyay, *Applied Materials Today*, 26 (2022) 101385
108. Y. Xue, T. Yang, Y. Zheng, E. Wang, H. Wang, L. Zhu, Z. Du, X. Hou and K-C Choua, *Journal of Materials Chemistry A*, 10 (2022) 21893–21904
109. P. Kum-onsa and P. Thongbai, *Journal of Materials Science: Materials in Electronics*, 32 (2021) 13985–13993
110. P. Kum-onsa, B. Putasaeng, J. Manyam and P. Thongbai, *Materials Research Bulletin* 146 (2022) 111603
111. B. S. Athira, A. George, K. Vaishna Priya, U. S. Hareesh, E. B. Gowd, K. P. Surendran and A. Chandran, *ACS Applied Materials & Interfaces*, 14(39) (2022) 44239-50

- 112.** S. Mondal , T. Paul, S. Maiti, B. K. Das and K. K. Chattopadhyay, Nano Energy 74 (2020) 104870
- 113.** A. Sasmal, S. K. Medda, P. S. Devi and S. Sen, Nanoscale, 12 (2020) 12 20908
- 114.** N. Soin, P. Zhao, K. Prashanthi, J. Chen, P. Ding, E. Zhou, T. Shah, S. C. Ray, C. Tsonose, T. Thundat, E. Siores and J. Luo, Nano Energy, 30 (2016) 470-480

Instruments and apparatus

3.1. Major synthesis apparatus

3.1.1. Furnace

A furnace is used to carry out any solid-state reaction, combustion and hydrothermal reaction as well as to anneal, sinter and harden any solid material. There are different types of furnaces. We used the box furnace to synthesize our desired material. The maximum operating temperature of the box furnace in our laboratory is 1100

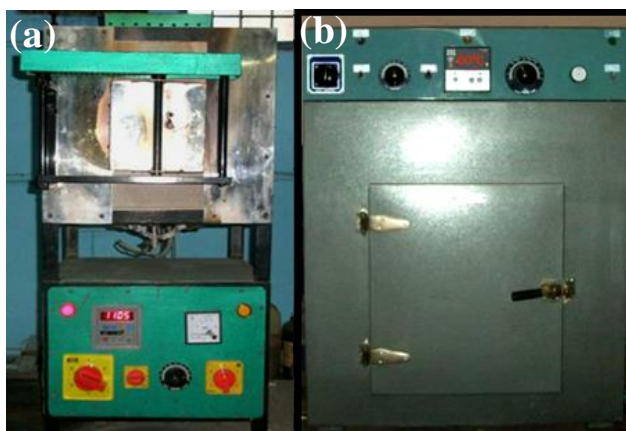


Fig. 3.1. Photograph of (a) high temperature box furnace and (b) oven

°C. The rate of heating is monitored by an electronic temperature regulating system with a precision of ± 2 °C. The insulating material inside the box retains the generated heat to get the maximum efficiency, which is also an economic benefit in respect of proper utilization of energy. In general, alumina boat and various types of ceramic crucibles are used to carry the solid material into the heating chamber. At a time more than one crucible can be inserted into the chamber if there is no risk of contamination from the vapor generated by the samples. The photograph of the furnace used in our experiment is shown in **Figure 3.1(a)**.

3.1.2. Oven

Hydrothermal reaction below 250 °C is well performed using a simple low temperature oven. Generally a thermostat is attached with the oven to control the temperature. The controlled heating rate helps in the growth of the product material. In our laboratory, the accuracy of the temperature monitoring rate of the oven is ± 0.5 °C. Along with the synthesis purpose, the ovens are also useful to dry the samples. A digital photograph of oven is shown in **Figure 3.1(b)**.

3.1.3. Autoclave

For a typical hydrothermal reaction Teflon lined autoclave is used as synthesis chamber. An autoclave is a pressurized device to carry hydro/solvothermal reaction at elevated temperature with respect to their boiling point and at a pressure greater than the ambient one. The

autoclave has two parts; the cylindrical chamber (basically made of iron) and an iron screw cap. The cap must be fitted very tightly with the chamber to create high pressure inside the cylindrical teflon tube for the required reaction. The cylindrical teflon tube is tightly fitted with a teflon cap which serves as the inner reaction chamber. The autoclave arrangement that is used to prepare BaSnO_3 micro-nanorod hydrothermally is shown **Figure 3.2**.



Fig. 3.2. Photograph of autoclave and teflon tube

3.2. Characterization techniques

3.2.1. Crystallographic study: X-ray diffraction (XRD)

X-ray diffraction is a non-destructive approach for examining the structural properties of solids. XRD pattern is like the signature of a solid material from which almost everything related to its crystallinity can be known. The following information regarding the structure of a material can be obtained from XRD pattern.

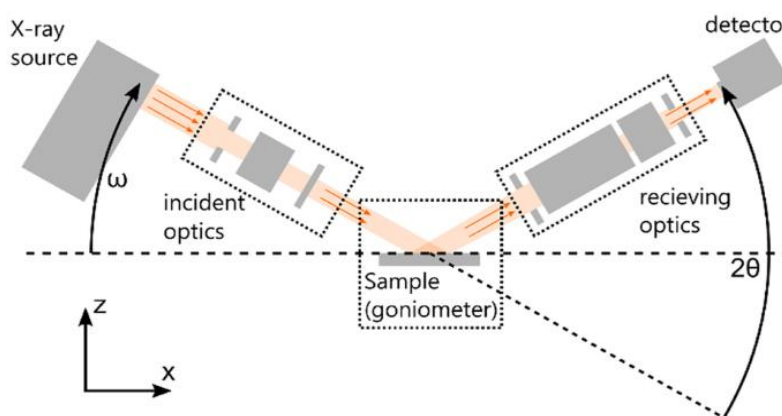


Fig. 3.3. Schematic diagram of an X-ray diffractometer

- Degree of crystallinity
- Phase verification
- Crystallite size
- Lattice parameter
- Lattice stress and strain

The main three components present in a typical X-ray diffractometer are one sample holder, a X-ray tube and a detector. With the application of a sufficiently high voltage, the thermally generated energy dense electrons from a tungsten filament are accelerated towards the target material (i.e. Cu, Co, Mo etc.) and dislodge the electrons from the inner shells. For filling up the vacancy of the inner shells, the outer shells electrons jump into the empty places, thereby emitting the characteristic X-ray photons in the cathode ray tube.¹ To obtain the required monochromatic radiation for diffraction, the undesirable wavelengths are filtered through crystal monochromator. The chosen monochromatic beam is then collimated in accordance to

the sample placed on the sample holder. When constructive interference occurs between the incoming X-ray and the atomic planes of the test material, the detector records the angle of diffraction and the intensity of the diffracted beam. Bragg's condition of diffraction used the fact that, constructive interference occurs between the two travelling waves if the path difference is equal to an integral multiple of the wavelength of the incident X-ray. So, in mathematical form, Bragg's condition for diffraction and can be written as

$$2d\sin\theta = n\lambda \quad (3.1)$$

where, d indicates the inter-planer spacing, θ means the incident angle, n is an integer and λ is the wavelength of X-ray. The schematic of an typical X-ray diffractometer is shown in **Figure 3.3**. In our experiments, all XRD data were collected using an X-ray diffractometer (Bruker D8 Advanced diffractometer). Cu-K α radiation having wavelength (λ) equal to 1.5418 Å was used as incident beam. The photograph of the X-ray diffractometer is shown in **Figure 3.4**.

Using Rietveld refinement more specific data regarding the structure of the sample can be evaluated from the X-ray diffraction pattern such as bond length, bond angle etc.



Fig. 3.4. Photograph of X-ray diffractometer

3.2.2. Microscopic techniques

3.2.2.1. Field emission scanning electron microscopy (FESEM)

Field emission scanning electron microscope is an electron (negatively charged) operated microscope unlike light microscope which is utilized to observe the morphological characteristics of the samples.² In FESEM highly energetic electrons are liberated from the electron gun following field emission mechanism. Prior to operation the total system is highly evacuated (10^{-8} Torr) by a pre-vacuum pump and turbo pump. Very thin and sharp needle like cathode (tip diameter is 10^{-7} - 10^{-8} m) made up of tungsten and lanthanum hexaboride are used as electron emitter because of their minimum turn on field and impressive emission capabilities. The released electrons are then accelerated by high electric fields and focused using various electromagnetic lenses to form a finer electron beam. As soon as the electron

beam falls on the atoms lie on the surface of the sample, different signal originates such as secondary electrons, backscattered electrons, characteristic X-rays and so on. The detector captures the low-energy secondary electrons and prepare electronic signal. The electronic signal is then amplified and converted to a video scan image of the surface of sample on the monitor screen. The simple line diagram of FESEM and the photograph of HITACHI S4800 model are shown in **Figure 3.5(a)** and **(b)** respectively. To avoid the problem of surface charge accumulation, the samples are coated using very thin layer (1.5-3 nm) of metal (like gold) using typical sputtering method.

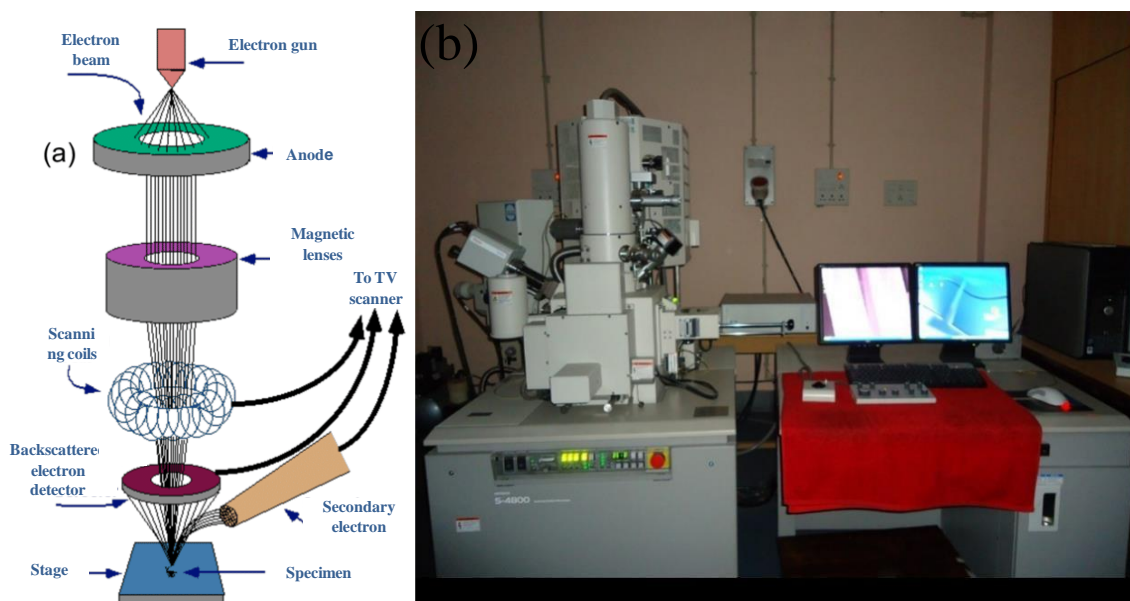


Fig. 3.5. (a) Simple line diagram and (b) photograph of FESEM

3.2.2.2. Transmission Electron Microscopy (TEM)

Transmission electron microscopy is a powerful tool to study important features like crystal structure, morphology, topography, chemical composition, dislocation and grain boundaries of the test material. Furthermore, using the high-resolution transmission electron microscope (HRTEM) a more accurate and high resolution image (atomic level) of the crystal structure can be demonstrated. The smaller de-Broglie wavelength of electrons make it capable for the instrument to observe fine detailing of the image even to a thousand times smaller than that captured by a light microscope.

To increase the electrons' mean free path and to avoid the collision among the electrons a high vacuum chamber ($\sim 10^{-4}$ Pa) is needed to operate the instrument. A TEM is typically composed of an electron emitting gun, electromagnetic lenses, electrostatic plates, magnification systems, sample holder and the detecting system. The electrons emitted from

the heated V-shaped filament are accelerated by the electric field. To emit sufficient no. of electrons (current density) the filament has to be heated to such extent that may cause thermal damage to it. For this reason, tungsten (high melting point) or LaB₆ (low work function) are used as filament material. The strength of the electron beam is much higher (150-250) kV than that used in SEM (5-30 kV). The electromagnetic lenses are used to make the electrons into a focused and finer electron beam by controlling the energy intensity. The condenser lens system enables the electron beam to focus the sample according to its size and the location. The diffraction beam generated because of the objective lenses in back focal plane passes through the sample and the image is recorded by a CCD camera.³

In imaging mode, there are two techniques to capture images. If the objective lenses are used to select the central beam, only the transmitted electrons can pass through and a bright image is obtained. On the other hand, if the signal from diffracted beam is allowed, a dark field image is generated.

The sample is prepared on a copper grid using a conventional technique. In general, a suspension of the sample was dropped onto the grid and allows the solvent to evaporate completely.

Figure 3.6(a) and (b) show a schematic of imaging and diffraction mode of TEM respectively and the **Figure 3.6(c)** is the photograph of the instrument used to characterize all the samples (HRTEM, JEOL-JEM 2100).

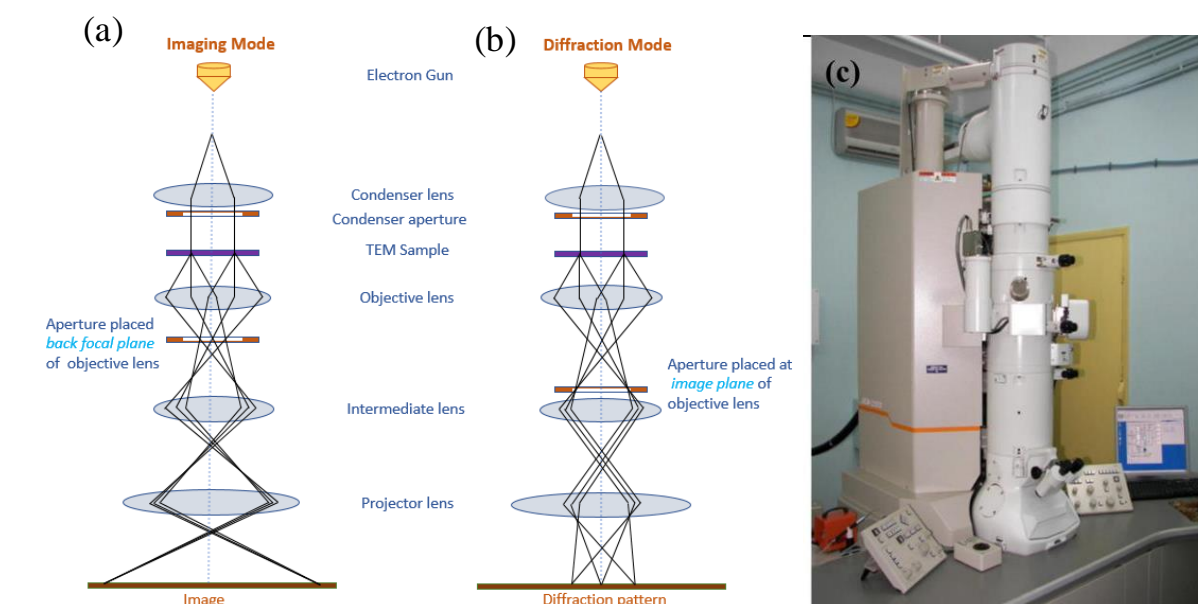


Fig. 3.6. Schematics of the lenses and apertures in (a) imaging mode and (b) diffraction mode, (c) photograph of HRTEM instruments

3.2.3. Spectroscopic techniques

3.2.3.1. Energy Dispersive X-ray Spectroscopy (EDX)

Energy Dispersive X-ray Spectroscopy is a technique to analyze the elemental composition of the desired sample. An electron beam with very high energy is bombarded upon the material knocking out characteristic X-rays from the sample. Since each element of the sample bears a specific atomic structure, a unique set of peaks appear for a specific sample on its electromagnetic emission spectrum. From the relative intensities of the peaks the approximate stoichiometric ratio of the compositional elements can be obtained. Generally, the instrument fails to detect the lighter elements properly for which the atomic number is below 6 (Carbon). There are three major parts of this system: an emitter, a collector and an analyzer. The parts (HITACHI S4800; working at 15 kV) are additionally connected to field emission microscope (FESEM, Hitachi S-4800).

3.2.3.2. X-ray photoelectron spectroscopy (XPS)

X-ray photoelectron spectroscopy is ultra surface-sensitive (depth upto 2-5 nm) quantitative spectroscopic technique, employed to investigate the elemental composition, electronic state of the dopant, density of the electronic states in the sample. XPS is typically composed of an

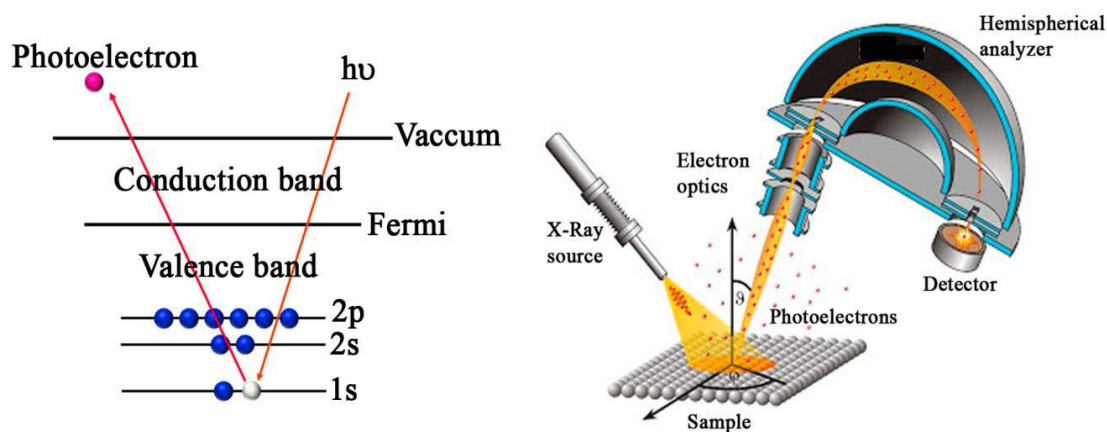


Fig. 3.7. Schematic of photoelectron emission process

ultra high vacuum (10^{-8} Torr) chamber, an X-ray source, a sample stage and an electron detection unit. The operating principle of XPS is based upon photoelectric effect. A monochromatic Al $K\alpha$ X-ray (1486.6 eV, with a hemispherical analyzer (SPECS, HSA 3500)) is shot onto the sample resulting ejection of photoelectrons with a certain kinetic energy. The kinetic energy of the emitted electrons is measured by the electron energy

analyzer. The principle of electron emission is depicted in **Figure 3.7**.

Once the kinetic energy (E_k) is measured, the binding energy (E_b) can be obtained from the following relation,

$$E_b = h\nu - E_k \quad (3.2)$$

where, ν is the frequency of the incident X-ray and h is the Planck's constant. The binding energy of any core-level electron is specific for a specific compound that leads to detect the surface elements.⁴ Moreover, the area under the curve provides the quantitative information of the elements on the sample surface. The chemical shift enables to find the atomic oxidation state of the element within a particular sample. The picture of the instrument is shown in



Fig. 3.8. Photograph of X-ray photoelectron spectrometer

Figure 3.8.

3.2.3.3. UV-Vis-NIR Spectroscopy

UV-Vis-NIR spectroscopy is one of the powerful tools to understand and study the optical properties of semiconducting nanoparticles.⁵ It is utilized to measure the percentage of absorbance, transmittance and reflectance of all the wavelengths starting from ultra violet to near IR region of the electromagnetic spectrum. This indicates that this particular spectroscopic technique provides researchers the necessary information about the optical behavior of the material under concerned. When the atoms/molecules in the ground state absorbed appropriate wavelength of light then the atoms/molecules get excited to the higher energy state. The technique can also be used for other than powder sample like liquid and films. Various parameters such as ionization energy, electron affinity of the test sample can be measured from the absorption spectrum and absorbance percentage. The utmost important parameter measured from this technique is the optical band gap. Barden proposed the following empirical correlation for the parabolic band structure,

$$\alpha h\nu = A(h\nu - E_g)^\gamma \quad (3.3)$$

Where, E_g and α are the band gap energy and the absorption coefficient of the sample respectively. The value of the transition probability (γ) defines electronic type of the band gap. The values of γ are 1/2, 2, 3, 3/2 for direct allowed transition, indirect allowed transition,

indirect forbidden transition and direct forbidden transition respectively. According to the Beer-Lambert law, the absorbance is proportional to the concentration of the solution and mathematically expressed as,

$$A = \log_{10} \frac{I_0}{I} = \epsilon cl \quad (3.4)$$

Where, A , I_0 , I , ϵ , c and l denote intensity of incident light, intensity of transmitted light, extinction coefficient, concentration of the sample and path length respectively. For calibration purpose a standard material (BaSO_4) is used at the time of measurement. The working principle is shown in the schematic diagram (**Figure 3.9(a)**). A photograph of UV-Vis-NIR spectrometer (Shimadzu, UV-3600) is shown in **Figure 3.9(b)**.

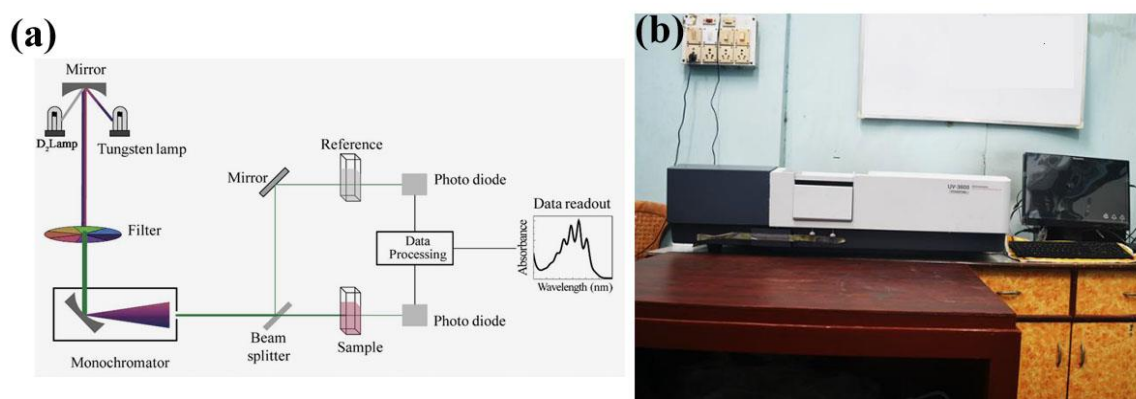


Fig. 3.9. (a) Schematic diagram and (b) photograph of UV-Vis spectrophotometer

3.2.3.4. Fourier Transform Infra-red (FTIR) Spectroscopy

In electromagnetic spectrum, starting from the lowest energy edge of visible light to the beginning of microwave zone is called Infrared (IR) region. The whole range of IR region is further classified into three sub-regions, named as near IR ($14000 - 4000 \text{ cm}^{-1}$), mid IR ($4000 - 400 \text{ cm}^{-1}$) and far IR ($400 - 20 \text{ cm}^{-1}$). In the mid IR frequency range, as most of the molecules alter their basic vibrational levels, the IR spectrometer is designed to record the IR spectra by detecting the interferogram of sample signal arising with the help of an interferometer. In an Infrared spectrometer the interaction of IR radiation with the test sample happens and the instrument records the frequencies of radiation absorbance by the sample and the corresponding intensities. The strength and the frequencies of radiation absorbed differ from sample to sample and thus the chemical bonding present into the sample can be known. The Beer-Lambert law is the foundation for all quantitative infrared spectroscopy.⁶ For FTIR, a Michelson interferometer is generally used in which a beam splitter is placed to collimate the polychromatic radiation generated by an infrared source. The beam splitter

splits the incoming beam into two parts, one half gets directed towards the fixed mirror and another half transmits through the splitter to the moving mirror. The reflected beams from the mirrors recombine, constructive or destructive interference takes place depending upon the position of the moving mirror with respect to the fixed one. When the path difference between the beam splitter and each mirror is same, constructive interference takes place for a zero path difference between the two optical signals, resulting in maximum signal intensity. The beam is then incident on the experimental sample and the selective absorption takes place. The beam is then detected by the detector which converts the signal into electrical signal. The interferogram is a signature of intensity vs. mirror position data which can't be used for practical analysis. For better understanding, the detector signal is converted into an IR spectrum using mathematical Fourier Transformation (FT). In our study Shimadzu FTIR-8400S spectrometers were used for IR spectroscopic analysis of the powders and films. A schematic of working principle and a digital photograph of the instrument are shown in **Figure 3.10**.

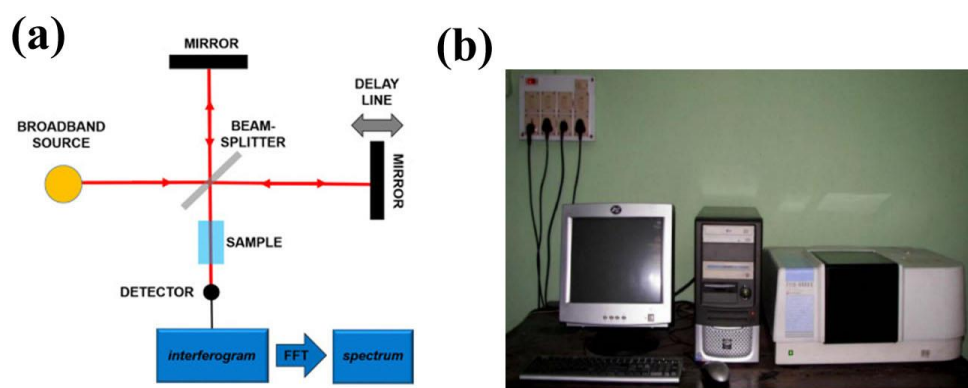


Fig. 3.10. (a) Schematic representation of the working principle and (b) photograph of the FTIR spectrometer

3.3. Impedance analyzer

AC impedance analyzer is generally used to observe the behavior of various electrical parameters such as impedance, capacitance etc with respect to frequency. This instrument not only measures the ratio between the voltage and current rms values, it also measures the phase difference between them. In our studies, the dielectric response of the test samples was measured using Agilent 4294A precision impedance analyzer (**Figure 3.11**). The operational frequency of the instrument varies from 40 Hz to 110 MHz. The basic accuracy for impedance measurements is $\pm 0.08\%$. The dc bias voltage and current can be tuned in the range of ± 40 V and ± 100 mA respectively. The range of the voltage (rms) and current (rms)

for the AC applied signal are 5 mV to 1V and 200 μ A to 20 mA respectively. Generally, the samples are used either in the form of pellets or film. For the measurements, the parallel plate capacitor model is used and an alternating electric field is applied to the conducting plates and the response is recorded with the help of a data recording system.



Fig. 3.11. Photograph of impedance analyzer

In our experiment, cylindrical pellets (diameter 12 mm and thickness 1 mm) were fabricated from the powder samples using a hydraulic press (pressure $\sim 2 \text{ Kgcm}^{-2}$). Before the measurements, the pellets were coated with silver paint to connect the copper wire and dried at 80°C .

3.4. Field emission measurement apparatus

Field emission is a quantum mechanical tunneling process to pull the electrons out from solid matter, subjecting the solid matter to a strong electric field. Due to the applied electric field the surface potential barrier is reduced in height along with a reduction in its width also. The reduced surface potential barrier enables the electrons to tunnel through the barrier.

The field emission measurements were performed in our laboratory made (**Figure 3.12**) diode like emission set up consisting of a cathode (the film of the sample) and an anode (stainless steel conical tip with a diameter of 1.5 mm).

At first, a double-sided conducting carbon tape (5 mm, Nisshin EM. Co. Ltd.) was pasted on S platform and then the sample was mounted over the carbon tape by pressing it with glass slide to form maximum uniform films. The inter-electrode distance was adjusted upto a few hundred micrometers by a screw gauge shifter (10 μm pitch). The entire working system was kept into a transparent high vacuum chamber. The base pressure of the working chamber was lowered upto $\sim 10^{-7}$ mbar using rotary and oil diffusion pump via roughing and backing operations. The transparent chamber allowed us to make sure that no discharge from the sample surface occurred during the application of high electric field. The output voltage was

measured using a multimeter (Agilent, 3440-1A) which was converted into emission current density using software.

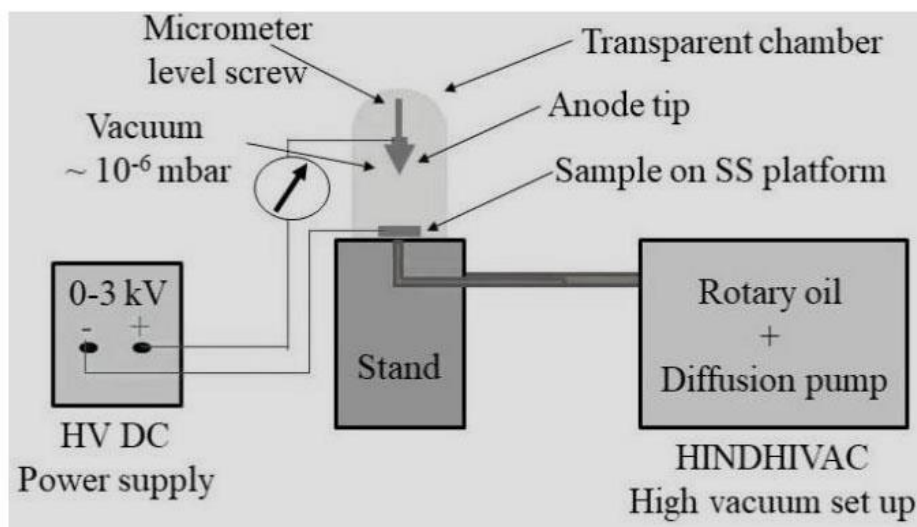


Fig. 3.12. Laboratory made field emission (FE) set up

3.4.1. High voltage D.C. power supply

Field electron emission requires high input electric field across the electrodes. For this purpose, a high voltage DC power supply (NTPL/91/03-04. Manufacturer: Neo Tele Tronix Pvt. Ltd.) was used. The input power supply is 3 kV-500 mA with 230 V-50Hz (Phase 1, AC) and the output can be increased upto 3 kV with 10V step.

3.5. Oscilloscope

The oscilloscope is an electronic signal test instrument which usually displays the waveform of voltage or current with respect to time. The analog oscilloscope comprises of four parts; a display unit, vertical control system, horizontal control system and trigger control system. These three control systems carry whole information about the electrical signal which is further reconstructed by the oscilloscope. The cathode ray tube (CRT) is the key part of the instrument consisting of a screen and a control unit which produce and channelize the stream of electron beam that bombard onto the backside of the screen resulting an



Fig. 3.13. Photograph of oscilloscope

illumination on the screen. The exact place of the CRT screen where the highly energetic electron beam strikes is supervised by the horizontal and vertical control units by an electrostatic field created between the plates. For our work, the output voltage was measured as a function of time where mechanical stress was played the role of input. The image of the oscilloscope used in our work (Keysight EDUX1002A) is shown in **Figure 3.13**.

3.6. References

1. M. J. Burger, X ray Crystallography, John Wily and Sons, New York, 3 edition (1962)
2. R. P. Jaya, 14-Porous concrete pavement containing nanosilica from black rice husk ash, New Materials in Civil Engineering, Butterworth-Heinemann, (2020) 493-527
3. S.J. Pennycook, Transmission Electron Microscopy, Encyclopedia of Condensed Matter Physics, Elsevier, (2005) 240-247
4. P. Van der Heide, X-ray photoelectron spectroscopy: an introduction to principles and practices, John Wiley & Sons, (2011)
5. V. Maria Vinosel, S. Anand, M. Asisi Janifer, S. Pauline, S. Dhanavel, P. Praveena and A. Stephen, Applied Physics A 125 (319) (2019).
6. D. Peak, Fourier transform infrared spectroscopy, Encyclopedia of Soils in the Environment, (2005), pp. 80–85

Effect of calcination
temperature on structural
and electrical properties of
nanocrystalline BaSnO₃

Abstract

BaSnO₃ nanocrystals were synthesized using simple solid-state reaction route varying the calcination temperature to investigate the effect of grain growth on electrical properties of this popular perovskite oxide. The duration of calcination was optimized to obtain the pure phase. The average crystallite size was found to increase from 35 nm to 49 nm whereas appreciable amount of decrement was observed in the level of porosity with tuning of calcination temperature. The dielectric constant was increased from 4690 to 8305 at a frequency of 60 Hz with calcination temperature whereas the tangent loss maximum was found to decrease by ~9%. The grain growth promotes the overall conductivity for high temperature calcination sample. Non-Debye type relaxation mechanism was confirmed for all the samples using Cole-Davidson relations. The outcomes of the electrical properties were correlated with the grain-grain boundary effect, porosity and brick layer model.

4.1. Introduction

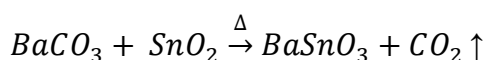
Wide band gap oxide perovskites are under extensive focus of materials research due to their flexible electrical and other opto-electronic properties. Those perovskites have been used in capacitive devices, solar energy conversion systems and switching devices.¹⁻³ Among the leading perovskites of this group, BaSnO₃ (BSO) is one of the most studied and widely multipurpose systems. Fabricating different electrical components involving BaSnO₃ has been attempted via doping, co-doping, forming composites etc.⁵⁻⁷ Though various other applications of BaSnO₃ have been reported so far, the most important property or most of the applications are directly or indirectly related to its electrical behaviour. The dielectric constant of this material was found to vary within wide range due to those techniques. However, the choice of the precursors and relevant parameters of systematic synthesis are the most important factors to obtain a successful tunable electrical system with BaSnO₃. The conductivity and dielectric permittivity are normally correlated with grain size and density.⁸⁻⁹ Tuning these parameters of BaSnO₃ may therefore have important consequences in this regard. However, tuning the grain size will additionally affect the crystallinity as this is closely related to long or short range ordering. The effect of sintering temperature and different sintering atmosphere is rather a well known technique for controlling the grain size, crystallinity and density of any popular system.⁹⁻¹¹ BaCO₃ is often used as a major precursor in most of the synthesis routes reported so far.¹²⁻¹³ It's availability and proper release of the primary ion have attracted researchers in this field from decades. However, this precursor

often causes inclusion of impure carbonate phase in BaSnO_3 when kept or operated in an unprotected ambience.¹⁴ But most of the systems involving BaSnO_3 (or other perovskites) must be operated in a general ambience in order to minimize application cost. Synthesis temperature can be a tricky parameter to remove that phase is therefore a very important factor in application aspect.¹⁵ Annealing duration, on the other hand is another important parameter in order to obtain pure phase of a system.¹⁶ For small annealing duration, the reactant counterparts often lag proper scope for diffusion, which in turn results into the mix or impure phase. With the increment in annealing duration and successive mechanical grinding, reactant components receive ample scope for diffusion and unreacted portion of the reactants are gradually exposed to high temperature leading further diffusion. Synthesis duration, especially the time of annealing is therefore an important factor to be tuned during optimization of solid-state synthesis techniques. A large number of samples may be obtained during variation of any synthesis parameters, but it is important that the electrical parameters must vary accordingly to establish the mechanism of variation of electrical behaviour correlated with synthesis parameters. Fabrication temperature is no exception and varying the synthesis temperature gradually should tune the electrical parameters of the targeted BaSnO_3 system with desired regularity. This work represents a two stage process, firstly, obtaining time duration for the synthesis which can result into the proper phase of BaSnO_3 and further varying the calcination temperature to modify the electrical behaviour of the same. Aiming this, BaSnO_3 samples were prepared employing solid-state method. The fabrication temperature was varied from 1000 °C to 1300 °C gradually to fabricate samples with different grain dimension and the effect of this variation was further studied in view of electrical properties by ac technique of impedance analysis. The advantage of this technique is to separate real and imaginary components of the electrical parameters which helps understanding the phenomena better. The electrical behaviour shown according to this approach is thus independent of sample geometry and thus more trustable. It was observed that the dielectric constant of the samples were increased from 4690 to 8305 at a frequency of 60 Hz with increment in annealing time and the impedance of the samples was found to decrease gradually. Both the grain and grain-boundary resistances were decreased with calcination temperature. The variation of various electrical parameters was further correlated with the grain-grain boundary effect, degree of porosity and brick layer model.

4.2. Experimental

4.2.1. Synthesis of BaSnO₃ powders

Nanocrystalline BaSnO₃ was synthesized via simple and traditional solid-state reaction method. Precursor materials used in this method are BaCO₃ (99.999%, Sigma) and SnO₂ (extra pure, Loba Chemie). The reagents were weighed to the desired stoichiometry and mixed using methanol. Methanol was used to form a paste like mixture. The volatile liquid was allowed to evaporate completely in the time of grinding and the mixture was calcined in air atmosphere for 18 h followed by furnace cooling. The calcination temperature was varied from 1000 °C to 1300 °C. The associated reaction can be written as



The samples annealed at temperatures 1000 °C, 1150 °C and 1300 °C were labeled as B18A, B18B and B18C respectively. For the measurements of impedance spectroscopy the powder samples were cold-pressed into cylindrical pellets of diameter 12 mm and thickness 1 mm using a hydraulic press under a pressure of ~2 kgcm⁻². The pellets were sintered at 800 °C for 5 h in air atmosphere to remove the polyvinyl alcohol (PVA) and to eliminate the fine cracks. Finally the pellets were polished with a fine emery paper to make the surfaces flat and then coated with conductive silver paint to attach conductive copper wires and dried at 80 °C for 3 h.

4.2.2. Characterizations

An X-ray diffractometer (XRD, BRUKER D8 Advance) with CuK_α (λ = 1.5406 Å) radiation was used to confirm the proper crystalline phase formation of the samples. Field emission scanning electron microscope (FESEM, Hitachi S-4800) was used to check the morphology of the samples. The grain morphology of the nanostructures was investigated using high resolution transmission electron microscopy (HRTEM, JEOL-JEM 2100). To study the elemental compositions energy dispersive X-Ray spectroscopy (EDX) (attachment with the FESEM) was carried out. For band gap determination a Jasco V670 spectrophotometer (UV-Vis) was employed. Complex impedance spectroscopy was studied using an impedance analyzer (Agilent 4294A precision Impedance Analyzer).

4.3. Results and discussion

4.3.1. Structural studies

The XRD patterns of the as prepared samples are presented in **Figure 4.1**. The presence of sharp diffraction peaks represents related diffraction planes [JCPDS card number: 000451471

(BaCO₃) 010770447 (SnO₂) and 000150780 (BaSnO₃)]. The diffraction peaks of the precursor materials BaCO₃ and SnO₂ were present in the mixture sample which can be seen from **Figure 4.1(a)**. In **Figure 4.1(b)** presence of unreacted phases of BaCO₃ and SnO₂ can easily be detected along with the characteristic peaks of BaSnO₃. Most of the prominent BaCO₃ diffraction peaks disappeared after calcination for 12 h (**Figure 4.1(c)**) and finally all precursor peaks symbolizing SnO₂ were removed after calcinations for 18h. The removal of

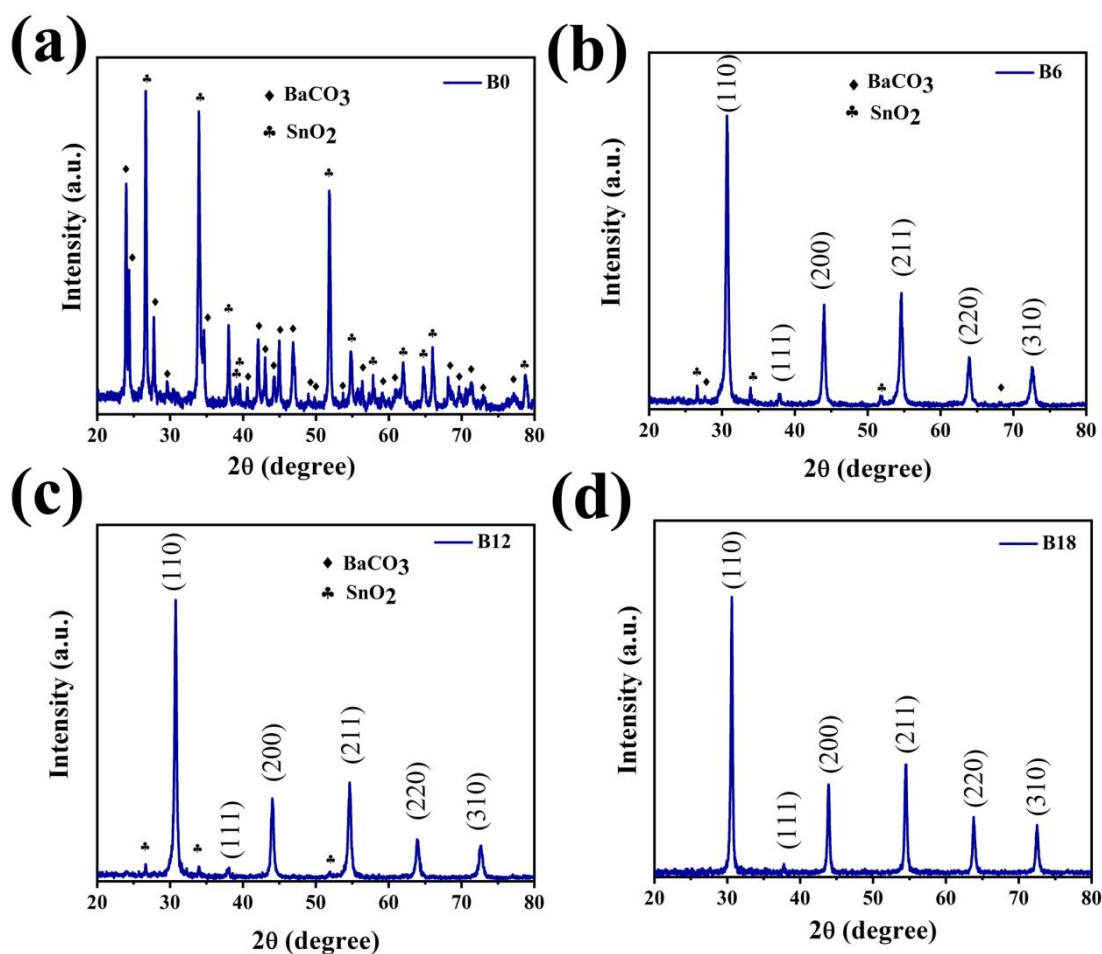


Fig. 4.1. XRD pattern of BaCO₃-SnO₂ mixture calcined at 1000 °C for different time

impurity peaks is directly associated with the phenomenon of diffusion of the reactant counterparts. This can be prescribed as represented in **Figure 4.2**.

Prior to calcination, the peaks consist only the diffraction peaks of the reactants as observed in **Figure 4.1(a)**. As the calcination starts, due to the diffusion of cations, target BaSnO₃ phase initially appear at the interface of BaCO₃ and SnO₂ grains. The newly generated BaSnO₃ remains bordered by the original reactant grains. However, the dimension of the border reactant grains gradually grows smaller as the calcination duration increased. This eventually causes fewer occurrence of diffraction from impurity crystals leading to a lower

intensity of BaCO_3 and SnO_2 peaks as depicted in **Figure 4.1(b)** and **Figure 4.1(c)**. With a further increment of calcination duration, entire amount of the reactants are expected to be converted into BaSnO_3 leaving behind no trace of the independent reactants (**Figure 4.1(d)**).

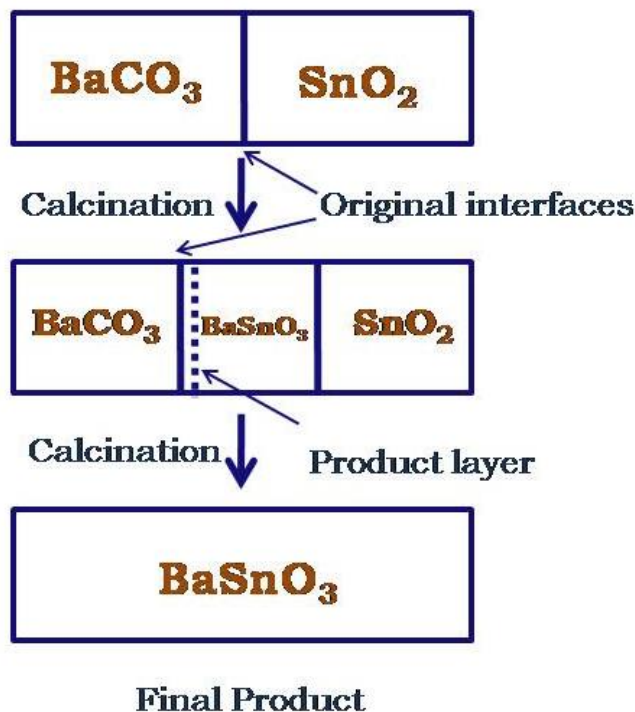


Fig. 4.2. Schematic diagram of the reaction of two crystals (BaCO_3 and SnO_2) sharing one face

After ensuring the appropriate phase formation, the synthesis temperature was further varied to achieve variation in grain dimension. The XRD pattern of the temperature varied samples is presented in **Figure 4.3**. It can be clearly seen that all samples B18A – B18C shows proper crystalline phase of BaSnO_3 [JCPDS card number: 000150780].

The average crystallite size of each sample was calculated using well known Debye-Scherrer's equation

$$D = \frac{0.9\lambda}{\beta \cos \theta} \quad (4.1)$$

where, D is the average crystallite size, λ ($= 1.5406 \text{ \AA}$) is the wavelength of X-Ray, θ is the Bragg's angle of diffraction (in degree) and β is the full width half maximum (FWHM) of the diffraction peaks (in radian). The average crystallite size was found to increase with increment in calcination temperature as presented in **Figure 4.3(b)**. The widening of grain dimension can directly be correlated with the diffusion of grain boundaries resulting in longer range of ordering. The lattice parameter of the cubic BaSnO_3 system was further calculated from the XRD patterns. It was observed that the lattice parameter of the samples gradually

increased with increment in annealing temperature (**Figure 4.3(b)**). These outcomes were further employed to investigate the probable variation of dielectric parameters of the samples.

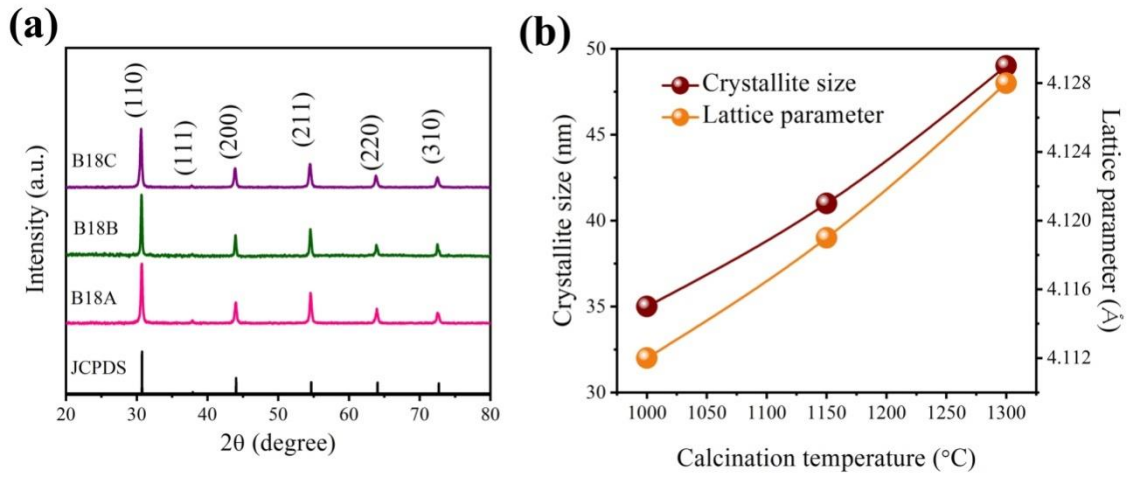


Fig. 4.3. (a) XRD pattern of BaSnO_3 samples calcined at different temperature; (b) variation of crystallite size and lattice parameter with calcination temperature

The X-ray density or theoretical density (ρ_{th}) of various calcination temperature of BSO was calculated using the following relation¹⁷

$$\rho_{th} = \frac{ZM}{N_A V} \quad (4.2)$$

Where, Z is the number of formula units per unit cell, M is the molecular weight (gm), N_A ($= 6.02 \times 10^{23} \text{ mol}^{-1}$) is the Avogadro's number and V is the volume of the unit cell (\AA^3) calculated from the lattice parameters obtained from XRD patterns. Moreover, the bulk densities (ρ_b) of the pellets were measured experimentally using Archimedes principle. The compactness or the relative densities (ρ_r) for the samples was deduced from the equation 4.3.¹⁸

$$\rho_r = \frac{\rho_b}{\rho_{th}} \quad (4.3)$$

Table 4.1. Bulk density, relative density and porosity of the samples calcined at different temperature

Sample	Bulk density (ρ_b in gm/cm^3)	Relative density (ρ_r)	Porosity (P in %)
B18A	5.913	0.814	18.60
B18B	6.289	0.871	12.93
B18C	6.420	0.894	10.60

Finally, the porosity (P in %) for the porous ceramics was determined from the equation written below.¹⁹

$$P = (1 - \rho_r) \times 100\% \quad (4.4)$$

The values of bulk densities, relative densities, porosities for the samples were listed in **Table 4.1**.

4.3.2. Morphological studies

The FESEM images of the samples are presented in **Figure 4.4(a,c,e)**. The samples in general exhibit agglomerated feature. However, the average dimension of the nearly cube like agglomerates was found to be minimum in case of sample B18A which gradually increased for sample B18C. The histograms of the particle size distribution are shown in **Figure 4.4(b,d,f)**.

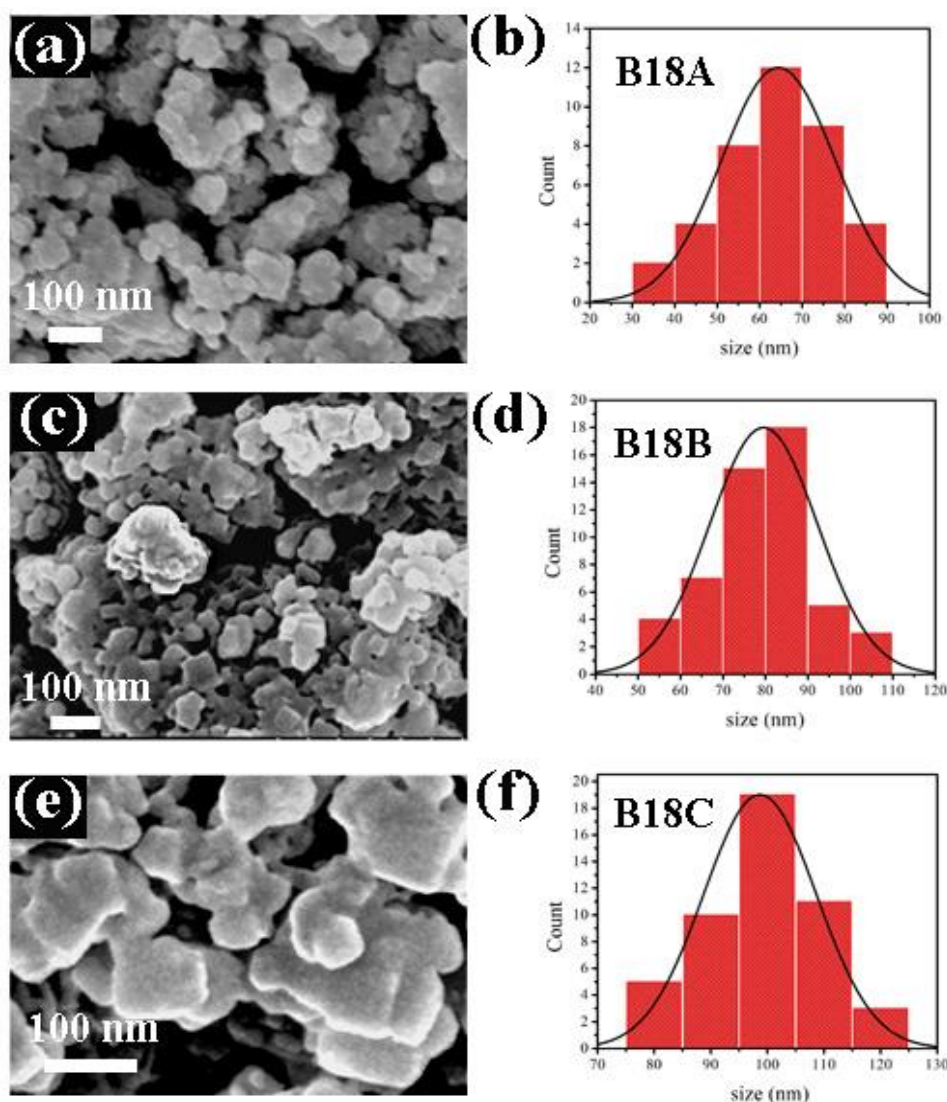


Fig. 4.4. FESEM images of the products (a) B18A, (c) B18B and (e) B18C; (b,d,f) corresponding histogram plots showing particle size distribution

The calculated average particle size for B18A, B18B and B18C are ~ 64.41 nm, ~ 79.57 nm and ~ 98.51 nm respectively. The increment in the dimension was considered to be occurring due to increment in synthesis temperature. Azad and Hon claimed that BaSnO_3 could not avoid porosity although it was synthesized with relatively high sintering temperature (1600°C).¹¹ Thus the presence of pores is obvious in our sample too, as observed in FESEM images. From the FESEM images the porosity of the samples was calculated using Image J software. The calculated values of porosity for B18A, B18B and B18C are 20.41%, 15.55% and 11.03% respectively which shows a good agreement with the result calculated from Archimedes principle.

4.3.3. Compositional and Optical studies

To ensure that the samples exhibit nearly stoichiometric elemental composition, EDX analysis was carried out and the elemental mapping for sample B18B is presented in **Figure 4.5(a)**. From the figure, uniform distribution of the constituent elements was inferred and the presence of the constituent elements was also ensured from EDX spectrum (**Figure 4.5(b)**).

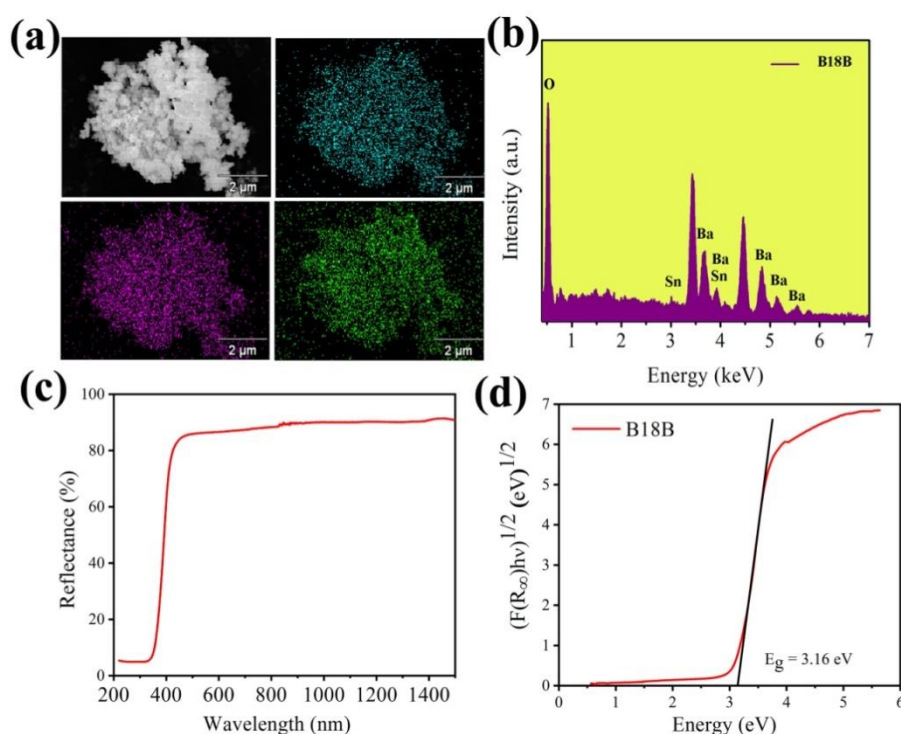


Fig. 4.5. (a) EDX mapping, (b) EDX spectrum, (c) UV-Vis reflectance spectra and (d) Band gap of sample B18B

To find the optical energy band gap of the sample, UV-Visible spectroscopic measurement was carried out. UV-Vis diffuse reflectance spectrum for B18B sample is shown in **Figure**

4.5(c). A sharp fall in R (%) was detected for the sample denoting high crystalline nature. The energy of incident photon (E in eV) was calculated from the wavelength (λ in nm) using the following relation

$$E = \frac{1240}{\lambda} \quad (4.5)$$

The band gap energy was calculated from Kubelka – Munk function using the formula

$$[F(R_{\infty})h\nu]^{\frac{1}{n}} = A(h\nu - E_g) \quad (4.6)$$

where, A is a proportionality constant, n is the index to characterize the type of energy band transition, $F(R_{\infty})$ is related to the reflectance (R) of the sample, E_g is the optical energy band gap. For BaSnO_3 , the value of n was taken equal to 2 for being an indirect band gap semiconductor. The optical band gap (E_g) was determined by extrapolating the linear regime of $[F(R_{\infty})h\nu]^{1/2}$ vs. $h\nu$ plot, shown in **Figure 4.5(d)**. The band gap energy of the sample was found to be 3.16 eV, which agrees well with other reported values.²⁰

4.3.4. Electrical properties studies

4.3.4.1. Dielectric permittivity analysis and relaxation formalism

Frequency dependent dielectric studies were carried out for understanding the electrical properties of the samples. The measurements were performed in a frequency range between 60 Hz and 110 MHz at room temperature (RT). The dielectric permittivity can be calculated using the relations

$$\varepsilon' = \frac{Cd}{\varepsilon_0 A} \quad (4.7)$$

$$\varepsilon'' = \varepsilon' \tan\delta \quad (4.8)$$

where ε' and ε'' are the real and imaginary part of the dielectric permittivity respectively, C is the measured value of capacitance, d and A are the thickness and cross-sectional area of the cylindrical pellet, ε_0 ($= 8.854 \times 10^{-14}$ F/cm) is the free space permittivity and $\tan\delta$ is the dielectric loss tangent. The frequency variations of the real part of dielectric constants are presented in **Figure 4.6(a)**. It can be seen that ε' was decreased with frequency in the low frequency range and attained nearly a constant value in the high frequency region. According to Maxwell-Wagner's model with Koop's phenomenological theory, the grain-boundaries and grains contribute to the dielectric and conductivity behaviours in low- and high-frequency regions respectively.²¹⁻²² In the low frequency region, the space-charge polarization along with the dipolar polarization dominates the polarization phenomenon in BSO ceramics. Accumulated space charges at grain-grain boundary junction need

comparatively larger time to overcome their inertia to follow the instantaneous change of input ac field. Thus at low frequency, this in turn increases space-charge polarization and show higher contribution in overall polarization. On the other hand, after application of higher frequency, space charges become unable to catch the faster ac field and thus the space charge polarization starts to cease.

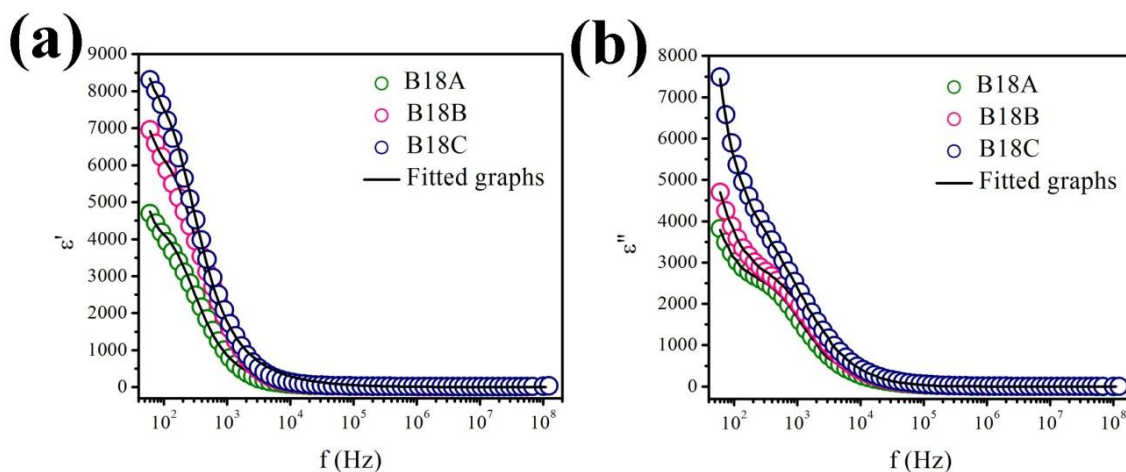


Fig. 4.6. The frequency variation of (a) real and (b) imaginary part of dielectric permittivity of the samples at RT; the solid lines indicate Cole-Davidson fitting

Again, during application of low frequency, dipoles are provided with much higher time to respond to the polarity inversion, resulting in high dipolar polarization. After increment in applied frequency, scope for responding in polarity inversion appreciably decreases resulting lower dipolar polarization of the system. These two contributing factors together cause higher dielectric constant in low frequency and its subsequent lowering after the application of higher frequency.²³ The decrement of the imaginary part of dielectric permittivity with frequency (**Figure 4.6(b)**) in the low frequency region and finally becoming independent of frequency in the high frequency region can also be associated with rapid polarization. It can be clearly seen that the values of real and imaginary parts of the dielectric constant increased significantly with increase in calcination temperature. The effective dielectric constant was increased with calcination temperature due to lowering the degree of porosity.²⁴ In porous ceramics the total polarization depends on the contribution from ceramics and the contribution from the air pores. In some earlier reports, it has been observed that porous materials face comparatively stronger inhomogeneity in local field than observed in compact system which imposes boundary conditions.²⁵ That means the presence of air pores having weaker polarization capability (low dielectric constant) lowers down the overall polarization effect. According to the Maxwell- Garnett formula the dielectric constant of a porous sample

should be increased as the porosity level decreases.²⁵ It was observed that the sample B18C exhibits least porous feature whereas B18A is the most porous one. Thus the degree of porosity has contribution in lower value of dielectric constant for sample B18A and its increment in case of sample B18C.

Another important factor favouring the increase in dielectric constant in the high temperature samples was the dipolar polarization. For samples treated in higher temperature, the lattice parameters were found to increase (**Figure 4.3(b)**). As a result, cubic BaSnO₃ exhibit higher inter-atomic distance. This in turn increases the dipole moment which in turn enhances the dipolar polarization of the system. Thus the dipolar polarization increased with increase in synthesis temperature. Hence, the sample B18C exhibits maximum dielectric constant.

The obtained experimental data were further fitted with Cole-Davidson relations to analyze the complex dielectric permittivity ($\epsilon^*(\omega)$) spectra.²⁶

$$\epsilon^*(\omega) = \epsilon_\infty + \frac{\epsilon_s - \epsilon_\infty}{(1 + j\omega\tau)^\beta} = \epsilon'(\omega) - j\epsilon''(\omega) \quad (4.9)$$

The real and imaginary parts of $\epsilon^*(\omega)$ are given by

$$\epsilon'(\omega) = \epsilon_\infty + (\epsilon_s - \epsilon_\infty)(\cos \Phi)^\beta \cos(\beta\Phi) \quad (4.10)$$

and

$$\epsilon''(\omega) = (\epsilon_s - \epsilon_\infty)(\cos \Phi)^\beta \sin(\beta\Phi) \quad (4.11)$$

where, $\Phi = \tan^{-1}(\omega\tau_{CD})$, $\Delta\epsilon (= \epsilon_s - \epsilon_\infty)$ is the dielectric relaxation strength and β denotes the shape parameter. τ_{CD} signifies the characteristic relaxation time and $\omega (= 2\pi f)$ is the angular frequency. The values of the fitting parameter β were found to be less than unity for all the samples which confirms non-Debye type of relaxation.

4.3.4.2. Tangent loss and Electrical conductivity studies

The dielectric loss is popularly considered to be a very important parameter governing the transport properties of any dielectric material. The variations of the tangent loss for the samples are shown in **Figure 4.7(a)**. The loss tangent ($\tan \delta$) is defined as the ratio of energy loss to energy stored in a periodical input electric field. This variation is also correlated with the dimension of the grains and grain boundaries. In wider grain boundaries the possibilities of charge scattering is higher which generally contribute in considerable dielectric loss in that region. After application of higher calcination temperature, the wider grains reduce the thickness of grain boundaries subsequently lowering the instances of scattering of charges. Also the minimization of porosity level enhances the intergrain connectivity. These can be responsible for lower dielectric loss in sample B18C. Additionally, relaxation time is another

controlling factor which can tune the dielectric loss in any system. Due to the application of an alternating electric field the molecules or dipoles faced constraints in changing their orientation along the direction of applied field. When the frequency of applied electric field and the rotational frequency of dipole match with each other a peak in the tangent loss spectrum arises. In the present work, it can be seen that there are broad loss spectra found for all the samples which signifies non-Debye type of relaxation phenomenon.²⁷ The easy formation of induced dipoles in the presence of the external electric field also decreases the dielectric loss of the B18C sample.

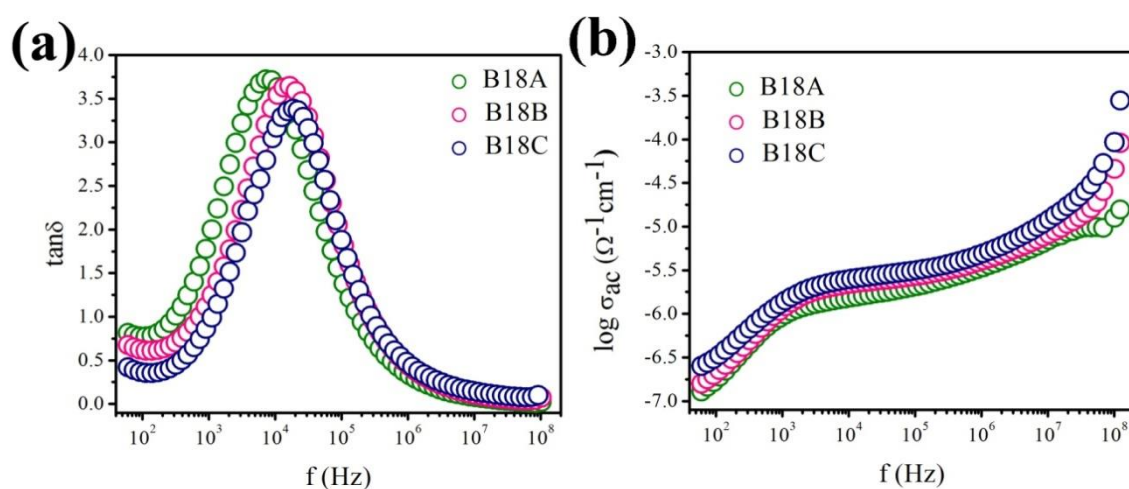


Fig. 4.7. Frequency variation of (a) loss tangent and (b) conductivity of all the samples

The ac conductivity spectra of the samples are shown in **Figure 4.7(b)**. The ac conductivity is found to be increasing with the calcination temperature. This gradual increment of the conductivity can be correlated with the grain growth due to higher calcination temperature. As the grain size increases the inter-granular hopping distance decreases. For a larger grain, the charge carriers can drift comparatively well due to ordered structure of wider grains and face lower hindrance at small grain boundaries which play charge scattering and trapping zones. Thus the growth in grain size promotes the mobility of the charge carriers which in turn enhance the bulk conductivity.

Both of the studies of dielectric loss and variation of ac conductivity with frequency directly indicate to better conducting properties achieved due to higher calcinations temperature.

4.3.4.3. Complex Impedance Spectra (CIS) analysis

The complex impedance data can be calculated from the complex dielectric data using the following equation

$$Z^* = Z' - jZ'' = \frac{1}{j\omega C_0 \varepsilon^*} \quad (4.12)$$

The representation of complex impedance is used to find the contribution of grain and grain-boundary separately. The frequency variations of the real and imaginary part of complex impedances are shown in **Figure 4.8(a)** and **Figure 4.8(b)** respectively.

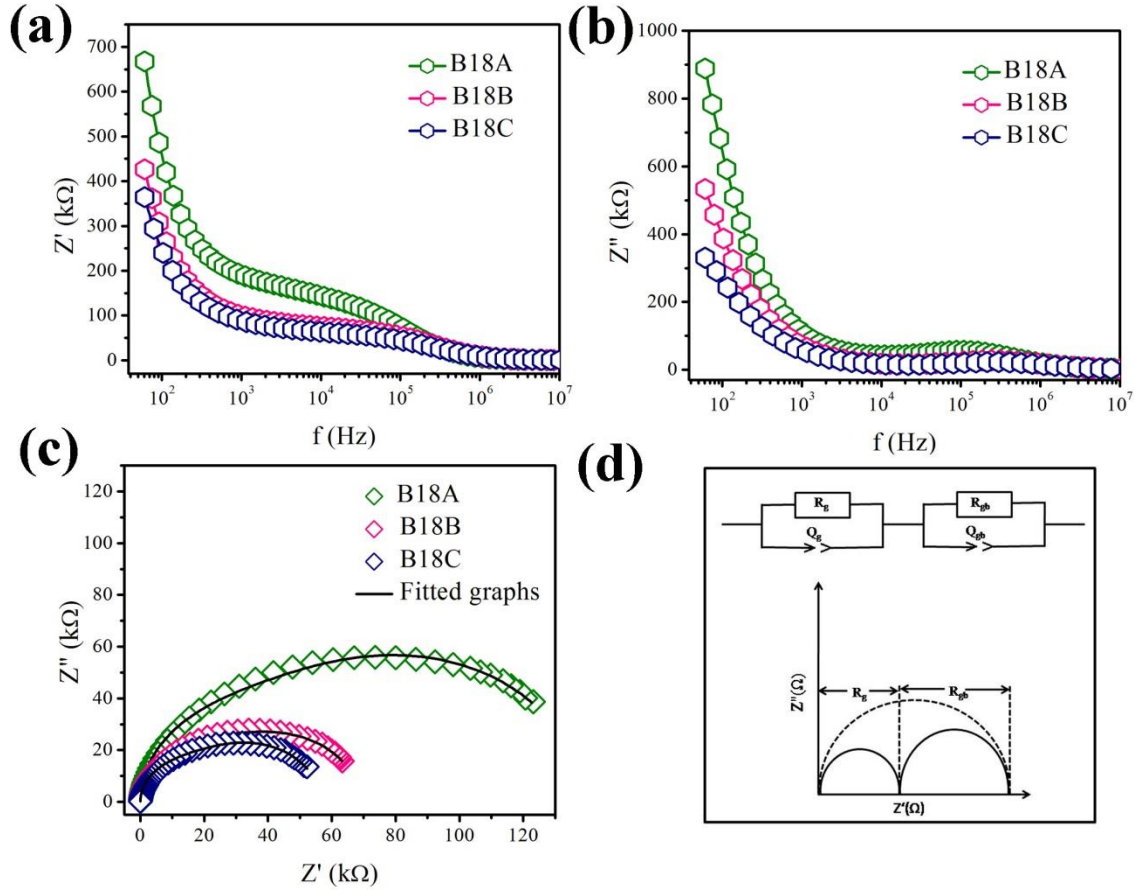


Fig. 4.8. Frequency variation of (a) real and (b) imaginary part of complex impedances for the samples; Cole-Cole plot for (c) B18A-B18C; the solid lines indicate the best fit of the experimental graphs; (d) A schematic diagram of the equivalent circuit.

It was found that the impedances decreased with the increment in calcination temperature. The grain dimension of a dielectric material is often correlated with grain and grain-boundary resistances which can be calculated from the Cole-Cole plot shown in **Figure 4.8(c)**. The resulting spectra can be well explained considering brick-layer model shown in **Figure 4.9**.²⁸ According to this model grain, grain boundary and electrode-ceramic interface have different and distinct contribution to the conductivity of the sample. The complex impedance plot normally consists of three semicircular loops. The smallest one found for high frequency is generally associated with the grain; the intermediate loop is accounted for the grain boundary whereas the last loop obtained for low frequencies is correlated with electrode-dielectric interface. In this present work, one depressed semicircle with centre below X-axis was

formed due to overlapping of two semicircles which represent grain and grain-boundary contribution. The presence of this type of depressed semicircle is an indication of the distribution of the relaxation time arising due to dipole-electric field interaction in grain and grain boundary regions.²⁹

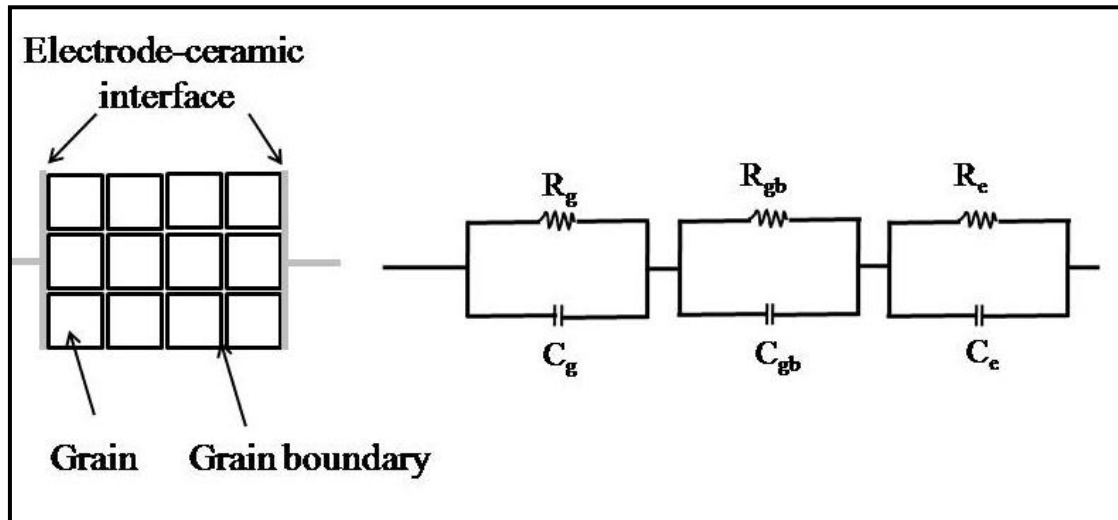


Fig. 4.9. The schematic diagram of brick-layer model along with the equivalent circuit

When the applied frequency is low, the oscillating electric field can act on the charges comparatively for a longer time before these charges move to the other end of the grain boundary following the direction of the applied electric field. As the thickness of grain boundaries are small compared to that of the grains, this accumulation of charges results a high capacitive effect at low frequency region. When frequency increases, only the bound charges or dipoles in the grains can follow the instantaneous change of polarity of the input electric field.³⁰

Proper fitting of these semicircles with appropriate equivalent circuit can provide the values of two types of resistances and capacitances. The equivalent circuit presented in **Figure 4.8(d)** consists of two parallel RQ combinations connected in series. Q (constant phase element) and C are related as

$$C = R^{\frac{(1-a)}{a}} Q^{\frac{1}{a}} \quad (4.13)$$

where, a is the degree of deviation with respect to the value of pure capacitor and R is value of the corresponding resistance.

The values of grain and grain boundary resistances and capacitances were determined via fitting (EC-Lab software) of the Cole-Cole plots. The fitted values of resistances and capacitances with the calculated values of relaxation frequencies corresponding to grain and

grain-boundary are listed in **Table 4.2**. It can be noticed that the grain and grain boundary resistances were decreased with higher calcination temperature and also the relaxation time (inverse of relaxation frequency) was decreased.

Table 4.2. Calculated values of grain and grain boundary resistances, capacitances and relaxation frequencies

Sample	R_g (k Ω)	R_{gb} (k Ω)	C_g (pF)	C_{gb} (pF)	ω_g (Hz)	ω_{gb} (Hz)
B18A	37.69	66.24	10.45	22.82	2538970	661552
B18B	28.90	50.36	10.74	23.57	3221794	842470
B18C	18.30	37.94	10.97	25.92	4981295	1016875

Abrantes *et al.* described the proper correlation of the values of resistivities with the dimensions of grains and grain boundaries.³¹ In brief; this involves the variation of movement of charges. The charges can flow smoothly when passing through a grain due to presence of ordered lattice atoms. These charges face appreciable hindrance in movement when it travels through the inter-grain boundaries due to inherent defects and open ended lattice at those positions. Therefore, reduction in grain boundary thickness or growth in grain size should enable smoother transport of electrons as inter-grain hopping will be easier. This in turn increases the conductivity of the sample B18C.

4.4. Conclusion

Particle size tuned BaSnO₃ perovskite nanocrystals were synthesized employing solid-state route via simple variation of calcination temperature. A wide variation of 6-18 h in synthesis duration was applied to establish the pure phase of the sample. The investigation was further continued with tuning the synthesis temperature over a range of 300 °C. The grain size was found to be increasing by 40% whereas the porosity was found to decrease with variation of synthesis temperature. Distribution uniformity of the constituent elements was ensured from EDX study. Thorough investigation of electrical properties of the samples by ac technique showed that increment of calcination temperature enhanced the effective dielectric constant of the sample from 4690 to 8305 at a frequency of 60 Hz. The dielectric loss was substantially decreased in turn. AC conductivity of the samples was also found to increase due to increase in synthesis temperature. These results were grossly correlated with the variation of grain size, lattice parameter and porosity due to increase in synthesis

temperature. Efficiency of larger grains with narrowed boundaries could influence the conductivity. This correlation was further established by brick layer model. This work opens up newer possibilities of tuning the electrical properties of BaSnO₃ and similar perovskite oxides by simple tuning of synthesis parameters.

4.5. References

1. R. A. Bucur, A. I. Bucur, S. Novaconi and I. Nicoara, *Journal of Alloys and Compounds*, 542 (2012) 142-146
2. Y. Yu, D. Zhao, C. R. Grice, W. Meng, C. Wang, W. Liao, A. J. Cimaroli, H. Zhang, K. Zhu and Y. Yan, *RSC Advances*, 6 (2016) 90248-90254
3. H. Fan, C. Chen, Z. Fan, L. Zhang, Z. Tan, P. Li, Z. Huang, J. Yao, G. Tian, Q. Luo and Z. Li, *Applied Physics Letters*, 111 (2017) 252901
4. S. Pal, N. S. Das, B. Das, B. K. Das, S. Mukhopadhyay and K. K. Chattopadhyay, *Applied Surface Science*, 530 (2020) 147102
5. A. Kumar, B. P. Singh, R. N. Choudhary and A. K. Thakur, *Materials Chemistry and Physics*, 99 (2006) 150
6. A. A. Kumar, J. Singh, D. S. Rajput, A. Placke, A. Kumar and J. Kumar, *Materials Science in Semiconductor Processing*, 83 (2018) 83
7. S. A. Salehizadeh, H. M. Chenari, M. Shabani, H. A. Ahangar, R. Zamiri, A. Rebelo, J. S. Kumar, M. P. Graça and J. M. Ferreira, *RSC Advances*, 8 (2018) 2100
8. Z. Cai, X. Wang, W. Hong, B. Luo, Q. Zhao and L. Li, *Journal of American Ceramic Society*, 101 (2018) 5487
9. V. R. Mudinepalli, L. Feng, W.C. Lin and B. S. Murty, *Journal of Advanced Ceramic*, 4 (2015) 46-53
10. X. W. Wang, P. B. Jia, X. E. Wang, B. H. Zhang, L. Y. Sun and Q. B. Liu, *Journal of Materials Science: Materials in Electronics*, 27 (2016) 12134
11. A. M. Azad and N. C. Hon, *Journal of Alloys and Compounds*, 270 (1998) 95-106
12. A. Kumar, R. N. Choudhary, B. P. Singh and A. K. Thakur, *Ceramic International*, 32 (2006) 73
13. Y. Zhang, Z. Cui, L. Zhu, Z. Zhao, H. Liu, Q. Wu, J. Wang, H. Huang, Z. Fu and Y. Lu, *Applied Physics Letters*, 117 (2020) 052406
14. Y. Wang, A. Chesnaud, E. Bevilion, G. Dezanneau and J. Yang, *Ceramic International*, 37 (2011) 3351

15. U. Kumar, J. Ansaree and S. Upadhyay, *Processing and Application of Ceramics*, 11 (2017) 177
16. A. Udomporn and S Ananta, *Materials Letters*, 58 (2004) 1154
17. A. A. Abd El-razek, E. M. Saed and M. K. Gergs, *Journal of Applied Physics*. 6(5) (2014) 20-29
18. C. Rayssi, S. E. Kossi, J. Dhahri and K. Khirouni, *RSC Advances*, 8(31) (2018)17139-50
19. T. Zeng, X. L. Dong, H. Chen, Y. L. Wang, *Materials Science and Engineering B* 131 (2006) 181–185
20. F. Zhong, H. Zhuang, Q. Guc and J. Long, *RSC Advances*, 6 (2016) 42474
21. K. W. Wagner, *Annals of Physics*, 345 (1913) 817
22. C. G. Koops, *Physical Reviews*, 83 (1951) 121
23. M. K. Shamim, S. Sharma and R. J. Choudhary, *Journal of Materials Science: Materials in Electronics*, 28 (2017) 11609
24. Q. Wang, K. Xue, P. Fu, F. Du, Z. Lin, Z. Chen, S. Wang and G. Wang, *Journal of Materials Science: Materials in Electronics*, 30 (2019) 6475-6481
25. F. Gheorghiu, L. Padurariu , M. Airimioaei, L. Curecheriu, C. Ciomaga, C. Padurariu, C.Galassi and L. Mitoseriu, *Journal of American Ceramic Society*, 100 (2017) 647-658
26. C. Zhao, C. Z. Zhao, M. Werner, S. Taylor and P. Chalker, *Nanoscale Research Letters*, 8 (2013) 1
27. S. Bag and B. Behera, *ECS Journal of Solid State Science and Technology*, 6 (2017) N127-N136
28. J. T. Irvine, D. C. Sinclair and A. R. West, *Advanced Materials*, 2 (1990) 132-138
29. T. Nagaraja, S. Matteppanavar, I. Shivaraja, S. Rayaprol and B. Angadi, *Journal of Alloys and Compounds*, 25 (2021) 159312
30. V. Khopkar and B. Sahoo, *Physical Chemistry Chemical Physics*, 22 (2020) 2
31. J. C. Abrantes, J. A. Labrincha and J. R. Frade, *Journal of European Ceramic Society*, 20 (2000) 1603

Exploring DC bias tuned
electrical properties and
non-Debye relaxation of
vanadium doped BaSnO_3
nanocubes

Abstract

Pure and vanadium doped BaSnO₃ samples were fabricated by using simple solid-state reaction method. X-Ray photoelectron spectroscopy confirmed the desired vanadium doping of the samples. For the first time detail investigation on the electrical properties of V doped BaSnO₃ under different DC bias voltages was studied. It was observed that dielectric constant and conductivity both were decreased significantly after higher doping ($x = 0.03$). These results were accounted for the change in grain and grain boundary sizes, degree of porosity with doping. The application of DC bias promoted the dipolar polarization which was identified as a key factor to increase the values of dielectric permittivity of all the samples in low frequency range (<10 KHz). The application of DC bias boosted the mobility of the charge carriers which further enhanced the electrical conductivity of the samples. V doping was identified as a crucial factor to tune the dielectric permittivity with DC bias voltage at room temperature. Non-Debye type relaxation was confirmed in pure and doped BaSnO₃ samples using Cole-Davidson formalism. Moreover, this method of electrical properties variation by DC bias tuned AC impedance spectroscopy technique may be extended for other perovskite systems also.

5.1. Introduction

Controlling the electrical properties of wide band gap metal oxides for utilizing them as transparent, thermally stable capacitor have always been under prime focus of materials physics.¹⁻³ Numerous methods have been developed to groom traditional semiconductors to smart multifunctional ones. Development of new family of materials like delafossites, perovskites are to be mentioned in this regard.⁴⁻⁶ Especially, perovskite oxides have drawn major attention due to their remarkable optoelectronic properties. They have often been used in solar cells, emission-based devices, sensors etc.⁷⁻¹² Organic molecules-based perovskites are also important due to their excellent photovoltaic performance.¹³ Recent studies show that strong ferroelectric material-based perovskites can be easily used for photovoltaic related applications due to their inherent quasi-polarization.¹⁴ However, electrical transport properties have been the major characteristics of these materials. Enhancing such electrical properties is therefore emerged as the real challenge. In this regard, employing direct method like impurity doping has been identified as one of the most successful measures to achieve the goal.¹⁵⁻¹⁷ Such modification normally influences the grain-boundaries and hence carrier

transport through them leading to appreciable variation of resistivity. This effect is even more important in low dimension due to higher volume fraction of atoms at grain boundaries of nanocrystals compared to their bulk form. Smart multi-elemental materials like copper delafossites, perovskites are designed to be the new-age transparent electronic devices with favorable optical and electrical properties. However, their application in devices is often assisted by some inevitable limitations like structural instability, high room temperature resistivity, non-reliable tuning of optical band gap etc.¹⁸⁻²¹ Common difficulties like low synthesis yield; experimental difficulties are other concerns which must be addressed in order to establish such materials as truly multifunctional ones. However, predicted drawbacks which are mentioned here are comparatively easier to deal with. Variation of electrical properties may occur with varying temperature, operational chamber vacuum, incident excitation etc.²²⁻²⁴ Those effects are inevitable in most of the cases. However, the correlation of such external factors in regulating various electrical parameters must be properly understood in order to achieve desired output. Impurity doping, facile nanostructure formation may influence the carrier concentration, magnetic response etc. but yet they affect various electrical parameters in all frequencies and external DC bias.²⁵⁻²⁷ This scenario is true for materials like BaTiO₃ and BaSnO₃ also. Analysis of grain boundary Schottky potential barrier and influence of applied bias voltage on the same may clarify the physics behind it.²⁸⁻

29

In this present work, the effect of bias voltage in pure BaSnO₃ was studied thoroughly. The effect of impurity doping on this variation was investigated further. The variation of different electrical parameters (like dielectric permittivity, loss, conductivity, impedances) in different frequencies under different bias voltages was investigated. Additionally, the grain boundary effect was identified as a direct consequence of impurity doping by vanadium. Choosing the foreign element to be incorporated within the host BaSnO₃ lattice was performed carefully and vanadium, capable of showing multivalent state (transition metal ion) was selected as the best one to tailor the electrical properties of BaSnO₃. Moreover, a simple synthesis technique involving only high temperature annealing was employed aiming to easy fabrication of the system. The synthesized samples were characterized for phase, composition, doping and morphology related properties via XRD, EDX, XPS, FESEM and HRTEM respectively. Finally, the pure and doped samples were thoroughly studied for electrical properties. As per our best knowledge, this is the first report related to electrical properties of BaSnO₃ under different DC bias voltages.

The results showed that V doping can effectively influence the electrical properties of pristine BaSnO₃ system under different bias voltages. These results opened up a new area of research for DC bias tuning BaSnO₃ based capacitors and may extend to other perovskite oxides also.

5.2. Experimental

5.2.1. Synthesis of vanadium doped BaSnO₃ nanocubes

BaSn_{1-x}V_xO₃ ($x = 0, 0.01, 0.03$) were synthesized by standard solid-state reaction method. BaCO₃ (99.999%, Sigma), SnO₂ (extra pure, Loba Chemie) and V₂O₅ (99.6%, Sigma) were used as reagents. They were used as received without further purification. All the reagents were weighed in a stoichiometric ratio and mixed with CH₃OH. Subsequently, the materials were ground mechanically in an agate mortar for 2 h and kept overnight to ensure that methanol get evaporated completely. The mixture was calcined in an alumina crucible at 1100 °C for 6 h. The calcined powder was thoroughly ground again and recalcined at same temperature and time for two times more. The samples with $x = 0, 0.01$ and 0.03 were labeled as V0, V1 and V3 respectively.

5.2.2. Characterizations

The crystalline phase formation was investigated using X-Ray diffraction (XRD, BRUKER D8 Advance) spectrophotometer with CuK_α ($\lambda = 1.5406\text{\AA}$) radiation whereas the overview of general morphology was scanned using field emission scanning electron microscope (FESEM, Hitachi S-4800). The stoichiometric information was collected using the energy dispersive X-Ray spectroscopy attachment with the FESEM. The detail nanostructural studies of the grains were carried out using high resolution transmission electron microscopy (HRTEM, JEOL-JEM 2100). The impurity doping was tested using X-Ray photoelectron spectroscopy (Specs, Germany) with a hemispherical analyzer (HSA 3500).

Cylindrical pellets for different V concentrations of diameter 12 mm and thickness ~ 1 mm was prepared by pressing the calcined powder. Polyvinyl alcohol (PVA) was used as the binder to prepare the sample pellets with a hydraulic press under a pressure of $\sim 2 \text{ kgcm}^{-2}$. This was followed by sintering the pellets at 800 °C for 5 h in air atmosphere. Before carrying out impedance measurements the pellets were coated with conductive silver paint and dried at 80 °C for 3 h. The pellets were subjected to detail impedance analysis using an impedance analyzer (Agilent 4294A precision Impedance Analyzer).

5.3. Results and discussion

5.3.1. Crystallographic studies

The XRD patterns of the prepared samples are presented in **Figure 5.1(a-c)**. The proper phase formation of crystalline BaSnO₃ was concluded from the result (JCPDS card number: 150780). The crystallite size of the as prepared samples was measured using the well-known Scherrer's equation

$$L = \frac{k\lambda}{\beta \cos \theta} \quad (5.1)$$

where, L is the average crystallite size, k is the shape factor having typical value 0.94, λ is the wavelength of X-Ray which is 1.5406 Å, β is full width half maximum (FWHM) of the most intense diffraction peak taken in radian and θ is the corresponding Bragg's angle of diffraction (in degree).³⁰ The calculated values are 37, 36 and 34 nm for V0, V1 and V3 samples respectively.

The lattice strain present in the samples were determined using the equation

$$\epsilon = \frac{\beta}{4 \tan \theta} \quad (5.2)$$

For further analysis of structural parameters like crystallite size, lattice strain, bond angle, bond length etc. Rietveld refinement analysis was done using Materials Analysis Using Diffraction (MAUD) software.³¹ The structural parameters obtained from the refined XRD pattern are given in **Table 5.1**.

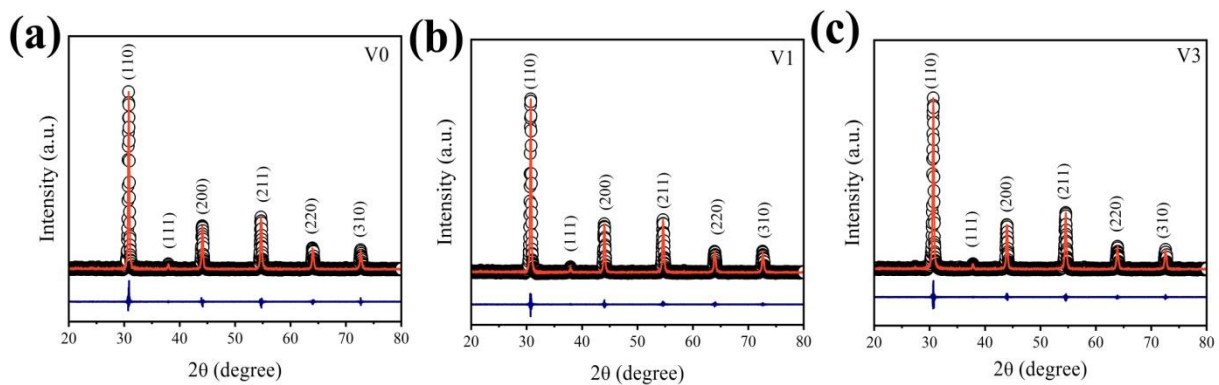


Fig. 5.1. XRD pattern of (a) V0, (b) V1 and (c) V3. The solid lines indicate Rietveld refined XRD patterns, the blue lines indicate the difference between observed and calculated intensity of XRD data

Average crystallite size was found to decrease with increasing amount of vanadium impurity whereas the lattice strain increased subsequently. The decrement in lattice strain was directly correlated to the difference in ionic radii of the dopant V (0.54 Å) and the target replacement

of the host ion Sn (0.69 Å).³² The change in bond length can be accounted for the increment of lattice strain after incorporation of dopant of different ionic radii.

Table 5.1. Lattice strain, bond lengths and bond angles for the samples $BaSn_{1-x}V_xO_3$

	Reported ³³	V0	V1	V3
ϵ	—	0.0035	0.0036	0.0038
GOF	—	1.30	1.47	1.39
Sn-O (Å)	2.058	2.0607	2.0605	2.0594
Ba-O (Å)	2.910	2.914	2.913	2.912
Ba-Sn (Å)	3.564	3.569	3.568	3.567
Sn-Sn (Å)	4.115	4.121	4.120	4.118
Sn-O-Sn (deg.)	180	180	180	180
O-Sn-O (deg.)	90	90	90	90

Moreover, the porosity (P) for the samples was calculated from the following equation³⁴

$$P = (1 - \rho_r) \times 100\% \quad (5.3)$$

Here, ρ_r is the relative density of the ceramics, calculated from bulk density (ρ_b) and X-ray density (ρ_{th}).³⁵ The values of bulk density, relative density and porosity for the pristine and V doped BSO ceramics are listed in **Table 5.2**.

Table 5.2. Bulk density, relative density and porosity of the samples doped with different concentrations of vanadium

Sample	Bulk density (ρ_b in gm/cm^3)	Relative density (ρ_r)	Porosity (P in %)
V0	6.321	0.876	12.40
V1	6.212	0.861	13.90
V3	6.032	0.835	16.50

5.3.2. Morphological studies

To have a deeper insight of the grain dimension, HRTEM studies were carried out. Though, the samples were not free from agglomeration, the grain sizes could be estimated due to

transmission micrographs. The TEM images are presented in **Figure 5.2(a,c)**. The average grain sizes of the samples were found to be ~52 nm for the pure samples which changed to ~38 nm after vanadium doping. The lattice patterns of the samples are presented in **Figure 5.2(b,d)**. The spacing is predominantly for (110) plane can be identified.

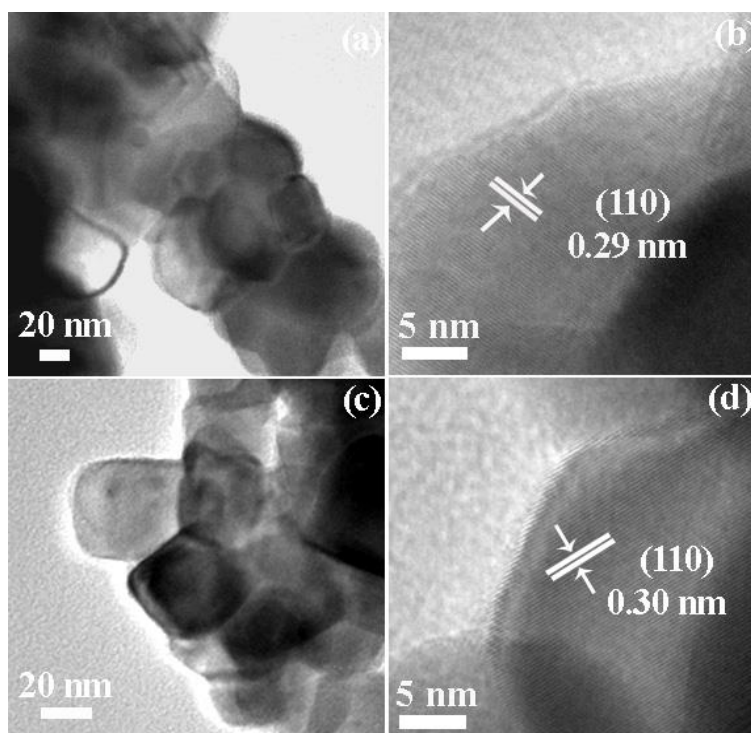


Fig. 5.2. TEM images of (a) V0, (c) V3 and lattice images of (b) V0, (d) V3

5.3.3. Compositional studies

Detail elemental analysis leading to compositional information is presented in **Figure 5.3** where presence of constituent elements Ba, Sn and O with uniform elemental distribution was confirmed. Also, for doped samples V was found with uniform distribution over the samples. To have better insight about the oxidation states of the constituent elements and the exact doping site of vanadium, thorough investigation via XPS was performed and the results are shown in **Figure 5.4**. All the XPS data were calibrated by reference to the C1s peak (B.E. = 284.6 eV). The XPS peaks of Ba 3d_{5/2} and Ba 3d_{3/2} were found at their characteristic positions near 778 and 793 eV respectively.³² Peaks of Sn 3d_{5/2} and Sn 3d_{3/2} were observed near 485 and 494 eV respectively.³² V 2p_{3/2} peak observed at 518.8 eV establishes the existence of vanadium as dopant.³⁶ The broadened XPS peak corresponding to O1s state observed near 530 eV was further deconvoluted to split into two peaks present at 528.4 and

530.2 eV which were identified to be occurred due to presence of lattice oxygen and oxygen from surface absorbed water respectively.³⁷

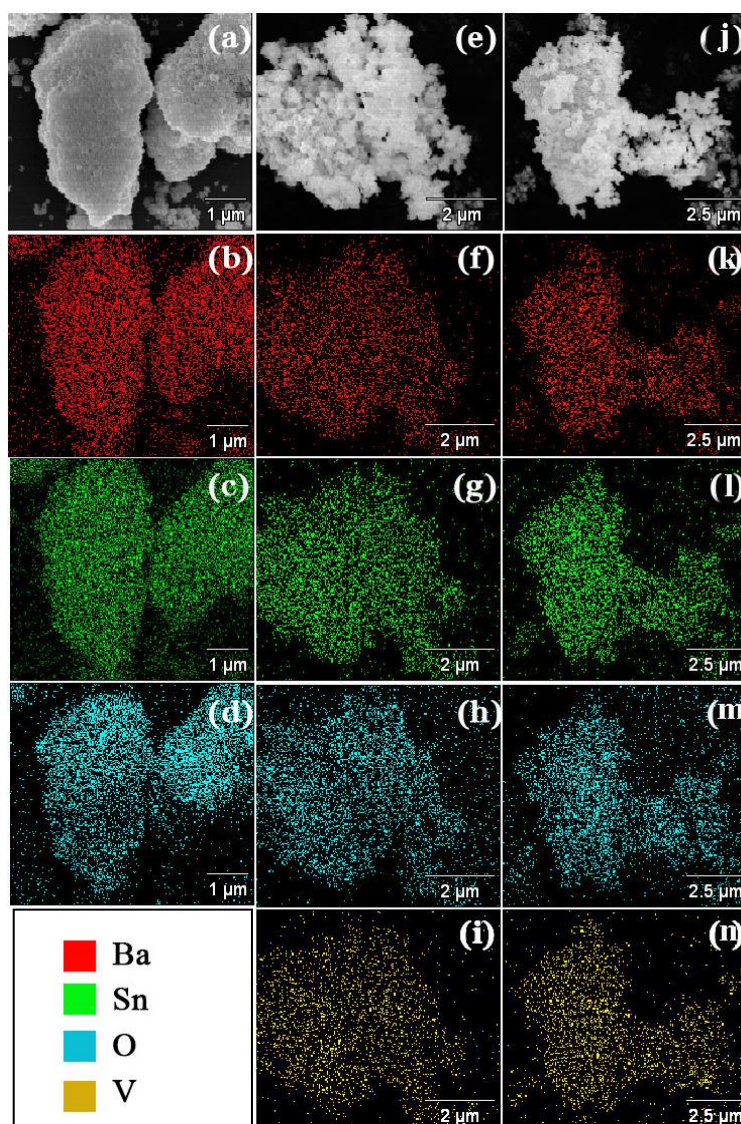


Fig. 5.3. Elemental mapping of (a)-(d) V0, (e)-(i) V1, (j)-(n) V3

Exact doping position of vanadium was predicted considering the possibilities both Ba and Sn being replaced by vanadium. Tolerance factor is often considered as a key parameter in this regard. Especially, for the perovskite structures, Goldschmidt tolerance factor is most commonly used to predict whether a particular site cation can fit within the gaps in ABO_3 system.³⁸ Tolerance factor is expressed as

$$t = \frac{r_A + r_O}{\sqrt{2}(r_B + r_O)} \quad (5.4)$$

where, r_A and r_B are the ionic radius of the A and B site cations and r_O is the ionic radius of the anion.³⁹ The values of 't' was found to be 0.66 and 1.09 for vanadium as A site and B site

cation respectively. It can be seen that 't' deviates more from standard value 1 if vanadium replaces Ba in the perovskite whereas it agrees well with standard value 1 if vanadium is considered to replace Sn. Additionally, quantitative ratio of O:Sn, determined from XPS peak area showed a significant decrement of Sn content in sample V3 compared to V0 which also indicate replacement of Sn by vanadium.

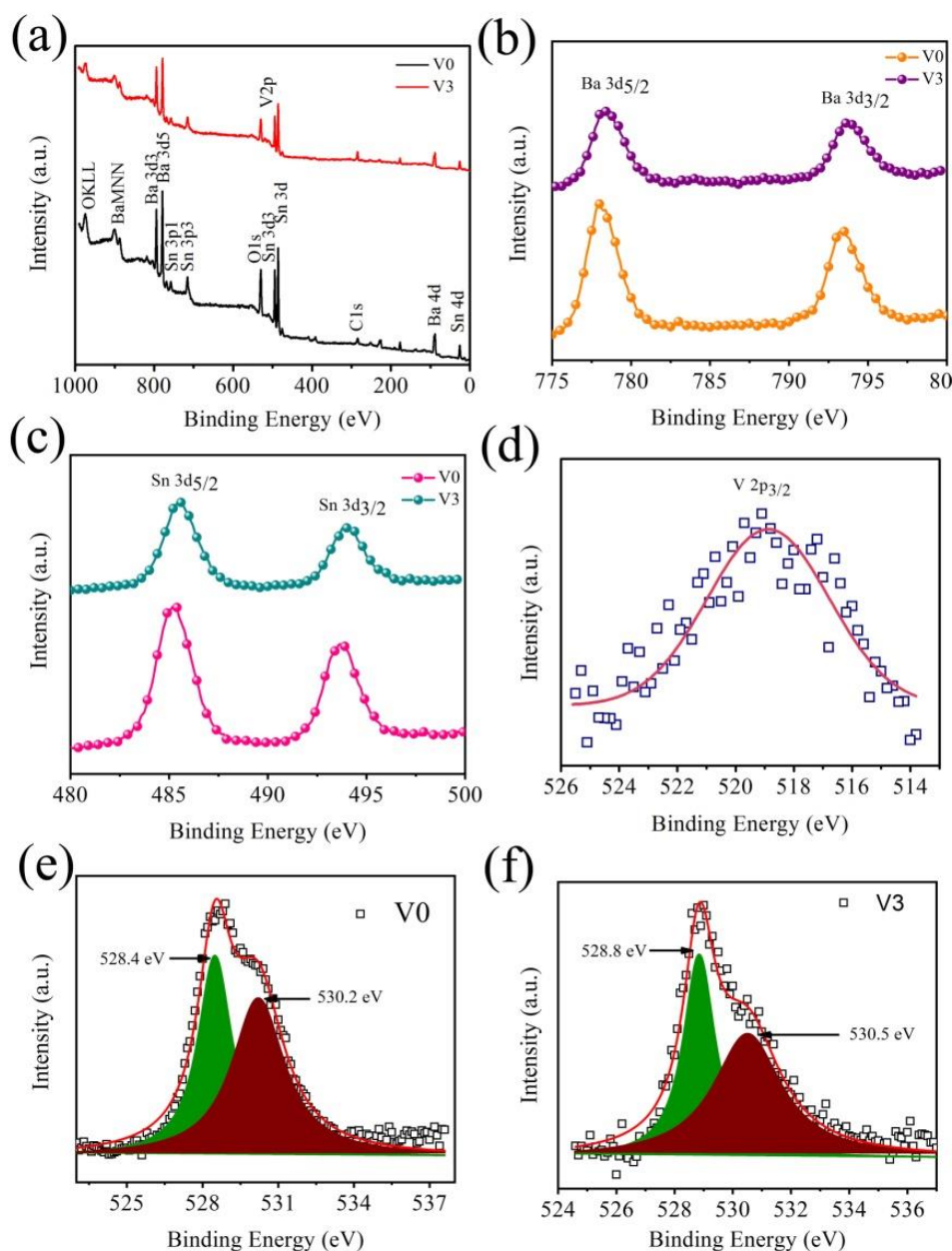


Fig. 5.4. XPS spectra of (a) survey, (b) Ba3d, (c) Sn3d of the samples V0 and V3; (d) V2p of V3; (e) O1s for V0; (f) O1s for V3

Moreover, least dissimilarity of ionic radii between V^{5+} ($R_{V^{5+}} = 0.054$ nm) and Sn^{4+} ($R_{Sn^{4+}} = 0.069$ nm) was also indicates favorable replacement of Sn by V^{5+} and thus the exact doping position of vanadium was confirmed from XPS studies.³²

5.3.4. Electrical properties studies

5.3.4.1. Dielectric permittivity, loss and electrical conductivity studies

The frequency dependent dielectric constant (ϵ_r) for pure and V-doped BaSnO₃ perovskites investigated at room temperature and at a DC bias 18 Volt is shown in **Figure 5.5(a)**. It can

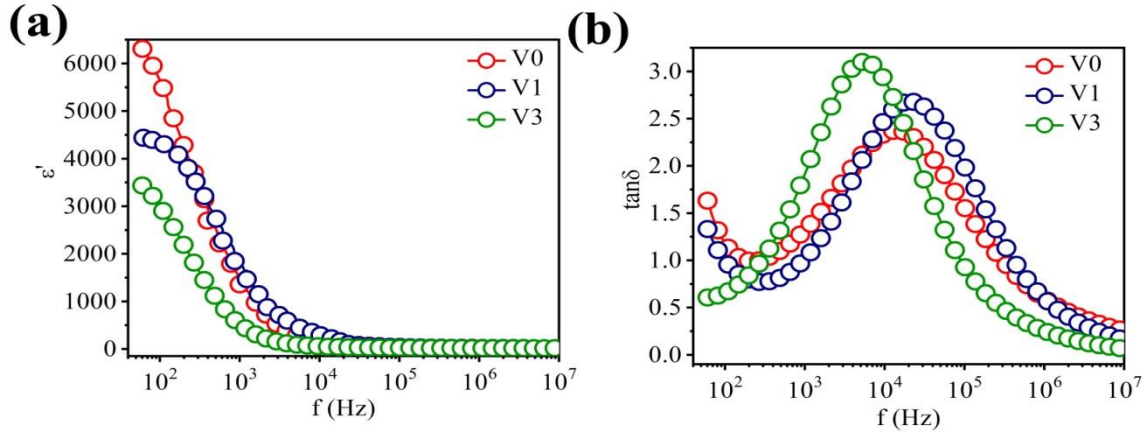


Fig. 5.5. The frequency variation of (a) real part of dielectric constant and (b) tangent loss of the samples at DC bias of 18 V

be seen that all samples exhibit high dielectric constants. A significant lowering in dielectric constant with higher doping percentage was observed for the samples. In case of polycrystalline solids like BaSnO₃, interfacial polarization along with orientational polarization is dominant factor in low frequency regime. In our previous work, we have shown that the effective dielectric constant (ϵ_{eff}) is inversely proportional to the ratio of thickness of the grain boundary to the grain size.

We can explain that the reduction of dielectric constant with increasing vanadium content occurred due to the grain size reduction.⁴⁰ Also, porosity or alternatively compactness is a key factor to determine the effective polarization of any porous system. According to Maxwell-Garnett equation the dielectric constant should have highest value for least porous sample.⁴¹ Thus, effective dielectric constant showed a lowering tendency with high vanadium doping. In addition to the study of variation of dielectric constant with various V doping concentrations, the variation of dielectric loss with same doping alteration was investigated in the same frequency range. Dielectric loss is a measure of power loss within the dielectric material. The obtained results are presented in **Figure 5.5(b)**.

The frequent appearance of grain boundary (charge scattering and trapping centers) due to smaller grain size resulting high loss for doped ceramics compared to pure one. Again, study of ac conductivity of pure and doped samples showed (**Figure 5.6(a)**) that an appreciable change in conductivity was observed for doped samples. The electrons can't be able to drift a

longer path due to smaller grains of the doped samples and their velocity gets hindered by the grain boundaries. Thus total conductivity was decreased with doping. This in turn showed an enhancement in impedance shown in **Figure 5.6 (b-c)**.

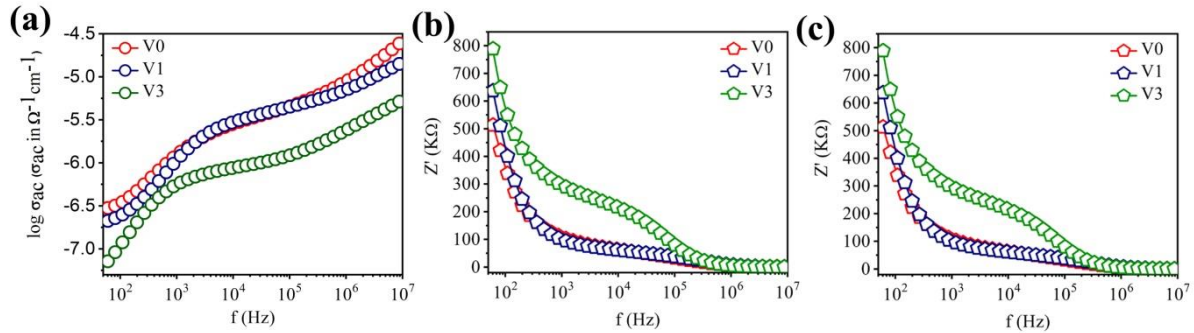


Fig. 5.6. Frequency dispersion of (a) conductivity, (b) real and (b) imaginary part of impedance for all the samples at a DC bias 18 Volt

5.3.4.2. Complex Impedance Spectra (CIS) analysis and DC bias

To correlate the variation of dielectric parameters with grain and grain boundary resistances, the obtained results were analyzed using an ideal equivalent R-Q network including two parallel combinations of R and Q (Constant Phase Element), as shown in **Figure 5.7**.⁴² Q and C are related as

$$C = R^{\frac{(1-a)}{a}} Q^{\frac{1}{a}} \quad (5.5)$$

where, a is the degree of deviation with respect to the value of pure capacitor.

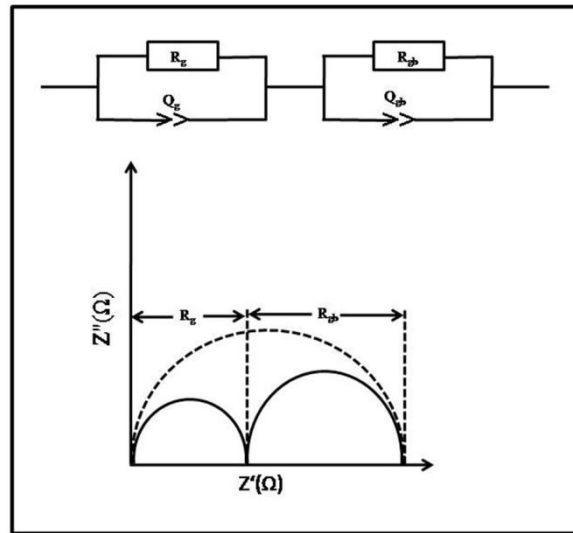


Fig. 5.7. Schematic of proposed equivalent circuit

The values of grain resistances R_g and grain boundary resistances R_{gb} were determined via fitting (using EC-Lab software programme) of the Cole-Cole plot as presented in **Figure 5.8**. With impurity, both the parameters (especially R_{gb}) increased appreciably (**Table 5.3**). The

reason may be explained considering the decrement in grain size. As the grains grow smaller carrier scattering at the grain boundary becomes more frequent leading to higher grain boundary resistivity. Due to the application of DC bias voltage, the electrons gain more energy to move and the mobility of the charge carriers increases. In addition, this external energy helps the charge carriers for inter-grain hopping also. Thus, the effective grain and grain boundary resistances showed a significant reduction after application of 18 V DC bias voltage.

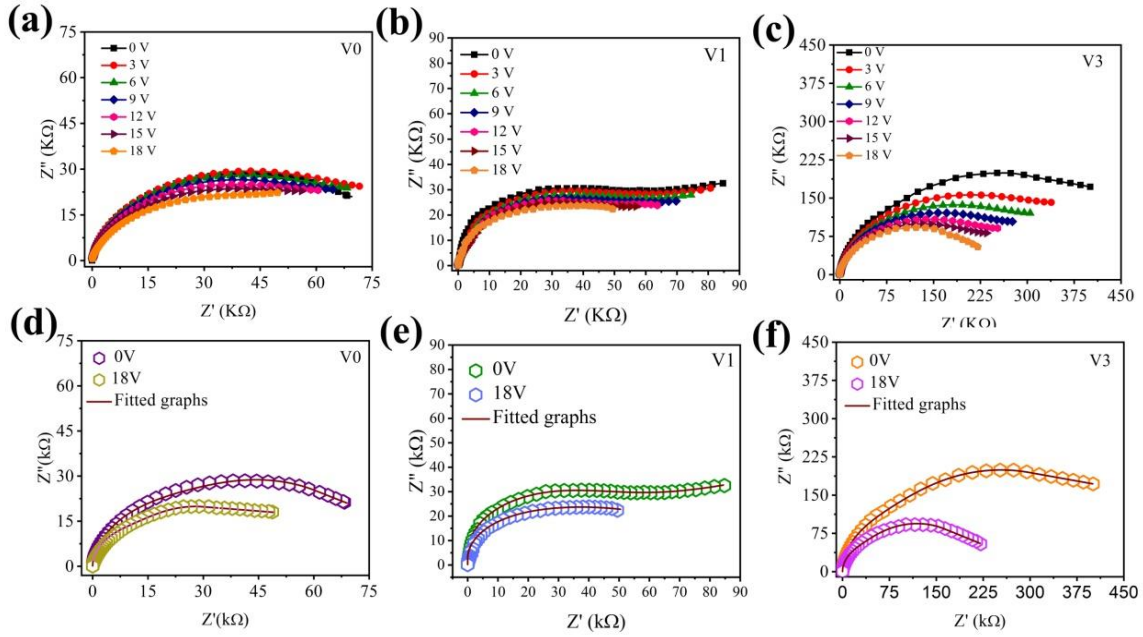


Fig. 5.8. Bias dependent Cole-Cole plot for (a) V0, (b) V1 and (c) V3; fitted Plots are shown for (d)V0, (e) V1 and (f) V3

Table 5.3. Calculated values of R_g and R_{gb} for 0 Volt and 18 Volt

Bias voltage	Sample	R_g (kΩ)	R_{gb} (kΩ)
0 V	V0	37.268	42.267
	V1	41.560	42.511
	V3	88.126	367.434
18 V	V0	12.661	35.548
	V1	22.114	35.576
	V3	39.834	174.676

5.3.4.3. Effect of DC bias on dielectric permittivity

In addition, dependency of dielectric permittivity on bias voltage for each sample was also performed. The bias voltage was varied from 0-18 V and corresponding variation of dielectric constant is presented in **Figure 5.9**. In **Figure 5.9(a)**, it can be clearly seen that the values of ϵ' do not vary much with applied bias for the pure sample within low frequency range (<10 kHz) but the variation of ϵ' becomes more prominent when the sample was doped with trace amount of vanadium as depicted in **Figure 5.9(b)**. Most dominant control by applied bias voltage was observed for higher V doping **Figure 5.9(c)**. The effect of DC bias was not prominent in high frequency range, i.e. the value of ϵ' show less fluctuation with bias voltage for all samples compared. The variation of dielectric parameters is no doubt predominantly occurring in the low frequency region. The reason may be correlated with different governing

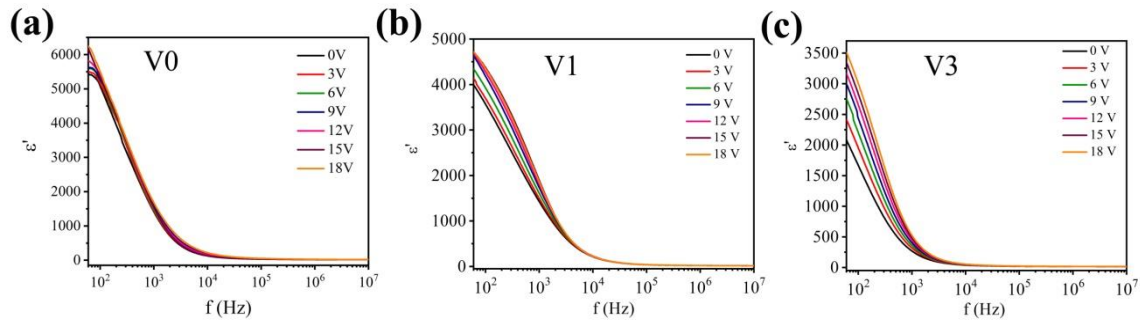


Fig. 5.9. Frequency variation of real part of dielectric permittivity for (a) V0, (b) V1 and (c) V3 at different DC bias voltages

factors active in low and high frequency region. The electronic and ionic polarizations are considered as major factors controlling the dielectric behavior of the samples at high frequencies whereas the dipolar and space-charge polarizations become the prime controlling factors at low frequency.

The defects at the grain boundaries often serve as charge carrier trapping and recombination centers. This also forms a potential barrier identical to Schottky barrier between two adjacent grains. However, considering the fact that there are two grains adjacent to a grain boundary region, this barrier may be considered as double Schottky barrier. When there is no applied bias voltage, both of the space charge layers are similar. But as soon as a finite bias voltage is applied, one of the charged layers is thickened and other one is narrowed depending upon the polarity of the bias. If the applied bias is increased further, the barrier height at the grain boundary changes appreciably. Also, when there is no external DC bias, the dipoles were arranged in random fashion due to thermal agitation. But when DC bias was employed prior to the application of external AC field, the dipoles get aligned along the direction of the bias

voltage. This means the system becomes more ordered than previous one and in this condition the application of AC field becomes more effective to make the system polarized. Thus for all the samples, dielectric constant was increased with the DC bias voltage.

The dipoles formed with V-O have lower inertia than the Sn-O dipoles as vanadium is lighter than Sn. When there was no DC bias because of the porosity and grain size, the effective dielectric constant became decreased with doping concentration. But with the application of DC bias the dipolar polarization increased for the doped samples as the lighter dipoles can follow the instantaneous polarity change of the input AC electric field. Thus the enhancement of dielectric constant due to the application of DC bias becomes more prominent for the samples containing more vanadium as dopant.

5.3.4.4. Modulus spectroscopy studies

The complex modulus is the reciprocal of the complex permittivity and can be expressed as

$$\begin{aligned}
 M^*(\omega) &= \frac{1}{\varepsilon^*(\omega)} \\
 &= \left(\frac{\varepsilon'}{\varepsilon'^2 + \varepsilon''^2} \right) + j \left(\frac{\varepsilon''}{\varepsilon'^2 + \varepsilon''^2} \right) \\
 &= M' + jM''
 \end{aligned} \tag{5.6}$$

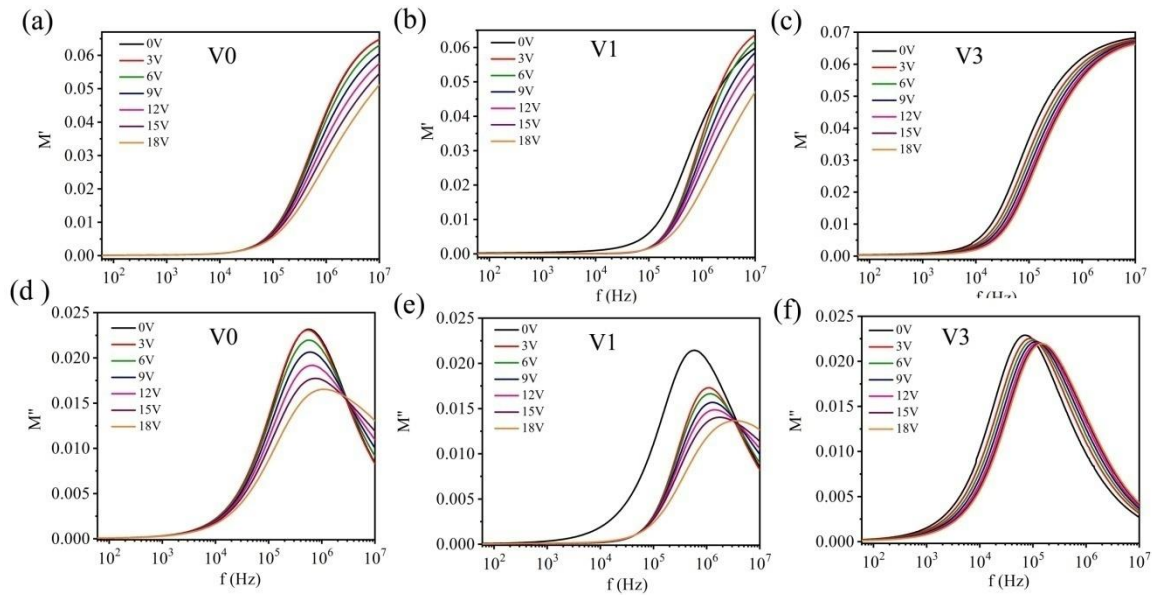


Fig. 5.10. Frequency dispersion of real (a-c) and imaginary (d-f) components of complex modulus at different bias voltages for the samples

The variation of M' with frequency for all samples in various bias voltages (**Figure 5.10(a-c)**) showed that M' increased at high frequency range which continuously due to short range mobility of carriers.⁴³ However, this mobility mainly occurred within the grain and due to high grain boundary resistance, as already demonstrated in previous section; signature of

inter-grain carrier hopping was not found. Moreover, the value of M' was found to decrease slightly with applied DC bias in accordance with the ϵ' vs f behavior. A wide variation of symmetry features of the peaks in M'' vs f plot can be observed in **Figure 5.10(d-f)** for all applied bias. Long range movement of the charge carriers is identified by its signature in low frequency tail which favors carrier hopping between two neighboring crystals. On the other hand, the high frequency tail of M'' peaks corresponds to the confinement of the carriers in their potential well allowing only localized movement. M'' peak represents the transition from long range to short range mobility.⁴³ Modulus spectra often reflect the nature of relaxation of any sample. Careful observation of the spectra presented in **Figure 5.10(d-f)** reveals that the modulus peaks gradually shifted towards higher frequency with increasing DC bias. Shift of this peak towards higher frequency indicates the decrement of relaxation time. Relaxation time can be determined using the following relation

$$\tau = \frac{1}{2\pi f_{max}} \quad (5.7)$$

It was observed that the relaxation time was decreased with increasing applied DC bias in case of all samples. The application of DC bias boosted the ordered state of dipoles in the system which in turn helps the dipoles to follow the external AC field.

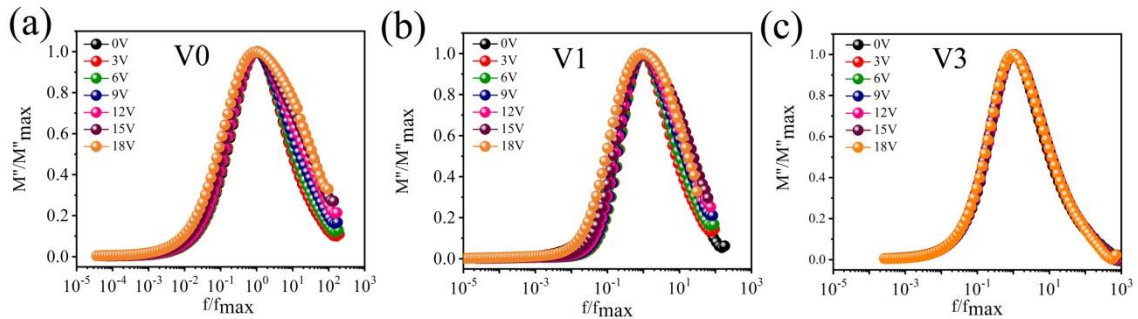


Fig. 5.11. Modulus master curve for (a) V0, (b) V1, (c) V3

In the modulus master curve which is the plot of (M''/M''_{max}) vs. (f/f_{max}) depicted in **Figure 5.11**, the peaks can be seen to coincide with each other for all voltages indicating that the same relaxation mechanism is responsible for all applied bias voltages. From the results, it can be clearly seen that the vanadium doping has enhanced the influence of DC bias on various electrical parameters of the samples and the same is highlighted in the low frequency region. Due to the incorporation of V into the perovskite system BSO, the dielectric constant or alternatively, capacitance can easily be tuned simply by varying DC bias at room

temperature. Thus the V doped BSO nanocubes are useful capacitor material in micro and nanoelectronics in which the capacitance value can be altered without varying temperature.

5.3.4.5. Dielectric relaxation formalism analysis

From the Cole-Cole plot (**Figure 5.8**), the center of the arcs appears to be below the X-axis which is a clear indication of non-Debye type relaxation. The asymmetry of the dielectric loss curve (**Figure 5.5(b)**) also indicates the non-Debye type relaxation occurring in the samples.

In order to achieve deeper insight on ‘non-Debye’ relaxation, the obtained data of frequency dependent dielectric constant were further fitted (**Figure 5.12(a,b)**) using the Cole-Davidson relation⁴⁴

$$\varepsilon^*(\omega) = \varepsilon_\infty + \frac{\varepsilon_s - \varepsilon_\infty}{(1 + j\omega\tau)^\beta} = \varepsilon'(\omega) - j\varepsilon''(\omega) \quad (5.8)$$

The real and imaginary parts of $\varepsilon^*(\omega)$ are given by

$$\varepsilon'(\omega) = \varepsilon_\infty + (\varepsilon_s - \varepsilon_\infty)(\cos \Phi)^\beta \cos(\beta\Phi) \quad (5.9)$$

and

$$\varepsilon''(\omega) = (\varepsilon_s - \varepsilon_\infty)(\cos \Phi)^\beta \sin(\beta\Phi) \quad (5.10)$$

where, $\Phi = \tan^{-1}(\omega\tau)$, β is the shape parameter, ε_s , ε_∞ are the relaxed and unrelaxed permittivity respectively. τ is the characteristic relaxation time and ω is the angular frequency.

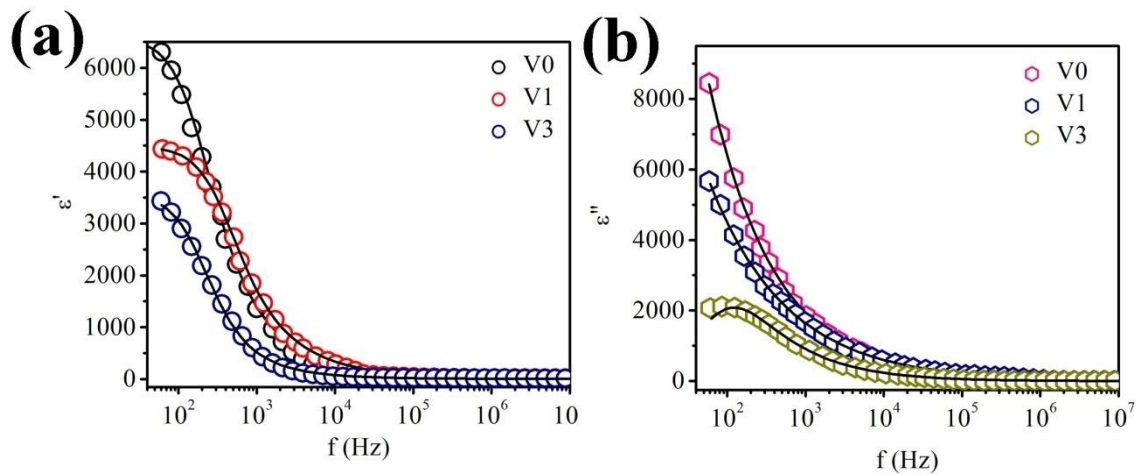


Fig. 5.12. The frequency variation of (a) real and (b) imaginary part of dielectric permittivity of the samples at a DC bias of 18 V; the solid lines indicate Cole-Davidson fitting of dielectric spectra

β was considered as the major fitting parameter and the value of β was identified as the decisive factor for the relaxation to be recognized as Debye type ($\beta = 1$) or non-Debye ($\beta < 1$) type.⁴⁵ The obtained values of β for different doping concentrations at a DC bias of 18 Volt were less than 1. Thus, the samples follow non-Debye type of relaxation.

Another indirect proof of the type of relaxation may be established from the FWHM of (M''/M''_{\max}) vs (f/f_{\max}) plot. The values of FWHM were found to be greater than 1.14 decade (breadth of Debye peak) which indicates non-Debye type of relaxation occurring in the samples.

5.4. Conclusion

Pure and vanadium incorporated BaSnO₃ samples were prepared via facile solid-state method. Thorough characterizations for investigating the structural, morphological and compositional features revealed proper phase formation, nano-particulate nature and uniform elemental distribution of the samples. The dielectric constants of the samples decreased from 6305 to 3432 in low frequency (60 Hz) with increasing V doping concentration which occurred due to the decrement of grain size, relative density and the defects generated upon doping into the grain boundaries. DC bias dependence of grain and grain boundary resistances was explained using double Schottky barrier theory. The range of variation of dielectric constants under different bias voltages gradually widened 1.6 times with incorporation of higher amount of dopant atoms in low frequency region and the same was identified to be governed by dipolar polarization. The samples were found to follow Non-Debye type ($\beta < 1$) relaxation which was confirmed by correlating the experimental data with Cole-Davidson relation and analyzing the modulus master curve widths (> 1.14 decade). This work is therefore showed that BSO:V system can be used as tunable capacitor material in micro-nanodevices at room temperature.

5.5. References

1. J. A. Aguilar-Martínez, M. B. Hernández, A. B. Glot and M. I. Pech-Canul, Journal of Physics D: Applied Physics, 40 (2007) 7097–7102
2. MD P. Ahmad, A. V. Rao, K. S. Babu and G. N. Rao, Materials Chemistry and Physics, 224 (2019) 79–84
3. M. S. Samuel, J. Koshy, A. Chandran and K. C. George, Physica B Condensed Matter, 406 (2011) 3023–3029

4. M. Lalanne, P. Demont and A. Barnabé, *Journal of Physics D: Applied Physics*, 44 (2011) 185401
5. S. Upadhyay, O. Parkash and D. Kumar, *Journal of Materials Science: Materials in Electronics*, 16 (1997) 1330–1332
6. F. Zeng, M. Cao, L. Zhang, M. Liu, H. Hao, Z. Yao and H. Liu, *Ceramic International*, 43 (2017) 7710–7716
7. A. Bera, K. Wu, A. Sheikh, E. Alarousu, O. F. Mohammed and T. Wu, *The Journal of Physical Chemistry C*, 118 (2014) 28494–28501
8. F. Xie, Y. Li, T. Xiao, D. Shen and M. Wei, *Electrochimica Acta*, 261 (2018) 23–28
9. H. J. Bian, X. F. Chen, J. S. Pan, W. Zhu and C. Q. Sun, *Applied Surface Science*, 255 (2009) 4867–4872
10. R. B. Kamble, N. Tanty, A. Patra and V. Prasad, *Applied Physics Letters*, 109 (2016) 083102
11. S. V. Manorama, C. V. G. Reddy and V. J. Rao, *Applied Surface Science*, 174 (2001) 93–105
12. J. Cerdà, J. Arbiol, G. Dezaneeu, R. Díaz and J. R. Morante, *Sensors & Actuators, B: Chemical*, 84 (2002) 21–25
13. Y. Zheng, C. Wang, J. Yu, F. Yang, J. Zhang, B. Wei and W. Li, *Journal of Physics D: Applied Physics*, 50 (2017) 475303
14. K. T. Butler, J. M. Frost and A. Walsh, *Energy & Environmental Science*, 8 (2015) 838–848
15. L. Zhu, J. Ye, X. Zhang, H. Zheng, G. Liu, X. Pan and S. Dai, *Journal of Materials Chemistry A*, 5 (2017) 3675–3682
16. H. B. Sales, V. Bouquet, S. Députier, S. Ollivier, F. Gouttefangeas, M. Guilloux-Viry, V. Dorcet, I. T. Weber, A. G. de Souza and I. M. G. dos Santos, *Solid State Sciences*, 28 (2014) 67–73
17. Y. Yuan, J. Lv, X. Jiang, Z. Li, T. Yu, Z. Zou and J. Ye, *Applied Physics Letters*, 91 (2007) 094107
18. S. Švarcová, K. Wiik, J. Tolchard, H. J. M. Bouwmeester and T. Grande, *Solid State Ionics*, 178 (2008) 1787–1791
19. W. Zhong and D. Vanderbilt, *Physical Review Letters*, 74 (1995) 2587–2590
20. D. Yamashita, S. Takefuji, M. Tsubomoto and T. Yamamoto, *Materials Science and Engineering C*, 173 (2010) 33–36

21. S. M. Ali, S. T. Hussain, S. A. Bakar, J. Muhammad and N. Rehman, *Journal of Physics: Conference Series*, 439 (2013) 012013
22. X. Q. Liu, B. W. Jia, W. Z. Yang, J. P. Cheng and X. M. Chen, *Journal of Physics D: Applied Physics*, 43 (2010) 495402
23. Fleming R *Jet a,l* Conductivity and Space Charge in LDPE Containing Nano- and Micro-sized ZnO Particles *IEEE Transactions on Dielectrics and Electrical Insulation*, 15 (2008) 118-125
24. E. J. Juarez-Perez, R. S. Sanchez, L. Badia, G. Garcia-Belmonte, Y. S. Kang, I. Mora-Sero and J. Bisquert, *The Journal of Physical Chemistry Letters*, 5 (2014) 2390–2394
25. K. K. James, P. S. Krishnaprasad, K. Hasna and M. K. Jayaraj, *Journal of Physics and Chemistry of Solids*, 76 (2015) 64–69
26. U. S. Alaam, P. Shafer, A. T. N'Diaye, E. Arenholz and Y. Suzuki, *Applied Physics Letters*, 108 (2016) 042106
27. K. Balamurugan, N. H. Kumar, J. A. Chelvane and P. N. Santhosh, *Journal of Alloys and Compounds*, 472 (2009) 9–12
28. T. Prakash, S. Ramasamy, and B. S. Murty, *Electronic Materials Letters*, 9 (2013) 207-211
29. N. Kumar, E. A. Patterson, T. Fro'mling and D. P. Cann, *Journal of Materials Chemistry C*, 4 (2016) 1782-17
30. U. K. H. Bangi, L. P. Deshmukh, H. H. Park and N. N. Maldar, *2nd International Symposium on Physics and Technology of Sensors* (2015)
31. R. A. Young, *The Rietveld Method* (London U.K.: Oxford University Press), (1993)
32. T. Alammari, I. I. Slowing, J. Anderegg and A. V. Mudring, *Chem Sus Chem*, 10 (2017) 1 – 16
33. W. Ncib, A. B. J. Kharrata, M. A. Wederni , N. Chniba-Boudjada, K. Khirounid and W. Boujelben, *Journal of Alloys and Compounds*, 768 (2018) 249-262
34. T. Zeng, X. L. Dong, H. Chen, Y. L. Wang, *Materials Science and Engineering B* 131 (2006) 181–185
35. C. Rayssi, S. E. Kossi, J. Dhahri and K. Khirouni, *RSC Advances*, 8(31) (2018)17139-50
36. B. C. Luo, J. Zhang, J. Wang and P. X. Ran, *Ceramic International*, 41 (2015) 2668–2672

37. W. Zhang, J. Tang and J. Ye, *Journal of Materials Research*, 22 (2007) 1859-1871
38. A. B. J. Kharrat, S. Mouss, N. Moutia , K. Khirouni and W. Boujelben, *Journal of Alloys and Compounds*, 724 (2017) 389-399
39. D. Chandran, L. S. Nair, K. R. Babu, M. Deepa and C. M. K. Nair, *International Journal of Advance Research in Science and Engineering* 6 (3) (2017) 30-33
40. A. Sen, U. N. Maiti, R. Thapa and K. K. Chattopadhyay, *Journal of Alloys and Compounds*, 506 (2010) 853–857
41. F. Gheorghiu, L. Padurariu , M. Airimioaei, L. Curecheriu, C. Ciomaga, C. Padurariu, C. Galassi and L. Mitoseriu, *Journal of American Ceramic Society*, 100 (2017) 647-658
42. A. Dey, J. Dhar, S. Sil, R. Jana and P. P. Ray, *Journal of Materials Engineering and Performance*, 27 (2018) 2727–2733
43. C. Zhao, C. Z. Zhao, M. Werner, S. Taylor and P. Chalke, *Nanoscale Research Letters*, 8 (2013) 456
44. G. G. Raju, *Dielectric Loss and Relaxation-I Dielectrics in Electric Fields* (Boca Raton: CRC Press), (2016)
45. E. Moreira, J. M. Henriques, D. L. Azevedo, E. W. S. Caetano, V. N. Freire, U. L. Fulco and E. L. Albuquerque, *Journal of Applied Physics*, 112 (2012) 043703

V doped BaSnO₃ nanocubes
as a potential cold cathode:
Theoretical and
experimental investigation

Abstract

In search of a truly multipurpose perovskite system with applications beyond photovoltaics, pure and vanadium doped BaSnO_3 nanocubes were prepared using facile solid-state reaction method. Theoretical simulation via ANSYS Maxwell software was employed to predict whether doping in nano- BaSnO_3 can lead to cold electron emission from the samples. The work function, a crucial factor for potential cold cathodes, was determined using density functional theory and the outcome was used to calculate the field enhancement factor. Encouraged by theoretical outcome, experimental investigation for field emission capability of the samples was carried out in a high vacuum chamber. Several factors like impurity doping, emitter dimension, decrement of work function were identified as tuning factors. The emission current density and the field enhancement factor of 5% doped sample were enhanced ~ 3 and 4.3 times respectively compared to the pure one with 30% reduction of the turn on field. The first ever investigation of field emission properties of pure and doped BaSnO_3 in this work, showed that the novel perovskite can serve as an environment-friendly cold cathodes in field emission display unit, electron microscopes etc. along with its other traditional applications.

6.1. Introduction

Low dimensional form of traditional semiconductors like ZnO , TiO_2 , CuO have already been established as multifunctional candidates showing remarkable contribution in fields like water purification, nanoelectronics, green energy harvesting, photo-electrochemical performance, gas sensors etc.¹⁻⁵ Among some special classes of novel materials, delafossites, perovskites are under strict analysis in this regard.⁶⁻⁷ Till now, perovskites are well known for their green energy harvesting and tunable electrical properties.⁹⁻¹⁰ Some limited studies are also there demonstrating green water treatment efficiency, electrochemical applications, magnetic properties and field electron emissions of those materials.¹¹⁻¹⁴ Among those limited explored fields, cold electron emission plays an important role in various vacuum micro-nanoelectronic devices like flat-panel display units, field emission electron microscopes, microwave power amplifiers etc.¹⁵⁻¹⁷ Cold electron emitters are capable of emitting electrons at room temperature and they do not require warm up time as well. On the other hand, employing quantum tunneling of electron in cold electron emission cause lesser input energy consumption is another eco-friendly aspect of cold cathodes.¹⁸ However, combining different properties for multidimensional applications of perovskites is the real challenge of this field. Though there are plenty of classical semiconductors like CNT , ZnS , MoS_2 and some

perovskites offering good electron emission behavior, they have their own limitations as well. Traditional field emitters like carbon derivatives often suffer morphological and property related inferiority under very high external field.^{14,19-23} Although perovskites are free of such risk due to their appreciable stability under harsh external perturbations, In some established perovskite field emitters like MALI, CsPbX₃ contain heavy metal Pb.²⁴⁻²⁵ In this regard, cultivation of cold emission properties from BaSnO₃ would have positive environmental aspects. BaSnO₃ is non-toxic and therefore expected to yield no hazardous residual gases or chemical even in case of minor malfunctions of emission based devices made out of BaSnO₃. Moreover, this novel perovskite can be prepared via simple synthesis procedures which do not produce any harmful sub-product. BaSnO₃ can be of more interest as theoretical simulation of field emission (FE) behavior requires inputs like electrical parameters and BaSnO₃ is already popular for its tunable electrical properties. Plenty of experimental results of electrical behavior with a variety of BaSnO₃ samples are already available in the literature.²⁶⁻²⁸ Moreover, due to well established synthesis routes, incorporation of new impurity in BaSnO₃ system is possible. In the selection of dopant, compatible ionic dimension, band gap and individual performance of the dopant based systems in the target applications are analyzed crucially. Vanadium, having multivalent states may be an interesting dopant candidate for carrier exchange with the host leading to exclusive electrical properties. V₂O₅ is itself a good field emitter system.²⁹⁻³⁰ V doped BaSnO₃ has already shown a reduction in dielectric constant, which may be an indirect boost for cold emission behaviour considering the fact that the core conducting grains are the emitters and the insulating grain boundaries are acted like the coated dielectric.³¹⁻³² Again, this novel variation should lead to rearrangement of electronic band configuration which in turn can modify the work function of the material.

This work was aimed to investigate the field emission behavior of BaSnO₃ for the first time. Additional multiple trial and prolong optimization were replaced via simple simulation-based investigation before carrying out actual cold cathode experiments. Others important parameters demonstrating the efficiency of FE behavior are turn on field and field enhancement factor. Theoretical calculation using density functional theory (DFT) was again used to determine the values of work functions which were used to calculate field enhancement factors for pure and vanadium doped BaSnO₃. Two unique facts were uncovered in this work; firstly, novel BaSnO₃ can work as efficient cold cathodes depending upon its shape and the FE properties of the samples can be properly tuned by factors like impurity doping, nanostructural dimension and electrode separation. When verified

experimentally, V doped BaSnO₃ samples showed higher emission current density with increasing doping concentration. Due to the combined effect of doping associated defects, emitter dimension and electrode separation, the variation of the field emission parameters were explained.

6.2. Experimental

6.2.1. Synthesis of BaSn_{1-x}V_xO₃ nanocubes

Using high purity BaCO₃, SnO₂ and V₂O₅ powders, vanadium doped BaSnO₃ (BaSn_{1-x}V_xO₃) was prepared via conventional solid-state reaction process. Stoichiometric ratio of all the precursors were mixed with CH₃OH and ground in an agate mortar for 2 h. Methanol was allowed to evaporate from the powder mixture completely. The dried powder mixture was placed in an alumina boat and calcined at 1100°C for 18 h. The samples with $x = 0, 0.01, 0.02, 0.03, 0.04, 0.05$ were labeled as BV0, BV1, BV2, BV3, BV4 and BV5.

6.2.2. Characterizations

All the samples were thoroughly characterized using different tools. The proper phase formation of as synthesized samples was confirmed using X-ray diffractometer (XRD, Bruker, D-8 Advance) with CuK_α radiation ($\lambda = 1.54056 \text{ \AA}$). Surface morphology was examined by Field emission scanning electron microscope (FESEM, Hitachi S-4800). The dimensions of grains were studied using high resolution transmission electron microscope (JEOL, 200 kV HRTEM). The elemental composition and their uniform distribution were analyzed by energy-dispersive X-ray spectroscopy (EDS, Thermo Scientific attached with HitachiS-4800). The impurity doping was confirmed via X-Ray photoelectron spectroscopy (XPS, Specs, Germany) with a hemispherical analyzer (HSA 3500). The dielectric properties of the samples were measured using an impedance analyzer (Agilent 4294A precision Impedance Analyzer). The simulation-based field emission properties were theoretically investigated by ANSYS MAXWELL software. Theoretical investigation to determine the work functions via Density Functional Theory (DFT) was carried out using first principle calculation. Finally, the actual field emission properties of the samples were investigated using our laboratory made high vacuum field emission set-up.

6.3. Results and Discussion

6.3.1. Structural studies

The X-ray diffraction (XRD) pattern presented in **Figure 6.1(a)** shows the proper crystallinity of the samples. The peaks at 30.93° , 38.08° , 44.19° , 54.78° , 64.11° and 72.75° were assigned to occur due to reflection from (110), (111), (200), (211), (220) and (310) planes of cubic BaSnO_3 lattice [JCPDS card number: 150780]. The most intense peak was obtained for (110) plane. Except a very small shift in the peak positions, no extra peak was noticed in the XRD pattern of the doped samples.

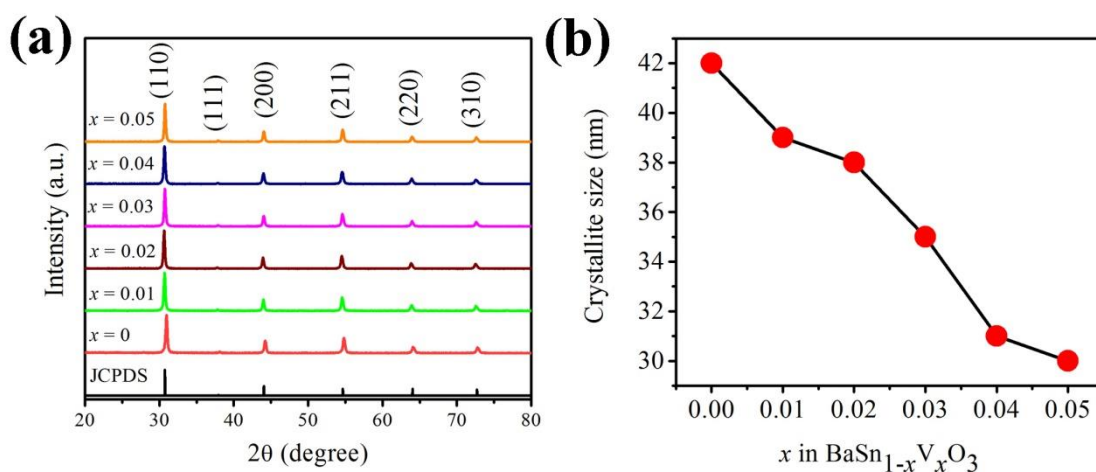


Fig. 6.1. (a) XRD pattern of $\text{BaSn}_{1-x}\text{V}_x\text{O}_3$ at different V contents (from $x = 0$ to 0.05); (b) corresponding change in average crystallite size

The average crystallite sizes of the pure and V doped samples were calculated using well known Scherrer's equation

$$L = \frac{k\lambda}{\beta \cos\theta} \quad (6.1)$$

Where, L is the average crystallite size, k is the shape factor with typical value 0.9, λ ($=1.5406 \text{ \AA}$) is the wavelength of X-ray, θ is the Bragg's angle of diffraction (in degree) and β is full width half maximum (FWHM) of the corresponding diffraction peak (in radian). The average crystallite size of the samples was found (**Figure 6.1(b)**) to decrease with vanadium doping. The decrement of the crystallite size was accounted for the dissimilarity of the ionic radii between the dopant ($R_{\text{V}^{5+}} = 0.054 \text{ nm}$) and the host system ($R_{\text{Sn}^{4+}} = 0.069 \text{ nm}$).³³ The undoped unit cell consists of a Sn^{4+} ion with a higher diameter, whereas the doped sample has a V^{5+} ion which is aimed to replace the Sn^{4+} ion. Considering the lower dimension of V^{5+} ion, the unit cell of the doped sample is expected to exhibit smaller cell volume. This is directly

related to the smaller dimension of the V doped BaSnO_3 (BV) system compared to the undoped one as verified from XRD study.³⁴

6.3.2. Morphological studies

To obtain a more specific idea about the actual dimensions of the BV nanostructures, HRTEM micrographs were recorded and presented in **Figure 6.2**. It can be seen from **Figure**

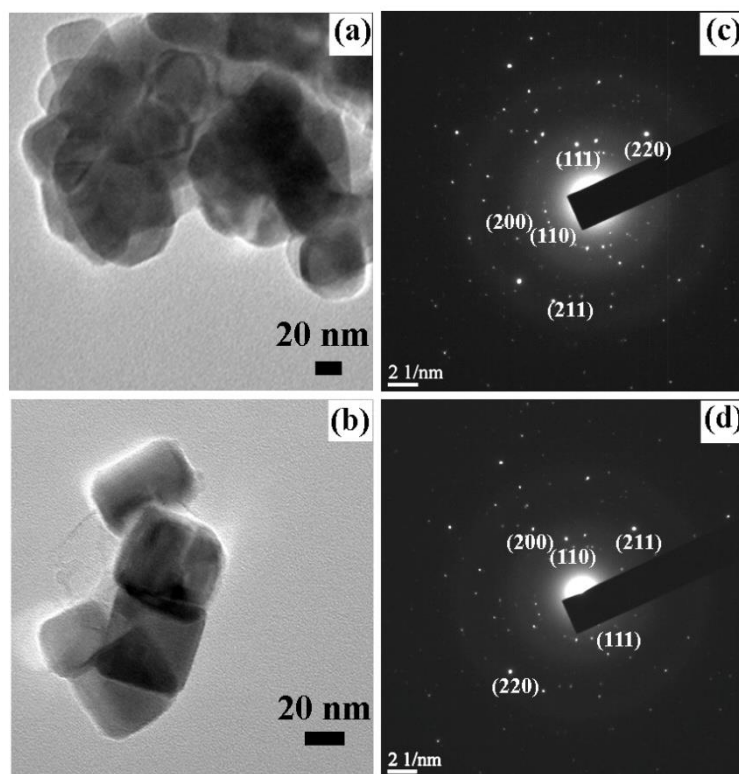


Fig. 6.3. HRTEM images of (a) BV0, (b) BV3 and SAED pattern of (c) BV0, (d) BV3

6.2(a, b) that samples grew smaller after V doping, which agrees well with our prediction from XRD analysis. The grain sizes of the pure sample were found to be ~ 52 nm which changed to ~ 38 nm for BV3 sample. The selected area electron diffraction (SAED) patterns showed in **Figure 6.2(c, d)** reveal the presence of different crystalline planes and are in full agreement with our XRD result.

6.3.3. Compositional studies

The energy dispersive X-ray (EDX) spectra of BV0, BV3 and BV5 including corresponding elemental mapping is presented in **Figure 6.3**. Presence of all the constituent elements can be confirmed from the elemental mappings. Proper uniformity in the distribution of constituent

elements Ba, Sn and O was found in all samples and vanadium was also found to be uniformly distributed over the entire samples (BV3 and BV5). Uniform distribution of the dopant ensured proper charge transfer of the entire amount of the synthesized samples. Chemical compositions of the samples were further studied via X-Ray photoelectron spectroscopy (XPS). The results obtained for BV3 are depicted in **Figure 6.4**. It can be seen that all the samples showed their characteristic peaks at appropriate positions. Ba 3d peaks were obtained at 794.1eV and 778.8eV indicating Ba^{2+} state and Sn 3d peaks were observed at 494.2eV and 485.6eV indicating Sn^{4+} valance state, as expected in BaSnO_3 .³⁵ O 1s peak was observed around 530eV which was further deconvoluted into two constituent sub-peaks at 528.9eV and 530.1eV.

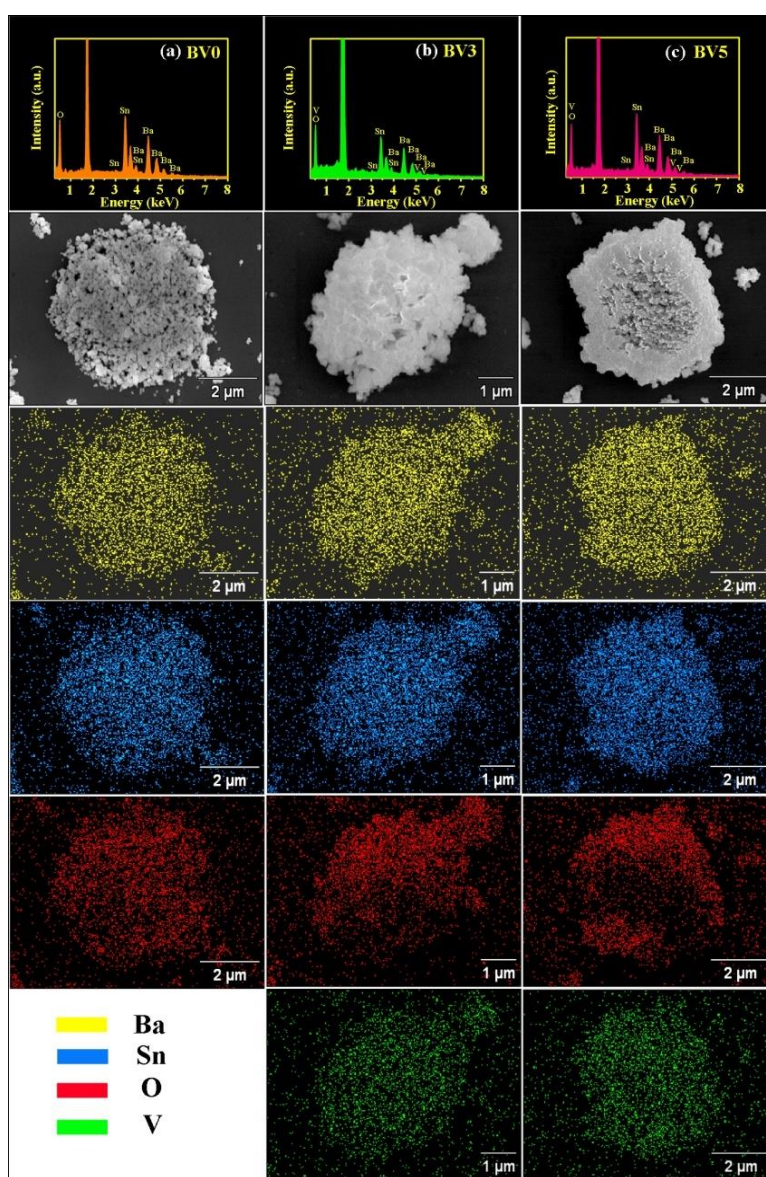


Fig. 6.3. EDX spectra for sample (a) BV0 (b) BV3 and (c)BV5; FESEM top view and corresponding elemental distribution of Ba, Sn, O and V in sample BV0 (left column), BV3 (middle column) and BV5 (right column)

The peak centered at 528.9 eV was assigned to the lattice oxygen of BaSnO₃ and the peak at 530.1 eV was identified to arise because of surface absorbed water.³⁶ The dopant, vanadium was detected by its characteristic peak at 518.4 eV corresponds to V 2p. The valance state of vanadium was identified as V⁵⁺, likely to replace Sn⁴⁺ ions.³⁷

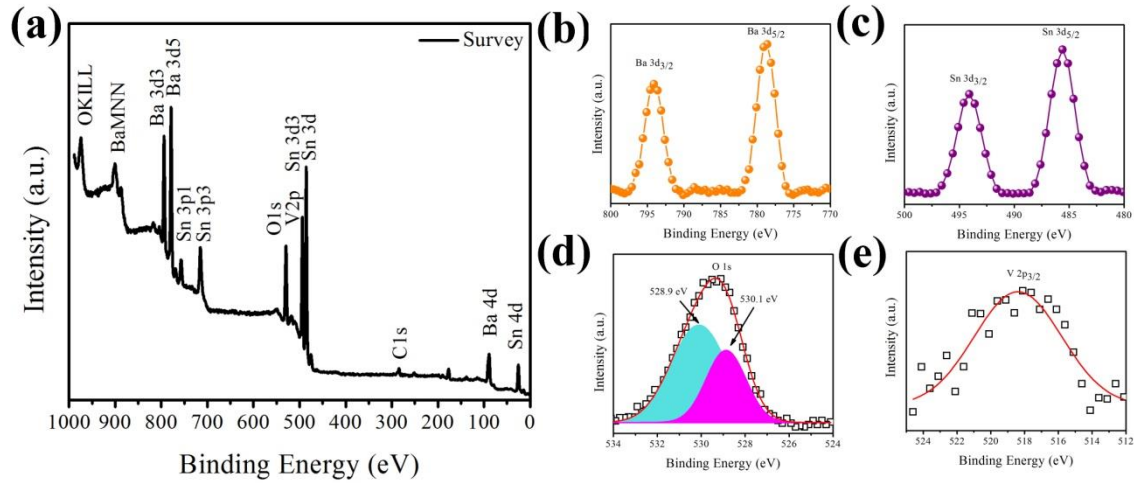


Fig. 6.4. XPS spectra of (a) Survey, (b) Ba 3d, (c) Sn 3d, (d) O 1s and (e) V 2p for BV3

6.3.4. Dielectric constant and resistivity analysis

BaSnO₃ is a well-established dielectric material and its electrical behavior was varied appreciably with vanadium doping. Frequency dependent variation of the real part of dielectric constant is presented in **Figure 6.5(a)** which indicates decrement of dielectric constant with vanadium doping. The dielectric constant vs. frequency graphs were fitted using Cole-Davidson relation.³⁸ The results can be explained considering the combined effects of size reduction and increased defects in the host system. As a consequence of vanadium doping, an appreciable number of defects were introduced into the host BaSnO₃ system which act as charged carrier scattering centres and thus the electrical properties are affected. Moreover, the effective dielectric constant is inversely proportional to the grain boundary thickness to grain size ratio.³⁹ Reduction in grain size in turn increased this ratio and hence the dielectric constant decreased with increasing vanadium content.

The Cole-Cole plots of the samples are also presented in **Figure 6.5(b)**. The centres of the suppressed semicircles are below the X-axis indicating the non-Debye type of relaxation occurring in the samples.

The DC resistivity (ρ) of the samples can be defined as

$$\rho = R \frac{t}{A} \quad (6.2)$$

Where, t and A are the thickness and the area of the pellet respectively and R is the resistance.⁴⁰⁻⁴¹ The resistances were determined by fitting the Cole-Cole plots using an ideal equivalent R-Q network, (via EC-Lab software program) where the constant phase element Q and capacitance C are related as

$$C = R^{\frac{(1-a)}{a}} Q^{\frac{1}{a}} \quad (6.3)$$

Where, a is the degree of deviation with respect to the value of pure capacitor.³¹

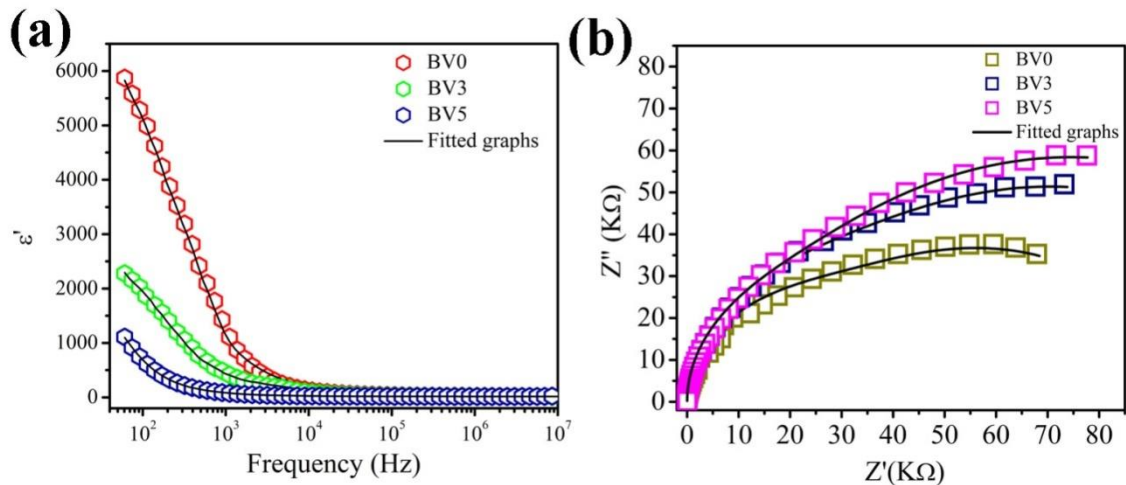


Fig. 6.5. (a) Frequency variation of the real part of dielectric constant for the samples $BaSn_{1-x}V_xO_3$ at RT; (b) Cole-Cole plots for $BaSn_{1-x}V_xO_3$ at RT. The solid lines indicate the best fit of the experimental graphs

The DC resistivity R was found to increase with V doping, which was accounted for the increased carrier scattering in boundaries of smaller grains.

6.3.5. ANSYS simulation studies

Observing appreciable variation of dielectric constant and resistivity with vanadium doping, scopes of cold electron emission studies by the samples were opened up. However, before performing actual FE experiments, theoretical simulation via ANSYS MAXWELL software was carried out. For this, 3D models of the samples were designed maintaining the dimensions as observed from morphological studies. Sample to collector distance was kept as per actual possible values, typically $180 \mu m$ in this case. The values of dielectric constant and DC conductivities were taken as determined from actual studies. Thus, a virtual replica of the actual field emission experiment was designed keeping the properties of samples, collector and ambient close to the original ones. An external electrical excitation of about $1.2 kV$ was applied virtually and the output electric field distribution was plotted in appropriate colour code. The results are presented in **Figure 6.6**. It can be seen that the magnitude of output

electric field enhanced appreciably at the proximity of the doped emitter compared to the pure ones. This is clearly reflected in increased area of higher field indicative colour near the emitter. The simulation indicated that the samples can exhibit higher output electric field after vanadium doping.

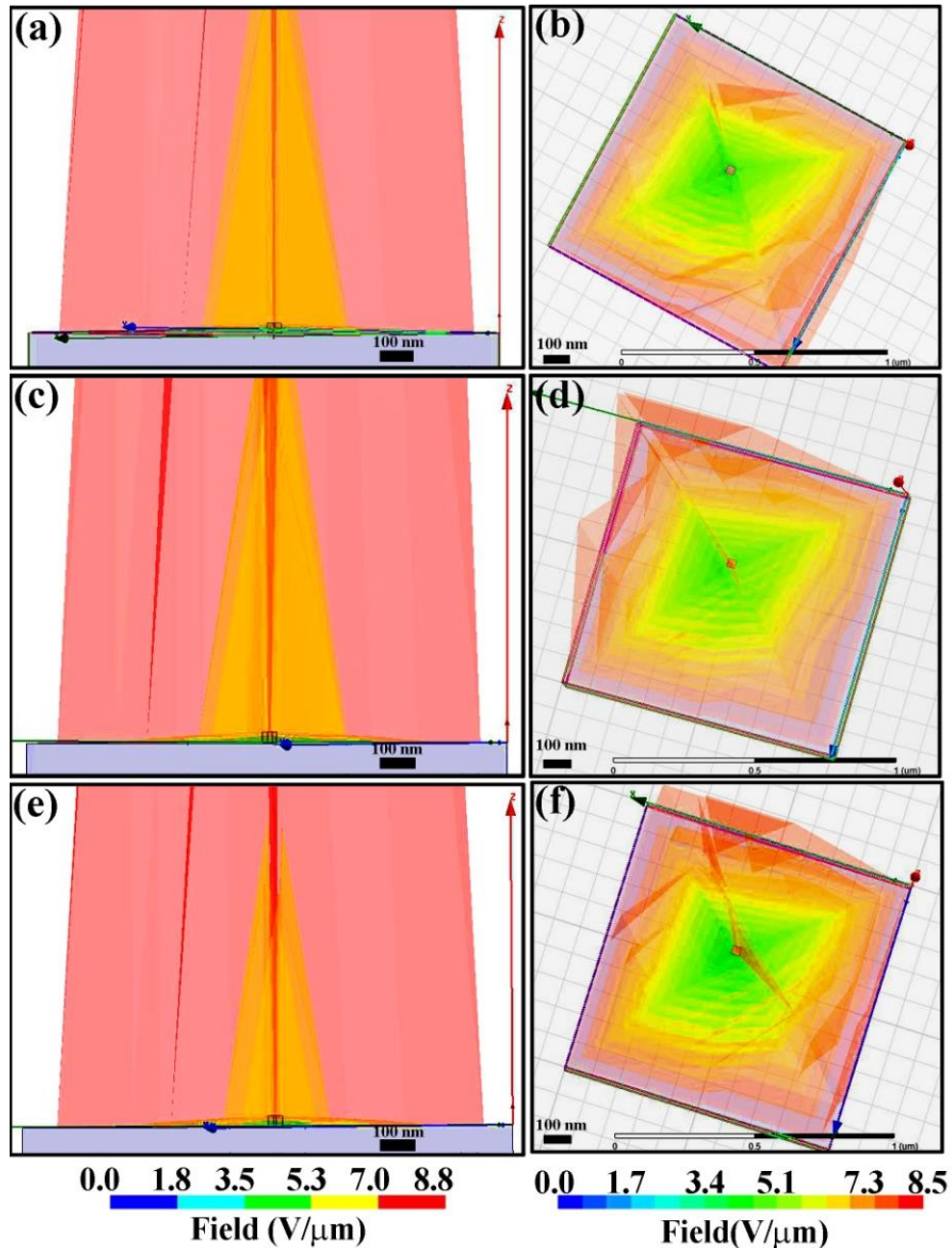


Fig. 6.6. ANSYS simulated field distribution for (a, c, e) side view of BV0, BV3, BV5 nanocubes and (b, d, f) top view of those samples respectively

This theoretical simulation also implies that the samples deserve thorough experimental investigation to find out their ability in emitting cold electrons by local enhancement of applied macroscopic field.

6.3.6. Density Functional Theory (DFT) studies for work function

Field emission performance of any sample is often quantified by its field enhancement factor. The enhancement factor is calculated using the value of work function. However, work function also depends upon the structure of the concerned material. Observing encouraging results from dielectric studies and especially from ANSYS simulation prediction, further investigation was performed via Density Functional Theory (DFT).

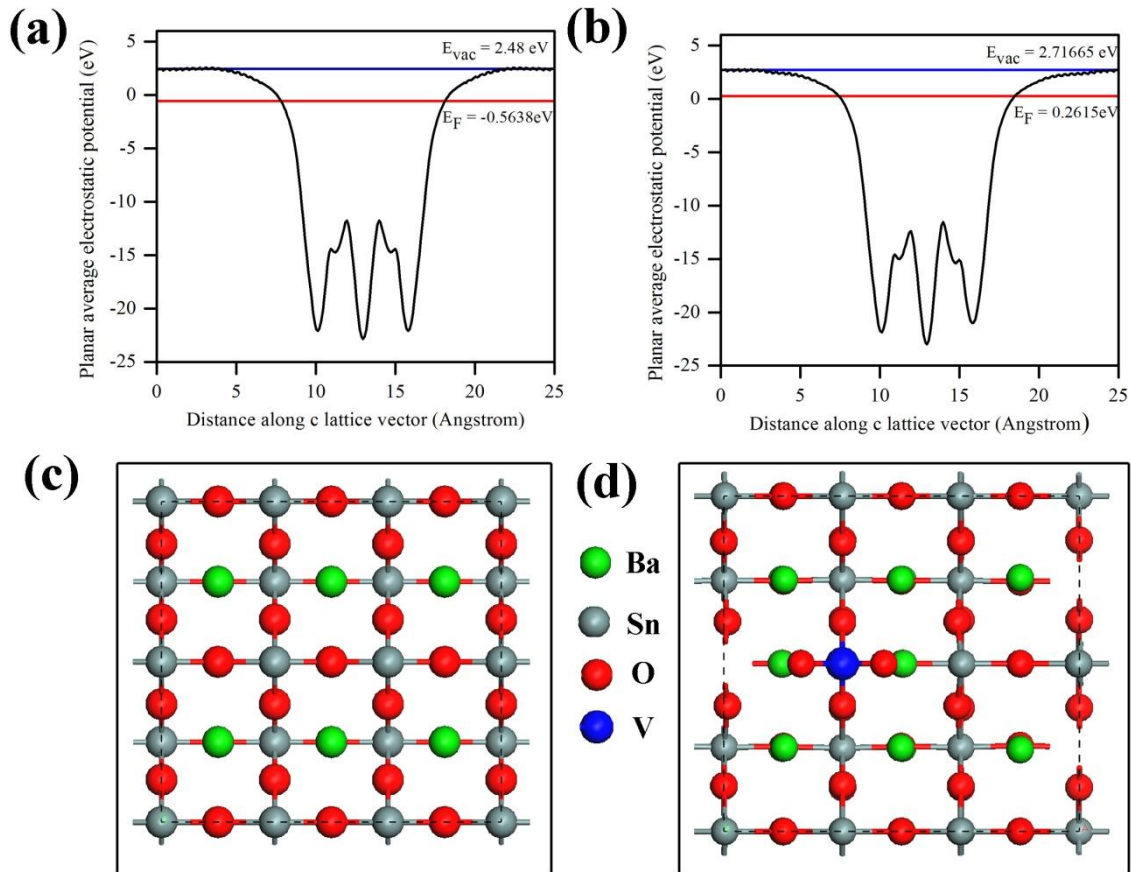


Fig. 6.7. Computational results showing the average potential profile of (a) BaSnO_3 , (b) V doped BaSnO_3 lattice; (c) and (d) are the (110) optimized surface for pure and doped samples respectively; obtained by DFT analysis

The first-principle calculations regarding this were performed using Vienna Ab initio Simulation Package (VASP) code which actually implements a supercell approach to DFT.⁴² Perdew–Burke–Ernzerh (PBE) functional within the generalized gradient approximation (GGA) was used to calculate the exchange-correlation term with the plane waves up to the energy cut-off 500.00 eV.⁴³ Brillouin zone integrations were done within the Monkhorst Pack scheme employing $2 \times 2 \times 1$ Γ -mesh. The system was allowed to fully relax until the forces converged below 10^{−5} eV/atom, so that geometrical optimization is achieved.⁴⁴ The maximum force converged to a value less than 0.05 eVÅ^{−1} and the displacement was

restricted within 0.002 \AA . Along the c axis, a vacuum slab of length 20 \AA was used to ward off the spurious interaction with its own periodic image. The results are presented in **Figure 6.7**, where it can be seen that the work function of the pure sample was about 3.044 eV and that reduced to 2.455 eV after vanadium incorporation within the supercell. A reduction in work function was indicated by theoretical studies which can favor electron emission by the samples after vanadium doping.

6.3.7. Cold Cathode emission studies

6.3.7.1. Field emission behaviour analysis and Fowler-Nordheim (FN) plot

The field emission experiment was carried out in our laboratory made high vacuum field emission set up by using a diode configuration. In this configuration, the sample, pasted on conducting carbon tape was considered to be the cathode and a stainless-steel tip of conical shape with a 1.5 mm diameter was the working anode. Before the measurement, the chamber was evacuated at a base pressure of $\sim 10^{-7} \text{ mbar}$. The separation of tip to sample (d) was varied to a few hundred micrometers by a micrometer screw and the experiments were performed keeping the separation of $180 \text{ }\mu\text{m}$, $200 \text{ }\mu\text{m}$ and $250 \text{ }\mu\text{m}$. During the entire experiment, the sample and the tip were monitored through the chamber view port, which ensured that no discharge occurred during the emission process and hence the samples exhibited purely cold field emission of electrons.

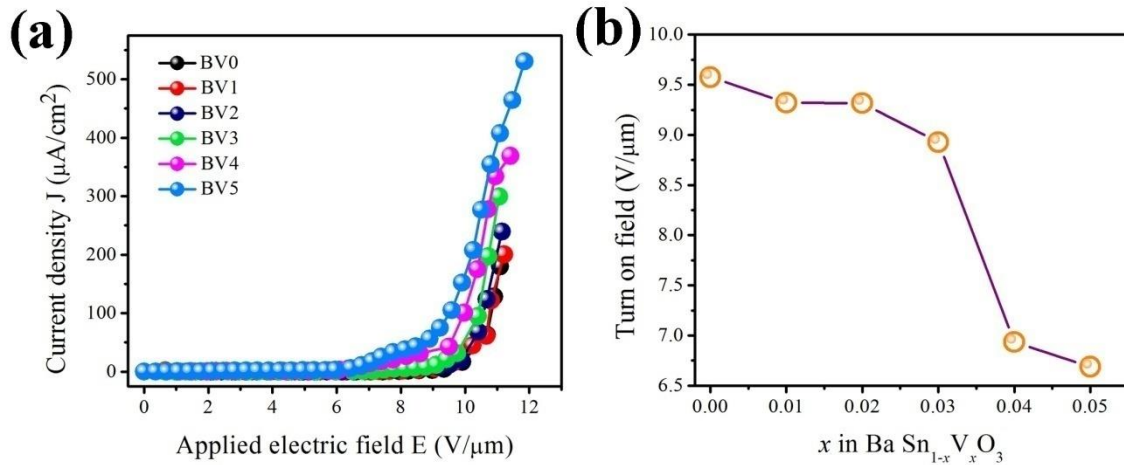


Fig. 6.8. (a) J - E characteristics of pure and V doped samples at $d = 200 \text{ }\mu\text{m}$, (b) plots of turn-on field vs. doping concentration

The current density vs. electric field plots are presented in **Figure 6.8(a)** where it can be seen that the perovskites exhibit excellent field emission current density, especially sample BV5 showed a very high emission current density of $\sim 530 \mu\text{A}/\text{cm}^2$. The highest current densities

gradually decreased with decreasing vanadium content and the pure sample registered emission current density of nearly $180 \mu\text{Acm}^{-2}$. The turn on field (defined at a current density of $10 \mu\text{Acm}^{-2}$) also varied with vanadium content and it was observed that the turn on field gradually decreased with increasing vanadium doping concentration (**Figure 6.8(b)**).

This variation in FE performance of different samples can be explained considering two important factors, *i.e.*, grain size of the emitters and increasing defect states in electronic band structures. As already observed in XRD and HRTEM studies, the samples show a considerable decrease in grain dimension due to vanadium doping. This indeed decreased the emitter dimension and effective number of emission sites are increased due to this. Moreover, after higher doping, intermediate states also emit electrons leading to enhanced emission current density. As a result, higher current density and low turn on field was obtained for sample BV5 compared to samples with lower vanadium concentration and sample BV0.

A better understanding about the cold emission process can be achieved from Fowler–Nordheim (F-N) analysis. The macroscopic field is calculated from the external voltage applied (V) per unit electrode spacing (d).

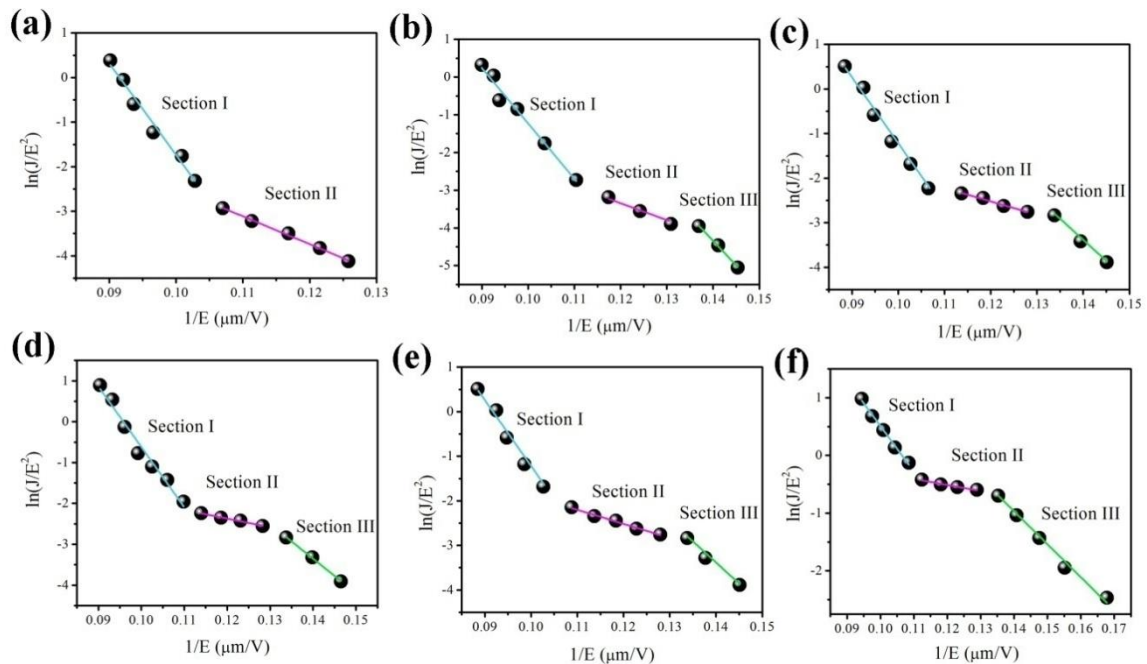


Fig. 6.9. F-N plots for (a) BV0, (b) BV1, (c) BV2, (d) BV3, (e) BV4 and (f) BV5 at $d = 200 \mu\text{m}$

Theoretically, the emission current I is related to the macroscopic electric field E by

$$I = Aa\phi^{-1}(\beta E)^2 \exp\left(\frac{b\phi_2^3}{\beta E}\right) \quad (6.4)$$

Where, ϕ is the local work function, the field enhancement factor is β , A the effective emission area, values of Fowler-Nordheim constants are $a = 1.54 \times 10^{-6} \text{ AeV}^2$ and $b = 6.83 \times 10^3 \text{ eV}^{-3/2} \text{ V}\mu\text{m}^{-1}$.⁴⁵ The F-N plots of the BV samples are presented in **Figure 6.9**. The straight-line nature and negative slopes of the F-N plots suggest that the electrons are emitted by cold field emission process. The local field enhancement factors were determined using the relation

$$\beta = -\frac{b\phi^{\frac{3}{2}}}{m} \quad (6.5)$$

Where, ϕ is the work function of the samples, m is the slope of $\ln(J/E^2)$ vs. $1/E$ plot. The value of work functions was taken as observed from DFT studies and the calculated values of field enhancement factors are presented in **Table 6.1**.

However, careful observation reveals that there is a two-section F-N slope for BV0 whereas the doped samples showed three-section F-N slopes. Presence of multiple straight linear sections in F-N slopes is often correlated with presence of internal defects and space charges. Moreover, those factors may not have equal contributions.⁴⁶ Dyke *et. al.* suggested that space charges play an important role at strong field (near low value of $1/E$) when inter-atomic spacing of the emitters become comparable to barrier potential.⁴⁷

Table 6.1. Comparative values of field enhancement factor (β) corresponding to various section

Work function (eV)		β values for		
		Section I	Section II	Section III
3.044	BV0	176	580	–
2.455	BV1	176	587	260
2.455	BV2	178	875	278
2.455	BV3	178	1238	312
2.455	BV4	290	1564	423
2.455	BV5	332	2505	459

These space charges may be contributed from ionization of trace amount of residual gases near the inter-electrode gap, ionization of desorbed gases from the anode or electrons emitted from the surface of emitters.

In the low field region, emitters cannot achieve sufficient electrical excitation to emit a high number of electrons. Moreover, applied low field is also unable to induce any space-charge by ionization at the proximity of the electrodes and thus a stiffer section of F-N slope (and low value of enhancement factor) was observed at section III of BV1- BV5.

At the section II, comparatively higher value of applied macroscopic field is able to extract electrons from edges of small emitter grains and also from doping induced levels. Additionally, increased applied field is also able to excite a high number of ionization induced charges. This enables enhancement of local field represented by comparatively flatter F-N slope and large enhancement factors. This section was observed for all the samples.

At section I, which is a high field region, should contain both space charge induced electrons and electrons originated from the emitters. Even in case of less active emitters, like BV0, signature of space charge induced emission should be reflected in the F-N plot. This was clearly reflected in the experimental results depicted in **Figure 6.9** where section I is also present for all samples. However, a more interesting fact is reflected in the variation of enhancement factors for section II and section I. For all the samples, field enhancement factor decreased in the highest field region (section I) compared to its value at section II. Activation of too many emission sites and presence of a large number of electrons near the anode effectively cause appreciable screening effects which lead to inferior enhancement of local field in section I.

6.3.7.2. Effect of inter-electrode separation for optimum device configuration

The effect of electrode separation is another important parameter for an efficient cold emitter. The samples presented here were tested keeping the electrode separations at 180 μm and 200 μm . The results are presented in **Figure 6.10**.

It can be clearly seen that the emission current density increases at higher electrode separation. As the electrode separation becomes higher, the anode can actually cover a larger surface area of the cathode which includes higher number of emitters as depicted in **Figure 6.11(a)**. This in turn increases the effective emission current density at higher inter electrode separation. However, the sample BV5, showing highest emission current density was

subjected to further increment of electrode separation of 250 μm (**Figure 6.11(b)**). At this stage, the emission current density was found to decrease. This happened due to the fact that placing the collector (anode) at very large distances may cause too high value of the barrier potential so that emitted electrons fail to tunnel through it. This cause lower current density at the anode.⁴⁸

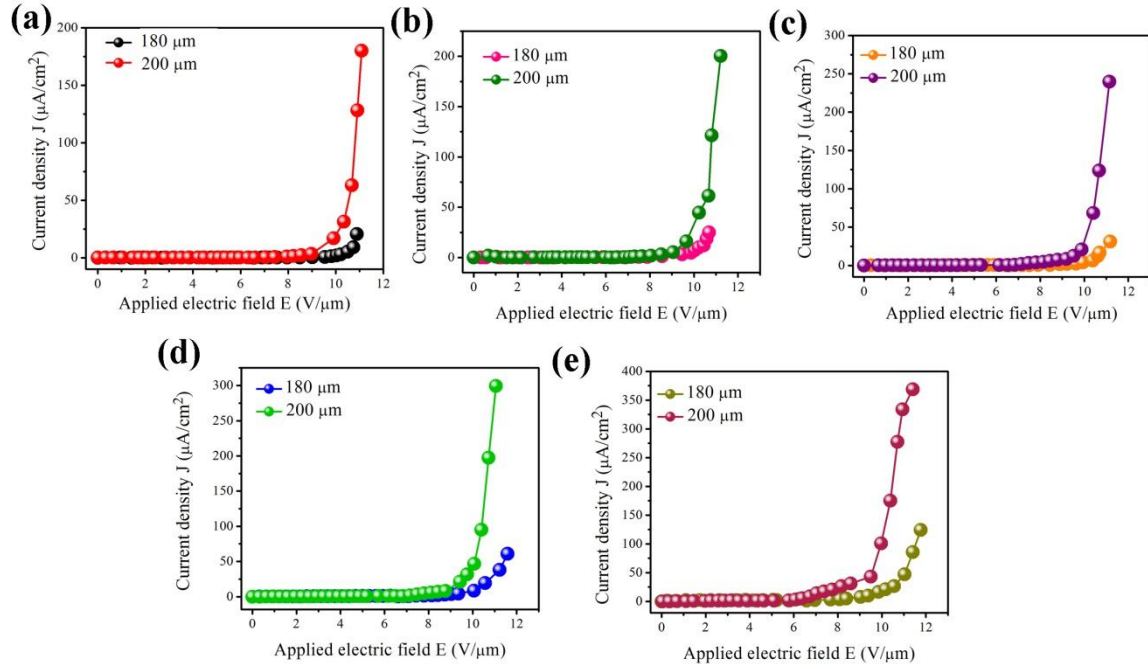


Fig. 6.10. *J-E characteristics of (a) BV0, (b) BV1, (c) BV2, (d) BV3 and (e) BV4 for various inter-electrode distances*

In addition to the inter-electrode distance variation, the stability of emission current is also an important factor in view of the application of any potential cold cathode into any sophisticated electronic instrument.

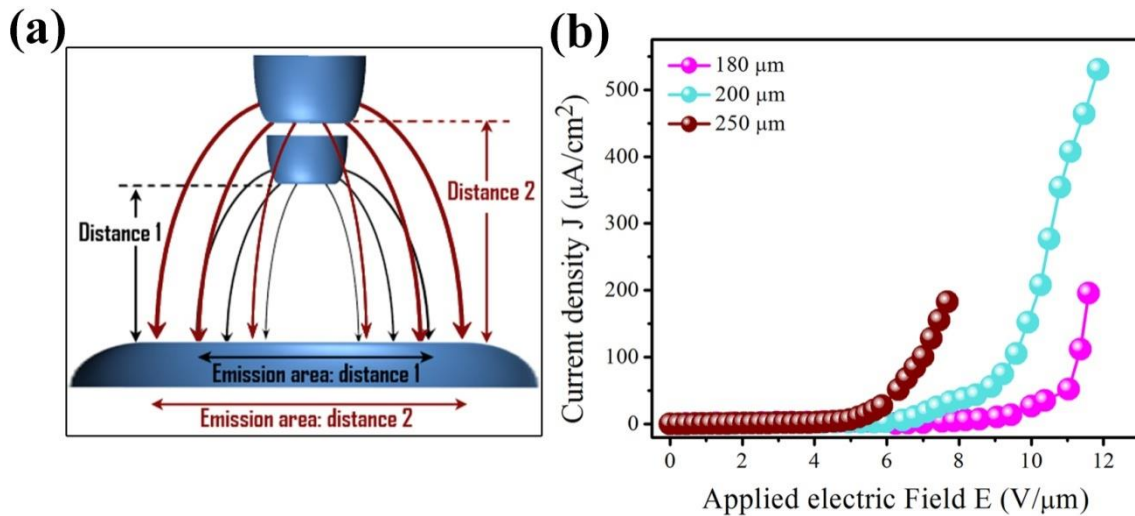


Fig. 6.11. (a) a schematic diagram of the effect of inter-electrode distance variation on effective emission area; J-E characteristics of (b) BV5 for various distances

In order to introduce BaSnO₃: V perovskites as potential future cold cathodes, their stability test was also performed keeping the excitation at $9\text{ V}\mu\text{m}^{-1}$ for 1h. The samples showing distinct and appreciable variation of FE parameters, *i.e.*, BV0, BV3 and BV5 were tested for current stability. The results are presented in **Figure 6.12**.

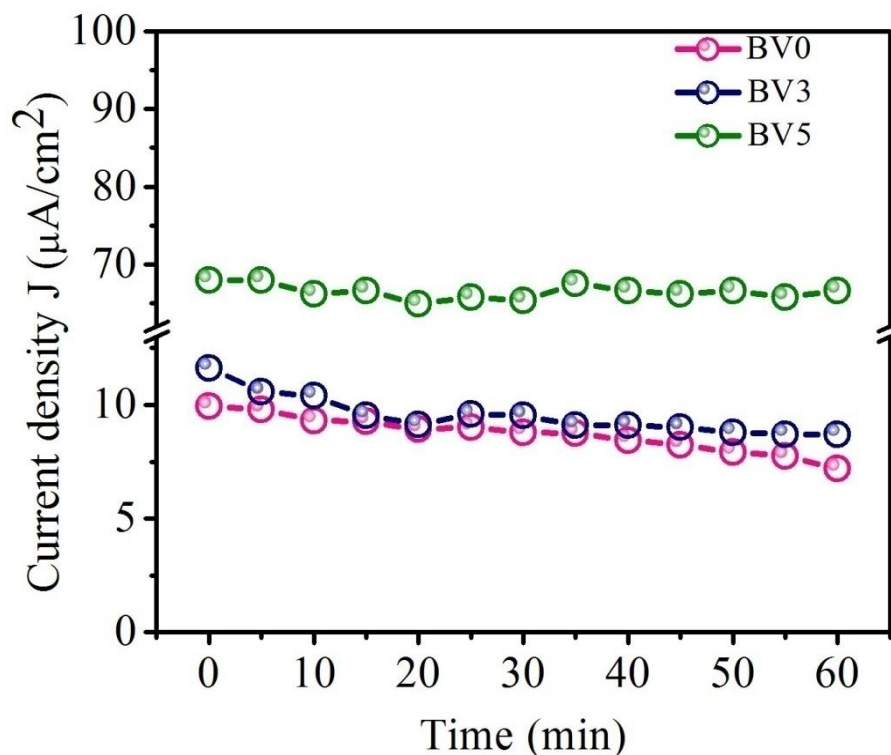


Fig. 6.12. Temporal FE current stability profile at $d = 200\ \mu\text{m}$ and $E = 9\ \text{V}\mu\text{m}^{-1}$ for BV nanocubes

It can be seen that all samples showed appreciable stability in view of emission current density. Interestingly, sample BV5 showed slightly better performance in emitting stable current than BV3 and BV0. Inclusion of higher number of emitters caused due to decreased grain size and presence of intermediate electronic energy levels due to high doping may be accounted for this enhancement of stability. Through those above-mentioned sections, it was established that novel BaSnO₃: V perovskite system can offer an important addition to the traditional cold emitter semiconductors. Moreover, in view of other important uses of this particular perovskite, this work opens up a new identity of multipurpose applications of BaSnO₃.

6.4. Conclusion

Pure and vanadium doped BaSnO₃ nanocubes were synthesized via easy solid-state reaction method. Thorough characterizations with XRD, FESEM, HRTEM and EDX confirmed proper phase, cube like morphology and chemical composition. Vanadium doping was

confirmed via XPS studies. Dielectric studies showed that the dielectric constant gradually decreased with vanadium doping, which was correlated to the effect of dimension reduction and the occurrence of defect states. Inspired by dielectric results, theoretical investigations using ANSYS MAXWELL and DFT software were carried out to predict whether the samples are capable of emitting cold electrons and to find out the variation of work function with doping. Obtaining positive outcomes from theoretical studies, actual field emission experiments were carried out which showed that the samples could exhibit lower turn on field and emission current density as high as $\sim 530 \mu\text{A cm}^{-2}$ after vanadium doping. This turns out to be an enhancement of 4.3 times (at most effective zone, section II) with respect to the pristine sample, whereas the turn on field was reduced by 30%. The results were accounted for the size reduction and the effect of defect states in the doped samples. This work opened up a new sector of application of traditional perovskites like BaSnO_3 as cold cathodes beyond their classic use.

6.5. References

1. P. Bharathi, S. Harish, J. Archana, M. Navaneethan, S. Ponnusamy, C. Muthamizhchelvan, M. Shimomura and Y. Hayakawa, *Applied Surface Science*, 484 (2019) 884–891
2. K. H. Al-Mayalee, N. Saadi, E. Badradeen, F. Watanabe and T. Karabacak, *Journal of Physical Chemistry C*, 122 (2018) 23312–23320
3. J. Huang, Z. Yin and Q. Zheng, *Energy and Environmental Science*, 4 (2011) 3861–3877
4. H. Yu, J. Ma, Y. Zhang, X. Zhang and W. Shi, *Electrochimica Acta*, 56 (2011) 6498–6502
5. A. Bera, K. Wu, A. Sheikh, E. Alarousu, O. F. Mohammed and T. Wu, *Journal of Physical Chemistry C*, 118 (2014) 28494–28501
6. B. Das, A. Renaud, A. M. Volosin, L. Yu, N. Newman and D.-K. Seo, *Inorganic chemistry*, 54 (2015) 1100–1108
7. L. Zhu, J. Ye, X. Zhang, H. Zheng, G. Liu, X. Pan, and S. Dai, *Journal of Physical Chemistry A*, 5 (2017) 3675–3682
8. A. A. Kumar, A. Kumar and J. K. Quamara, *Solid State Communications*, 269 (2018) 6–10
9. S. Rani, N. Ahlawat, K. M. Sangwan, R. Punia and A. Kumar, *Journal of Alloys and Compounds*, 769 (2018) 1102–1112

10. Y. K. V. Reddy and D. Merge, *Physica B*, 391 (2007) 212–221
11. A. Sahmi, R. Laib, S. Omeiri, K. Bensadok, M. Trari, *Journal of Photochemistry and Photobiology A*, 364 (2018) 443–448
12. S. Omeiri, B. Hadjarab, A. Bouguelia and M. Trari, *Journal of Alloys and Compounds*, 505 (2010) 592–597
13. K. Balamurugan, N. H. Kumar, J. A. Chelvane and P.N. Santhosh, *Journal of Alloys and Compounds*, 472 (2009)9–12
14. R. B. Kamble, N. Tanty, A. Patra and V. Prasad, *Applied Physics Letters*, 109 (2016) 083102
15. H. J. Jeong , H. D. Jeong , H. Y. Kim , J. S. Kim , S. Y. Jeong , J. T. Han , D. S. Bang , and G. W. Lee, *Advanced Functional Materials*, 21 (2011) 1526–1532
16. C. K. Huang, H. L. Andrews, R. C. Baker, R. L. Fleming, D. Kim, T. J. T. Kwan, A. Piryatinski, V. Pavlenko and E. I. Simakov, *Journal of Applied Physics*, 125 (2019) 164501
17. D. R. Whaley, B.M. Gannon, C. R. Smith, C. M. Armstrong and C. A. Spindt, *IEEE Transactions on Plasma Science*, 28 (2000) 727-747
18. F. Giubileo, A. Di Bartolomeo, L. Iemmo, G. Luongo and F. Urban, *Applied Sciences*, 8 (2018) 526
19. N. De Jonge, Y. Lamy, K. Schoots, T. H. Oosterkamp, *Nature*, 420 (2002) 393-395
20. L. L. Wang, C. Z. Zhao, L. P. Kang, H. C. Zhao, S. P Hao, Y. K. Zhang, Z. P. Chen and X. J. Li, *Applied Surface Science*, 384 (2016) 530-533
21. A. P. S. Gaur, S. Sahoo, F. Mendoza, A. M. Rivera, M. Kumar, S. P. Dash, G. Morell, and R. S. Katiyar, *Applied Physics Letters*, 108 (2016) 043103
22. H. J. Bian, X. F. Chen, J. S. Pan, W. Zhu and C. Q. Sun, *Applied Surface Science*, 255 (2009) 4867–4872
23. G. S. Borchorov and A. V. Eletskii, *Nanomaterials –Basel*, 3 (2013) 393-442.
24. N. Besra, S. Pal, B. K. Das and K. K. Chattopadhyay, *Physical Chemistry Chemical Physics*,19 (2017) 26708-26717
25. T. Paul, S. Maiti, N. Besra, B. K. Chatterjee, B. K. Das, S. Thakur, S. Sarkar, N. S. Das and K. K. Chattopadhyay, *ACS Applied Nano Materials*, 2 (2019) 5942–5951
26. H. Mizoguchi, P. Chen, P. Boolchand, V. Ksenofontov, C. Felser, P. W. Barnes and P. M. Woodward, *Chemistry of Materials*, 25 (2013) 3858-66
27. P. Singh, B. J. Brandenburg, C. P. Sebastian, P. Singh, S. Singh, D. Kumar and O. Parkash, *Japanese Journal of Applied Physics*, 47 (2008)3540–3545

28. Q. Li, M. Li, C. Wang, M. Zhang and H. Fan, *Ceramic International*, 45 (2019) 19822–19828
29. H. Çolak and O. Türkoğlu, *Journal of Mater Science: Materials in Electronics*, 23 (2012) 1750-1758
30. K. Dewangan, N. N. Sinha, P. G. Chavan, P. K. Sharma, A. C Pandey, M. A More, D. S. Joag, N. Munichandraiah, N. S. Gajbhiye, *Nanoscale*. 4 (2012) 645-651
31. S. Pal, N. S. Das, S. Bhattacharjee, S. Mukhopadhyay and K. K. Chattopadhyay, *Materials Research Express*, 6 (2019) 105029
32. V. V. Zhirnov, G. J. Wojak, W. B. Choi, J. J. Cuomo and J. J. Hren, *Journal of Vacuum Science and Technology A*, 15 (1997) 1733
33. T. Alammari, I.I. Slowing, J. Anderegg and A. V. Mudring, *Chem Sus Chem*, 10 (2017) 1-16
34. N. Aini, R. Ningsih, D. Maulina, F. F. Lami and S. N. Chasanah, *Material Science and Engineering*, 333 (2018) 012020
35. S. V. Manorama, C.V. Gopal Reddy and V. J. Rao, *Applied Surface Science*, 174 (2001) 93-105
36. B. C. Luo, J. Zhang, J. Wang and P. X. Ran, *Ceramic International*, 41 (2015) 2668–2672
37. C. Regmi, D. Dhakal and S. W. Lee, *Nanotechnology*, 29 (2018) 064001
38. C. Zhao, C. Z. Zhao, M. Werner, S. Taylor and P. Chalker, *Nanoscale Research Letters*, 8 (2013) 456
39. L. Marchin, S. Guillemet-Fritsch and B. Durand, *Journal of American Ceramic Society*, 91 (2008) 485–489
40. U. Mohan, P. Gogoi and S.K. Baruah, *Oriental Journal of Chemistry*, 32 (2016) 1003-1014
41. S. Lanfredi and A. C. M. Rodrigues, *Journal of Applied Physics*, 86 (1999) 2215-2219
42. G. Kresse, J. Furthmuller, and J. Hafner, *Physical Reviews B*, 47 (1993) 558
43. J. P. Perdew, K. Burke and M. Ernzerhof, *Physical Review Letters*, 77 (1996) 3865-3868
44. M. D. Segall, P. J. D. Lindan, M. J. Probert, C. J. Pickard, P. J. Hasnip, S. J. Clark and M. C. Payne, *Journal of Physics: Condensed Matter*, 14 (2002) 2717–2744
45. R.H. Fowler and L. Nordheim, *Proceedings of the Royal Society London A*, 119(1928)173–181

- 46.** S. Santra, N. S. Das, D. Sen and K. K. Chattopadhyay, Journal of Physics D, 47 (2014) 505301
- 47.** W. P. Dyke and J. K. Trolan, Physical Review, 89 (1953)799
- 48.** S. Maity, N. S. Das, S. Santra, D. Sen and K. K. Chattopadhyay, Current Applied Physics, 16(2016) 1293-1302

Enhanced electrical properties
of BaSnO₃/PVDF
nanocomposite: Mechanical
energy harvesting

Abstract

BaSnO₃ (BSO) nanorods were synthesized using hydrothermal method followed by calcination and then BSO/PVDF composite films were fabricated following simple solution-drop casting technique. The formation of composite system was not only enhanced the level of crystallinity of the films but also converted the non-polar α phase to polar β phase. A maximum β phase was enhanced to 84% for the composite system. The compatibility of dielectric permittivity between two components of the composite system allowed forming highly flexible, visibly transparent films with high dielectric permittivity (26.71 at 100 Hz) and low loss (0.066 at 100Hz). The rodlike morphology of BSO helped to achieve the percolation threshold with smaller volume fraction of BSO and also prevented agglomeration into the system. The open circuit voltage and short circuit current for the composite system was found to be enhanced upto 7.3 and 4.6 times respectively.

7.1. Introduction

With rapid growth of power electronics, the perovskite oxides with high dielectric constant and low loss serve significant importance in various applications, such as sensors, energy storage devices, multilayered capacitors etc.¹⁻⁵ Although the perovskite ceramics exhibit high dielectric permittivity but the high brittleness and low breakdown strength impose limitations in practical applications. On the other hand, the polymers have high flexibility, superior durability, large breakdown strength but low dielectric permittivity. Thus, many efforts have been given to prepare such perovskite ceramic/polymer composite which possesses the best characteristics of both the components. So, the escalating need of highly flexible, visibly transparent, lead free perovskite/polymer composites with high dielectric constant, low loss and large breakdown strength have been explored in recent years.⁶ Several perovskite oxides like BaTiO₃, LaFeO₃, ZnSnO₃ etc. were already used for this purpose and showed good efficiency but they have their own limitations.⁷⁻⁹ For example, dielectric permittivity incompatibility, high cost, brittleness, phase instability etc. Among the well known perovskite ceramics, BaSnO₃ has drawn the our attention due to its low cost synthesis method, interesting electrical properties, visible light transparency (optical band gap ~ 3.1 eV), high thermal stability (>1000 °C), environment friendly nature etc.¹⁰⁻¹¹ Also, the electrical properties of BSO can easily be tuned via appropriate cation

doping, external DC bias variation etc.¹² The particle size of this material can be tailored simply by calcination temperature variation, which has a significant role in formation of a agglomeration free composite system.¹³ Then again, polyvinylidene fluoride (PVDF) is the mostly studied piezoelectric semicrystalline polymer because of its easy formation, high dielectric permittivity (in comparison to other polymers), high thermal stability.¹⁴⁻¹⁵ Even though the polymer has been used in many contemporary electronic applications, including flexible pressure sensors, portable electronics, and energy storage systems, the raw PVDF has poor electrical properties that must be improved for practical applications.¹⁶ The piezoelectricity of PVDF mostly comes from the polar crystalline β and γ phase, rather than the non-polar α phase. The electroactive β phase is mainly responsible for the piezoelectric behavior of the polymer exhibiting maximum dipole moment per unit volume.¹⁷⁻²¹ Therefore, it is necessary to convert α phase (trans-gauche conformation TGTG) to β (all trans planar TTTT conformation) for achieving optimum polarization effect. Thus, the aim is to form BSO/PVDF composite to improve electrical and mechanical properties of the hybrid system. This work represents two stage procedures, firstly, the synthesis of BSO nanorods by hydrothermal treatment followed by calcination at 500 °C and secondly, fabricating BSO/PVDF composite films using solution-casting approach. The hybrid films not only became enriched with electroactive β phase but also exhibited optical eminence. In addition, the dielectric permittivities as well as conductivity for the hybrid samples were increased with BSO content and the loss was found to be low for all the samples. The high aspect ratio of BSO nanorods may be responsible for the enhanced interfacial polarization between the surface charges of BSO and the polymer.²² Also, this may be the reason for less agglomeration in the composite system, resulting in low loss. The open circuit voltage and short circuit current were enhanced significantly for the hybrid samples due to the increment in polarization and conductivity respectively. In this work for the first time, the improvement of electrical properties of BSO/PVDF nanocomposite films was analyzed and the output performances of the devices were demonstrated. In short, this work provides a comprehensive guideline for improving perovskite ceramic/polymer nanocomposites with high permittivity and low loss.

7.2. Methods & enumeration

7.2.1. Materials

Barium chloride dihydrate ($\text{BaCl}_2 \cdot 2\text{H}_2\text{O}$) (Sigma Aldrich), Stannic chloride pentahydrate ($\text{SnCl}_4 \cdot 5\text{H}_2\text{O}$) (Loba Chemie), Citric acid monohydrate ($\text{C}_6\text{H}_8\text{O}_7 \cdot \text{H}_2\text{O}$) (Merck), Hydrogen peroxide (Merck), Ammonia solution 25% (Merck), PVDF ($M_w \approx 275,000$ gm. /mol, Sigma-Aldrich, USA), Acetone (Merck), N, N-Dimethylformamide (Merck). Absolute ethanol and deionized water were also used to wash the sample.

7.2.2. BaSnO_3 nanorod synthesis

BaSnO_3 (BSO) nanorods were synthesized via hydrothermal reaction followed by calcination. Stoichiometric amount of $\text{BaCl}_2 \cdot 2\text{H}_2\text{O}$ and $\text{SnCl}_4 \cdot 5\text{H}_2\text{O}$ were dissolved into 50 ml deionized water under constant stirring at room temperature. Additionally, appropriate of aqueous NaOH solution was poured drop by drop into the precursor solution under vigorous stirring until the pH turned ~ 12 . The solution was stirred for 1 h continuously to get a white homogeneous solution. Then, the solution was transferred into 100 ml teflon-lined stainless steel autoclave and kept at 150°C for 24 h. The solution was allowed to cool down naturally and then washed with deionized water and ethanol until the pH becomes neutral. After drying the precipitate at 80°C in vacuum oven, the white powder was calcined at 500°C for 4 h to obtain phase pure BSO.

7.2.3. PVDF film fabrication

1.5 gm commercial PVDF pellets were allowed to dissolve into a mixture solution of 12 ml acetone and 8 ml acetone under vigorous stirring at 70°C for 2 h. A transparent homogeneous solution with proper concentration was then carefully transferred onto pre-cleaned glass slides to form self-poled uniform layers which were kept at 60°C in vacuum oven overnight without disturbing. After natural cooling down to room temperature, the films were peeled off from the glass slides and used further for analysis.

7.2.4. BSO/PVDF composite film fabrication

Appropriate amount of BaSnO₃ powder sample was added to the solution of PVDF at the time of stirring. According to the concentration of BSO the hybrid films are labelled as PBS0, PBS1, PBS2, PBS3 and PBS4 respectively.

7.2.5. Experimental techniques

The X-Ray diffraction data of BSO and composites were acquired using XRD, BRUKER D8 Advance spectrophotometer with CuK_α ($\lambda = 1.5406\text{\AA}$) radiation with a scan rate of 0.05 min^{-1} . A field emission scanning electron microscope (FEI INSPECT F50, Netherlands) was used to explore the morphology of the samples. To determine the band gap and optical transparency of the bare and composites a Jasco V670 spectrophotometer was employed. The elemental distributions over bare and composite samples were collected using the energy dispersive X-Ray spectroscopy attachment with the FESEM. Fourier transform infrared spectroscopy was carried out by Shimadzu FTIR spectrometer, IR prestige. An Agilent precision impedance analyzer with an operating range of 40 Hz–110 MHz was operated to record impedance spectra for electrical property analysis. A MIM (metal-insulator-metal) geometry was fabricated by depositing Ag electrodes on both sides of the films suitable for AC impedance analysis. Electroactive response of the as-prepared composite samples was studied using a KEYSIGHT InfiniiVision DSOX2012A digital storage oscilloscope.

7.3. Results and discussion

7.3.1. Structural analysis

The X-ray diffraction pattern of as-synthesized perovskite BSO was recorded in a range of 2θ between 20° to 80° is shown in **Figure 7.1(a)**. The presence of sharp peaks confirmed the crystalline phase formation. All the Bragg's peaks were indexed and matched with the JCPDS card no. 150780 for cubic BSO. Absence of any other extra peak confirmed the phase purity of the sample. The average crystallite size was calculated using well-known Scherrer's equation

$$D = \frac{0.9\lambda}{\beta \cos \theta} \quad (7.1)$$

Here D is the average crystallite size, λ is the incident wavelength of the source ($= 1.54 \text{ \AA}$ for $\text{CuK}\alpha$ source), β is the FWHM of the Bragg's diffraction peak (in radian) and θ is the angle of diffraction (in degree). Considering five intense peaks, the calculated value of mean crystallite size was 22 nm.

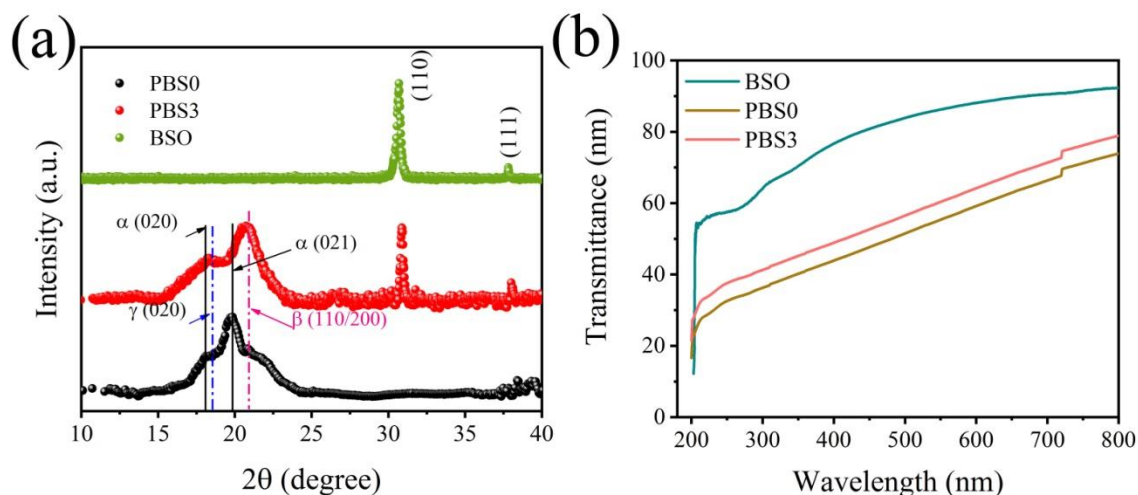


Fig. 7.1. (a) XRD pattern and (b) UV-Vis transmittance for the samples

The phase and crystallinity of BSO/PVDF nanocomposite were confirmed from the XRD pattern analysis; see **Figure 7.1(a)**. The bare PVDF was mainly consisted of the peaks assigned for non-polar α phase (17.99° , 19.90°) whereas, the electroactive β phase (20.28°) was found to increase for PBS3 composite due to formation of the composite. Also, the XRD peak at 30.7° and 37.8° in composite sample were attributed to BSO. Weak trace of γ phase (18.45°) of PVDF was also noted in bare and composite sample. Due to the formation of the perovskite/polymer composite system, the electroactive β phase was found to dominate over the non-polar α phase.

7.3.2. Optical property studies

The UV-Vis transmittance spectra for BSO, PBS0 and PBS3 are presented in **Figure 7.1(b)**. A high transmittance ($\sim 80\%$) in the visible range was found for BSO. PBS0 showed a transmittance of $\sim 50\%$ in the visible optical range which increases slightly for the composite sample PBS3.

7.3.3. Morphological studies

For morphological analysis of the perovskite/PVDF under concerned, FESEM was carried out.

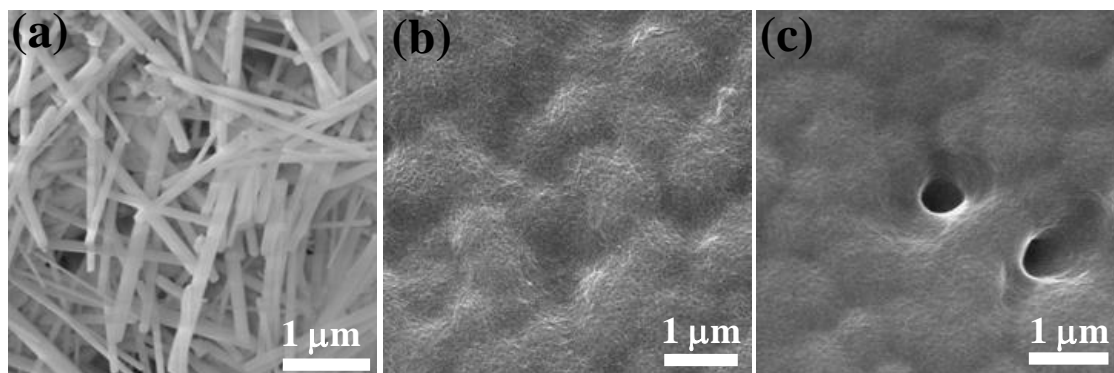


Fig. 7.2. FESEM images of (a) BSO, (b) PBS0 and (c) PBS3

Figure 7.2(a) illustrates that BSO nanorods have mean length of $\sim 2.5 \mu\text{m}$ with a mean diameter of $\sim 15 \text{ nm}$. Homogeneous growth of BSO crystals can be observed from the slight variation in the average diameter of the rods. The significantly smaller crystallite size calculated from the XRD pattern relative to the dimension obtained from the FESEM image denotes the polycrystalline nature of the sample. The surface morphology of PBS0 and PBS3 films are shown in **Figure 7.2(b)** and **(c)** respectively. Any rodlike morphology was not visible for the sample PBS3 because BSO particles may be concealed inside the polymer matrix at the time of composite formation. The rodlike morphology of the perovskite may promote the formation of all-trans configuration of the polymer with less volume fraction which also prevents agglomeration in the system.

7.3.4. Compositional analysis

Energy dispersive X-ray (EDX) analysis was conducted for compositional analysis. The EDX spectra in **Figure 7.3(a)** did not show any peak of Cl which rules out the possibility of presence of any chloride precursor in BSO. The EDX scan profile of PBS0 and PBS3 sample shown in **Figure 7.3(b,c)** indicate that all the constituent elements (C and F in PBS0) and (Ba, Sn, O, C and F in PBS3) were present over the inspected regions of respective samples. Uniform elemental distribution was further inferred from the elemental mapping of BSO, PBS0 and PBS3 as shown in **Figure 7.3(d-f)** which is another evidence of formation of BSO/PVDF composite.

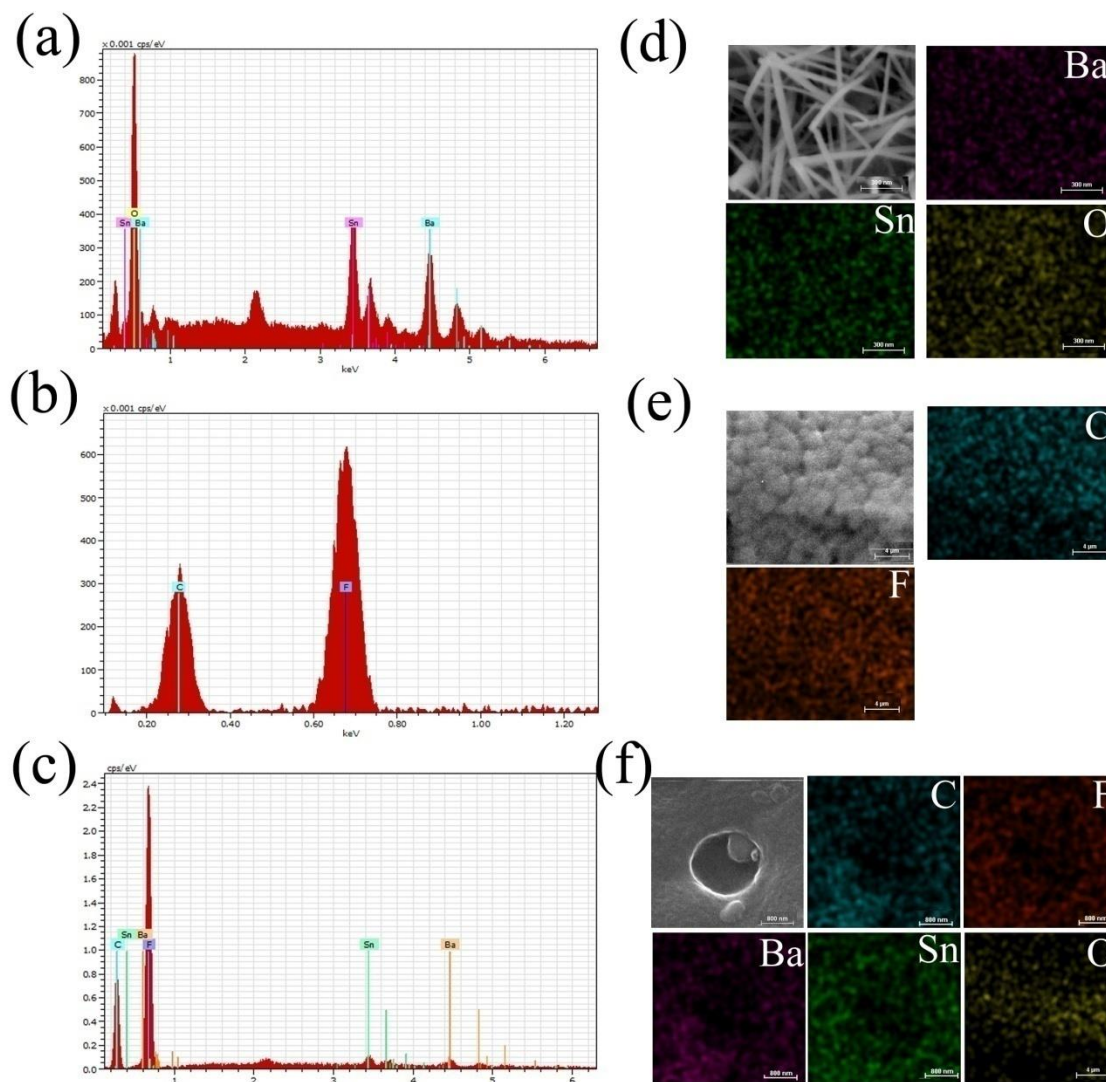


Fig. 7.3. EDX spectra of (a) BSO, (b) PBS0 and (c) PBS3; elemental mapping of (d) BSO, (e) PBS0 and (f) PBS3

7.3.5. FTIR analysis

Analysis of FTIR spectra for the composite sample is obvious for the assurance of the chemical attachment of BSO and PVDF. **Figure 7.4(a) and (c)** presents the room temperature FTIR spectra for all the films prepared collected under absorbance mode. The five distinct phases of PVDF (α , β , γ , δ and ϵ) can be determined from the carbon chain and the C-C bonds present in chemical configuration of PVDF.²⁰ The comparative spectra clearly delineates the orientation of PVDF chain was converted from TGTG to TTTT and partially to T3GT3G systematically due to

the formation of BSO/PVDF composites.^{24,25} The spectra from 1600-400 cm^{-1} is depicted in **Figure 7.4(a)** and the peaks for different crystalline phases are also indexed with different color. The absorption bands appeared at 532, 613, 764, 796, 976 and 1160 cm^{-1} are referred to the non-polar α phase whereas, the vibrational bands at 840 and 1279 cm^{-1} denotes the presence of highly polarized phase β . A very weak peak of semipolar γ phase was appeared at 812 cm^{-1} .^{26,27} It can be well observed from the comparative spectra that the peak intensity of nonpolar α phase was strongest for the PBS0 sample which starts to diminish with the composite formation and the peak at 840 cm^{-1} indicating polar β phase grew stronger for the composite samples with higher concentration of BSO. The result proves the enhancement of electroactive β phase of PVDF for the composite samples. The interfacial interaction between the molecular dipoles ($-\text{CH}_2$ or $-\text{CF}_2$) of poly-vinylidene chloride and the charges resides at the surface of BSO nanorods might be responsible to align the dipoles in a more ordered direction and thus to enhance the β phase. It is evident from the spectra that the peak intensity of γ phase (812 cm^{-1}) was also increased for the composite film.

Although the composite films showed enhancement of β and γ phase together, the β phase fraction was higher than γ phase fraction which is evident from the absorption band ratio of A_{1279}/A_{1234} .²⁸ The electroactive phase proportions for the films were calculated using the following equation

$$F_{EA} = \frac{A_{EA}}{\frac{K_{\alpha}}{K_{\beta}} A_{764} + A_{EA}} \quad (7.2)$$

Where, A denotes the area under the curve and the subscripts are used for the corresponding vibrational bands, K_{α} ($7.7 \times 10^4 \text{ cm}^2\text{mol}^{-1}$) and K_{β} ($6.1 \times 10^4 \text{ cm}^2\text{mol}^{-1}$) are the absorption coefficient for the absorption intensity at 764 cm^{-1} and 840 cm^{-1} respectively. The area under the curve for α and β phases were calculated for each curve separately and the quantitative value of electroactive phase (in %) for all the films are illustrated in **Figure 7.4(b)**. Initially, at lower concentration of BSO, the conversion of α to β phase was not reached to optimum level due to insufficient surface charge availability of BSO to interact with the molecular dipoles of PVDF. But for PBS3 sample, the interaction was sufficient to make maximum dipole aligned and thus the conversion of β phase from α phase was significant. The maximum value of F_{EA} was 84%

for PBS3 and then started to fall. Due to the over concentration of BSO nanorods, the agglomeration starts, which in turn boosts misalignment of PVDF dipoles.

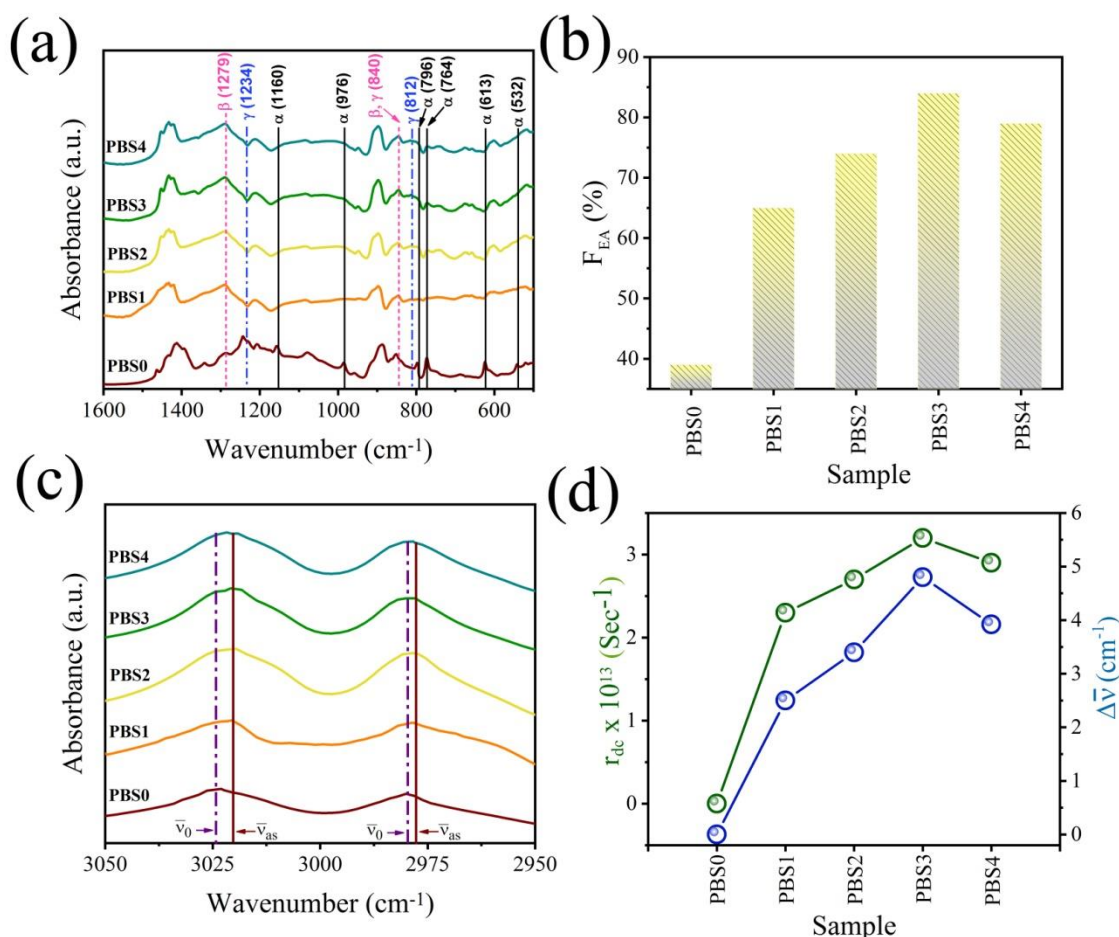


Fig. 7.4. (a) FTIR spectra of the samples in the range 500-1600 cm⁻¹, (b) variation of electroactive phase content for the samples, (c) FTIR spectra of the samples in the range 2950-3050 cm⁻¹, (d) r_{dc} and $\Delta\bar{\nu}$ values for the samples

The frequency shifting of vibrational bands in the range between 3050 cm⁻¹ and 2050 cm⁻¹ is illustrated in **Figure 7.4(c)**. This shifting of symmetric (ν_s) and antisymmetric (ν_{as}) stretching vibration bands in composite films portrays the interfacial interaction between BSO and PVDF.²⁹ The interfacial interaction further causes damping to the natural inherent vibration and makes the dipoles of PVDF lighter resulting a shift of bands towards lower frequency as compared to the bare one.^{28,20} For a better insight, the damping constant was calculated for the bare and composite films and the values for different concentration of BSO are shown in **Figure 7.4(d)**. To evaluate the damping constant (r_{dc}) the following relation was used.^{30,31}

$$r_{dc}^2 = \omega_0^2 - \omega_d^2 \quad (7.3)$$

Here ω_d and ω_0 denote the angular frequencies for the damping and damping free natural vibration respectively. In terms of wavenumber, the above equation can be rewritten as,

$$r_{dc}^2 = 2\pi c(\bar{\nu}_0^2 - \bar{\nu}_d^2) \quad (7.4)$$

Where, c denotes the velocity of light in free space. The damping constant along with the frequency shift was raised for the composite samples and after reaching a maximum for PBS3 film it started to fall. This suggests the afore-mentioned interfacial interaction and enhancement of β phase of PVDF upto PBS3.

7.3.6. Electrical properties studies

The application of external electric field induces polarization within all the films. The piezoelectric coefficient of the composite system is linearly proportional to the dielectric constant or the polarization of the system. Thus, the performance of the hybrid films due to the mechanical stress can be roughly estimated by observing the variation of dielectric constant without presence of any external DC field. Hence, the frequency dispersion of dielectric constant, loss and conductivity were thoroughly studied. The dielectric constant was calculated considering parallel plate capacitor structure and the below mentioned formula was used for evaluation.

$$\epsilon_r = \frac{\epsilon}{\epsilon_0} = \frac{Cd}{\epsilon_0 A} \quad (7.5)$$

C is the capacitance of the MIM capacitor, A is the effective electrode area, d is the thickness of the film and ϵ_0 ($= 8.854 \times 10^{-14}$ F/cm) is the dielectric constant of vacuum. **Figure 7.5(a-c)** narrate the frequency dispersion of dielectric constant (ϵ_r), tangent loss ($D = \tan\delta$) and ac conductivity (σ_{ac}) of all the films in the range from 40 Hz to 10 MHz. Due to space charge and interfacial polarization, the dielectric constants of all the films were higher in the low frequency range which began to decrease as frequency increased.³² As frequency increases, the dipoles in the composite system fail to chase the instantaneous polarity change of the external ac field and as a result the polarization lags behind the input field.^{33,34} The high polarization at low frequency exhibited by all the films called Maxwell-Wagner interfacial polarization (MWIP) and was

aroused because of the interactions occurring between the space charges of BSO and the tiny molecular dipoles of PVDF.³⁵ Dielectric loss or tangent loss is another important factor to note. It is the relaxation loss of the system arises due to the phase lag of the oscillating dipoles with respect to the applied electric field. The tangent loss ($\tan \delta$) or the dissipation factor (D) physically signifies the ability of storing energy and the loss dissipated as heat. It can be deduced from the relation

$$D = \tan \delta = \frac{\varepsilon''}{\varepsilon'} \quad (7.6)$$

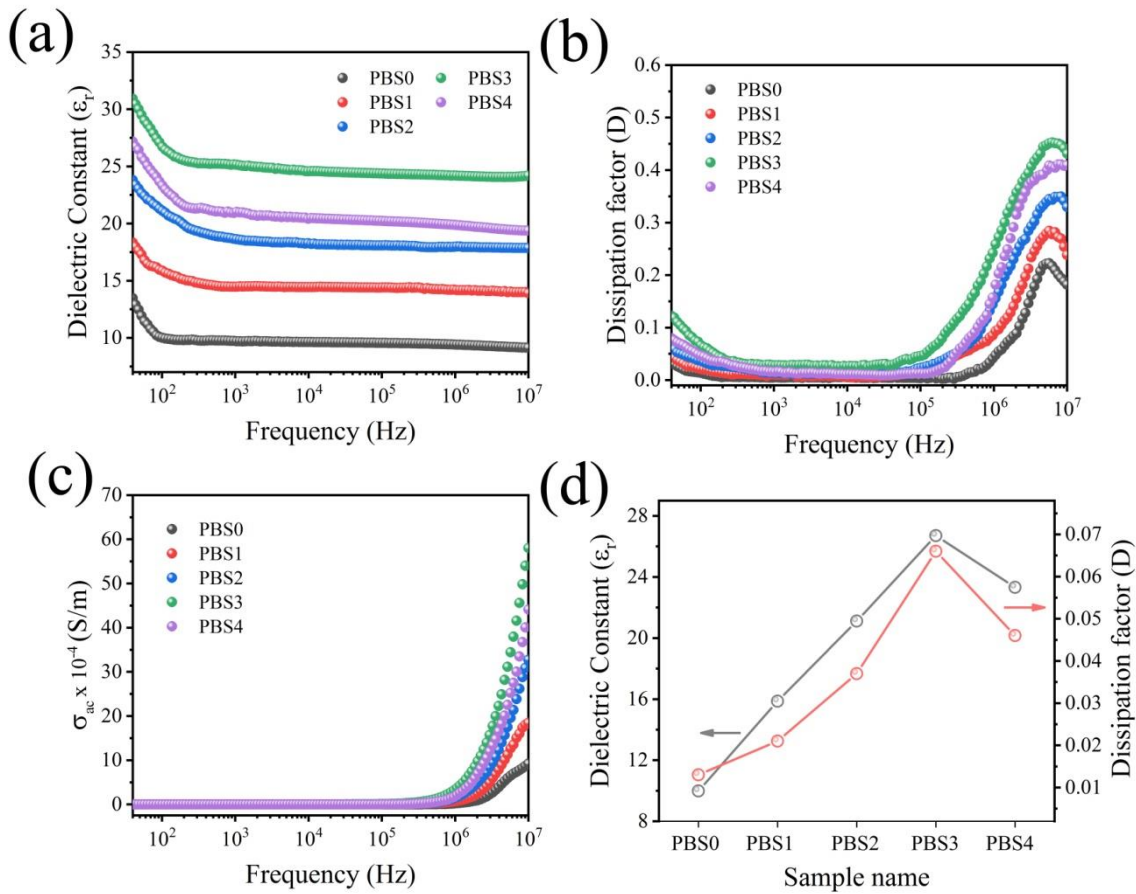


Fig. 7.5. Frequency dispersion of (a) dielectric constant, (b) dissipation factor and (c) ac conductivity for the samples; (d) the variation of dielectric constant and dissipation factor with the BSO content at frequency 100 HZ

ε' and ε'' are the real and imaginary components of the complex dielectric permittivity respectively. The homogeneous distribution of nanorods results a very low tangent loss (<0.5) throughout the total frequency range which is desired criteria for practical application.³⁶ The

variation of dielectric constant and dissipation factor for different films at 100 Hz are presented in **Figure 7.5(d)**. The high aspect ratio nanorods were capable to convert the polymer chain into all-trans configuration with lower volume fraction (3%), by providing high interface region. This in turn boosts interfacial polarization and dielectric constant for hybrid films. Although, the dielectric constant was increased upto PBS3 film, the same was decreased with more introduction of BSO. Excess perovskite loading may leads to the formation of agglomeration which reduces the interfacial polarization and thus the dielectric constant.³³ The frequency variation of ac conductivity was evaluated from the following relation

$$\sigma_{ac} = 2\pi\varepsilon_0\varepsilon_r\tan\delta \quad (7.7)$$

The conductivity for the hybrid films showed a significant increment at higher frequency where polarization was minimum. The conductivity was also increased most for the PBS3 film. The increment in conductivity helps to enhance the output current from the device. The dielectric constant is directly related to the piezoelectric coefficient of the polymer. Thus the piezoelectric coefficient (d_{33}) was expected to increase with the enhancement in dielectric constant.

7.3.7. The output performance of BSO/PVDF nanocomposite films

To examine the response of the BSO/PVDF hybrid films, MIM structured devices with dimension of $1.5 \times 1.5 \text{ cm}^2$ were formed using aluminum foil as electrode material and Cu wires were used for connection. The devices were laminated to reduce external effects affecting the original output from the devices. Without using any additional electrical poling activity, the piezoelectric outputs of all devices were taken. For free hand repetitive hammering (while wearing lab gloves) in a vertical direction, the output responses of all the devices were recorded. The PBS0 sample yielded 5.27 V open circuit voltage (V_{oc}) and 0.78 μA short circuit current (I_{sc}) whereas, the PBS3 sample exhibited 38.51 V and 3.59 μA respectively under similar vertical pressure. The responses are shown in **Figure 7.6 (a,b)**. These data also point to the improved output performance of PBS3 as compared to PBS0. Better piezoelectric response was reflected from the stronger electroactivity of PBS3 which generated ~ 7.3 times more V_{oc} and ~ 4.6 times more I_{sc} than PBS0 under identical mechanical strain. The occurrence of electrical potential difference because of the application of mechanical strain is the reason behind this behavior. An potential difference may be aroused between both the electrodes to remunerate this internal

potential created due to the proper alignment of the dipoles. This potential difference results as a current flow in the external circuit, the output signal of the devices. In the reverse condition, *i.e.* when the external mechanical strain was removed, the charges accumulated at both sides of the films were flowed back to the opposite ends generating another electric impulse. In this case, the difference was only the direction of response.³⁷ As a result, a pulse type signal was generated for the periodic press-release input. It was observed that there was an asymmetry in the peaks of output voltage and current for positive and negative directions. Actually, the difference between applied forces on the device at the time of pressing and releasing is the reason behind it.

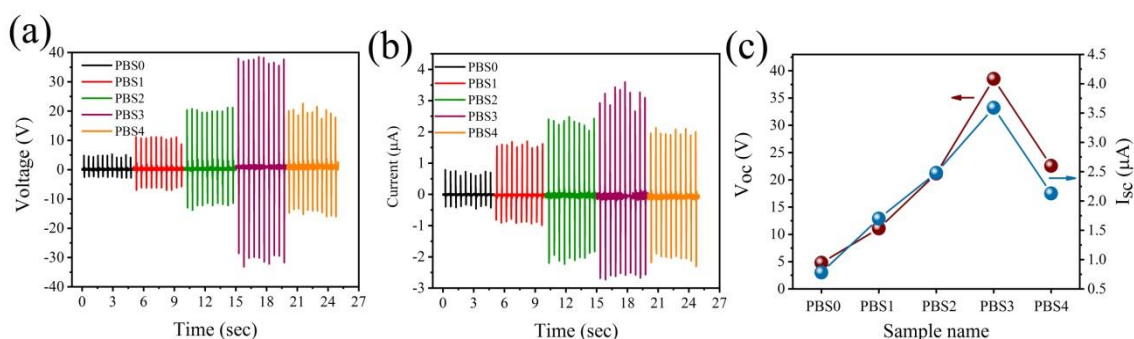


Fig. 7.6. (a) Open circuit voltage, (b) short circuit current for all the devices and (c) the plot of maximum V_{oc} and I_{sc} for the samples

To understand the difference of performance between PBS0 and PBS3 devices, the realization of the role of BSO is utmost important. The inclusion of BSO into the hybrid films enhanced the β phase of the films which was confirmed from the XRD and the FTIR analysis. Along with the enhancement in the electroactive β phase, the association also exhibited high dielectric constant, which further enhanced the piezoelectric charge coefficient d_{33} . Additionally, BSO's rod-like morphology made it easier to reach the percolation limit, and the best device was made with a lower volume fraction of BSO. The variation of open circuit voltage and short circuit current for all the devices are shown in **Figure 7.6 (c)**.

Considering all the results, the supremacy of the film PBS3 was established and thus further work was conducted on it. The forward and reverse voltage and current for PBS3 are shown in **Figure 7.7 (a,b)**. The results indicate that the output response is due to piezoelectric phenomenon *i.e.* the appearance of pulse like voltage/ current signal is not due to any arbitrary mechanical or electrical disruptions. The enlarged view of those output signals are presented in

the inset respective figure. For the practical high-power DC source, the PBS3 was employed to a bridge rectifier circuit and the rectified output was recorded using an oscilloscope. As observed from the **Figure 7.7(c)**, the maximum rectified voltage for the best performed device was 34.57 V under periodic free hand hammering. The zoom view of this output is illustrated in **Figure 7.7(d)** along with the used circuit diagram for rectification (shown in the inset). By stabilizing the pulse like output signals with full-wave rectifiers and voltage regulators, these hybrid devices can also be used to power electronic devices.

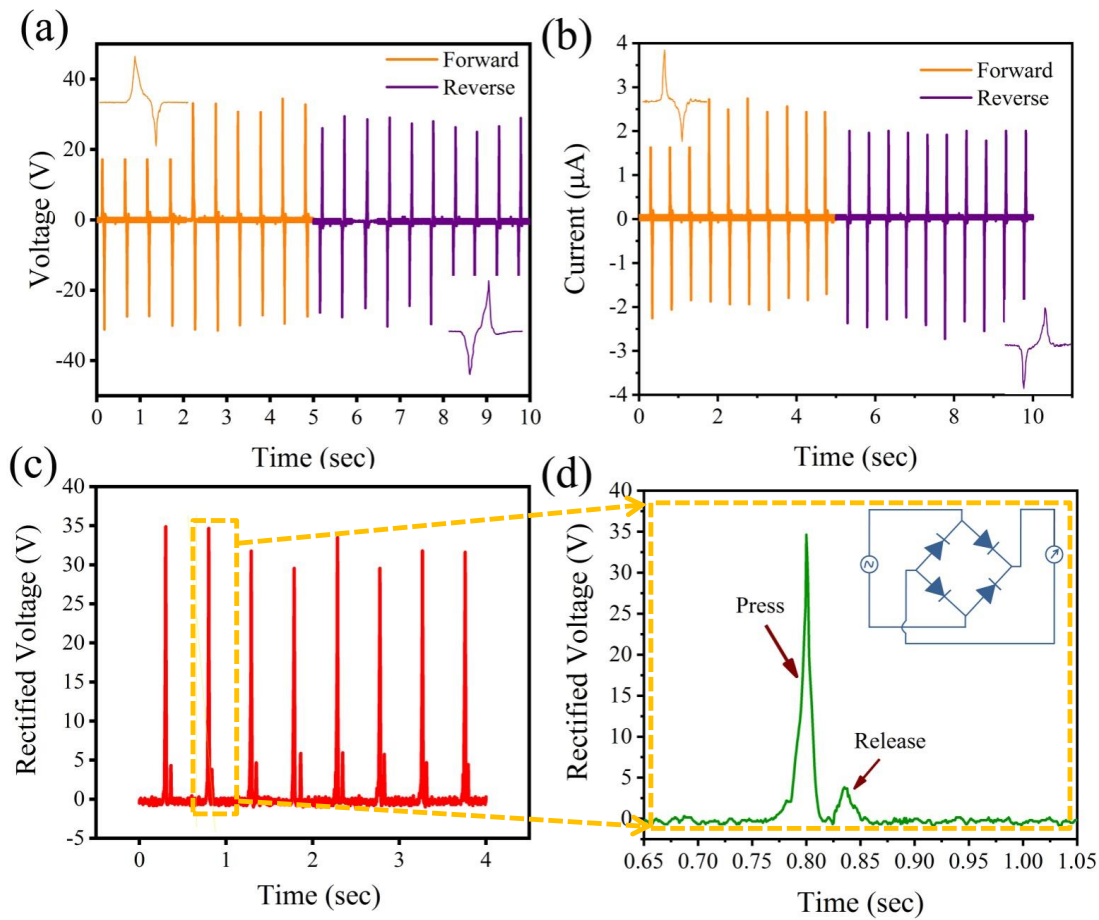


Fig. 7.7. Forward-reverse (a) voltage and (b) current for PBS3; insets are the corresponding enlarged views; (c) rectified voltage and (d) its enlarged version. The schematic of the circuit of bridge rectifier is shown in inset of (d)

During periodic hammering, the charge (Q) accumulated by PBS3 device with a force of 12N, measured by a load cell was evaluated by integrating positive half of J_{sc} (short circuit current per unit area) with respect to time *i.e.* $\int J_{sc} dt$. The piezoelectric coefficient was estimated from the

formula, $|d_{33}| = \frac{Q}{F}$.³⁸ The assessed values of $|d_{33}|$ for the PBS0 and PBS3 are 65 pC/N and 21 pC/N respectively. As previously mentioned, the devices were well laminated using professional lamination device to eliminate all the external and tribo-electric effects. The piezoelectric voltage coefficient was calculated using the relation $g_{33} = \frac{d_{33}}{\epsilon_0 \epsilon_r}$.³⁹ The values of g_{33} for PBS0 and PBS3 were 0.24 Vm/N and 0.30 Vm/N respectively. Thus, the calculated value of the figure of merit ($\text{FOM} = d_{33} \times g_{33}$) for the device PBS3 ($19.5 \times 10^{-12} \text{ Pa}^{-1}$) was enhance 3.86 times from the device PBS0 ($5.04 \times 10^{-12} \text{ Pa}^{-1}$).⁴⁰ These results validate the high performance capability of PBS3 device as a piezoelectric device.

7.4. Conclusion

Barium stannate nanorods with average diameter 15 nm and length 2.5 μm were synthesized using hydrothermal method followed by calcination at 500°C. Highly flexible, visibly transparent BaSnO₃/PVDF nanocomposite films were fabricated using solution-drop casting method. From the X-ray diffraction analysis and Fourier transform infra-red spectroscopy it was confirmed that the electroactive phase for the hybrid samples was enhanced (84%) with the perovskite content. The composite system showed a high dielectric permittivity of 26.71 at 100 Hz with a loss 0.066. The high aspect ratio nanorods helped to improve the electrical properties of the composite sample by enhancing the interfacial polarization between the surface charges of the perovskite and the polymer. The highest open circuit voltage (38.5 V) and short circuit current (3.59 μA) were found for the composite sample exhibiting highest electroactive phase. Furthermore, the best performed device was employed to a bridge rectifier circuit for utilizing the devices to power electronic equipments.

7.5. References

1. S. Wu, M. Lin, Q. Burlingame and Q. M. Zhang, Applied Physics Letters, 104 (2014) 0729031–0729034
2. T. Wang, L. Jin, C. Li, Q. Hu, X. Wei and D. Lupascu, Journal of American Ceramic Society, 98 (2014) 559–566
3. Q. Li, K. Han, M. R. Gadinski, G. Zhang and Q. Wang, Advanced Materials, 6 (2014) 6244–6249

4. K. Yu, Y. Niu, F. Xiang, Y. Zhou, Y. Bai and H. Wang, *Journal of Applied Physics*, 114 (2013) 1741071–1741075
5. H. X. Tang and H. A. Sodano, *Nano Letters*, 13 (2013) 1373–1379
6. P. Kum-onsa and P. Thongbai, *Journal of Materials Science: Materials in Electronics*, 32 (2021) 13985–13993
7. F. Ram, P. Kaviraj, R. P. Pramanik, A. Krishnan, K. Shanmuganatha and A. Arockiarajan *Journal of Alloys and Compounds*, 15 (2020) 153701
8. A. Sasmal, S. K. Medda, P. S. Devi and S. Sen, *Nanoscale*, 12 (40) (2020) 20908-21
9. P. Kum-onsa, B. Putasaen, J. Manyam and P. Thongbai, *Materials Research Bulletin* 146 (2022) 111603
10. H. Mizoguchi, P. Chen, P. Boolchand, V. Ksenofontov, C. Felser, P. W. Barnes and P. M. Woodward, *Chemical Materials*, 25 (2013) 3858–3866
11. K. N. D. K. Muhsen, R. A. M. Osman and M. S. Idris, *Journal of Materials Science: Materials in Electronics*, 30 (2019) 7514–7523
12. S. Pal, N. S. Das, S. Bhattacharjee, S. Mukhopadhyay and K. K. Chattopadhyay, *Materials Research Express*, 6 (2019) 105029
13. S. Pal, N. S. Das, B. Das, S. Mukhopadhyay and K. K. Chattopadhyay, *ECS Journal of Solid State Science and Technology*, 10 (2021) 071018
14. P. Martins, A. C. Lopes and S. Lanceros-Mendez, *Progress in Polymer Science*, 39 (2014) 683–706
15. V. K. Thakur and R. K. Gupta. *Chemical Reviews*, 116 (2016) 4260–4317
16. S. Egusa, Z. Wang, N. Chocat, Z. M. Ruff, A. M. Stolyarov, D. Shemuly, F. Sorin, P. T. Rakich, J. d. Joannopoulos and Y. Fink, *Nature materials*, 9(8) (2010) 643-8
17. X. Cai, T. Lei, D. Sun and L. Lin, *RSC Advances*, 7 (2017) 15382–15389
18. N. Soin , P. Zhao , K. Prashanthi , J. Chen , P. Ding , E. Zhou , T. Shah , S. C. Ray , C. Tsonos , T. Thundat and E. Siores, *Nano Energy*, 30 (2016) 470–480
19. D. Mandal, K. Henkel and D. Schmeiser, *Physical Chemistry Chemical Physics*, 16 (2014) 10403–10407
20. S. Jana, S. Garain, S. Sen and D. Mandal, *Physical Chemistry Chemical Physics*, 17 (2015) 17429–17436

21. A. Sultana, M. M. Alam, P. Sadhukhan, U. K. Ghorai, S. Das, T. R. Middya and D. Mandal, *Nano Energy*, 49 (2018) 380–392
22. J. Fu, Y. Hou, , M. Zheng and M. Zhu, *Journal of Materials Science*, 53 (2018) 7233–7248
23. F. Zhong, H. Zhuang, Q. Guc and J. Long, *RSC Advances*, 6 (2016) 42474
24. L. Li, M. Zhang, M. Ronga and W. Ruan, *RSC Advances*, 4 (2014) 3938–3943
25. S. Jana, S. Garain, S. Sen, D. Mandal, *Physical Chemistry Chemical Physics*, 17 (2015) 17429–17436
26. P. Thakur, A. Kool, B. Bagchi, S. Das and P. Nandy, *Applied Clay Science*, 99 (2014) 149–159
27. S. Mondal, T. Paul, S. Maiti, B. K. Das, K. K. Chattopadhyay, *Nano Energy*, 74 (2020) 104870
28. A. Anand and M. C. Bhatnagar, *Materials Research Express*, 6 (2019) 055011
29. A. Sultana, P. Sadhukhan, M. M. Alam, S. Das, T. R. Middya and D. Mandal, *ACS applied materials & interfaces*, 10 (2018) 4121–4130
30. S. Sarkar, S. Garain, D. Mandal and K. K. Chattopadhyay, *RSC Advances*, 4 (2014) 4 8220–4 8227
31. D. Mandal, K. Henkel and D. Schmeiser, *Physical Chemistry Chemical Physics*, 16 (2014) 10403–10407
32. S. Nayak, T. K. Chaki and D. Khastgir, *Industrial & Engineering Chemistry Research*, 53, (2014) 14982–14992
33. C. Behera, R. N. P. Choudhary and P. R. Das, *Journal of Polymer Research*, 24 (2017) 56
34. G. Chen, X. Wang, J. Lin, W. Yang, H. Li, Y. Wen, L. Li, Z. Jiang and Q. Lei, *Journal of Materials Chemistry C*, 4 (2016) 8070–8076
35. A. C. Lopes, C. M. Costa, R. S. i Serra, I. C .Neves, J. G. Ribelles and S. Lanceros-Mendez, *Solid State Ionics*, 235 (2013) 42–50
36. A. Sasmal, A. Patra, P. S. Devi and S. Sen, *Composites Science and Technology*, 8(213) (2021) 108916
37. S. Mondal, T. Paul, S. Maiti, B. K. Das, B. K.; Chattopadhyay, K. K. *Nano Energy* 2020, 74, No. 104870

38. A. Sultana, S. K. Ghosh, M. M. Alam, P. Sadhukhan, K. Roy, M. Xie, C. R. Bowen, S. Sarkar, S. Das, T. R. Middy and D. Mandal, ACS Applied Materials Interfaces, 11 (2019) 27279–27287.
39. C. Ghosal, S. K. Ghosh, K. Roy, B. Chattopadhyay and D. Mandal, Nano Energy, 93 (2022), 106843.
40. S. K. Ghosha and D. Mandal, Nano Energy, 53 (2018) 245–257.

Conclusion and Future outlook

In this chapter a comprehensive summary for the main conclusions of the research presented in the chapters 4-7 of the thesis and outline of future research directions will be addressed.

8.1. Conclusion

To summarize, the works presented in this thesis narrate (i) the synthesis of pure perovskite oxide BaSnO_3 by monitoring synthesis temperature and time, (ii) thoroughly discuss the effect of calcination temperature on grain size along with its effect on electrical properties, (iii) study the effect of DC bias tuning on the electrical properties of pure and vanadium doped BaSnO_3 extensively, (iv) design efficient BaSnO_3 based cold-cathodes, (v) fabricate BSO/PVDF composite films with significant increment in polarization and conductivity and demonstrate their performance.

In chapter 4, the phase pure nanocrystalline BaSnO_3 using solid-state reaction method was achieved by optimizing the duration of heating. The effect of grain size and the level of porosity with calcination temperature were thoroughly investigated. A systematic collaboration between enhancement in capacitive nature of BaSnO_3 and the aforesaid two morphological characteristics was established.

Chapter 5 furnished the bias dependent impedance spectroscopy to analyze the electrical properties for the intrinsic and vanadium doped BaSnO_3 which was attempted to unlock the associated relaxation mechanisms particularly in radio frequency zone. The effect of grain size reduction and enhancement in porosity became responsible for low dielectric permittivity and high loss for doped samples than the pristine one. The DC bias variation played a key role to enhance the overall dielectric permittivity and to reduce effective grain and grain-boundary resistances of vanadium doped BaSnO_3 nanocubes which in turn can boost the tuning capacitive performance at room temperature in different micro-electronic devices.

The lack and necessity of exploring field electron emission from lead free perovskite materials was realized and hence, investigation in this direction was carried out extensively which is described in chapter 6. Motivated by simulation outcomes, actual experiment was executed which shows prominent and stable field emission properties of vanadium doped BaSnO_3

nanocubes, with turn on of $6.6 \text{ V}/\mu\text{m}$ for 5% vanadium doped sample. The effect of inter-electrode separation was also studied to locate the optimum device configuration.

Chapter 7 addressed the enhancement of electrical properties of BSO/PVDF nanocomposite films due to increase in the amount of BaSnO_3 . The electroactive phase was enhanced upto 84% for the best performing composite film. The high aspect ratio of nanorods plays a significant role to enhance the interfacial polarization and to prevent agglomeration, generally causes loss into the composite system. The high dielectric constant of BaSnO_3 promotes the BSO/PVDF system to become easily polarized which in turn enhance the device performance.

8.2. Future outlook

Although some notable and important results from the perovskite oxide BaSnO_3 have been achieved and presented in this thesis but still there are some areas which can be improved and some can be explored. I would like to mention some areas on which I wish to work if I get chance in future.

- Development of some cost-effective and low temperature synthesis strategies.
- Tuning the electron emission by controlling morphology and light illumination.
- Suitable doping in anionic site and study the electrical properties.
- Fabrication of compatible BaSnO_3 composite to enhance the electrical properties of BaSnO_3 /PVDF composite system.
- Tailoring the morphology and study the photocatalysis application which is rarely explored area for BaSnO_3 .